Investigating the Effects of Thermally Driven Degradation in Solid Oxide Fuel Cells

Thomas Michael McDougal Heenan

Submitted in part fulfilment of the requirements for the degree of Doctor of Philosophy at University College London

Electrochemical Innovation Lab
Department of Chemical Engineering
University College London

2018

Declaration

I, Thomas M. M. Heenan confirm that the work presented in this thesis is my own. Where information has been derived from other sources, I confirm that this has been indicated in the thesis.

Signature ……

Date ……

Acknowledgements

I would like to start my acknowledgements where my PhD journey began: a research placement during the second summer of my undergraduate. My undergraduate tutor, Paul Shearing, had not so long ago persuaded me against the awful mistake of leaving my undergraduate; his imploration during those discussions is the first thanks, of many, that I owe him.

Leon Brown, a PhD student at the time, mentored me through the eight week placement where we developed technology for real-world applications the likes of which I had never been exposed to before. This really triggered my interest in a career in research, and his guidance during this time remains invaluable.

After finishing the summer placement and returning to my undergraduate, I began eyeing up potential PhD positions. Discussions with friends and family led me to conclude that I should search for exemplary supervisors in order to obtain everything that I wanted from a PhD. Luckily for me, I had already found them: Paul Shearing and Dan Brett. These two are tremendously intelligent but so down-to-earth that conversations, whether technical or otherwise, are always effortless. I have a lot of respect for both Dan and Paul, their leadership spans way beyond the requirements of a supervisor and I wouldn't be where I am today without them.

Having established my two supervisors, I began working in the lab as a PhD student and was introduced to James Robinson. James taught me a great deal, particularly in my early years, guiding me through the transition from undergraduate to postgraduate. I owe him a lot of thanks for this. He has also always been there for me outside of the lab which requires a second thanks.

Now I would also like to give a special thanks to Trevor Hansel, without whom I may never have ventured to London in the first place! Trev has made sure that I stay true to my Swansea roots while helping me navigate my research career. I am very thankful for all of his help.

The next couple of people that I would like to thank were office neighbours: Donal Finegan and Bernhard Tjaden. Both unique and very inspirational people, I have many fond memories with these two both in and out of the office. Thanks should also be directed to who has probably been my closest collaborator and gym partner Xuekun Lu. We have worked on many projects together (and hopefully many more) but also made sure to spend equally as many hours in the gym.

Naturally, one requires a support network outside of the office too, and I would like to note a particular thankyou for the Spa Bros: Maximilian Maier and Chunmyson Tan. Other important drinking buddies are the eccentric duo Vidal Bharath and Erik Engebretsen and my fellow Swansea-man Rhod Jervis. Another noteworthy individual is Tom Budd, my friend and fellow UCL-alumni, Tom has been with me every step of the way. Lastly, I would also like to acknowledge my assemblage of loyal Swansea pals: Tom Davies, Craig Seaman and Sam Roberts and the many others.

Of course there are also many others that are worthy of a thank you so I would like to acknowledge all of the following, both old and new: the UCell members, fellow PhD students, Post-Docs, the lab management, the department office staff, CDT students from across the UK and my many collaborators.

Finally I would like to thank my family: my wildly intelligent brother, who is always keeping me on my toes; my loving mother, who continues to look after me even though I am hundreds of miles away, and my genius father, the fountain of knowledge whose workshops initially catalysed my interest in engineering.

Abstract

One of the most promising devices for low-carbon energy conversion is the solid oxide fuel cell (SOFC). Theoretically, SOFCs show great potential; operating at temperatures between 600-1000 °C the SOFC allows fast reaction kinetics and fuel versatility without the need for expensive platinum catalysts. However in practice, SOFCs can suffer from considerable losses in electrochemical performance due to a multitude of complex degradation mechanisms. This thesis aims to expand our understanding of such mechanisms. Techniques for the three-phase segmentation of SOFC anode materials using nano X-ray computed tomography (CT) and 4D X-ray CT are demonstrated using lab-based instruments, previously only possible using specialist synchrotron facilities. Subsequently, a series of degradation studies are conducted across multiple length-scales using a combination of absorption and diffraction X-ray characterisation methods. Firstly a macroscopic X-ray CT investigation is carried out at cell-level inspecting the effect of start-up time on the delamination of the anode from the electrolyte. Secondly, a microscopic X-ray CT study is conducted on the particle-particle interaction within the anode during operational thermal cycling. Finally, a crystallographic investigation is conducted using synchrotron X-ray powder diffraction to understand the thermo-mechanical properties of anode materials. The experiments reported here improve our understanding of the intrinsic link between the mechanical and electrochemical performance of SOFCs and the influence of microstructure. Understanding is gained from the importance of the materials chosen during manufacturing to the effects of the thermal profiles during operation. These findings are expected to influence the future of SOFC technology from fundamental research to commercial application.

Impact Statement

One of the most promising devices for low-carbon energy conversion is the SOFC. This thesis presents original research techniques, methodologies and analysis which have been disseminated in the form of international conference talks, journal publications, journal covers and public engagement activities.

Several techniques which have been developed by the author are explained fully allowing their reproduction and application to future studies. These techniques have been extended into the analysis of several prominent mechanisms responsible for fuel cell degradation through a combination of established and novel analysis techniques. The author presents significant discoveries across multiple length and time scales. These results may impact further fundamental research via the employment of the same investigative techniques to inspecting different parts of the operational profile or materials. The information may be used to aid in the development of next-generation materials and optimised cycling profiles, the implications of which will be seen from cell manufacture to operation. Consequently the dissemination of this work is not limited to academia but also extends into the commercial sectors.

These findings have predominantly been disseminated through open-access journal publications, journal covers and a mixture of national and international conference talks. The author also organised a conference which was held in Oxford that brought together academics and industrial partners from over twenty institutions from as far as Tsinghua University, China. The author has collaborated with colleagues from many UK universities and also international institutions such as the European Synchrotron Radiation Facility (ESRF, Grenoble, France), The Paul Scherrer Institute (PSI, Villigen, Switzerland),

Argonne National Labs (ANL, Lemont, USA), the National Aeronautics and Space Administration (NASA, Houston, USA) and the National Renewable Energy Labs (NREL, Colorado, USA). The author has also accumulated hundreds of hours of community engagement through the delivery of workshops and talks to members of the public from a variety of ages and backgrounds. Open discussions such as this improve the public perception of emerging technologies and enable the public to observe the application of fundamental research to real-world applications.

Ultimately this work has disseminated improved understandings of the critical mechanisms which currently inhibit fuel cell competitiveness within the commercial market. These results have bridged many fields of discipline from fundamental science to applied engineering and have involved a wealth of national and international collaborations. Through the engagement across many platforms from typical academic outlets, such as journals, to public activities and teaching, this work has reached many areas of the public from the layman to the specialists.

Contents

Table of Contents

Tables

Figures

Nomenclature

Activation Overpotential	η_{act}
Actual path length that a species must travel	L
Alkaline Fuel Cell	AFC
Alumina or Aluminium Oxide	Al_2O_3
Angle, e.g. diffracted radiation or cell wall	θ
Angular divergence	Θ_s
Anode Functional Layer	AFL
Anode Support Layer	ASL
Attenuation length	λ_a.
Auxiliary Power Unit	APU
Average correlation coefficient	CC_{Avg}
Bandwidth	BW
Bipolar-Plate	BPP
Brilliance	B_s
Bulk generic variable notation	$\bar{v}$
Carbon Monoxide	CO
Centre for X-ray Optics	CXRO
Ceramic-Metal Composite	Cermet
Change in local lattice parameters	dL
Charge-Coupled Device	CCD
Chromium	Cr
Combined Heat and Power	CHP
Computed Tomography	CT
Concentration Overpotential	η_{con}

Conductivity	σ
Copper	Cu
Correlation coefficient	CC
Crack diameter	$\emptyset$
Crack length	l
Cross-sectional area of the beam	A
Current Density	j
Digital Volume Correlation	DVC
Effective conductivity	σ^{Eff}
Electron	e^-
Energy Dispersive X-ray	EDX
Equivalent diameter	d_{eq}
Euclidean distance between the initial and final locations	L_E
European Synchrotron Radiation Facility	ESRF
Face-Centred Cubic	FCC
Feldkamp-Davis-Kress algorithm	FDK
Feret diameter, for phase *j*	$\emptyset_j$
Field Of View	FOV
Flow of an empty volume for volume V	Q_{empty}
Focused Ion Beam Scanning Electron Microscope	FIB-SEM
Four-Dimensional (3 spatial + time)	4D
Fractal dimension	D
Fuel Efficiency	ξ_{fuel}
Gadolinium Doped Ceria	GDC

High Resolution (imaging mode)	HRes
Horizontal displacement	Δx
Hydrogen	H_2
Incident radiation intensity	I
Infrared	IR
Initial condition defined by lattice parameter	L_i
Insertion Device	ID
Internal Combustion Engine	ICE
Inverse of the mathematical constant e (=2.71828 to 5 d.p.)	e^{-1}
Lanthanum Strontium Cobalt Ferrite	LSCF
Lanthanum Strontium Manganite	LSM
Large Field Of View (imaging mode)	LFOV
Lattice parameter	L
Lattice spaces	d
Linear Accelerator	Linac
Linear attenuation coefficient	μ
Linear scaling factor	f
Local generic variable notation	v
Mass attenuation coefficient	μ_m
Mass density	ρ
Mass fractions	w_i
Maximum correlation coefficient	CC_{Max}
Maximum lattice parameter	L_0
Methane	CH_4

Methanol	CH_3OH
Microstrip System for Time-Resolved Experiments	MYTHEN II
Miller indices	h,k and l
Minimum correlation coefficient	CC_{Min}
Mixed Ion Electronic Conductor	MIEC
Molten Carbonate Fuel Cell	MCFC
Molybdenum	Mo
National Aeronautics and Space Administration	NASA
National Chemical Database Service	NCDS
National Institute of Standards and Technology	NIST
National Renewable Energy Labs	NREL
Nickel Oxide	NiO
Nickel	Ni
Nitrogen	N_2
Ohmic Overpotential	η_{ohm}
Open Circuit Potential for Temperature T	V_{OCV}^{T}
Operating Voltage	V_{op}
Orthogonal planes	x, y and z
Overall Efficiency	ξ_{overal}
Oxide ion	O^{2-}
Oxygen	O_2
Paul Scherrer Institute	PSI
Phase percolation values, for phase *j*	p_j
Phase-specific volume fraction	φ_j

Phosporic Acid Fuel cell	PAFC
Platinum	Pt
Polymer Electrolyte Membrane Fuel cell	PEMFC
Power Density	P
Ratio of the attenuation coefficients	η_A
Ratio of the greyscale values	η_G
Reduction and Oxidation Reactions	REDOX
Region of Interest	ROI
Representative Volume element	RVE
Silver	Ag
Simulated flow for volume V	Q_{sim}
Solid Oxide Fuel Cell	SOFC
Swiss Light Source	SLS
Temperature at which a non-linear peak occurs	T_{peak}
Temperature increment	dT
The total number of voxels within the ROI	n
Thermal driven deformation	TDD
Thermal Expansion Coefficient	TEC
Thermal Expansion Coefficient non-linear peak	TEC_{peak}
Thermal strain	$\varepsilon_{thermal}$
Thermal stress	$\sigma_{thermal}$
Thermodynamic Efficiency	ξ_{thermo}
Thermomechanical Anlysis	TMA
Thickness	t

Three-Dimensional (spatial)	3D
Tortuosity	ξ
Tortuosity-factor	τ
TPB density	ρ_{TPB}
TPB length	L_{TPB}
TPB percolation	p_{TPB}
Transmission	T
Transmitted radiation intensity	I_0
Triple-Phase Boundary	TPB
Tungsten	W
Two-Dimensional (spatial)	2D
Uninterruptable Power Supply	UPS
Unmanned Aerial Vehicle	UAV
Vertical displacement	Δz
Voltage Efficiency	$\xi_{Voltage}$
Volume analysed	V
Volume of a particle	V_p
Volume specific interfacial contact area, for phases *j* and *k*	$A_{j,k}$
Volume specific surface area, for phase *j*	A_j
Wavelength of the X-ray beam	λ
X-ray Diffraction	XRD
Young's modulus	E
Yttria-Stabilised Zirconia	YSZ

Chapter One: Introduction

1.1. Introduction to Chapter One

This chapter will discuss the motivations for investigating SOFC degradation, the scientific background required to provide sufficient context for the work, and the objectives and structure of the thesis.

1.2. Research Motivation

Depletion of traditional fuel stores has been accompanied by increasing pollution levels. Consequently, motivations to lower carbon-emissions have elevated. To ensure change is achieved on a global scale, a multinational agreement was achieved in 2015 at the Paris climate conference whereby 195 countries agreed a legally binding global climate deal, the first of its kind (1). There are many electrochemical technologies that may be suitable low-carbon substitutes for energy conversion, and the future energy market will likely be formed of several technologies rather than a single replacement (2; 3; 4; 5). However, the social acceptance of emerging technologies, economic infeasibilities in scale-up, and insufficient performance during use are some of the many barriers to market (6; 7). In order to meet targets and support the mass-employment of low-carbon technologies, significant advancements are required in improving the commercial viability of electrochemical devices.

1.3. Scientific Background

One of the most promising electrochemical energy conversion devices is the SOFC. SOFCs operate at high temperatures (600 – 1000 °C) which permits fast reaction kinetics negating the need for expensive platinum catalysts. SOFCs are

highly versatile and can operate on a variety of fuels, including more traditional gases such as hydrocarbons; hydrocarbon operation may provide a useful stepping stone for the transition to a hydrogen economy (8; 9). Unfortunately, the use of high temperatures and impure fuels results in the degradation of the cell; deterioration of the catalyst, delamination of the constituent materials, cracking throughout the structure and deposition of undesirable chemicals are all issues which SOFCs have to overcome. In order to minimise these issues, planar SOFCs typically require very long start-up times on the order of hours or days and although tubular SOFCs are able to withstand higher thermal ramp-rates, issues such as catalyst deterioration remain problematic and insufficiently understood (10; 11).

1.4. Thesis Objectives and Structure

This thesis presents a series of studies into the thermally driven degradation of SOFCs with particular focus on the anode and its interaction with the ceramic electrolyte which is a known cause of cell degradation during operation. The investigations presented here intend to improve our understanding of the complex mechanisms responsible for performance losses during operation: from material choice in manufacturing, to heterogeneities in fabrication, to degradation mechanisms during operation. Several techniques for the characterisation of material structures are explained, including: the three-phase segmentation of anode materials and 4D imaging of materials exposed to operationally relevant environmental conditions. Both techniques use lab-based X-ray nano computed tomography (CT) and were previously only possible using specialist synchrotron

radiation facilities. A series of investigations are presented starting at the macroscopic scale inspecting delamination of the electrolyte from the anode and subsequent cracking within the anode support, moving to the particle-particle interactions and the consequent influences on the reaction site densities, and finally looking to the crystallographic properties of anode materials by X-ray diffraction (XRD) with thermal cycling and the influence of ceramic choice in fabrication. Looking forward, these findings are concluded and assessed across the multiple length scales investigated and consideration is given to the future research of SOFC degradation.

Chapter Two: Literature Review

2.1. Introduction to Chapter Two

This chapter will cover the fundamentals of electrochemical engineering that are essential in order to understand the thermodynamic limitations of the SOFC, as well as the history and commercial development of products, the materials involved in fabrication, their degradation during operation and how one may characterise them.

2.2. Fundamentals of Electrochemical Engineering

Electrochemical cells employ the redox reactions of chemical species to produce a current from the conversion of chemical energy to electrical energy plus heat. Fuel cells are a type of electrochemical cell and operate through the reaction of a fuel, such as hydrogen (H_2), and an oxidising agent, such as oxygen (O_2). These reactions occur within the anode and cathode electrodes which are separated by an electrically insulating membrane that permits the conduction of ions but forces the electrons to pass around an external circuit, producing a current. Fuel cells are typically classified according to the membrane material and operate under various conditions. Common examples are summarized in Table 1.

For the case of an SOFC, oxygen is reduced at the cathode (Equation 1) and hydrogen is oxidised at the anode (Equation 2). The reduction of oxygen produces an oxide ion (O^{2-}) which travels through the ceramic electrolyte and two electrons which travel around the external circuit producing the current. Overall, hydrogen and oxygen are used to convert chemical to electrical energy plus heat (Equation 3) (9; 8).

Table 1 Classification of common fuel cell types including operation temperature and fabrication materials.

Fuel Cell Membrane	Anode/ Cathode	Interconnect	Fuel	Temperature / °C
Alkaline (AFC)	Pt, Ni/Ni	Graphite, Carbon composite, Metallic	H_2	50 – 150
Polymer Electrolyte Membrane (PEMFC)	Pt/Pt		H_2, CH_3OH	50 – 200
Phosphoric Acid (PAFC)	Pt/Pt	Graphite	H_2	150 – 50
Molten Carbonate (MCFC)	Ni alloy/NiO	Metallic	H_2, CO, CH_4	600 – 700
Solid Oxide (SOFC)	Ni Cermet/ Lanthanum-based	Metallic		600 – 1000

Equation 1 $$\frac{1}{2}O_2 + 2e^- \rightarrow O^{2-}$$

Equation 2 $$H_2 + O^{2-} \rightarrow H_2O + 2e^-$$

Equation 3 $$H_2 + \frac{1}{2}O_2 \rightarrow H_2O$$

The performance of an SOFC is often characterised by the power density (P) which the cell can produce. The power density is quantified by the product of the

current density (*j*), *i.e.* the current per unit electrode area, and the cell operating potential (V_{OP}) (Equation 4).

Equation 4 $$P = j \times V_{op}$$

As the current density is increased, the operating cell potential (V_{op}) reduces from the potential at open circuit i.e. the potential at zero current (V_{OCV}^{T}), due to overpotentials ascribed to the activation, Ohmic and concentration losses (Equation 5). The operating cell potential and power density with respect to the current density is often characterised by polarisation and power curves (Figure 1).

Equation 5 $$V_{op} = V_{OCV}^{T} - \eta_{act} - \eta_{ohm} - \eta_{con}$$

The overall efficiency (ξ_{overal}) is quantified by the product of the three efficiencies which contribute to the cell electrical output: the thermodynamic (ξ_{thermo}), voltage ($\xi_{Voltage}$) and fuel (ξ_{fuel}) efficiencies (Equation 6). The SOFC can achieve relatively high efficiencies, for instance, the thermodynamic efficiency exceeds 94 %; the electrical efficiency can often exceed 60 % (12) and fuel utilisation can routinely exceed 80 % (13). Therefore, cell electrical efficiencies can be expected to be around 45 – 50 % and once integrated with systems to recover the heat losses, the overall efficiency can exceed 80 % (14).

Equation 6 $$\xi_{overal} = \xi_{thermo} \times \xi_{Voltage} \times \xi_{fuel}$$

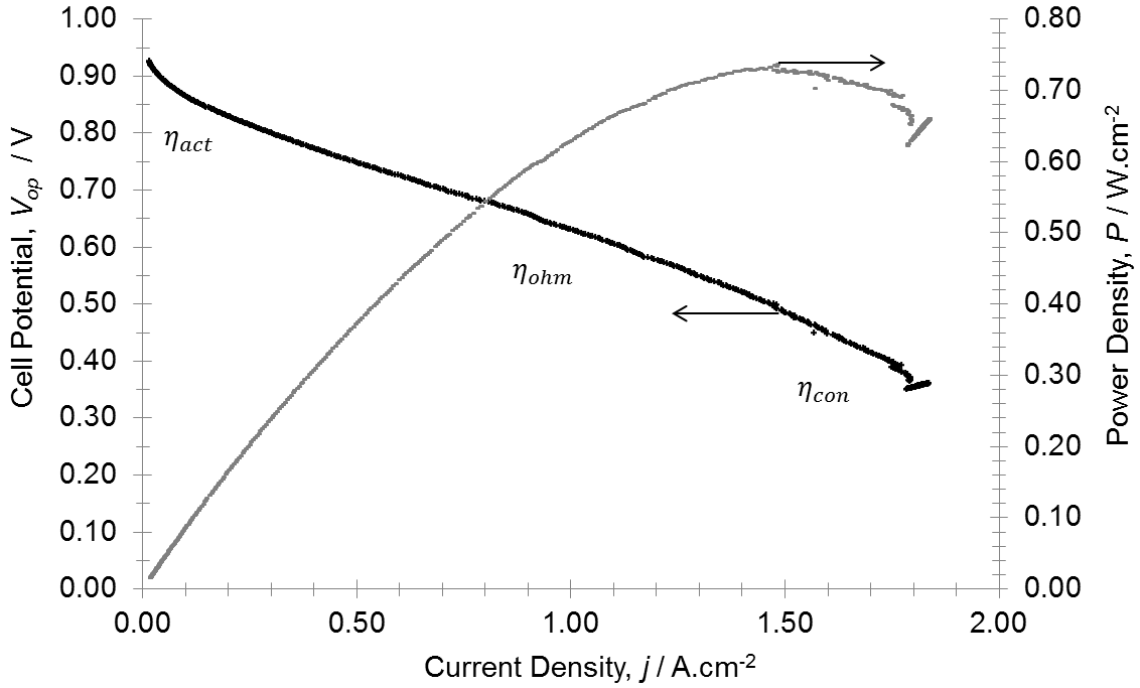

Figure 1 The fundamentals of an SOFC: example polarisation and power curves obtained from a planar cell at 800 °C.

2.3. A Brief History of the Solid Oxide Fuel Cell

Grove proposed the first fuel cell from his home in Swansea in 1839 (15). In 1890, Nernst discovered that zirconia possessed ion conductive properties which were a function of temperature (8) and it was later demonstrated that zirconia could also be used in a fuel cell arrangement by Baur and Preis in 1937 (16).

Significant developments in fuel cell technology came in the 1950s as both the Gemini and Apollo space programmes employed technologies based upon advancements of the Grove-cell, to the Bacon cell. However, improvements in the internal combustion engine (ICE) diverted attention away from electrochemical devices. In 1962 Weissbart and Ruska investigated SOFCs with platinum catalysts for a variety of fuels, demonstrating their versatility in application (16). The drive for commercial production has since been accelerated by rising global temperatures and subsequent monitoring of carbon emissions. As a result, the turn of the century has seen several companies that have established the manufacture of SOFC products on a commercially viable scale (17), some of which have deployed tens of megawatts of power units (18).

2.4. Commercial Applications

Due to the scalability and fuel flexibility that SOFCs offer, applications can range from small single cells to very large stacks; however, SOFCs have become most competitive in the medium to high power market: hundreds of watts to hundreds of kilowatts.

Smaller units considered as single to hundreds of watt installations have been used for powering unmanned aerial vehicles (UAV) and on-board larger vehicles as auxiliary power units (APU) (19). Whereas medium sized applications where single to tens of kilowatts are installed have become popular in residential combined heat and power (CHP) units whereby both the heat and electrical power are both utilised in a single integrated unit (20). Larger stationary units employing hundreds of kilowatts or even megawatt installations have found a market in back-up power generation as a source of uninterruptable power supply (UPS) particularly for applications where power-cuts can be extremely costly (18).

2.5. Components and Materials

Figure 2 displays a simplified schematic of the operational set-up for the two most commonly employed geometries for a single cell: planar and tubular. As can be seen within the figure, the hydrogen-containing fuel is supplied to the anode and the oxidant gas is supplied to the cathode. The two electrodes are separated by a dense electrolyte which is sealed with surrounding gaskets. The current is removed from the electrode surfaces with a metallic mesh or directly through the bipolar-plates (BPP) which also supply the flow fields that aid in gas diffusion. In order to produce high-power units, these cells can be combined in series to form a stack with an increased voltage and the electrode surface area can be increased to raise the net current.

The cell is composed of three key components: two porous electrodes, the anode and cathode which are separated by a dense electrolyte. The electrolyte material must be ionically conducting, electronically insulating, dense to prevent gas crossover and stable in both reducing and oxidising environments. Commonly employed materials include the ceramics Yttria-stabilised zirconia (YSZ) and gadolinium doped ceria (GDC) (21). These ceramics permit oxide ion (O^{2-}) transport from one electrode to the other via the hopping of ions along oxide vacancies. The concentration of such vacancies thus the ionic conductivity is often a function of the amount of dopant *i.e.* amount of yttria or gadolinium added during fabrication (22).

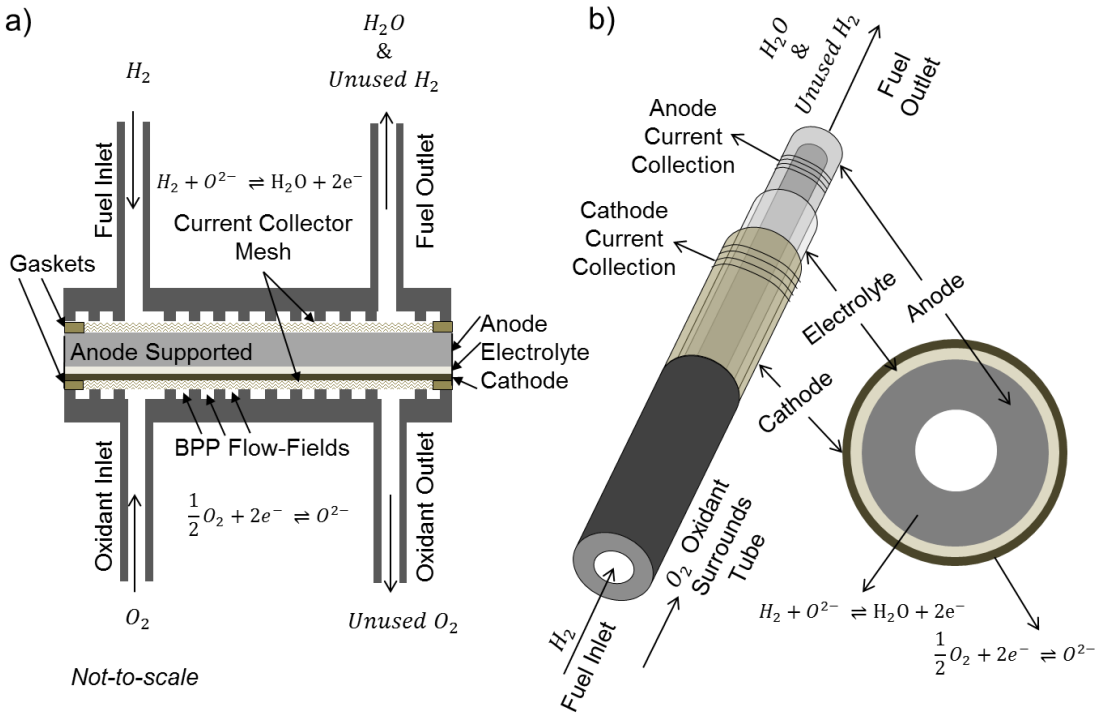

Figure 2 The fundamentals of an operating SOFC unit: a simple schematic of the operational set-up for a) planar and b) tubular cells.

At the cell level the electrodes appear as solid layers however they are actually composed of complex microstructures more comparable to the simplified depiction of an SOFC anode in Figure 3 (23). Complex structures are required in order to effectively promote the three transport processes in the ionic, electronic and gaseous phases, achieved with use of either mixed ionic electronic conductors (MIECs) or composite cermet materials (24). Commonly employed anode materials include metal-ceramic ‘cermets’ of Ni-YSZ or Ni-GDC whereas cathodes are typically perovskite-based compounds such as lanthanum strontium manganite (LSM) or lanthanum strontium cobalt ferrite (LSCF) and are also often combined with ceramics to form composites such as LSM-YSZ (25).

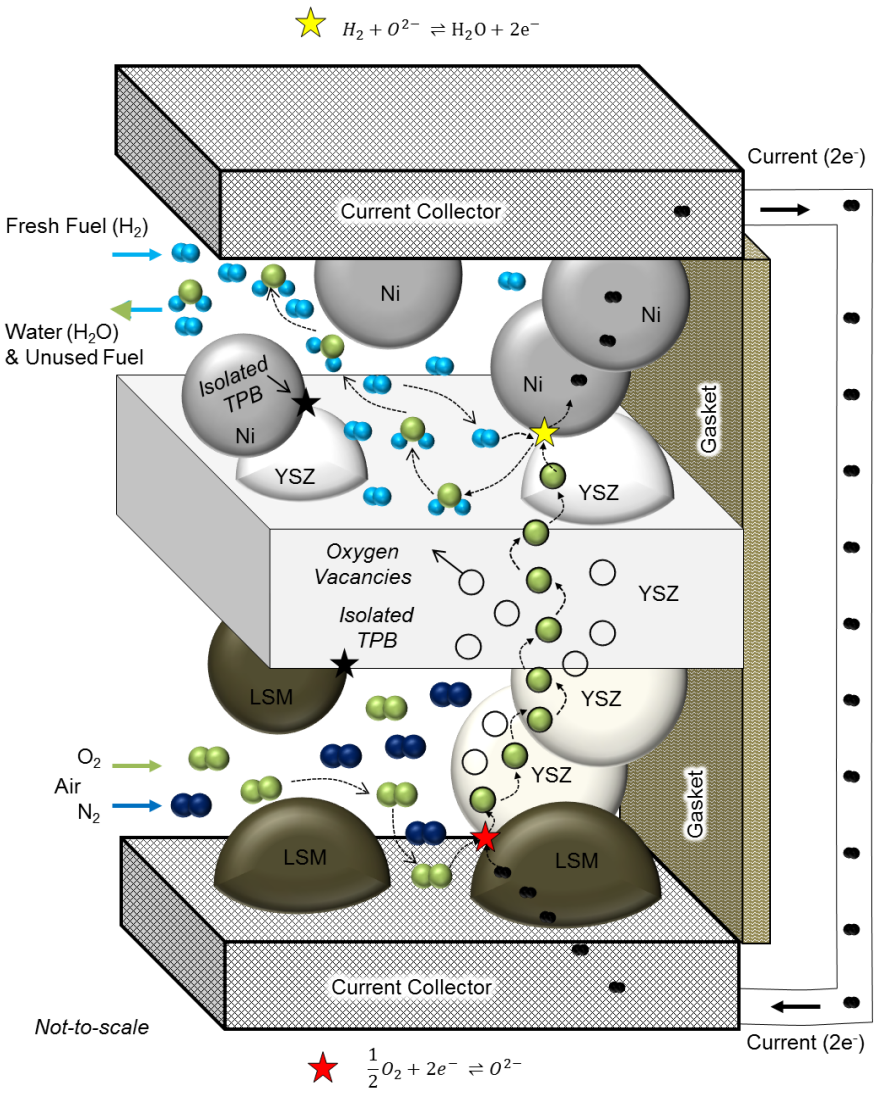

Figure 3 The fundamentals of electrochemistry within an SOFC: a simple schematic of the electrochemical processes within a single cell.

The locations within composite cermet materials where all three phases meet are defined as triple phase boundaries (TPBs) which are considered to strongly influence the electrochemical performance at the cell level (26) as that is where the half reactions are thought to occur (Equation 1 & 2). The sample composition, particle size distributions and phase percolation all contribute to the active TPB density (27; 28).

2.6. Cell Degradation

In order for SOFCs to be competitive with existing technologies they must be able to deliver power within a suitable start-up time and consistently deliver that power throughout the device lifetime. Unfortunately, SOFCs experience degradation during operating and as a result suffer performance losses due to a multitude of complex mechanisms (29).

The nickel metal is typically deposited as nickel oxide (NiO) and reduced to Ni during the first operational start-up cycle. Once reduced, the electrical conductivity within the nickel is high, especially compared to the ionic conductivity within the ceramic *e.g.* the electrical and ionic conductivities of Ni and YSZ at 800 °C are approx. 2.4 S μm^{-1} and 4.3 x 10^{-6} S μm^{-1} respectively (26). However, if re-oxidised for instance during gasket failure (Figure 4) conductivity plummets, impeding electron transport and possibly isolating what were previously percolated reaction sites *e.g.* electrical conductivity of NiO at 800 °C can be around 2.0 x 10^{-6} S μm^{-1} (30). Moreover, re-oxidation is accompanied by a volume change which may be irreversible; the oxidation of nickel can be accompanied by a volume expansion of approximately 70 vol% (31) which, if re-reduced back to nickel, may not be recovered due to the formation of internal voids. This volume change also results in a reduction of the porosity which may impede gas diffusion, particularly problematic at high current densities.

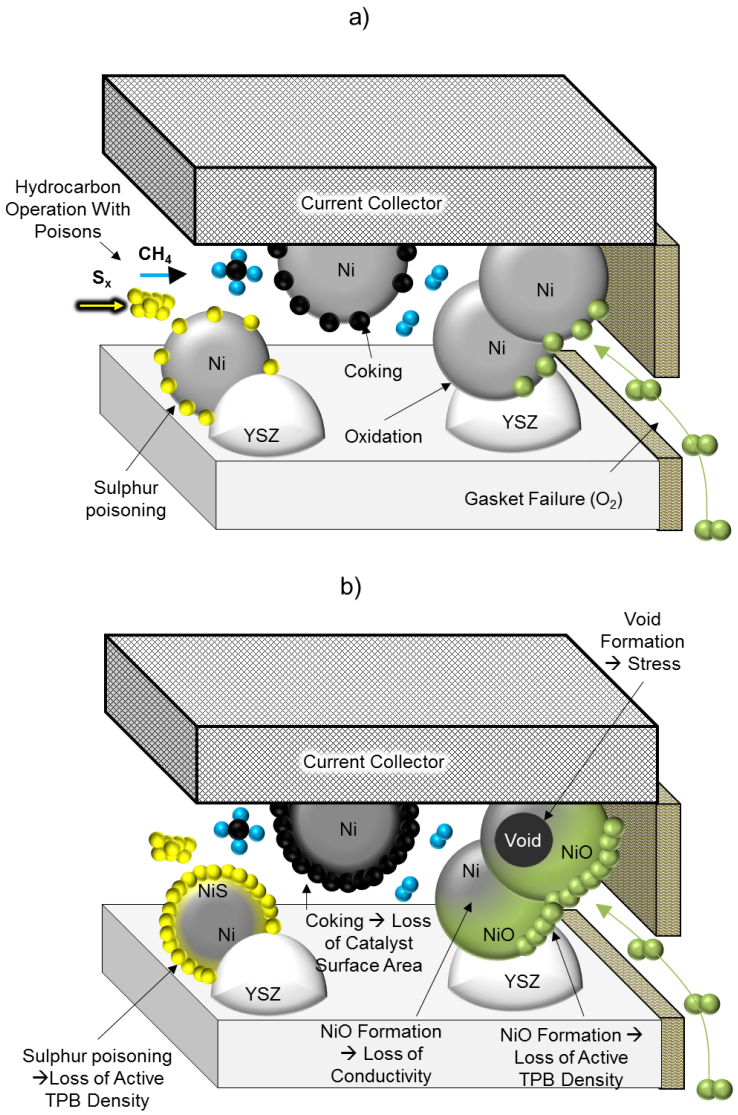

Figure 4 A simplified summary of some critical chemical degradation mechanisms responsible for performance loss in SOFCs.

Suitable start-up times vary between uses (32): during rapid start-up the cell and components are exposed to significant thermal ramp rates in order to reach the operating temperature. Moreover, each material within the unit will expand with a unique thermal expansion coefficient (TEC) inducing strain throughout the cell.

This is particularly problematic for the electrode and electrolyte layers where aggressive thermal strain induced by TEC mismatch between the anode and electrolyte during ramping or cooling can cause cracking or delamination (33).

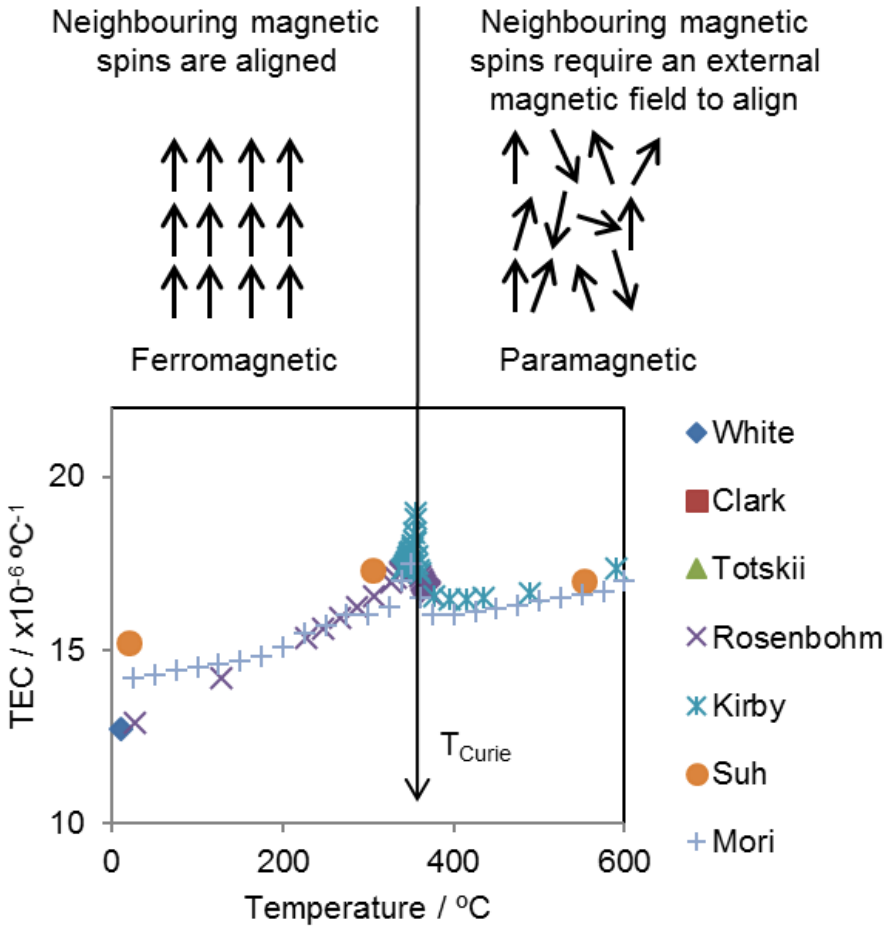

Figure 5 The TEC as reported by multiple authors for pure Ni metal on passing the Curie temperature. (34; 35; 36; 37; 38; 39; 40).

During thermal ramping the NiO and Ni experience magnetic shifts on passing the Néel and Curie temperatures respectively. The Néel temperature is the temperature at which the antiferromagnetic NiO becomes paramagnetic and, the

Curie temperature is the temperature at which the ferromagnetic Ni becomes paramagnetic. These mechanisms occur at *ca.* 250 °C and 360 °C respectively. The transitions are known to cause significant structural changes observed in the TEC of the Ni, resulting in an expansion mismatch peak observed at the crystallographic to macroscopic scale on the passing of the magnetic change (34; 35; 36; 37; 38; 39; 40), see Figure 5.

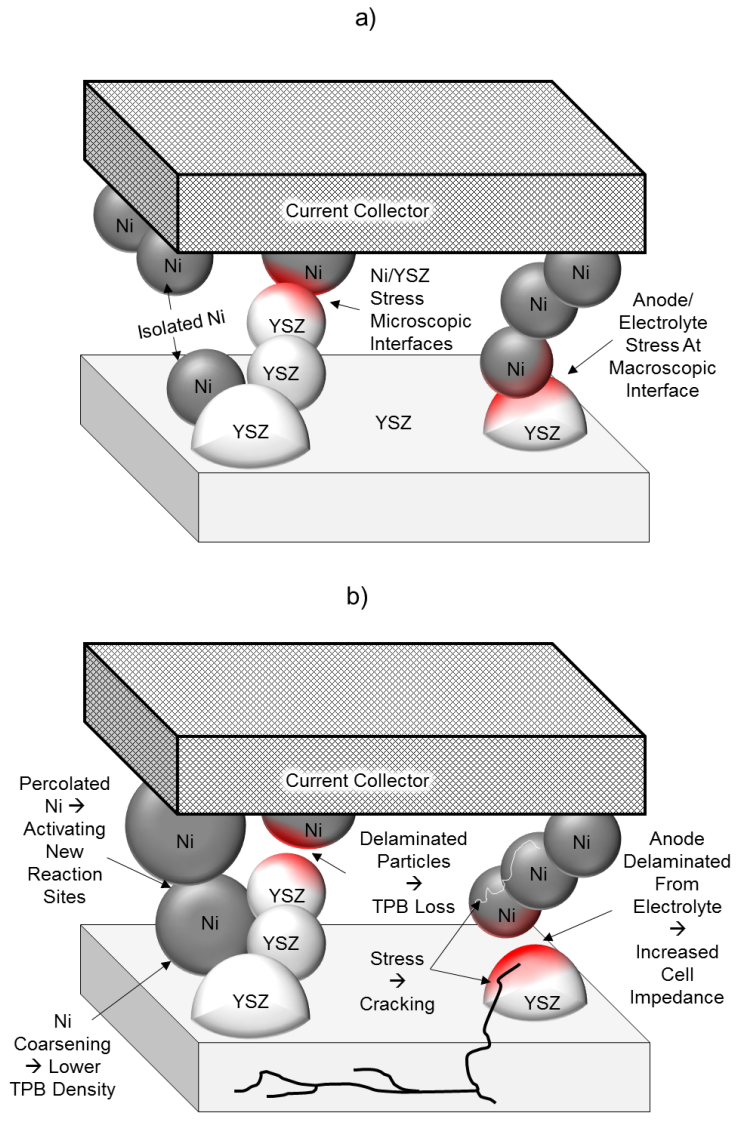

Figure 6 A simplified summary of some critical mechanical degradation mechanisms responsible for performance loss in SOFCs.

Spatial temperature variations can also occur in the form of thermal gradients in non-isothermal environments. Analogous to the TEC mismatch experienced during start-up, these thermal gradients can cause strain throughout the cell; however, strain has been observed to be non-linear due to complex mechanisms responsible for crystallographic stress distributions (41). Stress can lead to cracking and delamination at both a particle and cell level (31; 8), see Figure 6.

Although thermally cycling can cause significant performance loss, cell degradation is not limited to start-up and shutdown; it is considered that sintering effects cannot be neglected at temperatures above 50 % of the melting point of the material, namely the Tamman temperature (42). Ni melts around 1455 °C therefore has a Tamman temperature around 728 °C. To produce consistent power, the cell must retain its current density. And therefore, reduction in the TPB density must be minimised during operation. The TPB density is a function of the particle size and smaller particles can be expected to produce a larger TPB density (28), alas, the higher operating temperatures of an SOFC (800 – 1000 °C) typically exceed the Tamman temperature of nickel. Therefore sintering mechanisms can result in reduced performance due to the reduction in the number of TPB reaction sites, particularly problematic for electrodes with nanostructures (43).

Addition of ceramic to the electrodes increases the TPB density as well as bringing the further benefit of reducing the macroscopic TEC mismatch between the electrode and electrolyte layers (40). Ceramic addition is also thought to inhibit agglomeration mechanisms since the restricting ceramic skeleton limits the routes for Ni mobility (44). Although the cermet materials are thought to reduce

the macroscopic effects of TEC mismatch, it has been suggested that microscopic strain peaks may be observed at the metal-ceramic interface between individual particles, possibly promoting delamination and cracking at a microscale (45; 46). Furthermore, each component within the SOFC unit will have a unique TEC value giving rise to further expansion mismatch problems.

One of the key advantages of the SOFC is in its fuel versatility; the high-temperature operation and Ni metal catalyst can support hydrocarbon reforming reactions directly on the electrode surface allowing the use of hydrocarbons which can be fed directly into the SOFC; however, the reduction of hydrocarbons can also result in the formation of carbon deposits or ‘coking’, and great difficulty can come in eradicating hydrocarbon fuels entirely of impurities such as sulphur which can coat the nickel surface further reducing catalytic activity and even trigger irreversible volume expansion analogous to oxidation (47).

2.7. Microstructural Characterisation

As discussed, the electrode microstructures are complex in order to optimise performance. Specifically, in order to maximise the TPB densities, and thus the performance of the cell, it is essential to understand electrode microstructures in three dimensions (3D). This was first achieved by Wilson *et al.* using focused ion beam scanning electron microscopy (FIB-SEM) (48) and has subsequently been used extensively in SOFC characterisation (49; 50; 51; 52; 53; 54; 55); however, milling techniques such as FIB-SEM result in the destruction of the sample preventing repeated analysis. Therefore non-destructive techniques such as X-ray CT rose in popularity. However, initial studies relied entirely upon the use of synchrotron facilities in order to map the three-phases (56; 57; 58; 59; 60; 61), because lab-based X-ray instruments were only capable of resolving the solid and pore phases (62).

In order to accurately inspect degradation mechanisms the 3D microstructure must be analysed with respect to time (so called 4D methods). As mentioned, FIB-SEM results in the destruction of the sample, preventing 4D analysis. Moreover, sample preparation for X-ray CT must be sufficiently robust in order to permit repeated analyse of the same region of interest (ROI). This has been achieved in a few select cases (63; 64; 65) but detailed 4D studies remain insufficiently explored within the literature. A concise review of the literature on the microstructural characterisation of SOFCs from SEM to X-ray CT can be found by Jouttijärvi *et al.* (66).

A great benefit of 4D tomography studies lies in the ability to perform quantification of the displacement of material using methods such as Digital

Volume Correlation (DVC) (67). Methods such as this employ correlation techniques to determine the displacement of features within the ROI after deformation producing 3D displacement and strain fields (68).

X-ray investigations are not limited to the attenuation information that can be obtained from absorption techniques; crystalline materials diffract X-rays (XRD), allowing the analysis of the crystallographic data probing structural information beyond the micro- and nanostructures. Point and raster XRD has been employed across a host of studies focusing on the crystallographic structures within SOFCs (41; 69; 70; 71; 72; 73; 74; 75; 76).

2.8. Conclusions from Chapter Two

SOFC technology has developed considerably in recent years with companies achieving the production of commercially viable products with tens of megawatts currently installed. The thermodynamics of SOFCs permit potentially high net efficiencies while allowing operation on a range of fuels making them a promising alternative to traditional carbon-intensive technologies. However, overpotential voltages attributed to the activation, Ohmic and concentration losses limit performance during operation and are exacerbated by a host of degradation mechanisms from delamination due to TEC mismatch during start-up to metal sintering due to the elevated temperatures during operation. A critical metric in achieving and maintaining sufficient performance is the TPB, and should be maximised in terms of volumetric density in order to optimise the electrochemical performance. Significant work has therefore been applied to the study of these devices in 3D at high resolutions to better understand the structures for optimal performance and the mechanisms responsible for their degradation. Although initially dominated by destructive techniques such as FIB-SEM, X-ray absorption CT and XRD have become the prominent techniques for the structural characterisation of SOFC however published literature on 4D studies remain limited.

Chapter Three: Methodology

3.1. Introduction to Chapter Three

This chapter will describe the techniques for sample preparation, operational thermal cycling, materials characterisation and the subsequent data analysis. Sections of this work have been peer reviewed and are either published or in-press in the following journal articles: Heenan, T. M. M., *et al.* Electrochemical Society 165 (11), (2018): F921-F931; Heenan, T. M. M., *et al.* Electrochemical Society 165 (11), (2018): F932-F941; Heenan, T. M. M., *et al.* Solid State Ionics, 314, (2018), 156-164; Heenan, T. M. M., *et al.* Nano Energy 47, (2018): 556-565; Heenan, T. M. M*., et al.* Materials Today 20, no. 3 (2017): 155-156.

3.2. Fundamentals of X-ray Characterisation

X-rays are electromagnetic waves with wavelengths between 0.005 – 10 nm and were discovered by Röntgen in 1895. It was later found that an anode target bombarded with electrons would emit primary X-rays characteristic of the anode material. This knowledge formed the basis of lab-based X-ray production and energy dispersive X-ray (EDX) characterisation. Bremsstrahlung radiation is another important form of X-rays, which are generated when an electron is deflected by the electric field of an atomic nucleus. The distance of the electron from the nucleus determines the degree of deflection and, hence, the energy of the radiation emitted. Lab-based X-ray instruments employ an X-ray tube whereby electrons are released from a cathode via thermionic emission and bombard an anode material chosen according to its characteristic X-ray emission spectrum. The anode can experience extreme temperatures, and so are typically fabricated on a support material designed to efficiently dissipate heat and are

often rotated at high-speeds bringing the additional benefit of improved stability in the beam profile. Common anode materials are chromium Cr, copper Cu, molybdenum Mo, silver Ag and tungsten W, and are summarised in Table 2. A simplified lab-based X-ray source is depicted in Figure 7.

Table 2 A summary of the characteristic emission peaks expected from commonly employed lab-based X-ray anodes (77).

Element	Chromium	Copper	Molybdenum	Silver	Tungsten
Symbol	Cr	Cu	Mo	Ag	W
Atomic Number	24	29	42	47	74
Characteristic Peak / keV	5.4	8.0	17.5	22.2	59.3

X-rays can also be generated at specialist synchrotron facilities (78), whereby electrons are created using an electron gun and fed into a linear accelerator (linac), followed by a booster ring and finally a storage ring (Figure 8). The electron paths are controlled in these arrangements using powerful magnetic fields. When a charged particle travels in a curved trajectory radiation is emitted, as discussed in the aforementioned Bremsstrahlung radiation. Magnetic fields can be employed to take advantage of this mechanisms to create well-defined X-ray beams.

Equation 7 $$B_s = \frac{N_{pho}}{A\Theta_S\ 0.1\%BW}$$

The brilliance (B_S) of synchrotron radiation can be ten to twenty orders of magnitude higher than lab-based radiation from X-ray tubes (79). Brilliance is defined as the number of photons per second (N_{pho}) falling within a bandwidth (BW) of 0.1% of the central frequency (*0.1%BW*) corrected for angular divergence (Θ_S) and cross-sectional area of the beam (A) (Equation 7).

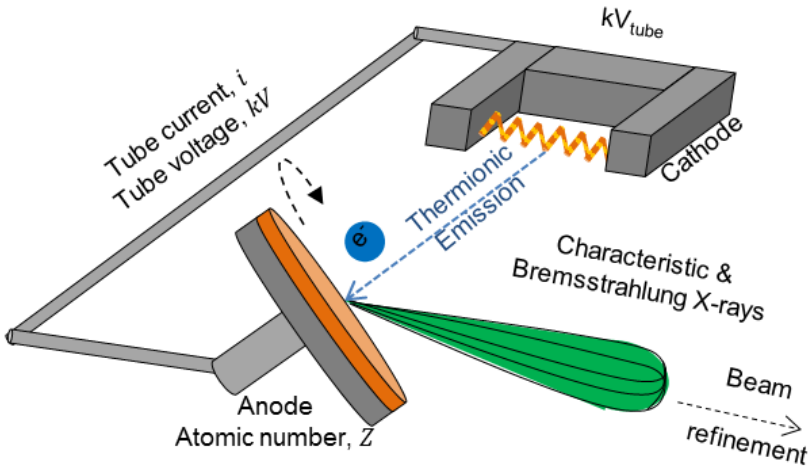

Figure 7 X-ray production in a lab source: a simplified set-up for X-ray production from electron bombardment on a rotating anode target.

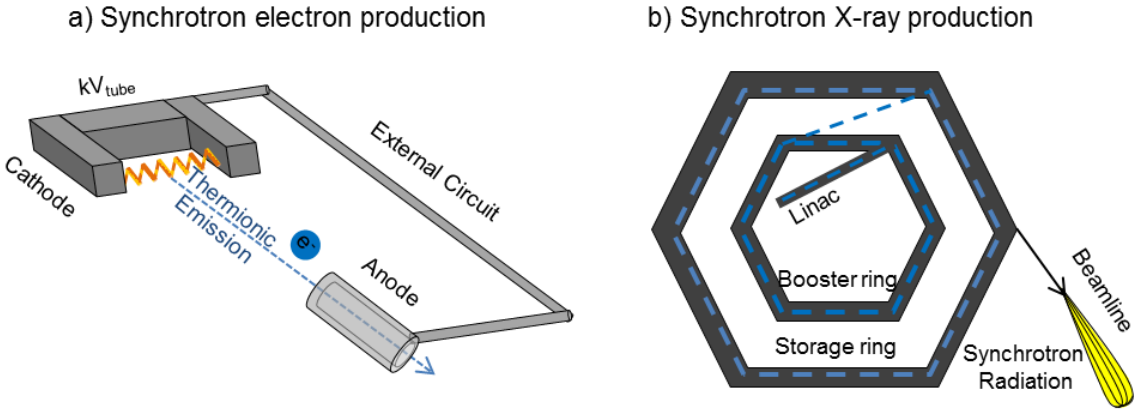

Figure 8 X-ray production in a synchrotron source: a simplified set-up for X-ray production from electron gun for entry into b) the linear accelerator, and, the booster and storage rings, to the beamline.

After being generated, X-rays are typically refined into well-defined beams. A well-defined beam is one that has a sufficiently controlled temporal and/or spatial coherence determined by the degree of monochromaticity and collimation, respectively. Beam-refinement is common in both lab and synchrotron sources. Figure 9 depicts some of the many instruments that are used to refine X-ray beams within lab and synchrotron environments. Firstly, beams can be classified into two geometries: cone or parallel. Because beams are naturally divergent, less refinement is required to produce suitable cone beams. However, the generation of parallel beams demands condensers and other collimation devices. Due to the divergence of cone beams, geometric magnification can be achieved without optical magnification, however optics are often also employed, achieved through the use of high-precision apparatus such as zone-plates and lenses (80). Charge-Coupled Device (CCD) detectors are often used for X-ray detection and can come in many forms as reviewed by Gruner (81).

X-rays interact with matter in a variety of ways: diffraction when passing through a crystalline material, attenuation when passing through any medium outside of a vacuum, and the emission of the aforementioned secondary X-rays. When X-rays pass through a crystalline material with lattice spaces (d) near that of the X-ray wavelength, the radiation is diffracted by discrete angles (θ) as described by the Bragg equation (Equation 8). X-rays will also be absorbed when passing through any material due to several mechanisms (82), but the degree of absorption can be approximated by an exponential law of transmission (T) for a specified thickness (t) through a material with a linear attenuation coefficient (μ) (Equation 9). Attenuation can also be quantified in the form of the mass

attenuation coefficient (μ_m) and the attenuation length (λ_a). The attenuation length is defined as the length at which the incident intensity of the X-ray beam has been attenuated to e^{-1} and is the inverse of the linear attenuation coefficient (Equation 10).

Equation 8 $$n\lambda = 2d\sin\theta$$

Equation 9 $$T = I/I_0 = \exp(-\mu t)$$

Equation 10 $$\lambda_a = \frac{1}{\mu} = \frac{\rho}{\mu_m}$$

There are also characteristic X-ray absorption energies, named edges, where the X-ray transmission reduces significantly as the incident energy is equal to the binding energy of a particular electron, *i.e.* the K-edge would be located at the energy where the incident energy is equal to the binding energy of a K-shell electron. Numerous sources for information on the X-ray properties of materials exist on the National Chemical Database Service (NCDS), the National Institute of Standards and Technology (NIST) and the Centre for X-ray Optics (CXRO), which often include data libraries (82; 77). A brief introduction to the properties of X-rays has been discussed here, but thorough discussions can be found by Van Grieken *et al.* and Assmus *et al.* (83; 84) .

X-ray characterisation discussed in this thesis comes two forms: XRD as described by Equation 8 and transmission CT as described by Equation 9. Unless stated otherwise, all mentions of X-ray CT discussed in this thesis are with

regards to absorption transmission methods. XRD is collected in the form of continuous pattern with discrete intensity peaks corresponding to the crystallographic properties. X-ray CT data is collected in the form of intensity attenuation integrated for the entire beam-path from source to detector.

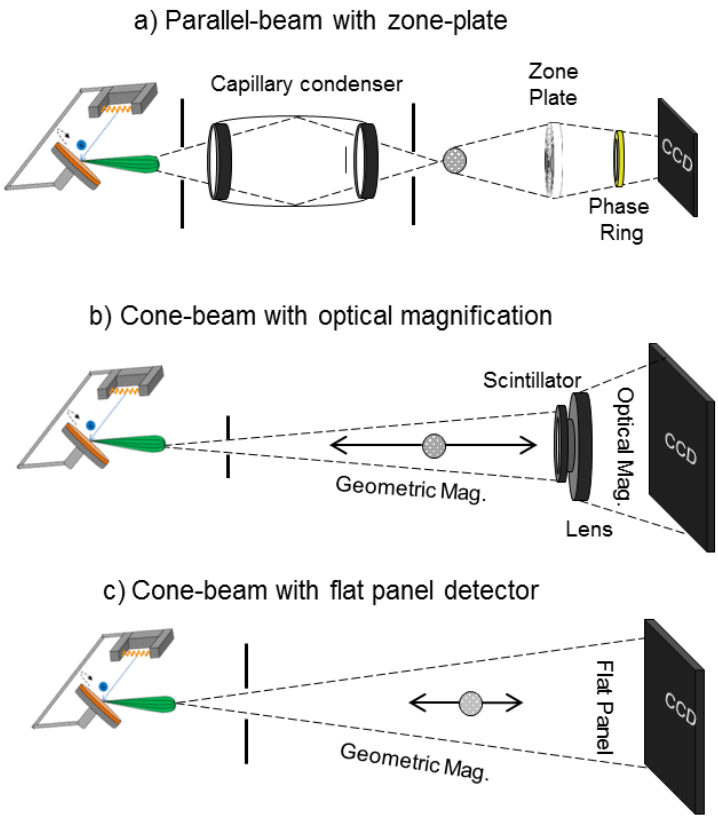

Figure 9 Simplified set-ups for lab-based X-ray tomographs a) parallel-beam with use of a zone-plate, b) cone-beam with optical magnification and, c) cone-beam with a flat panel.

In order to obtain 3D data, many projections can be collected at multiple angles using a tomograph. After being corrected with reference images, the data is

combined using reconstruction algorithms to spatially resolve the information. The type of reconstruction algorithm can vary but filtered back-projection procedures are most common (85). The reconstructed 3D dataset is called a tomogram and is comprised of many voxels which each containing a number assigned to the X-ray attenuation at that point in space. Typically, lab-based instruments (Figure 9) and synchrotron-based beamlines (Figure 10) differ according to their imaging capabilities; different stations will focus on different length scales and methods. The spatial resolution of zone-plate imaging is limited by the ring spacing which, in turn, is limited by the precision of the manufacturing methods. However, both lab and synchrotron facilities can achieve spatial resolutions on the order of tens of nanometres (86; 87).

The suitability of the X-ray beam is typically determined by the energy and brilliance of the incident X-ray. Low brilliance will increase the exposure time required to achieve an acceptable ratio of signal-to-noise, which in turn may require more projection angles, further increasing the scan time. The incident energy will determine the transmission and the angles of diffraction. The image quality can be improved substantially by the use of precise sample preparation techniques; FIB milling has been used considerably in the preparation of small samples (56), but the recent development of laser lathes has seen their use increase considerably (88). The optimal sample geometry for tomographic characterisation is cylindrical, with diameter and height equal (or marginally larger) than the field of view (FOV). This minimises unnecessary attenuation of the beam, as well as maximising the volume of sample that can be analysed, thus improving the statistical representation.

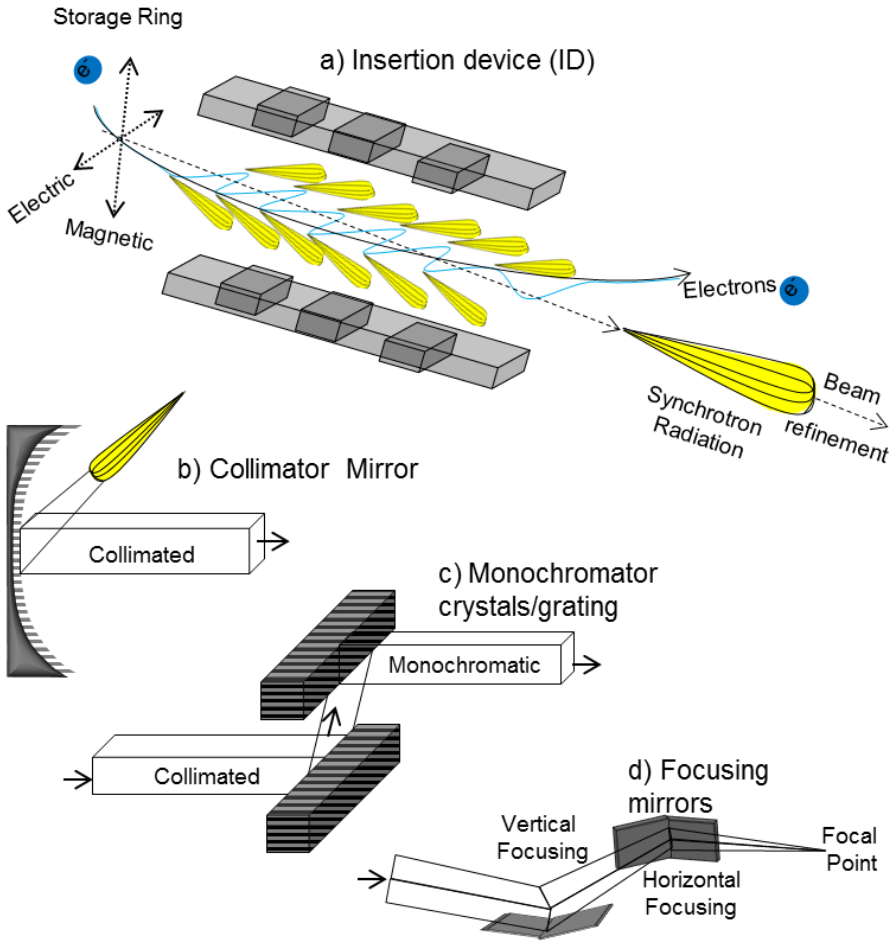

Figure 10 simplified set-ups for typical beamline apparatus: a) an insertion device (ID) for the creation of synchrotron radiation, optical refinement devices b) collimator mirrors, c) monochromator crystals/gratings and d) focusing mirrors.

3.3. Materials and Preparation Methods

Two types of fuel cell materials are investigated in this thesis: electrode powders and pre-fabricated cells. Powder samples provide various model microstructures of known composition ideal for technique development, and pre-fabricated cells provide an example of what would be expected in commercial applications.

Powders can be formed into cylindrical pellets by 12 tonnes of iso-static pressing for 15 minutes and subsequently being sintered. Powders are typically then reduced in a hydrogen containing atmosphere with the reduction confirmed using techniques such as Raman or EDX. The reduced pellets can then be ground into powders using diamond files to be mounted for XRD or X-ray CT. Whereas, pre-fabricated cells typically do not require sintering but may require reduction if supplied in the metal-oxide form.

X-ray CT samples can be prepared either manually using a scalpel or using a high precision laser. Manual preparation involves the removal of fragments from the reduced pellet bulk using a sharp razor producing sample diameters smaller than the largest X-ray FOV. Each fragment can then be attached to a pin-head with the use of an epoxy to secure the sample; minimising drift during the scan, thus artefacts in the reconstruction. In order to conduct 4D studies a specific sample mounting procedure is required (Figure 11). The following sample-mounting procedure is applicable to the full range of X-ray CT techniques from nanometre to sub-millimetre resolutions. This mounting is resilient to moisture, stable to temperatures above 700 °C, as well as both oxidising and reducing environments, and also contains non-flammable materials with no volatile organic compounds. To produce these samples a primary base

coating of high-temperature cement (Aremco Products, New York, U.S.A.) is firstly applied to the tip of an alumina, Al_2O_3, tube ca. 3 mm in diameter (Multi-lab, England, U.K.). This primary layer is then dried in air at room temperature for 3 hours. For the most aggressive conditions it is recommended that the primary layer is cured at 200 °C for 3 hours in air ramped at a low rate, ca. 1 °C min^{-1}. Once set, the primary surface is coated in a secondary layer with the sample immediately mounted on top of this before drying is able to take place. This should again be dried in air at room temperature for 3 hours. If required, the sample can then be refined to a suitable diameter *via* techniques such as high-precision laser lathing (88) or FIB milling (56). The versatility of this technique can be extended by the use of hollow alumina tubes during the mounting procedure; hollow tubes allow for a disposable metal pin to be attached to the base of the alumina tube, securing into a sample-holding chuck. Utilising disposable pins, specific to the end-station in use, allows for the samples to be entered into any CT instrument or synchrotron beamline independent of the mounting stage dimensions.

Sample mounting for XRD can be achieved through the use of anode powders that are pressed into pellets, sintered, reduced and prepared back into powders using a diamond file. These powders can be loaded into small quartz capillaries *ca.* 10 cm in length and *ca.* 580 μm in diameter. To enable gas flow that can prevent re-oxidation during in-situ experiments, the capillaries can be mounted with a brass button seal into a goniometer head for analysis (HUBER Diffraktionstechnik GmbH & Co. KG, Germany).

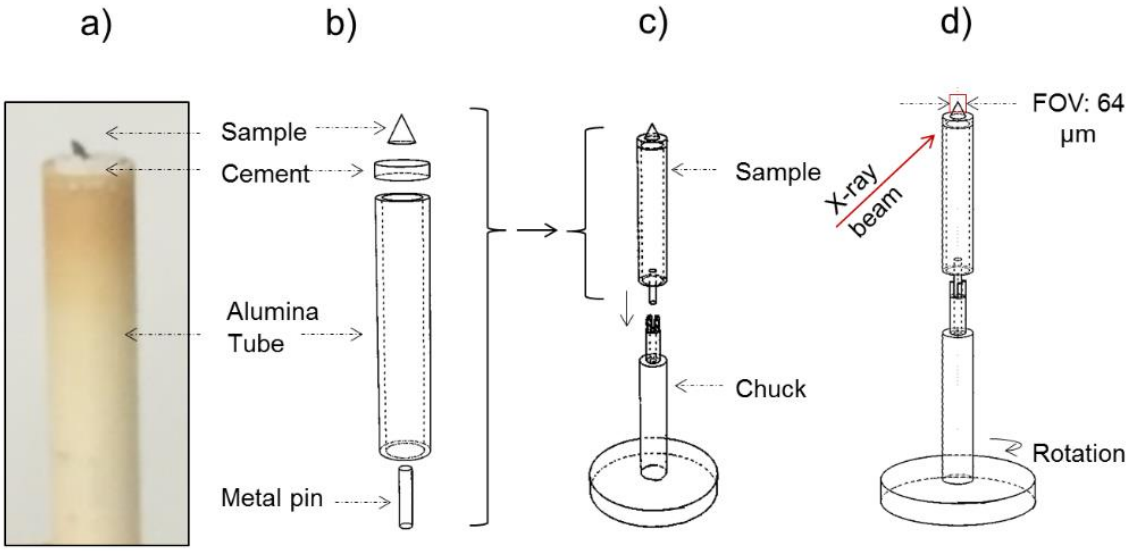

Figure 11 Procedural diagram for the preparation of the robust cement-mounting technique utilised for high resolution 4D X-ray CT imaging of thermally induced microstructural evolution: a) mounted sample photographed post-curing, b) schematic diagram of the constituent materials and their location in the mounting assembly, c) schematic diagram of the sample insertion into the mounting chuck, and d) the orientation of the X-ray beam.

3.4. Methods for Thermal Cycling

Four separate thermal techniques are discussed in this thesis: a box furnace, a tubular furnace, a laser heating gun, and a hot-air blower.

A box furnace is typically used for very high temperature treatments such as sintering processes. The sample can be set on a ceramic bed near electrical resistance coils that elevate the temperature within the box. With the furnace door closed the sample environment is thermally isolated from the environment but not gas-sealed *i.e.* contains natural air from the environment. The sintering temperature can then be controlled by the current that is applied to the resistance coils within the insulated furnace.

A tubular furnace employs a similar heat source through the use of high-resistance coils however, the sample is not only thermally isolated from the environment but also gas-sealed through the use of a quartz tube *ca.* 5 cm in diameter and *ca*. 70 cm in length. The filaments contour the external surface of the tube and the sample sits inside the tube on an alumina support. Gases can be flown over the sample at a desired flowrate through the use of a device such as a rotameter.

Laser heating can be achieved by aligning a sample at the focal-point of a High Performance Diode Class 4 980-999 nm laser (LIMO Lissotschenko Mikrooptik GmbH, Dortmund, Germany) and subsequently heating in air by increasing the laser power. The temperature can be pre-calibrated for nickel-based samples to establish the relationship between the beam power and the heating temperature using a fast-responding, nickel-based thermocouple placed

at the focal point of the beam. The calibration curve for high-temperature heating of Ni-based samples can be seen in Figure 12.

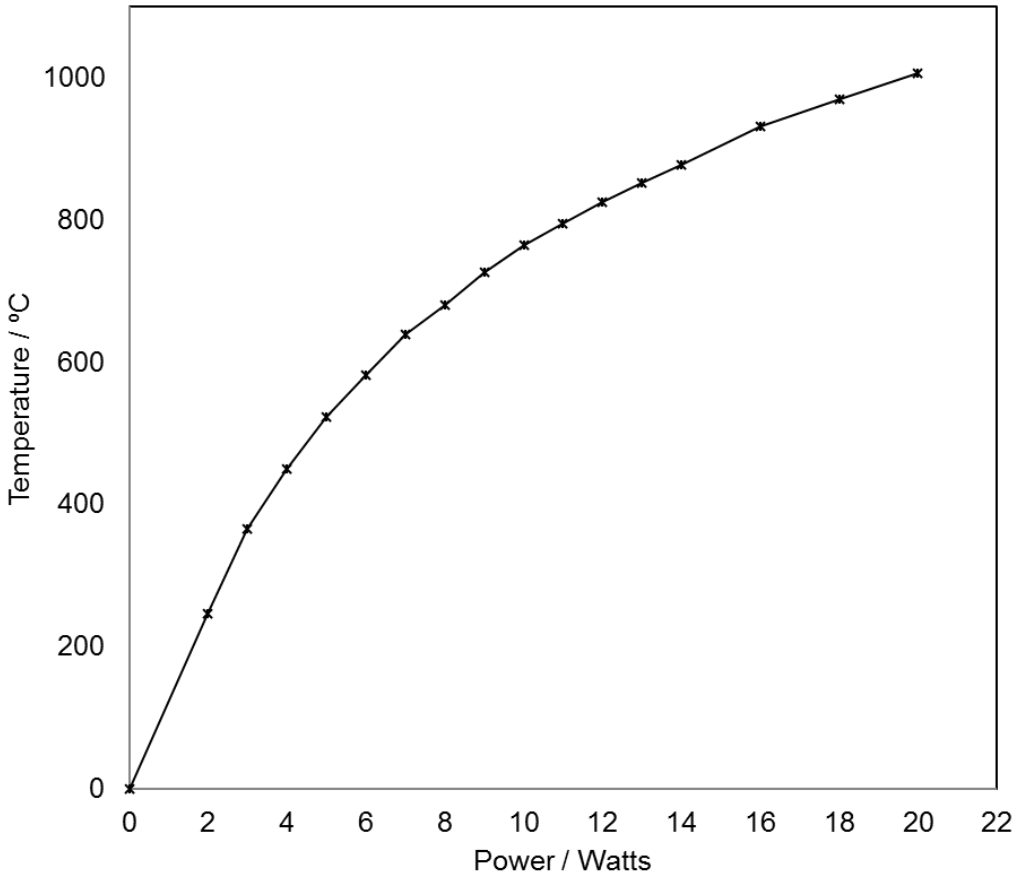

Figure 12 Calibration output for the high-temperature laser heating of Ni-based samples using a High Performance Diode Class 4 980-999 nm laser (LIMO Lissotschenko Mikrooptik GmbH, Dortmund, Germany).

For in-situ powder XRD investigations a hot-air blower can be employed to elevate the local temperature. Similar to the box and tubular furnaces, the hot-air

blower employs high-resistance electrical coils to raise the temperature of the air surrounding the coils; however, the hot air blower also employs a fan to blow the hot air upwards, forcing convection. Powdered samples that have been placed into capillaries can be secured into a goniometer head using brass button seals, as discussed in Section 3.2. The hot-air blower can then be placed below the capillary and hot air can be blown over the capillary to raise the temperature of the sample. In order to ensure that the metal remains reduced, a gas can be flown over the sample from the goniometer head.

3.5. X-ray Computed Tomography (CT)

Two types of lab-based X-ray instruments are used in this work: the 520 Versa X-ray micro-CT instrument (Zeiss Xradia 520 Versa, Carl Zeiss., CA, USA) and the 810 Ultra X-ray nano-CT instrument (Zeiss Xradia 810 Ultra, Carl Zeiss., CA, USA). The Ultra and Versa respectively operate with chromium and tungsten anodes producing characteristic X-ray emission peaks at 5.4 and 59.3 keV. The Ultra has a fixed energy source and is considered to have a quasi-parallel, quasi-monochromatic beam, whereas the Versa operates with cone-beam and variable power supply voltage up to 160 kV. The Ultra has two imaging modes depending upon the zone plate used: large field of view (LFOV) and high resolution (HRes). The two imaging modes differ in resulting voxel length and FOV. The Versa has four imaging modes: 0.4x, 4x, 20x and 40x. The imaging set-ups in relation to Section 3.1 are visualised with the reproduction of the generic schematics presented in Figure 9 tailored for the two instruments in Figure 13, with the set-up for the sample mount displayed in Figure 14.

Table 3 Summary table of the X-ray tomography imaging parameters for each imaging mode.

	Characteristic Emission / keV	**Pixel Length (Binning 1) / nm**	**FOV / µm x µm**
Versa 20×	59.3	400	768x768
Versa 40×		200	384x384
Ultra LFOV	5.4	64	64x64
Ultra HRes		16	16x16

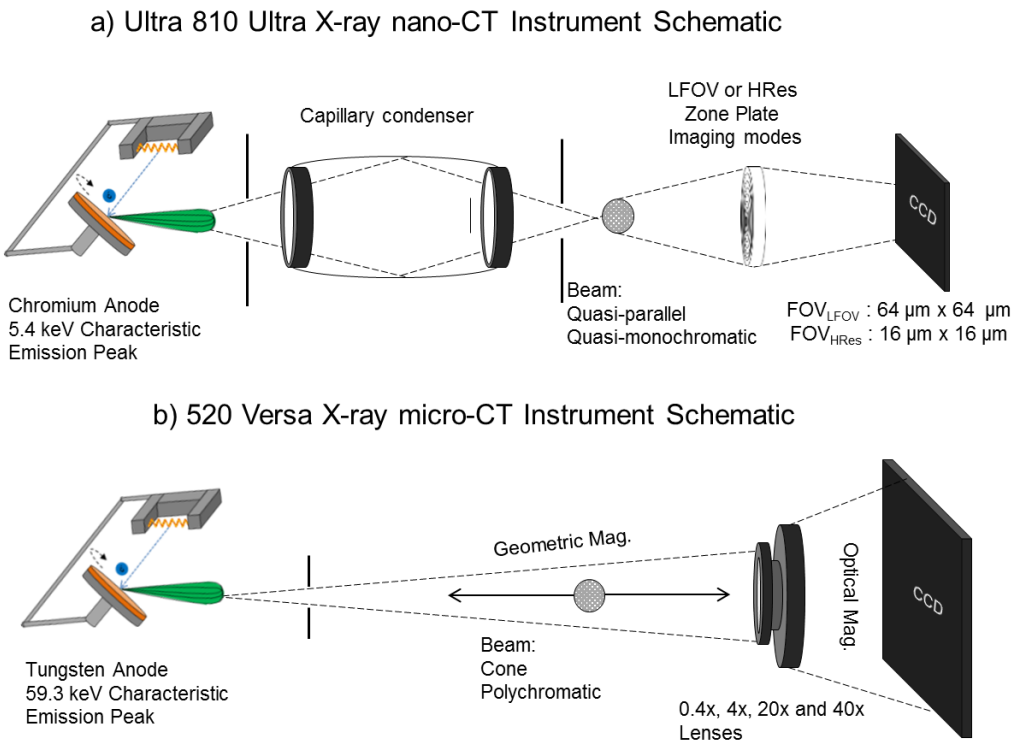

Figure 13 Simplified set-ups for lab-based X-ray tomographs a) Ultra 810 X-ray nano-CT instrument, b) Versa 520 X-ray micro-CT instrument.

3.6. Tomogram Quantification

3.6.1. Spatial Orientations and Notation

The orthogonal planes (*x, y, z*) that are referenced in Figure 14 can be used to identify the orientation of the sample with respect to its position within an operating stack, i.e. the orientation of the fuel and air inlets, when correlated as in Figure 15. Unlike imaging purely anode materials, if an electrolyte layer sits within the FOV of the X-ray CT, then the spatial orientation of the microstructure with respect to the stack geometry can be extracted from the reconstructed tomogram; i.e. the z-plane can be defined as the axes perpendicular to the anode/electrolyte interface, whereas the x- and y-planes can defined as both parallel to the interface and perpendicular to one another.

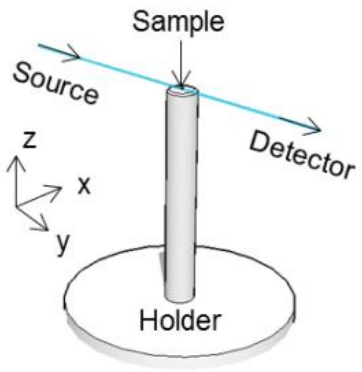

Figure 14 Spatial orientation of the X-ray beam-path for X-ray CT.

Variables, *v*, that are phase-specific can be denoted v_j where j = Ni, YSZ or pore, directional variables can be denoted v_i where i = x, y or z, and, variables which involve two phases are denotes, $v_{j,k}$ where k = Ni, YSZ or pore and k ≠ j. Metrics can also be presented as either local (v) or bulk values ($\overline{v}$). Bulk metrics are

calculated for the entire volume and are presented as an average value, whereas, the local metrics are calculated on a slice-by-slice basis to examine the variation throughout the volume. Avizo's material statistics algorithm can be used to calculate slice-by-slice metrics.

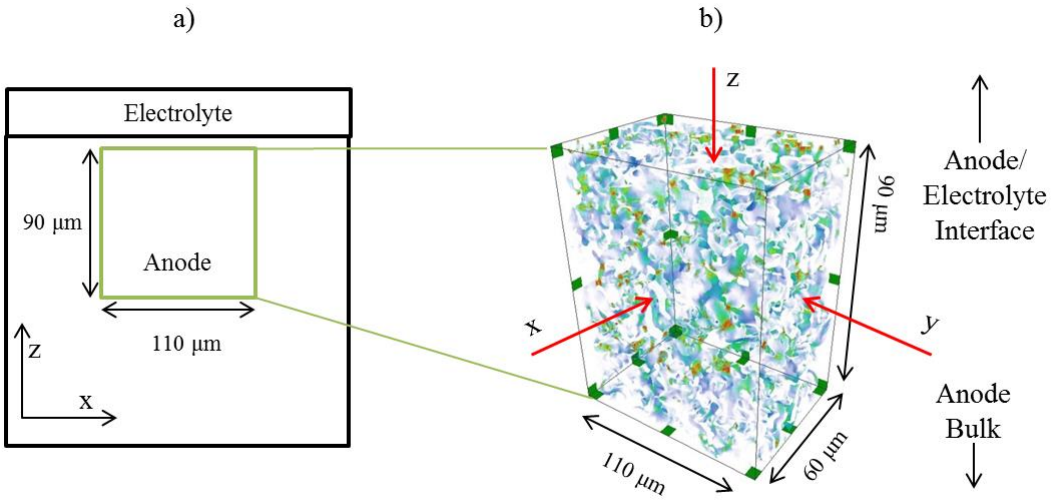

Figure 15 Spatial orientation of the tomogram datasets: a) 2D geometric reference and b) accompanying 3D sub-volume.

3.6.2. Segmenting Data from a Quasi-Monochromatic Beam

The constituent phases, Ni, YSZ and pore within an X-ray CT tomogram obtained from an SOFC anode can be differentiated according to the greyscale values of the individual voxels. The greyscale observed in the reconstructed tomogram scales proportionally with the transmitted beam intensity, and hence the local attenuation coefficient of the materials. Therefore the attenuation of two or more materials can be visualised by the greyscale histogram of the reconstructed tomogram: materials that are highly attenuating appear with high greyscale value

(bright white), while low attenuation regions, such as a pores, appear with low greyscale values (dark grey or black). Consequently, if two materials are imaged under the same incident beam energy and exposure time (or during the same tomography), the difference in their greyscale values can be compared directly to their attenuation coefficients.

Although elemental data for the attenuation properties of SOFCs is readily available, many materials contain several elements in order to achieve the desired thermo-mechanical and electrochemical properties. Examples being YSZ, GDC, LSM and LSCF. Equation 11 in combination with the X-ray equations presented in Section 3.1 can be employed to obtain the mass attenuation coefficients for compound materials via the summation of the *i* constituent elements weighted according to their respective mass fractions (w_i) in compound k (77).

Equation 11

$$\mu_{m_k} = \sum_i w_i \left(\frac{\mu_i}{\rho_{m_i}}\right)$$

The 5.4 keV Ultra beam is considered quasi-monochromatic, consequently the data can be supported using the theoretical greyscale values; although the greyscale histograms may differ from sample to sample the attenuation properties of the materials remain constant; therefore, the location of the greyscale peaks within the histogram can be predicted. Describing generally for a two component system (*A* and *B*) the histogram plot produced from an X-ray tomogram using beam energy (E) will have a peak for each material which corresponds to greyscale value (G_A and G_B). At beam energy (E) materials A and B will also have

attenuation coefficients (μ_A and μ_B). A ratio taken of the two greyscale values (η_G) can be considered approximately equal to the ratio of the attenuation coefficients (η_A) (Figure 16).

Equation 12 $$\eta_G = \frac{G_i}{G_j}$$

Equation 13 $$\eta_A = \frac{\mu_i}{\mu_j}$$

Equation 14 $$\eta_A \sim \eta_G$$

This method can be applied to polychromatic beams however the calculations become significantly more complex, as each wavelength, as its contribution to the beam profile, must be considered. However, the use of greyscale fiducials can circumvent these issues. For instance, by referencing greyscale values of a known material within the X-ray FOV with regards to other materials within the same tomogram, several materials can be distinguished. This reduces computation significantly while still allowing sufficient quality in the segmentation of the constituent phases.

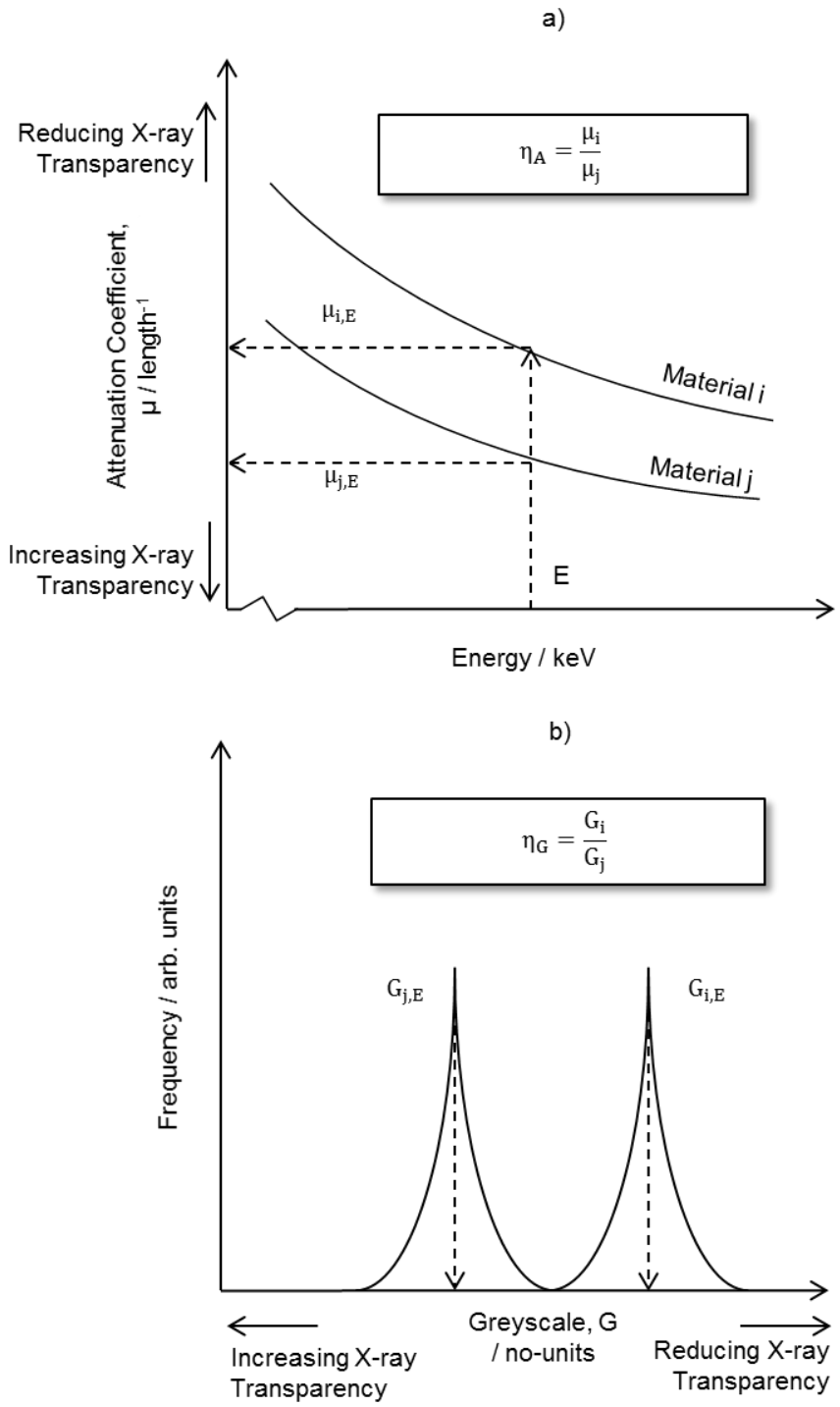

Figure 16 Correlating the difference in attenuation coefficient to the separation of greyscale peaks for two materials. A general example of the difference in a) attenuation coefficient and b) greyscale for materials i and j.

3.6.3. Composition

The compositions can be calculated using Avizo's volume fraction algorithm and TauFactor and presented in the form of a phase-specific volume fraction (φ_j). Composition calculations can be based on the summation of all voxels containing the phase of interest ($voxel_i$) and dividing that number by the total number of voxels within the ROI (n).

Equation 15 $$\varphi_j = \frac{\sum voxel_i}{n}$$

3.6.4. Percolation

Percolation is defined as the percentage of the volume fraction for a particular phase that is connected either between two faces or between a face and a particular point in space. This can be calculated by the search of an uninterrupted series of voxels containing the same phase between the two points. Percolation can be quantified through the production of percolation values (p_j) using TauFactor for each direction, for each phase.

3.6.5. TPB Mapping

The TPB length (L_{TPB}) and TPB density (ρ_{TPB}) values can be quantified with the use of several methods such as those discussed by Cooper *et al.* (89) and Lu *et al.* (28). The TPB mapping algorithm discussed by Lu can be simplified into the two following steps: firstly, the matrix must be expanded by adding an additional voxel between each pre-existing voxel and then secondly the volume must be

searched for locations where Ni, YSZ and pore are situated in neighbouring voxels. Once mapped, the TPB length can be quantified by the summation of all TPB locations by the length of a single voxel, and finally the TPB density can be obtained by dividing the TPB length by the volume analysed (V).

Equation 16 $$\rho_{TPB} = \frac{L_{TPB}}{V}$$

The percolated TPB densities can be calculated by methods such as those discussed by Golbert *et al.* (90) whereby only TPB locations that neighbour three percolated phases can be considered *'active'* or *'percolated'*.

3.6.6. Phase Surface Area and Interfacial Contact

The volume specific surface area (A_j) of each particle can be quantified with use of the TauFactor application. Values are produced for each phase. The volume specific interfacial contact area ($A_{j,k}$) for instance for Ni-YSZ, Ni-pore and pore-YSZ, can also assessed using TauFactor and MATLAB.

Surface area calculations were based on the same algorithm as the TPB whereby the volume can be searched for neighbouring voxels containing different phases *i.e.* searching the volume for all voxels of phase *i* that are in contact with voxels not equal to *i*. All of these 'surface voxels' ($surfacevoxel_j$) are then summated and multiplied by the area of one pixel to obtain an approximation for the total surface area (A_j^{Tot}). Finally, to obtain the specific surface area (A_j) the total surface area is divided by the volume analysed (V).

Equation 17 $$\mathrm{A_j} = \frac{\mathrm{A_j^{Tot}}}{V}$$

The interfacial contact areas are calculated using the same procedure however with different search conditions; surfaces are only considered if they are found between two particular phases, *e.g.* j and k.

3.6.7. Particle Size and Distribution

The particle sizes can be assessed through the quantification of Feret diameters ($\emptyset_j$) using ImageJ software (ImageJ, National Institute of Health, U.S.A) (91). This method employs the calculation of the Euclidean distance between the two outermost particle walls. The particle size distribution can then be presented in the form of a particle Feret diameter histogram for each phase, for each tomogram. The particle size can also be assed by an equivalent diameter (d_{eq}) based on a sphere of the same volume as the particle (V_p).

Equation 18 $$d_{eq} = 2\left(\frac{3V_p}{\pi 4}\right)^{1/3}$$

3.6.8. Tortuosity and the Tortuosity-Factor

Tortuosity (ξ) describes the convolution of the path which a species must travel between two points and is very useful in describing the transport processes within SOFCs. The tortuosity can be described by the ratio of the actual path length that

a species must travel (L) to the Euclidean distance between the initial and final locations (L_E).

Equation 19 $$\xi = \frac{L}{L_E}$$

TauFactor can be employed to assess the tortuosity of 3D structures through the production of tortuosity-factor values (89). TauFactor simulates diffusion throughout the structure of a particular phase with a fixed potential applied to two opposite faces of the volume. The ratio of the simulated flow (Q_{sim}) to the flow of an empty volume of the same dimensions (Q_{empty}) is then taken to obtain the tortuosity-factor (τ). Tortuosity-factors can be produced for each phase, in each direction for each tomogram. The tortuosity-factor is related to the tortuosity by the power of two (Equation 20) as described by Epstein (92).

Equation 20 $$\tau = \xi^2$$

3.6.9. Deformation

The deformation of the cell can be quantified by four metrics: electrolyte thickness (t), cell-wall angle (θ), horizontal (Δx) and vertical (Δz) displacements (Figure 17). The angular and horizontal displacement quantifies the contraction of the cell wall perpendicular to the anode/electrolyte interface, whereas the vertical displacement describes the magnitude of the cell curvature. These metrics can be quantified with use of the angular and 3D length measurements conducted on

greyscale data in Avizo Fire software (Avizo, Thermo Fisher Scientific, Waltham, Massachusetts, U.S.). The volume specific interfacial contact area between the solid-anode and solid-electrolyte layers (A) can be quantified using TauFactor (89) (Figure 17). Care should be taken to ensure that the sub-volumes are tangental to the anode/electrolyte interface, accounting for interfacial curvature. An example of this is given in Figure 17 where sub-volumes are taken at the centre (r_0) through to the cell wall (r_{175}) where the subscript denotes the location of the sub-volume in relation to the cell radius.

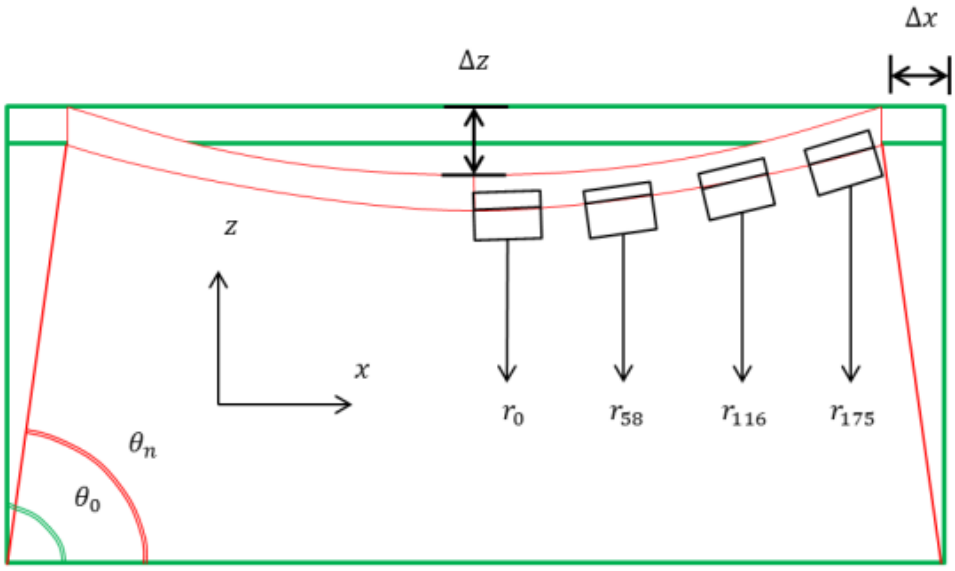

Figure 17 Geometric orientations for the quantification of cell deformation: a schematic outlining the cell-wall angle (θ), horizontal (x) and vertical (z) cell displacement.

3.6.10. Mapping and Quantifying Cracks

The micro- and nanoscale cracking can be quantified by segmentation of the crack from the greyscale tomogram and mapping of its centroid path. Segmentation can be achieved by cropping a volume that tightly encloses the meander of a crack path, followed by the segmentation of all pores (including cracks), with use of a greyscale threshold with reference to the greyscale of the space surrounding the sample. Once all of the porous phase is segmented, a 'top-hat' transform is computed on the image, allowing the distinction of cracks from the pore (93). A central skeleton of the crack network can then be mapped in 3D using Avizo's 'Auto-Skeleton' algorithm which employs a medial axis-based method using distance ordered homotopic thinning (DOHT) (94) to determine the phase diameter by calculating the distance between the skeleton to the phase boundary. Detailed descriptions of such algorithms can be found elsewhere (95).

The local crack diameter (∅) can then be inspected with the accompanying crack length (*l*) and finally a crack-diameter histogram can be calculated. To inspect the crack propagation, the minimum, maximum, average and standard deviation of the crack diameters can be computed for each crack and assessed with respect to the respective crack length.

3.6.11. Effective Conductivity

The effective conductivities (σ^{Eff}) for instance of Ni and YSZ, can be inspected using the calculated tortuosity-factor and conductivity (σ) for a particular set of conditions e.g. temperature, and the calculated volume fraction (Equation 21).

Equation 21 $$\sigma^{Eff} = \frac{\varphi}{\tau}\sigma$$

3.6.12. Fractal Computations

It has previously been observed that values for the TPB density quantified for the same sample at differnet resolutions results in a differnet TPB densities (96); i.e. for the same sample, the higher the resolution employed, the higher the TPB desnity extracted. Building upon this, Bertei *et al.* investigated the influence of resolution on the reaction site density by the definition of a TPB fractal dimension obtained through FIB-SEM characterisation (97). These fractal properties were then employed to improve an electrochemical model. This fractal relationship between resolution and characterised length is based upon work by Mandelbrot whereby a measured length such as the length of a country's coastline (98) or the micro-features in fractured metal (99) increases in detail, thus magnitude, with increasing resolution. Although fractal properties have been extensively reported since (100; 101; 102; 103), knowledge of the fractal properties of electrochemical materials remains limited.

In order to obtain data with reduced resolutions the sample can be imaged at different magnifications as discussed in the Section 3.4 or the greyscale tomogram can be binned after reconstruction through the combination of several pixels in the formation of a single larger pixel using resampling algorithms such as those employed by Avizo Fire software (Avizo, Thermo Fisher Scientific, Waltham, Massachusetts, U.S.).

The reaction site density can be calculated for each voxel length to inspect the effects of resolution. The ρ_{TPB} values can then plotted on log-log axes in order

to obtain a fractal dimension (D) and Linear scaling factor (*f*) using the Mandelbrot relation as explained by Bertei *et al.* (97), presented in Equation 22 and Equation 23 whereby the resolution (r) is presented as the isotropic voxel length.

Equation 22 $$\rho_{TPB} = f\, r^{1-D}$$

Equation 23 $$Log_{10}(\rho_{TPB}) = f + (1-D)Log_{10}(r)$$

3.6.13. Representative volumes

The sample volume investigated should be maximised in order to ensure that the tomogram is statistically representative of the material under investigation; a representative volume should be achieved (104; 65; 56). In order to compare the statistical significance of a sample, a representative volume element (RVE) analysis can be conducted for a given parameter (TPB, VSSA, vol % etc.) typically utilising a region growing algorithm considering sub-samples of successively larger volumes and extracting the metric of interest. At volumes below the RVE, oscillations in the considered metric will be observed, which are expected to dampen and disappear as the sample volume approaches the RVE.

3.7. Digital Volume Correlation (DVC)

Digital volume correlation (DVC) can be computed and mapped using '*TomoWarp2',* a Python-based open-source software developed by Tudisco *et al.* (105). TomoWarp2 utilises correlation techniques such as those employed by Gates *et al.* (106), whereby the movement of features within a material are tracked and quantified.

3.7.1. Correlation Methods

In order to track movements two tomograms are required from the exact same ROI containing the 'initial' and 'deformed' structure. By locating the same feature within the initial and deformed structures the displacement of said feature can be quantified. To do this, a local sub-volume is drawn which encloses the feature within the initial structure, a similar sub-volume is then drawn within the deformed structure and rastered throughout the volume until the feature is found. To find the feature within the deformed volume, the brightness distribution functions of the initial and deformed volumes are compared and their difference is minimised. The degree of confidence in the location of the feature within the deformed volume is quantified in the form of a correlation coefficient (CC), whereby an optimum match in the brightness distribution functions would result in a CC value of 1. The various methods of calculating the CC values have been discussed and compared by Tong (68) although, confidence is typically only placed in displacement data that has obtained CC values above 0.97 (107).

3.7.2. DVC Computations

To conduct the DVC computations, first a regular grid of 3D nodes has to be defined according to the ‘node spacing’ over each tomogram. A ‘correlation window’ is then centred over each node for the correlation analysis and a ‘search window’ is defined to constrict the search for the displaced material within a local volume. In order to visualise the displacement and strain data obtained from the DVC computations, Avizo Fire software (Avizo, Thermo Fisher Scientific, Waltham, Massachusetts, U.S.) can be employed to generate 3D displacement vector fields and strain volume renders. Quantifications can be achieved with use of ImageJ (ImageJ, National Institute of Health, U.S.A) (91).

3.8. X-ray Diffraction (XRD)

The X04SA-MS beamline at the PSI Swiss Light Source (SLS) is capable of conducting high-speed in-situ powder XRD (108) (Swiss Light Source, Paul Scherrer Institute, Switzerland).

Samples can be prepared as described in Section 3.2 and mounted above a hot-air blower as described in Section 3.3 producing the arrangement seen in Figure 18. Diffraction patterns can then be collected at two theta angles from -60^{O} to +60^{O} in a symmetric arrangement at a chosen beam energy using a MYTHEN II (microstrip system for time-resolved experiments) detector covering 120 ° with over 60,000 channels on a double layer for a 0.0036 ° intrinsic resolution.

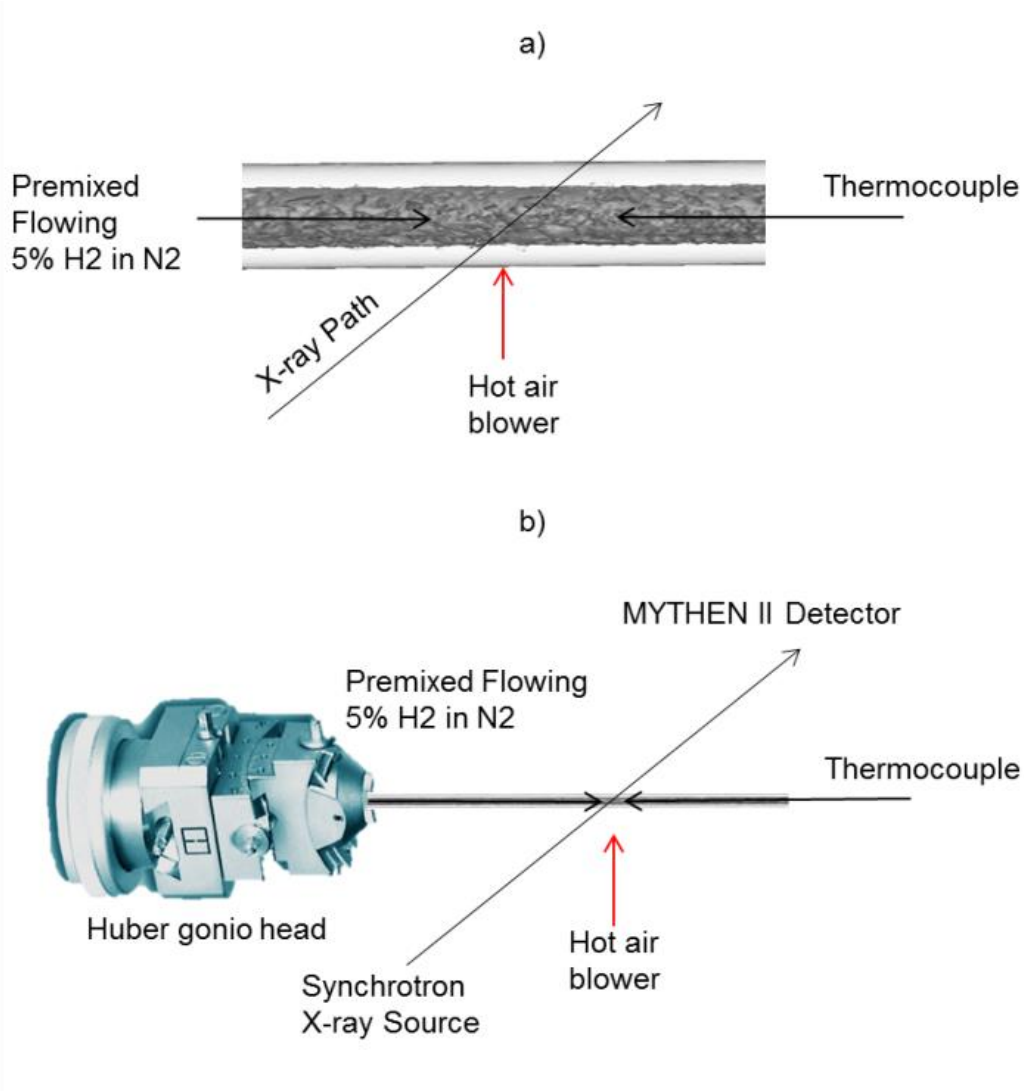

Figure 18 Experimental set-up for diffraction collection at the X04SA-MS Beamline: a) four coincident paths of the hot-air blower, forming gas, thermocouple and X-ray beam, and b) sample mounting *via* a quartz capillary packed with sample powder.

3.9. Diffraction Quantification

The average interplanar distances (d) can be obtained from the diffraction angle (θ) and the wavelength of the X-ray beam (λ), using Bragg's law with the positive integer (n) equal to unity, Equation 8. Having a face-centred cubic crystal structure, the lattice parameters (L) for nickel are obtained from the diffraction angle using the Miller indices (h,k and l) and the relation for a cubic system, Equation 24.

Equation 24 $$L = d \times \sqrt{h^2 + k^2 + l^2}$$

Thermal strain ($\varepsilon_{thermal}$) is calculated from the lattice variation with respect to a chosen state; for example the point of zero strain can be taken at the maximum temperature, thus the maximum lattice parameter (L_0), Equation 25.

Equation 25 $$\varepsilon_{thermal} = \frac{L - L_0}{L_0}$$

The thermal stress ($\sigma_{thermal}$) is obtained from the product of the thermal strain and the Young's modulus (E) of the material, Equation 26.

Equation 26 $$\sigma_{thermal} = E \times \varepsilon_{thermal}$$

A local TEC can be calculated through the thermal cycle of each material using the change in local lattice parameters (dL) at each temperature increment (dT), Equation 27.

Equation 27 $$TEC = \frac{1}{L}\frac{dL}{dT}$$

Thermal driven deformation (TDD) can be quantified by the change in lattice parameter with respect to an initial condition (L_i), Equation 28.

Equation 28 $$TDD = \left[\frac{L}{L_i} - 1\right] x\ 100$$

3.10. Conclusion from Chapter Three

This chapter has explored the materials of particular interest in SOFC degradation, preparation techniques for analysis, methods to emulate operational thermal cycling, and methods for materials characterisation.

In this thesis cermet and ceramic materials are of particular interest; consequently, this chapter has explored methods for the preparation of cermet powders or pre-fabricated cells for operational thermal cycling and characterisation. Powders can be pressed into pellets, sintered and reduced, before being refined into samples for characterisation, whereas pre-fabricated cells need only be reduced and refined before characterisation. Sample refinement is required to obtain sample sizes suitable for the characterisation instrument employed, and can come in the form of either filing the sample into a powder using a diamond blade or, cutting a sample from the material bulk using either a high-precision laser lathe or manually using a scalpel. Sample preparation can be found in Section 3.2.

Once a sample has been prepared, operational thermal cycles can be emulated by heating the sample to many hundreds of degrees using either a furnace, hot-air blower or a laser. A tubular furnace offers gas-sealing, enabling a reducing environment to be maintained during the operational cycles, preventing oxidation of the anode metal. Similarly, the use of capillaries in the mounting of samples for powder XRD allows a gas to be flowed over the sample through the capillary, also preventing oxidation. The laser heating described here is done so open to the atmosphere, i.e. in the presence of air; however, a gas

environment for laser heating would also be conceivable. Methods for operational thermal cycling can be found in Section 3.3.

Once prepared, a sample can be characterised either before, after or during operational cycling. This can be achieved through many techniques but of particular interest in this thesis are X-ray-based characterisation methods such as X-ray CT and XRD. As discussed in the literature review (Chapter 2) the degradation of SOFC structures is complex and occurs across multiple length scales, from the macro- to, micro- to, crystal-structure. As a result, a range of characterisation methods are required that span multiple length-scales in order to capture such mechanisms. Section 3.4 explores the use of various X-ray beam geometries, optics and energies in order to achieve micro- and nano-CT of the SOFC anode micro- and nano-structures, which in combination with Section 3.6 completes the multi-length scale analysis through the description of powder XRD analysis of the crystal-structure. Sections 3.5 and 3.7 build upon these through the explanation as to how quantitative conclusions can be drawn from the characterisation.

Overall, this chapter describes the methods for preparing SOFC samples for operational cycling and characterisation, from which quantitative analyses can be drawn in order to improve understanding of thermally driven degradation that occurs across multiple length scales within these complex structures.

Chapter Four: Proof-Of-Concept Results

4.1. Introduction to Chapter Four

TPBs are an important microstructural metric to assess the performance and durability of SOFC electrodes. Furthermore, their abundance, or lack of, is known to significantly influence the performance at cell level. The mechanisms that are responsible for the reduction in the number of TPBs and subsequent loss of cell and stack performance are often 4D in nature, i.e. 3D microstructural features that develop over time. In order to observe these developments with time, the sample cannot be destroyed during characterising (as in FIB-SEM) which historically has required the use of nano-CT at specialist synchrotron facilities.

This chapter will begin by demonstrating the first example of the application of lab-based X-ray nano-CT for non-destructive, microstructural characterisation of SOFC electrode materials, where three-phase segmentation has been achieved. Secondly, due to the multi-length scale nature of such mechanisms, the influence of instrument resolution during characterisation is explored, exposing the fractal properties of SOFC microstructures. Finally, methods for achieving 4D tomography at sub-micron resolutions using lab-based X-ray instruments are established.

Sections of this work have been peer reviewed and are either published in the following journal articles: *Heenan, T. M. M., et al., Fuel Cells 17, no. 1 (2017): 75-82; Heenan, T.M.M., Brett, D.J.L. and Shearing, P.R., (2017), In Journal of Physics: Conference Series 849, No. 1, p. 012017. IOP Publishing; Heenan, T. M. M., et al., Nano Energy 47 (2018): 556-565.*

4.2. Establishing a Method for the Characterisation of TPBs in SOFC Electrodes Using Lab-Based X-ray CT.

4.2.1. An Introduction to TPB Characterisation

In widely used composite anodes, the electron, ion and gas transport occurs through the Ni, YSZ and pore networks respectively. Locations where these three networks meet are named TPBs and are known to greatly influence the electrochemical performance of the cell (109; 110; 111). The abundance of TPBs has emerged as a key metric in the evaluation of SOFC electrodes, often presented as a TPB density for direct comparisons. It is therefore desirable to locate and map these points in order to link microstructural and electrochemical characterisation.

To date, there have been two favoured methods for the quantification of TPBs within SOFC anodes: FIB-SEM and synchrotron X-ray CT. FIB-SEM requires the milling of a sample face using an ion beam with sequential 2D imaging via an electron microscope (23). This technique can achieve three-phase segmentation (48; 112; 50; 113; 49) via the high quality, lab-based imaging of electron microscopes; however, FIB-SEM also results in the destruction of the sample, removing the possibility of future analysis. X-ray CT is a widely applied, non-destructive characterisation technique: radiographs are taken at many projections achieved via the rotation of either the source or sample, which are reconstructed into a virtual 3D volume. It is then possible to segment different materials according to their greyscale value, which is dependent on the X-ray attenuation of each constituent material (23).

In previous work, two-phase segmentation of SOFC anodes has been achieved with the use of lab-based equipment (61; 62; 114). Whilst two phase data cannot provide TPB information, the microstructural data can be used to investigate metrics such as pore size distribution, tortuosity and diffusive flux (114; 64). In order to map the TPBs within a microstructure three phases must be segmented, however, to date this has relied on the application of specialist synchrotron facilities which provide high brilliance, tuneable monochromatic radiation (64; 104). In synchrotrons, high spatial resolutions are obtainable through the use of focusing and magnifying optics, although comparable resolutions are now obtainable using lab-based equipment which can achieve voxel sizes down to 16 × 16 × 16 nm^3.

Here, for the first time, the non-destructive three-phase segmentation of Ni-YSZ electrodes using X-ray nano-CT is reported using a laboratory setting. The results demonstrate the possibility for the identification and quantification of not only metrics derived from two-phase information such as pore size distribution, but also solid phase composition, distribution and TPBs. The sample volumes and voxel sizes demonstrated here are comparable to those currently available from synchrotron sources (61; 59; 104). Due to the greater availability of lab-based techniques in comparison to the limited accessibility of synchrotron facilities, lab-based X-ray CT offers the potential to accelerate microstructural analyses and the design of improved electrodes.

4.2.2. Nanoscale TPB Characterisation Investigation Procedure

To perform this study, model SOFC anode samples (S411 – S414) of varying microstructure were prepared using 12 tonnes of iso-static pressing of NiO-YSZ powder (Fuel Cell Materials, OH, USA) to form cylindrical pellets which were subsequently sintered at 1200 °C for 2.5 hours in air within a box furnace. The pellets were then reduced to Ni-YSZ in forming gas (4% H_2 in 96 % N_2) for 2 hours at 800 °C in a tubular furnace. Reduction was confirmed by EDX chemical analysis and SEM imaging. Further detail on the use of furnaces for sintering and thermal cycling can be found within the mythology (Section 3.3.).

Table 4 Experimental procedure for chapter section 4.2: establishing a method for the characterisation of TPBs in SOFC electrodes using lab-based X-ray CT.

Sample	Preparation and Scanning
S411	Powders pressed into pellets; Sintered 1200 °C 2.5 hrs in air; Reduced 800 °C 2hrs in forming gas (4% H_2 in 96 % N_2); Four samples prepared using a scalpel and each scanned in HRes and LFOV of the Ultra
S412	
S413	
S414	
S415	Pre-Fabricated anode-supported half-cell; 5 µm electrolyte on 500 µm anode; Reduced 800 °C 2 hrs in forming gas (4% H_2 in 96 % N_2); Laser Prepared: 800 µm pillar removed from bulk and refined to 350 µm; One sample scanned in the Versa at 40X magnification

Table 5 Imaging conditions for chapter section 4.2: establishing a method for the characterisation of TPBs in SOFC electrodes using lab-based X-ray CT.

Sample	Investigation	Scan	Instrument	Projections	Exposure Time / s	Voxel Size / nm	FOV / µm
S411	I411 Nano- CT	D411	Ultra LFOV	1101	45	127	64
		D412	Ultra HRes	1501	65	33	16
S412		D413	Ultra LFOV	1101	45	127	64
		D414	Ultra HRes	1501	65	33	16
S413		D415	Ultra LFOV	1101	45	127	64
		D416	Ultra HRes	1501	65	33	16
S414		D417	Ultra LFOV	1101	45	127	64
		D418	Ultra HRes	1501	65	33	16
S415	I412 Micro-CT	D419	Versa 40X	2401	30	395	384

The expected heterogeneity within the samples prepared here provides model microstructures of known composition ideal for technique development. To conduct 3D microstructural analyses of the samples, fragments were removed from the reduced pellet bulk using a sharp razor producing sample diameters smaller than the largest X-ray FOV, *ca.* 50 µm. Each fragment was then attached to a pin head with the use of an epoxy to secure the sample; minimising drift during the scan and thus artefacts in the reconstruction. Tomography scans D411 – D418 were conducted with the use of a lab-based X-ray nano-CT instrument (Zeiss Ultra 810, Carl Zeiss., CA, USA). Whilst this sample preparation technique has acknowledged limitations (115), it has been successfully applied to prepare

SOFC materials (40) and was deemed adequate for the provision of model samples required here. The sample preparation and scanning parameters are tabulated in Table 4 and Table 5, respectively.

4.2.3. Four Anode Samples Inspected at Two Resolutions

The ability to map and quantify TPBs is of great importance when analysing the influence of microstructure on the electrochemical performance of the electrode, but electrode microstructures can vary greatly between samples and within the same sample over time; heterogeneous microstructures can limit TPB density. Therefore heterogeneous samples have been chosen for this study to demonstrate the versatility and application of such techniques. Four samples (S411 – S414) were imaged using the lab-based CT technique at both HRes and LFOV resolutions resulting in a total of eight tomograms. More information can be found on the use of HRes and LFOV imaging modes within the methodology (Section 3.4). Once segmented, compositional data was obtained via the summation of all voxels containing Ni, YSZ or pore, presented as a volume percentage for each phase. This was repeated for each tomogram. The 2D slices for each of the four samples (S411 – S414) can be seen in both LFOV and HRes in Figure 19 b and c, respectively, with accompanying compositional data in Figure 19 d.

It is widely acknowledged that, when imaging the complex heterogeneous microstructures characteristic of electrochemical devices, the resolution requirement will depend on which microstructural property is under investigation (116). For example, when determining pore or particles sizes, the effective spatial resolution must be sufficient to capture the volumetric features in their entirety. Similarly, when assessing 2D properties such as surface area, the resolution should be sufficient to capture the materials surface roughness.

To allow direct comparison between the two imaging modes adopted here (LFOV and HRes) the same ROI has been analysed at the two length scales for each of the four samples (S411 – S414) to determine whether resolution significantly affects the TPB measurement. Slices from the two segmented volumes are displayed in Figure 20. A comparison of the two modes has been conducted by examination of the volumetric composition, solid volume composition and TPB density, all displayed in Table 6.

Microstructural data is comparable across the two length scales for volume and solid volume percentage compositions and the average solid volume percentages broadly match with that expected after reduction according to the manufacturer's data: 56 % YSZ to 44 % Ni (117). As with all image-based quantification techniques, it is only possible to capture particles that are larger than the effective spatial resolution; whilst the inspected volume element should be sufficient to ensure statistical significance of these solid volume fractions. It is noteworthy that the largest departure from the manufacturer's stated volume fraction occurs for HRes scans with small FOVs (scans D412 and D416). This further highlights the benefits of a multi-scale imaging approach.

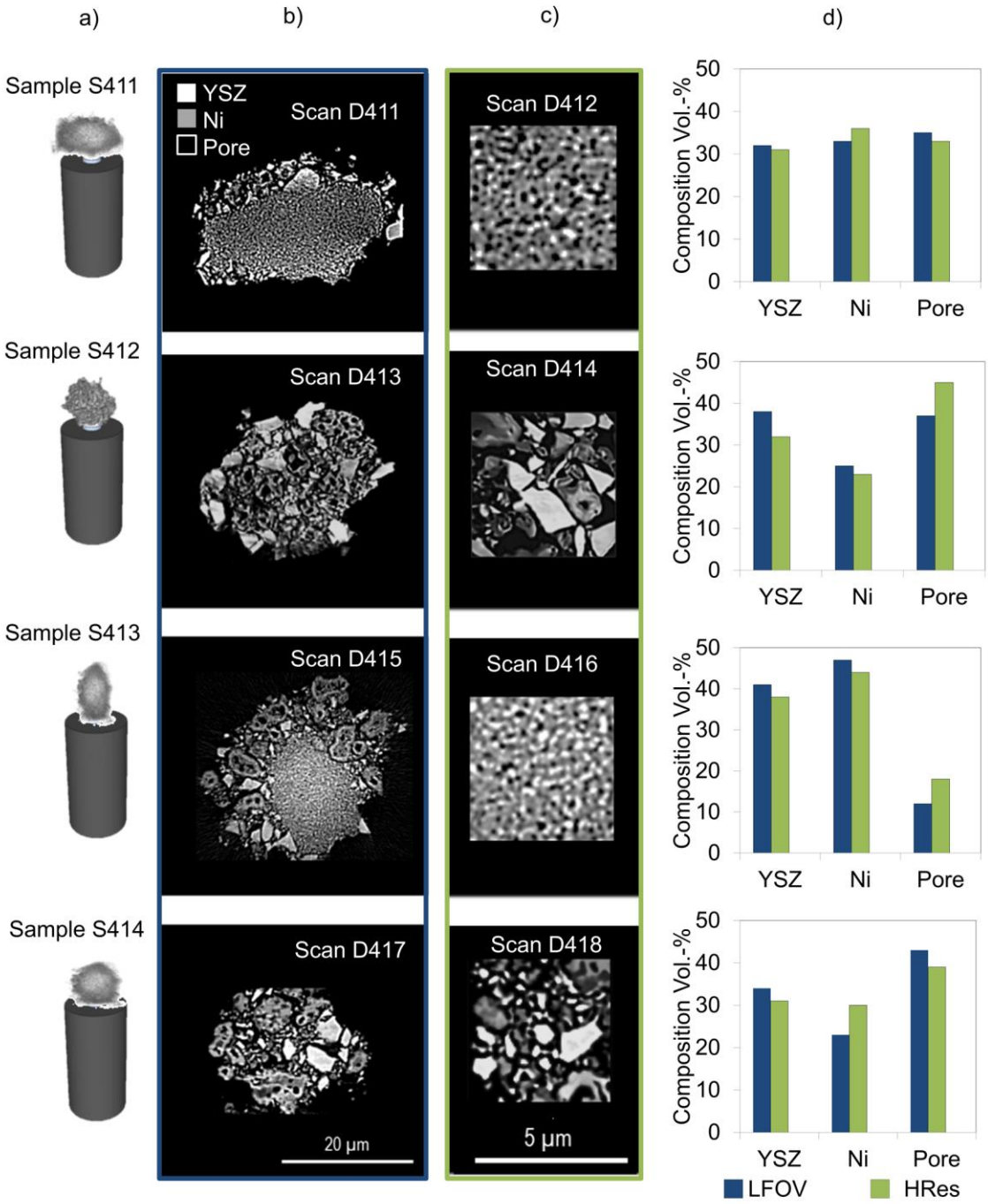

Figure 19 Microstructural information obtained from four Ni-YSZ SOFC anode samples using lab-based X-ray CT at two length scales: HRes and LFOV. Four samples 4.1.1 – 4.1.4 a) each with two tomograms of b) LFOV, and c) HRes, with d) compositional information for LFOV (blue) and HRes (green).

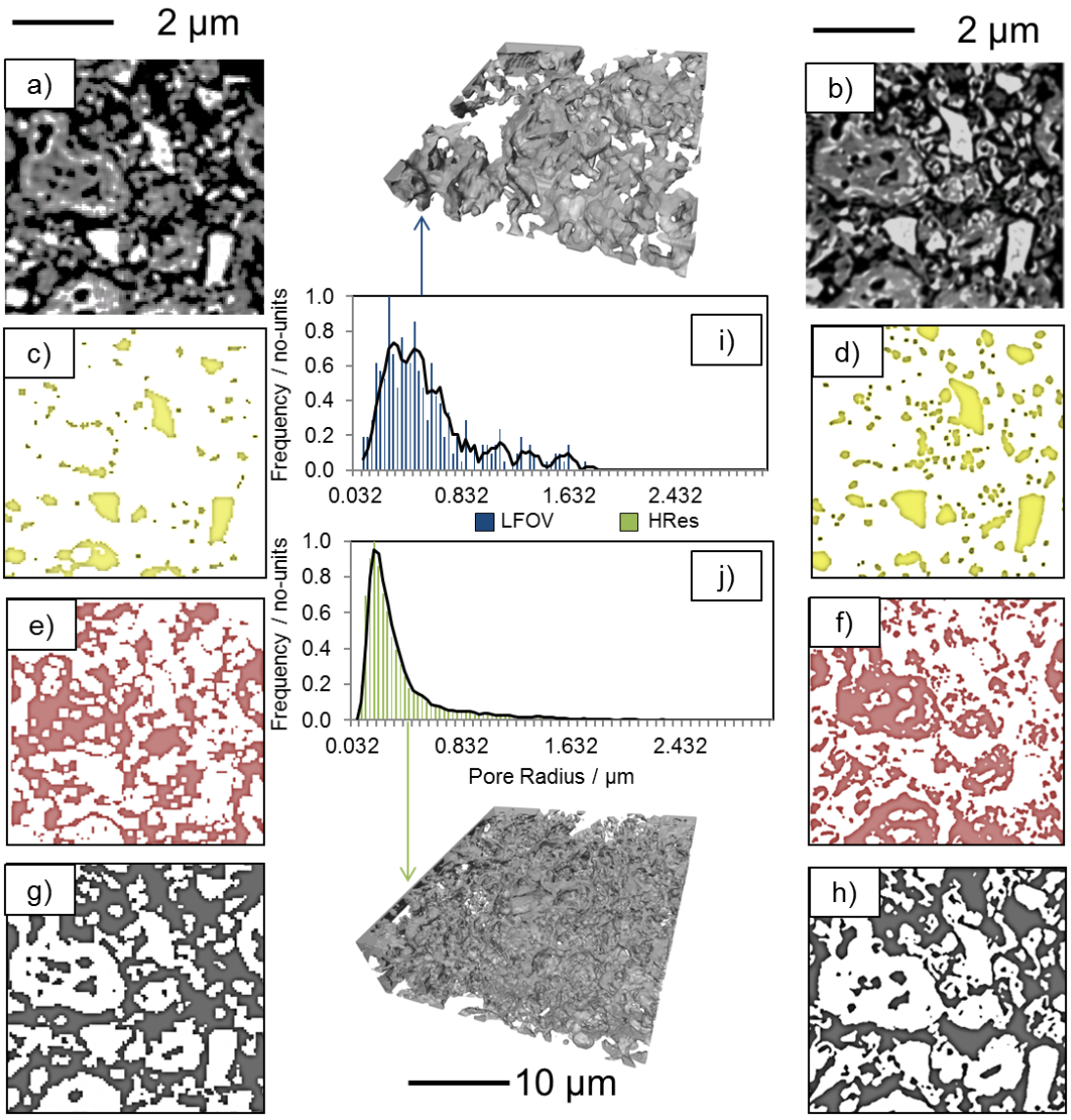

Figure 20 Demonstration of three-phase segmentation in the same ROI at two resolutions LFOV (a, c, e and g) and HRes (b, d, f and h): a and b) smoothed greyscale images, c and d) segmentation of the YSZ, e and f) Ni and g and h) pore, with pore phase reconstruction with accompanying pore size distribution for i) LFOV (blue) and j) HRes (green).

TPB data is compared across the two length scales (Table 6) resulting in values similar to that presented previously for comparable microstructures (61; 118). Small deviation is seen resulting in a higher TPB value recorded at HRes due to the higher resolution detecting an increased number of small particles, as described above.

Table 6 Microstructural information for Ni-YSZ SOFC anode samples S411 – S414 obtained using lab-based X-ray CT at two length scales: HRes and LFOV.

Sample	Technique	Volume Composition / %			Solid Volume Composition / %		ρ_{TPB} / μm^{-2}
		Ni	YSZ	Pore	Ni	YSZ	
S411	LFOV	33	32	35	51	49	2.1
	HRes	36	31	33	54	46	2.6
S412	LFOV	25	38	37	40	60	1.7
	HRes	23	32	45	42	58	2.8
S413	LFOV	47	41	12	53	47	4.0
	HRes	44	38	18	54	46	5.6
S414	LFOV	23	34	43	40	60	2.4
	HRes	30	31	39	49	51	3.3

4.2.4. Repeatability Examined Through Correlating Greyscale to Attenuation

Microstructural investigations into SOFC materials often require repeated imaging to understand the development of structural changes over time. It is therefore of great importance to understand the repeatability of this technique, particularly as some changes in microstructure are known to be subtle (64). One method of testing the consistency of the tomogram data would be by examination of the constituent greyscale values; if two materials are imaged using the same energy, and exposure time the difference in their greyscale values can be compared directly to their attenuation coefficients, as discussed within the methodology (Section 3.5). This method has been applied to the four samples (S411 – S414) analysed at both length scales (HRes and LFOV). As a result the ratio of the greyscale values could be calculated for each of the eight tomograms from the greyscale histograms of the Ni and YSZ particles.

Common laboratory X-ray sources using copper, Cu, or chromium, Cr, for X-ray generation provide characteristic peak emissions at 8.0 and 5.4 keV respectively. Hence, when inspecting the variation of attenuation properties across the commonly employed range of dopant concentrations used during *x*YSZ fabrication (x = 3 – 8 mol% yttria addition to zirconia) a fixed energy of 5.4 keV was chosen. It was found that the compound mass attenuation coefficient for *x*YSZ deviated by insignificant amounts through the entire dopant range; the *x*YSZ mass attenuation coefficient reduced by less than 0.5 $cm^2\ g^{-1}$ from 3 to 8 mol %. The elemental contribution to attenuation properties was then inspected by considering the difference in mass attenuation coefficient between zirconium,

the primary element within *x*YSZ, and Ni; $\mu_{m,Zr}$ is *ca.* 166 % larger than $\mu_{m,Ni}$ at 5.4 keV. Concluding that at 5.4 keV the ability to obtain three-phase segmentation is greatly dependent upon the elemental contribution whereas doping level has negligible effect for *x*YSZ. At 5.4 keV and using mass densities of 5.9 g cm^{-3} and 8.9 g cm^{-3} (31) for 8YSZ and Ni respectively the attenuation coefficients for μ_{8YSZ} and μ_{Ni} are approximately 1762 cm^{-1} and 1346 cm^{-1} (77), producing a ratio of the attenuation coefficients, η_A, of *ca.* 1.31. In order to obtain greyscale values, three Ni particles were chosen from each of the eight tomograms, with a central cube removed from each particle to determine the local greyscale value, the three greyscale values were then averaged. This was then repeated for YSZ and the ratio of the greyscale values, η_G, was calculated for each tomogram. One η_G calculation is demonstrated in Figure 22 displaying the local greyscale histogram for each particle. Table 7 compares the calculated η_A to the average η_G obtained from the eight tomograms and Figure 22 displays the η_G for each of the eight tomograms in comparison to the calculated η_A. It is seen that the η_G obtained for each sample is consistent with the η_A. The minor discrepancy between the experimental average (1.36) and the theoretically calculated value (1.31) may be attributed to small nano-pores within the Ni microstructure that are beyond the resolution of the imaging instrument. This would explain the slightly larger ratio than expected.

Table 7 Greyscale information obtained from each of the four samples (S411 – S414) at both HRes and LFOV displaying the greyscale values for Ni (G_{Ni}) and (G_{YSZ}) with accompanying η_G for each sample at both LFOV and HRes.

Sample	Technique	Greyscale Value / no units		η_G /no units
		G_{Ni}	G_{YSZ}	
S411	LFOV	114	148	1.30
	HRes	129	168	1.30
S412	LFOV	129	211	1.64
	HRes	150	227	1.52
S413	LFOV	121	156	1.29
	HRes	98	121	1.24
S414	LFOV	143	195	1.36
	HRes	129	164	1.27
Experimental Average	LFOV & HRes	127	174	1.36
Theoretical	Attenuation Calculation	-	-	1.31

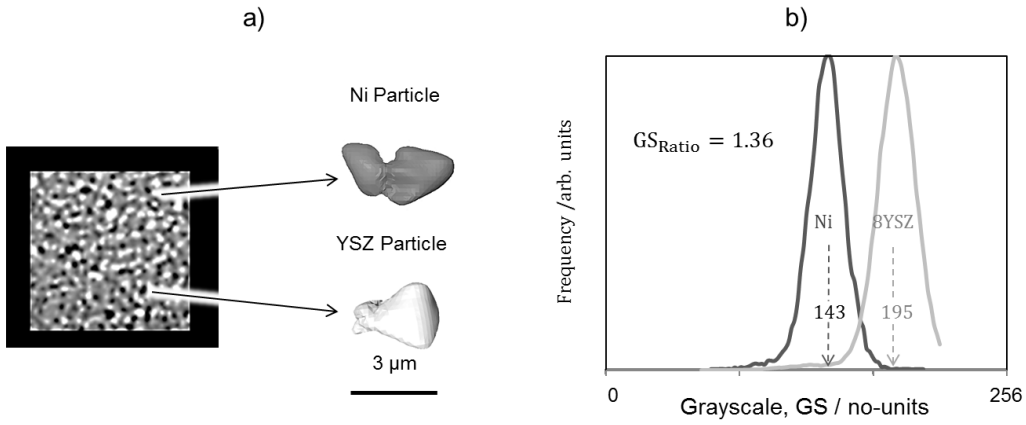

Figure 21 Correlating the difference in attenuation coefficient to the separation of greyscale peaks for two materials: Ni and YSZ: a) A greyscale slice and extraction of two particles: grey Ni and white YSZ and b) greyscale peaks for a LFOV sample data set.

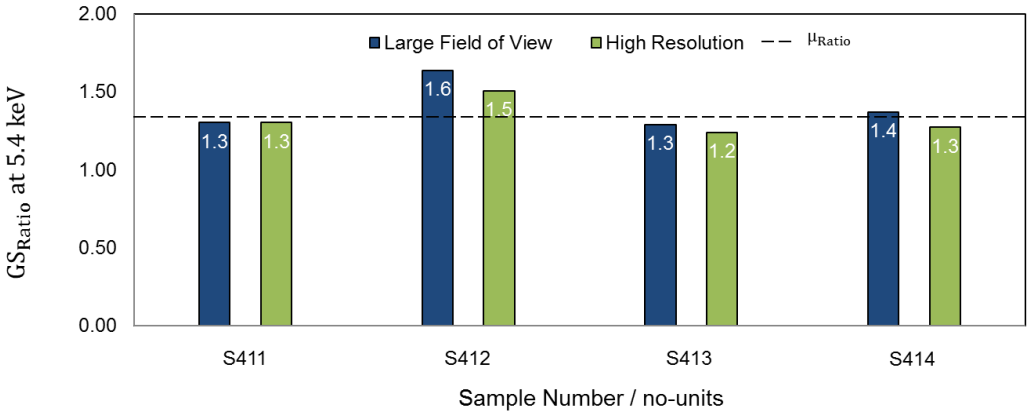

Figure 22 Correlating the difference in attenuation coefficient to the separation of greyscale peaks for two materials: greyscale ratios for all four samples (S411 – S414) at both length scales, HRes and LFOV with comparison to the attenuation coefficient ratio.

4.2.5. Achieving Statistically Representative Volumes at the Nanoscale

The sample volume investigated should be maximised in order to ensure that the tomogram is statistically representative of the material under investigation; a representative volume should be achieved (61; 104; 116). In order to compare the statistical significance of a sample, a representative volume element (RVE) analysis can be conducted for a given parameter (TPB, VSSA, vol %, etc.) typically utilising a region growing algorithm considering sub-samples of successively larger volumes and extracting the metric of interest, as discussed in the methodology. At volumes below the RVE, oscillations in the considered metric will be observed, which are expected to dampen and disappear as the sample volume approaches the RVE. Typically the RVE will be quoted as the sample volume where oscillations between successive regions are small enough to keep within a defined tolerance, say <2%, however for samples where there are heterogeneities on more than one length scale, this approach may not be sufficiently robust (119).

For example, it is conceivable that in a given sample, oscillations for a ‘nanoscale’ heterogeneity would disappear at a much smaller RVE than for a ‘microscale’ heterogeneity in the same sample. Noting the heterogeneities in these microstructures, the following approach is proposed: once the oscillation is noted to fall below a tolerance of 2.5 % between successive regions, the region growing algorithm is continued for a pre-defined additional volume, monitoring the parameter of interest for the onset of any additional oscillations. This additional ‘stability’ window provides increased confidence in the RVE analysis

where multi-scale heterogeneity is expected. The size of the stability window can be defined by the user, 50 μm^3 is chosen here for HRes and 100 μm^3 for LFOV corresponding to ca. 10% of the overall scan volumes, with TPB as the metric of interest, the results of which are displayed in Figure 4 (95).

Eight RVE analyses were conducted producing TPB density variation with volume analysed, seen in blue for LFOV and green for HRes for all four samples (S411 – S414) in Figure 23. The LFOV data for samples S411 and S413 show convergence around 700 μm^3 while LFOV samples S412 and S414 reach a convergence but above 1000 μm^3, an anticipated variation due to the increased heterogeneity within samples S412 and S414. All samples within the HRes appear to stabilise within ca. 400 – 500 μm^3 although this may not be representative of the macroscopic heterogeneities. When investigating TPBs, the LFOV imaging technique provides sufficient statistical relevancy for the samples displayed here, through robust repeatability within large sample volumes. However, this may present lower accuracy than the HRes technique due to the fractal-type nature of the TPB quantity, indeed this resolution dependence is a common problem throughout materials characterisation (120). Therefore, although HRes offers potentially higher accuracy in TPB quantification, additional volume may be required for confidence in statistical relevancy, this can be achieved via the vertical stitching of two or more data sets or through the multi-scale approach adopted here.

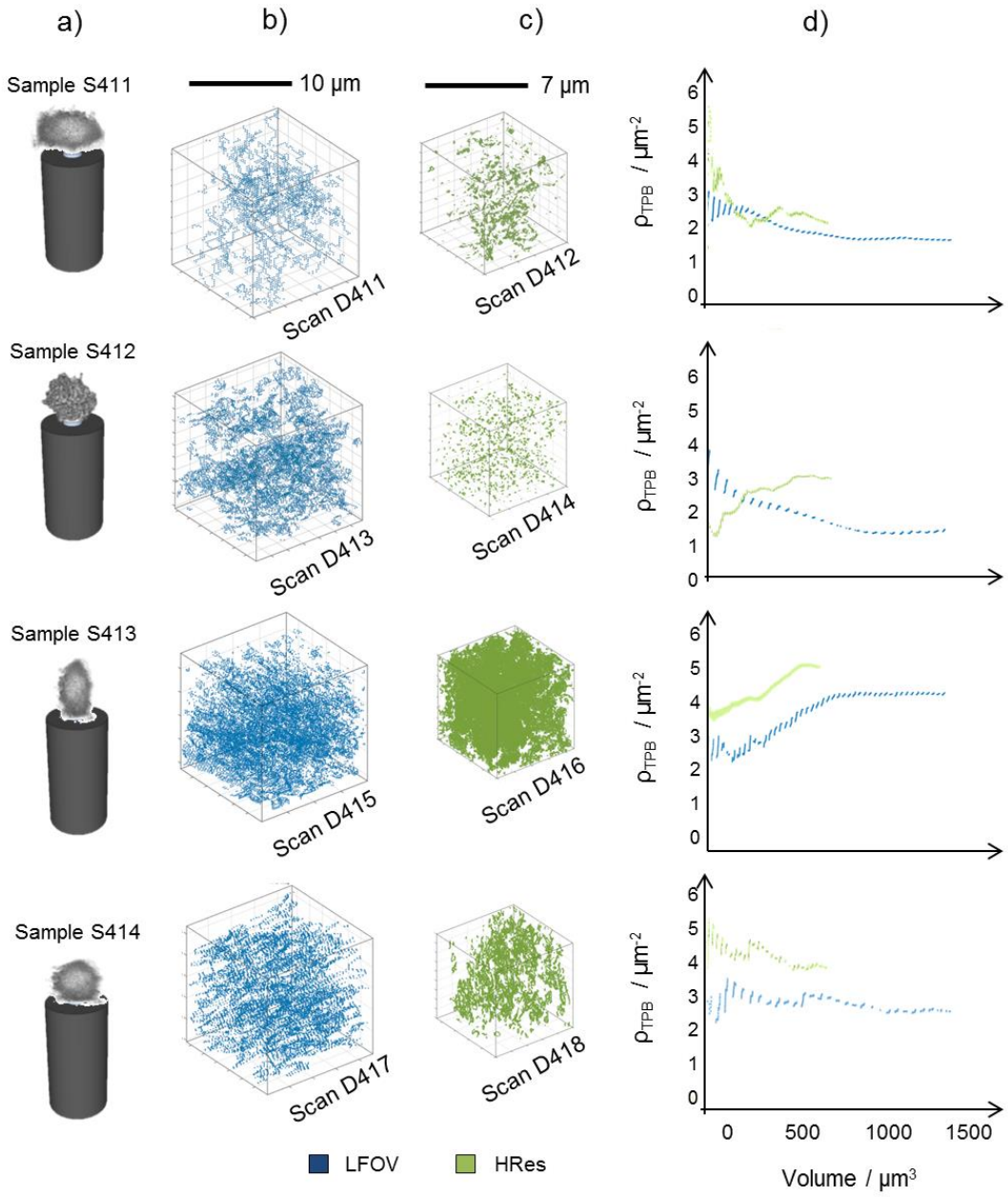

Figure 23 TPB maps with accompanying representative volume element analysis conducted via an expanding cube algorithm: a) samples S411 – S414, b) LFOV TPB maps, c) HRes TPB maps and d) RVE analysis with LFOV presented in blue and HRes presented in green.

4.2.6. Macroscale TPB Characterisation

Thus far, this chapter has discussed the three-phase segmentation of samples characterised using the Zeiss Xradia 810 Ultra which employs a quasi-monochromatic beam to inspect the TPB using nano-CT for high-resolutions and relatively small sample volumes. However, degradation is known to occur across multiple length scales (95) often requiring the use of several instruments with various optics, as discussed within the methodology (Section 3.1). And although two nano-CT imaging methods: LFOV and HRes have been demonstrated here, in order to examine macroscopic degradation methods for micro-CT imaging must also be developed.

4.2.7. Macroscale TPB Characterisation Investigation Procedure

The following segmentation method was developed for the Zeiss Xradia 520 Versa which, unlike the Ultra, employs a polychromatic beam. Imaging with an 80 kV source voltage will produce a characteristic emission peak at 58 keV with Bremsstrahlung radiation observed both above and below this peak with a maximum emission observed at 80 keV. Therefore due to the range of wavelengths emitted from the source, the verification of the Versa segmentation required a different approach.

To explore this an 800 μm diameter pillar was therefore removed from a planar, anode supported anode/electrolyte SOFC (Fuel Cell Materials, OH, USA) using an laser micro-machining technique (A Series/Compact Class 4 532 nm Laser Micromachining System, Oxford Lasers, Oxford, UK) as described elsewhere (88). The cell consisted of a 500 μm NiO - 8mol% YSZ (8YSZ) cermet

(NiO-8YSZ) anode and a 10 μm 8YSZ ceramic electrolyte, as specified by the manufacturer. Once removed from the bulk, the 800 μm pillar was attached to an alumina tube using high-temperature cement before being milled further to ca. 350 μm in diameter, the mounting procedure can be found within the methodology (Section 3.2).

Prior to the collection of any structural information the metal within the fuel cell anode was first reduced from NiO to Ni, producing a Ni-8YSZ cement. Reduction was conducted within a tubular furnace under the flow of forming gas (4% H_2 96% N_2) using a 3 ºC min^{-1} thermal ramp rate to 800 ºC where the sample (S415) was held isothermally for 2 hours before being allowed to cool passively. Once reduced to Ni-YSZ the sample (S415) was imaged using a lab-based X-ray micro-CT instrument (Zeiss Xradia 520 Versa, Carl Zeiss., CA, USA). 2401 radiograph projections were collected at an exposure of 30 s each achieving an isotropic pixel length of 395 nm (binning 2) with a square FOV of 384 μm × 384 μm. The radiographs were reconstructed using commercial software (‘XMReconstructor Scout-and-Scan’, Zeiss, Carl Zeiss., CA, U.S.A.) using cone-beam filtered back projection algorithms, resulting in a sample volume of approx. 2×10^7 μm^3.

4.2.8. Greyscale Fiducials for Three-Phase Segmentation

For macroscale TPB characterisation known materials within the X-ray FOV were used as greyscale fiducial markers from which reference points within each tomogram’s histogram could be established, and used as a basis for the segmentation of the rest of the anode. The first greyscale-fiducial was the

electrolyte: known to be at the top of the sample (S415) and *ca*. 10 μm in thickness (Figure 24), a large volume of bright greyscale values from the electrolyte bulk were referenced to the whole tomogram's histogram. A large volume of dark greyscale values from the open pore above the electrolyte was used as the second greyscale-fiducial; again, these greyscale values were referenced to the tomogram's histogram (Figure 24 and Figure 25). Using these two references, the voxels which were considered to represent ceramic and pore materials were removed from the 3D volume and the remaining voxels were considered to be occupied entirely by Ni.

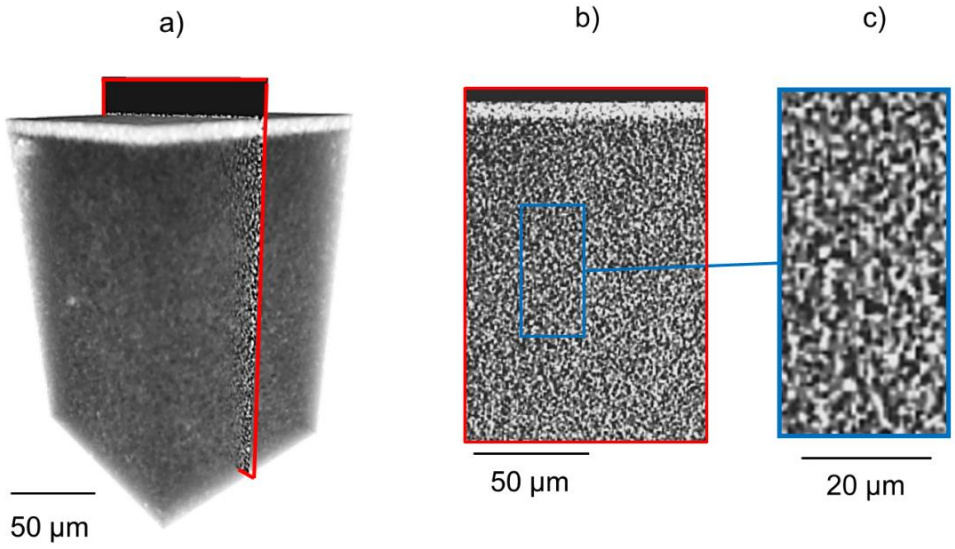

Figure 24 X-ray CT analysis of an anode supported anode/electrolyte SOFC: a) 3D volume render of a sub-volume removed from the greyscale tomogram with an x-z orthogonal slice bisecting the volume and b) extracted, c) magnified.

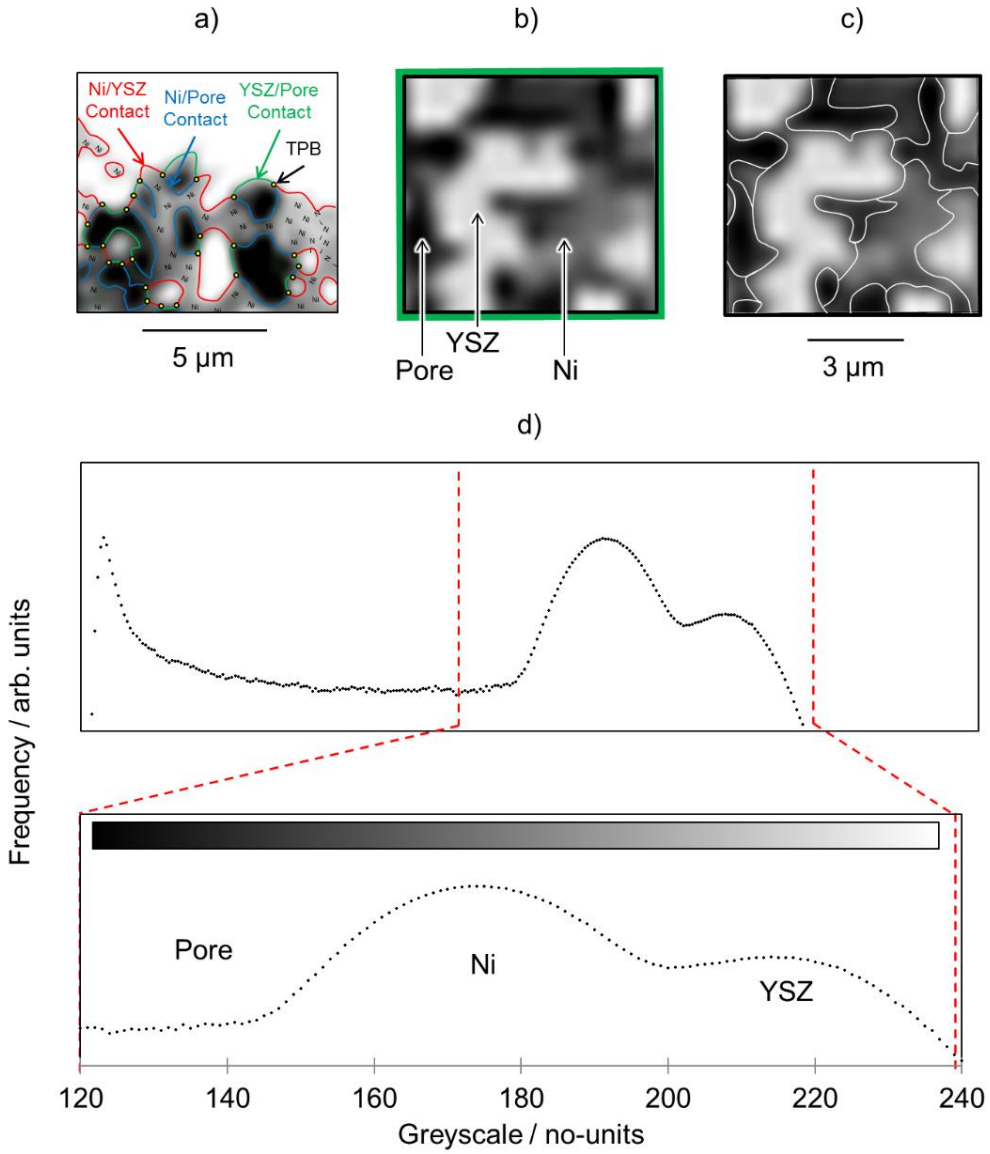

Figure 25 X-ray CT analysis of an anode supported anode/electrolyte SOFC: a) outlines of phase boundaries and TPB locations on an interfacial sub-slice, b) greyscale slice with indication of the three constituent materials: Ni, YSZ and pore, c) with outlined segmentation boundaries, d) the accompanying greyscale histogram with cropped values for segmentation.

4.2.9. Achieving Statistically Representative Volumes at the Macroscale

RVEs for the composition and TPB density were conducted for the macroscale structure and are presented in Figure 26. The RVE analysis was conducted by calculating the chosen variable for a sample volume of a single slice then increasing the sample volume by one slice at a time until the full ROI was investigated, i.e. a constant area, growing volume analysis. Each variable stabalised sufficiently within the ROI, providing confidence in the metric extraction.

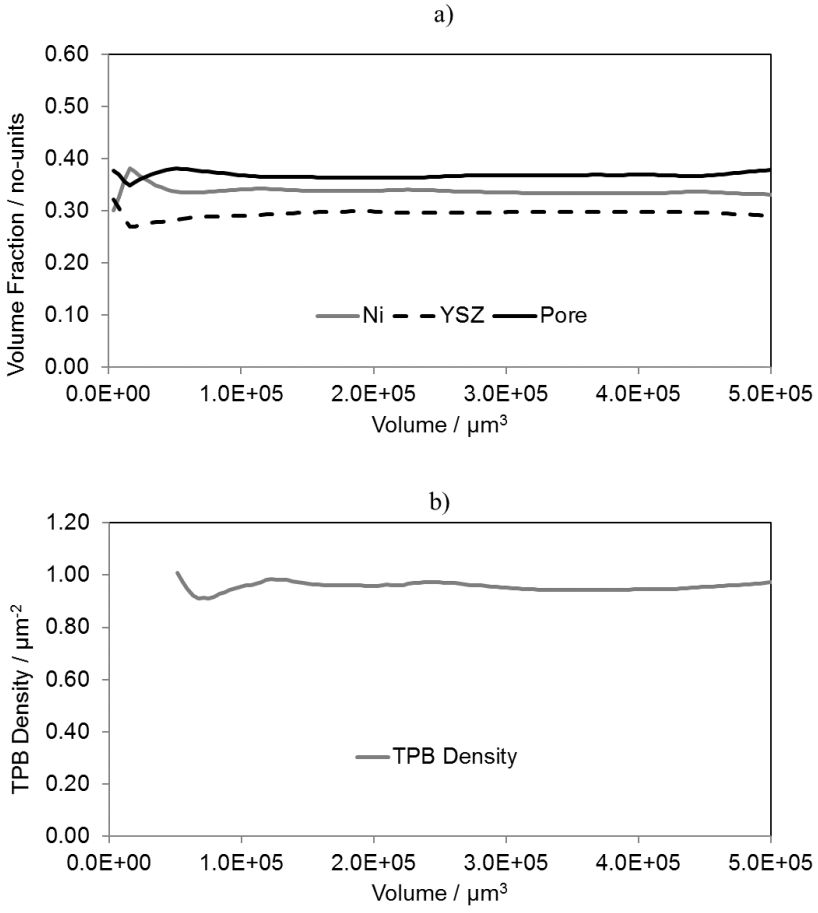

Figure 26 X-ray CT analysis of an anode supported anode/electrolyte SOFC with RVE analysis of the a) composition and b) TPB density.

4.2.10. Conclusions from TPB Characterisation

Three-phase segmentation of Ni-YSZ SOFC electrodes has been achieved for the first time using multi-scale, non-destructive, lab-based X-ray CT. This technique allows for the analysis of both large sample volumes and high resolutions, comparable to that which are currently achievable at synchrotron facilities.

For structures observed through the use of nano-CT the solid phase segmentation has been compared to values expected upon reduction of the NiO to Ni, showing similarity and consistency throughout a variety of model microstructures. The greyscale histograms for the 3D data sets have been analysed at LFOV and HRes length scales and compared to the expected attenuation coefficients of the two solid materials, Ni and YSZ, showing small variation but close correlation on average at both length-scales. Demonstration of the application of such three-phase data has been shown via the mapping and quantification of the TPBs including an analysis of the volume required for the measured TPB densities to be representative of the material bulk. This technique has shown robustness in the quantification and mapping of TPBs across various volumes and microstructures. For structures observed through the use of micro-CT, greyscale fiducials using known materials with the X-ray FOV were employed to segment the data into three phases. Proceeding segmentation, the metrics were also analysed for statistical relevancy through RVE analysis of the compositon and TPB density.

Due to the inherent link between structure and electrochemical performance, many microstructural properties have been explored in the pursuit

mitigating degradation though intelligent electrode design. Instruments such as lab-based X-ray tomographs are now capable of imaging across multiple length scales, where the smallest resolutions are comparable to specialist synchrotron facilities. However, the influence of resolution on the resulting microscopic roughness that is observed has, until now, not be investigated using X-ray CT, and has only recently been explored using FIB-SEM (97) The following chapter section will, for the first time, explore the effect of X-ray CT characterisation resolution for several key metrics of SOFC performance. Moreover, the study is extended through the use of multiple instruments and beam geometries for a variety of sample microstructures. This work introduces the importance of the fractal properties of microstructures characterised using X-ray CT, not limited to SOFCs but extending throughout the field of X-ray CT.

4.3. Inspecting the Influence of Resolution and Associated Fractal Dimensions when Characterising SOFCs.

4.3.1. An Introduction to Resolution Effects and Fractal Dimensions

There are several examples of how electrochemical modelling has been enhanced through the use of X-ray CT, for instance the extraction of tortuosity information, often in the form of a tortuosity-factor (τ) (121) has improved the accuracy in the prediction of effective transport properties such as diffusion and, electrical and ionic conductivities. Furthermore, the incorporation of characterisation across multiple length-scales has allowed diffusion modelling to accommodate continuum physics through to Knudsen flow via real microstructures (122). However, multi-length scale characterisation is still a growing field and understanding of the effects of resolution on the metrics compared at different resolutions remain limited. TPB characterisation is particularly prevalent in SOFC research and steers the advancement of cell performance by the comparison of cell microstructures via electrochemical models (90). It is therefore imperative to ensure accuracy in the comparison of different ρ_{TPB} values.

It has previously been observed that the ρ_{TPB} value quantified for the same sample at higher resolutions consistently results in a higher reaction site density (96). Building upon this, Bertei *et al.* investigated the influence of resolution on the reaction site density by the definition of a TPB fractal dimension obtained through FIB-SEM characterisation (97). These fractal properties were then employed to improve an electrochemical model. This fractal relationship between resolution and characterised length is based upon work by Mandelbrot whereby

a measured length such as the length of a country's coastline (98) or the micro-features in fractured metal (99) increases in detail, thus magnitude, with increasing resolution. Although fractal properties have been extensively reported since (123; 102; 103; 100), knowledge of the fractal properties of electrochemical materials remains limited. Additional aspects of investigations into fractals has been explored in the litrerature review and methodology. The following studies will investigate the fractal properties of SOFC microstructures and the influence of the resolution in characterising structural metrics.

4.3.2. Micro-CT Investigation Procedure

Firstly, the effective electrical conductivity of porous Ni is inspected at two resolutions using the Versa (cone-beam X-ray micro-CT). To do this, porous Ni metal (Novamet Specialty Products Corp, Lebanon) powder was pressed into a cylindrical pellet under pneumatic compression. Once formed, the pellet was sintered for 2.5 hours at 1200 °C in air within a box furnace and subsequently reduced to Ni for 2 hours at 800 °C in forming gas (4% H_2 in 96% N_2) within a tubular furnace. A sample (S421) was then prepared by extracting a small particle from the material bulk using a sharp scalpel and attached to the top of a pin using fast-set epoxy (96). For this micro-CT analysis, the sample (S421) was prepared with a diameter of ca. 400 µm. Lab-based micro-CT was achieved through the use of an Xradia 520 VERSA X-ray instrument (Zeiss 520 VERSA, Carl Zeiss inc., CA, USA). at two magnifications, namely, 40X and 20X, both with a binning of 2 applied during acquisition with voxel sizes of 400 nm and 800 nm, respectively. Reconstruction was accomplished using Feldkamp-Davis-Kress

(FDK) algorithm using commercial software (‘Reconstructor Scout-and-Scan’, Carl Zeiss Inc., CA, U.S.A.). No resolution resampling was applied to this part of the study. Sample preparation and imaging conditions can be found in Table 8 and Table 9.

Table 8 Experimental procedure for chapter section 4.3: inspecting the influence of resolution and associated fractal dimensions when characterising SOFCs.

Sample	Preparation
S421	Ni powder pressed into pellets; Sintered 1200 °C 2.5 hrs in air; Reduced 800 °C; 2 hrs in forming gas (4% H_2 in 96 % N_2); One sample prepared using a scalpel; First CT conducted in the Versa at 20X magnification; Second CT conducted in the Versa at 40X magnification
S422	Ni-YSZ powder pressed into pellets; Sintered 1200 °C 2.5 hrs in air; Reduced 800 °C 2 hrs in forming gas (4% H_2 in 96 % N_2); Prepared using a scalpel; Four samples prepared using a scalpel; Three samples imaged in both the LFOV and HRes of the Ultra and the last sample imaged only in the Ultra LFOV
S423	
S424	
S425	

Table 9 Imaging conditions for chapter section 4.3: inspecting the influence of resolution and associated fractal dimensions when characterising SOFCs.

Sample	Investigation	Scan	Instrument	Projections	Exposure Time / s	Voxel Size / nm	FOV / µm
S421	I421 Ni Conductivity	D421	Versa 20X	2401	30	800	768
		D422	Versa 40X	2401	30	400	384
S422	I422 YSZ conductivity	D423	Ultra HRes	1501	65	32	16
		D424	Ultra LFOV	1101	45	130	64
S423	I423 TPB comparison of two structures	D425	Ultra HRes	1501	65	32	16
		D426	Ultra LFOV	1101	45	130	64
S424		D427	Ultra HRes	1501	65	32	16
		D428	Ultra LFOV	1101	45	130	64
S425	I424 Percolation	D429	Ultra LFOV	1101	45	130	64

4.3.3. The Influence of Resolution on Predicting Ni Conductivity

Inspecting the two data sets it can be seen (Table 10) that the Ni phase tortuosity-factor is significantly higher for the lower resolution tomogram, *i.e.* $\tau_{Ni\,800\,nm} > \tau_{Ni\,400\,nm}$, regardless of directional orientation. However, the directional trend remains: *i.e.* $\tau_{Ni_x} > \tau_{Ni_y} > \tau_{Ni_z}$ for both $400\ nm$ and $800\ nm$ voxel lengths. Unlike

the tortuosity-factor, the effect of resolution on the two-phase composition is negligible, *ca.* 2%. Deviations in the tortuosity-factor and composition with resolution are displayed in Figure 27 and Table 10.

Table 10 Microstructural properties for porous nickel obtained via micro-CT with two isotropic voxel lengths: 400 and 800 nm.

	Voxel Length / nm	**τ_{Ni} / no-units**				**Volume fraction / no-units**
		x	**y**	**z**	**Avg.**	
Ni	400	2.43	2.15	2.07	2.22	0.53
	800	3.38	2.70	2.41	2.83	0.51
Pore	400	3.04	2.81	2.11	2.65	0.47
	800	2.86	2.67	2.04	2.52	0.49

These tortuosity and composition values were then inserted into the effective conductivity equation (see Section 3.6.11) in order to inspect variation with temperature for the three orientations.These factors result in a difference between the effective conductivity characterised with voxel lengths of 400 nm and 800 nm of 28, 20 and 14 % in the x, y and z orientations, respectively. These are considerable discrepancies however, resistance attributed to the electrical transport in Ni is typically assumed to be negligible compared to resistance of ion transport within the ceramic. Therefore although the voxel length employed in characterising the Ni properties can strongly influence the effective conductivity, electrical conductivity values remain orders of magnitude larger than that which are attributed to ionic transport.

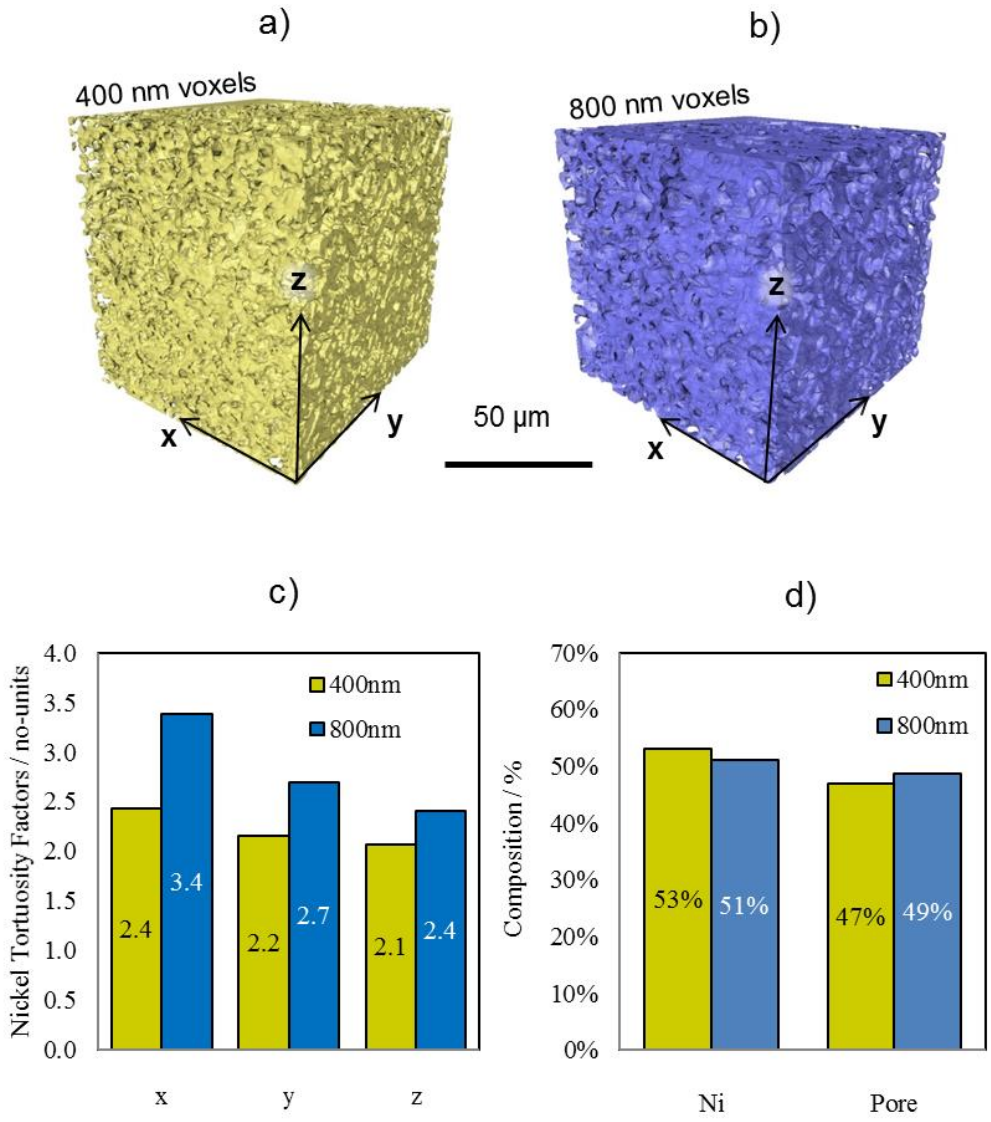

Figure 27 Influence of resolution on the effective electrical conductivity of Ni metal: 3D surface generations from tomograms obtained using cone-beam X-ray micro-CT at two resolutions a) 400 nm and b) 800 nm, with accompanying c) directional tortuosity-factors and d) phase compositions.

Table 11 Effective electrical conductivity values for nickel calculated for the operating temperatures of SOFCc corrected using microstructural data obtained via micro-CT with two data sets of isotropic 400 nm and 800 nm voxel lengths.

Temperature / °C	σ_x **/** $\times 10^6\ S\ m^{-1}$		σ_y **/** $\times 10^6\ S\ m^{-1}$		σ_z **/** $\times 10^6\ S\ m^{-1}$	
	400 nm	**800 nm**	**400 nm**	**800 nm**	**400 nm**	**800 nm**
600	5.75	4.13	6.50	5.17	6.75	5.80
700	5.19	3.73	5.86	4.67	6.09	5.23
800	4.71	3.38	5.32	4.24	5.53	4.75
900	4.29	3.09	4.85	3.86	5.04	4.33
1000	3.93	2.83	4.45	3.54	4.62	3.97
Offset	28 %		20 %		14 %	

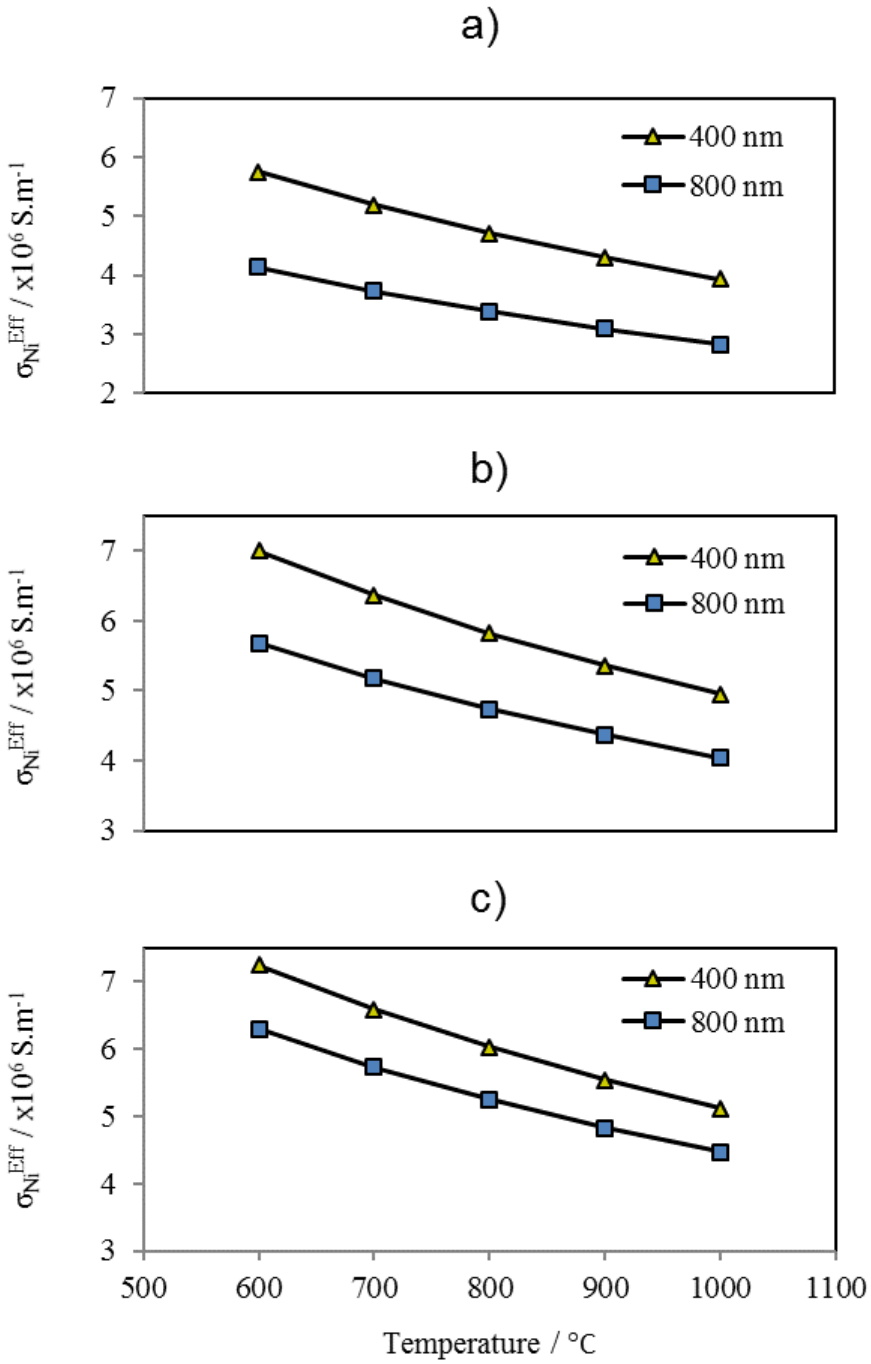

Figure 28 Influence of resolution on the effective electrical conductivity of Ni metal: directional effective conductivity variation with temperature in the a) x,b) y, and c) z directions.

4.3.4. Nano-CT Investigation Procedure

For the nano-CT studies, four Ni-YSZ samples (S422 – S425) were created. In order to conduct these investigations, porous NiO-YSZ cermet (Fuel Cell Materials, OH, USA) powder was pressed into several cylindrical pellets under pneumatic compression. Once formed, the pellets were sintered for 2.5 hours at 1200 °C in air within a box furnace and subsequently reduced to Ni-YSZ for 2 hours at 800 °C in forming gas within a tubular furnace (4% H_2 in 96% N_2). Four samples (S422 – S425) were then prepared by extracting small particles from the material bulk using a sharp scalpel and attached to the top of pins using fast-set epoxy (96).

As these samples (S422 – S425) were for nano-CT analysis, a smaller diameter was required than the micro-CT: ca. 40 µm. The nano-CT was conducted using a lab-based Xradia 810 ULTRA X-ray instrument (Zeiss 810 Ultra, Carl Zeiss inc., CA, USA) with two magnifications; namely, LFOV and HRes, both with a binning of 2 applied during acquisition achieving voxel resolutions of 126 nm and 32 nm, respectively. Both LFOV and HRes imaging modes were applied for the first three samples (S422 – S424) but only LFOV was applied for the fourth sample (S425) to examine percolation variation with resolution. Reconstruction was accomplished using a filtered back-projection algorithm for the datasets using commercial software (‘Reconstructor Scout-and-Scan’, Carl Zeiss Inc., CA, U.S.A.). Unlike the micro-CT analysis, the nano-CT data contained more voxels per feature size allowing resampling of the data to obtain lower resolutions. In order to obtain data with reduced resolution, each greyscale tomogram was artificially binned after reconstruction by combining two

or more pixels into one pixel of larger dimension via resampling in Avizo Fire software (Avizo, Thermo Fisher Scientific, Waltham, Massachusetts, U.S.). Preparation and scanning information can be found in Table 8 and Table 9.

4.3.5. The Influence of Resolution on Predicting YSZ Conductivity

This investigation is regarding the effective ionic conductivity within porous Ni-YSZ and is inspected at four resolutions using the Ultra (parallel-beam X-ray nano-CT). Ion conduction is assumed to only occur within the ceramic phase therefore, only YSZ is characterised. Firstly, unlike the metallic tortuosity-factors discussed previously, the ceramic tortuosity-factor reduces with increasing voxel size $\tau_{YSZ\ 260\ nm} < \tau_{YSZ\ 130\ nm} < \tau_{YSZ\ 64\ nm} < \tau_{YSZ\ 32\ nm}$. Since this material contains three phases, the percolation values are also inspected: the YSZ percolation is independent of directional orientation *i.e.* $p_{YSZ\ x} = p_{YSZ_y} = p_{YSZ_z}$ for resolutions from 32 nm to 260 nm, to 1 d.p. The tortuosity-factor and percolation values are presented in Table 12. Although the tortuosity values are directionally heterogeneous the effects of resolution on the degree of heterogeneity are minor. Furthermore, through a resolution change from 32 nm to 260 nm an increase of 20 %, 12 % and 22 % in conductivity is observed in the x, y and z directions respectively. Hence resolution considerably affects the prediction of oxide conductivity within YSZ although the effect of temperature is more considerable. The effective conductivity is presented for various temperatures and resolutions within Figure 29.

Table 12 Microstructural YSZ properties within porous Ni-YSZ cermet anode obtained via nano-CT resulting in four resolutions, 32, 64, 130 and 260 nm.

Resolution / nm	τ_{YSZ} / no-units				Percolation / %			
	x	y	z	Avg.	x	y	z	Avg.
32	1.93	1.66	2.11	1.90	99.4	99.4	99.4	99.4
64	1.74	1.44	1.74	1.64	99.7	99.7	99.7	99.7
130	1.65	1.50	1.77	1.64	99.7	99.7	99.7	99.7
260	1.54	1.46	1.65	1.55	99.9	99.9	99.9	99.9

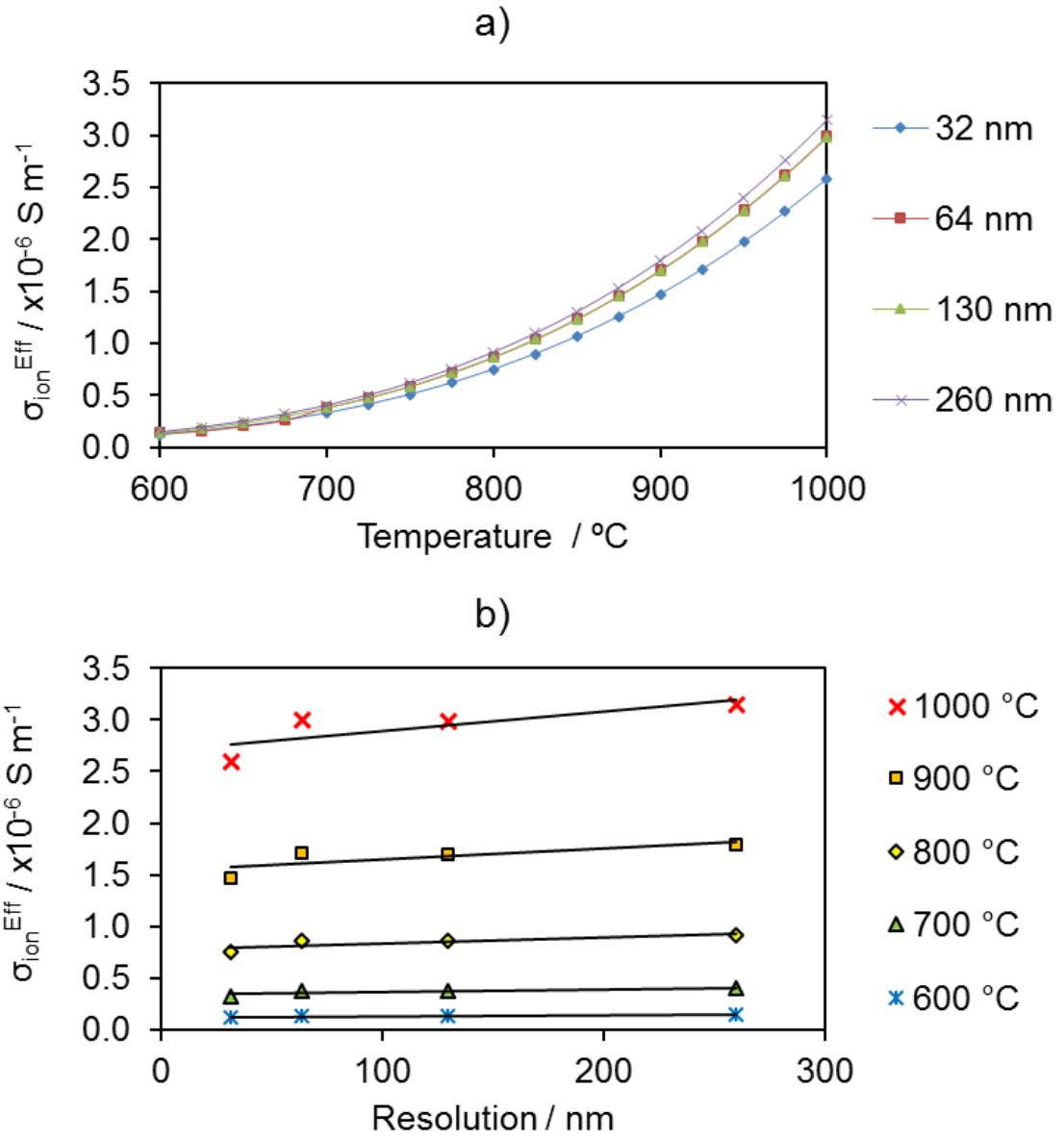

Figure 29 Effective ionic conductivity values for YSZ calculated for the operating temperatures of SOFCs corrected using microstructural data obtained via nano-CT resulting in four resolutions, 32, 64, 130 and 260 nm: a) variation in the effective ionic conductivity within YSZ with temperature for various resolutions, and b) variation in the effective ionic conductivity within YSZ with resolution for various temperatures.

4.3.6. The Fractal Dimension of the TPB within Two Ni-YSZ Structures

The following investigation studies the extraction of the reaction site fractal dimension and roughness factor for two samples (S423 and S424) of varying Ni microstructure. The source of materials, sample preparation and X-ray imaging methods were identical to the previous investigation however several samples were made until sufficiently different microstructures were found. These data sets were also resampled in the same way as the previous study. The analysis of two porous Ni-YSZ samples of varying Ni microstructure provides example microstructures for possible degradation mechanisms of interest. The variation in the two samples (S423 and S424) is quantified by the average particle Feret diameter for each phase and the TPB density, presented in Table 13.

Through application of the Mandelbrot relationship, the fractal dimensions of the two samples (S423 and S424) were extracted with accompanying linear scaling factors, values were obtained from the two samples (S423 and S424) for both LFOV and HRes, and are all presented in Table 14. Minor variation was observed between the $D_{1,LFOV}$ and $D_{1,Hres}$ fractal dimensions for sample S423: 1.79 and 1.88, similarly, the fractal dimension for sample S424 was comparable for both $D_{2,LFOV}$ and $D_{2,Hres}$: 2.31 and 2.14. The linear scaling factors showed an equivalent trend; f_{LFOV} and f_{HRes} values were similar but varied between samples (S423 and S424). These values are similar to that which has previously been reported by Bertei *et al.* (97). These techniques produce consistent fractal properties using the two techniques even for very different microstructures. The fractal properties are therefore dependent upon the microstructure inspected but

are relatively independent of the characterisation technique employed, this is visualised in Figure 3 whereby the gradients of the two linear plots on the log-log axes for HRes and LFOV are very similar. All four sets of fractal properties presented coefficients of determination above 0.97; the fractal properties were highly linear.

Table 13 Average particle Feret diameters for Ni, YSZ and pore within a cermet anode obtained via nano-CT using HRes imaging at an isotropic voxel length of 32 nm.

Sample	Ni	YSZ	Pore	ρ_{TPB}
S423	1.1	1.0	2.6	6.87
S424	1.8	1.0	2.7	3.17

Table 14 Fractal properties for the reaction site densities within porous Ni-YSZ cermet anodes of varying Ni microstructure obtained via nano-CT using two imaging methods: HRes and LFOV.

Sample and Imaging Mode	S423		S424	
	HRes	LFOV	HRes	LFOV
Gradient, m	-1.14	-1.31	-0.88	-0.79
Fractal dimension, D	2.14	2.31	1.88	1.79
Linear scaling factor, f	2.54	2.99	1.81	1.61
Coefficient of determination, R^2	0.99	0.97	0.99	1.00

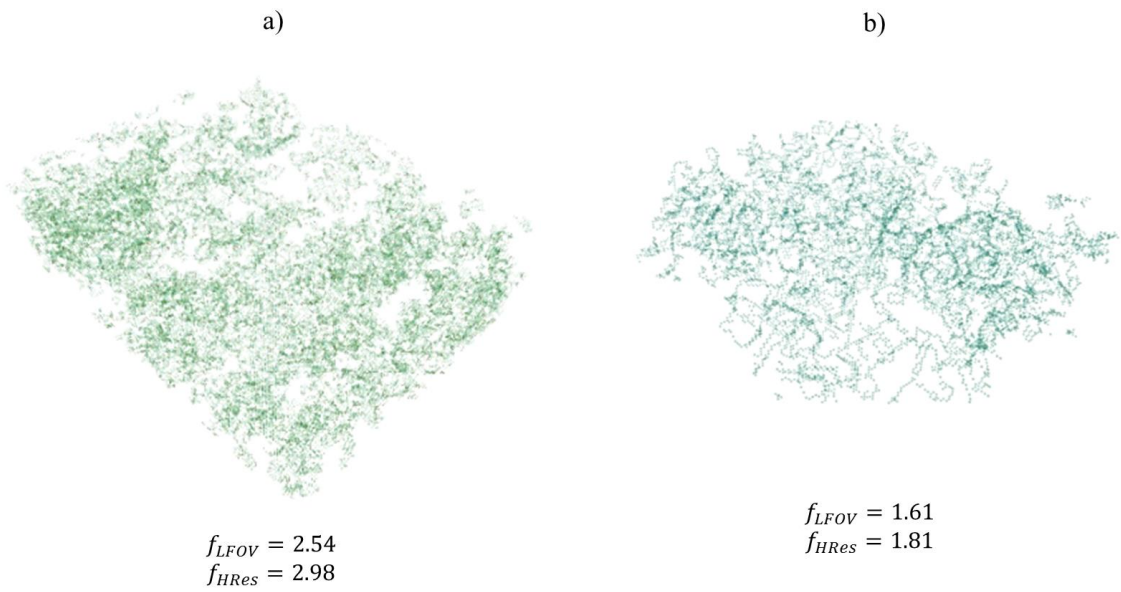

Figure 30 Inspecting the influence of voxel length when characterising the TPB within SOFC anodes by comparing two samples of differing Ni microstructure: 32 nm resolution TPB map for samples a) S423 and b) S424.

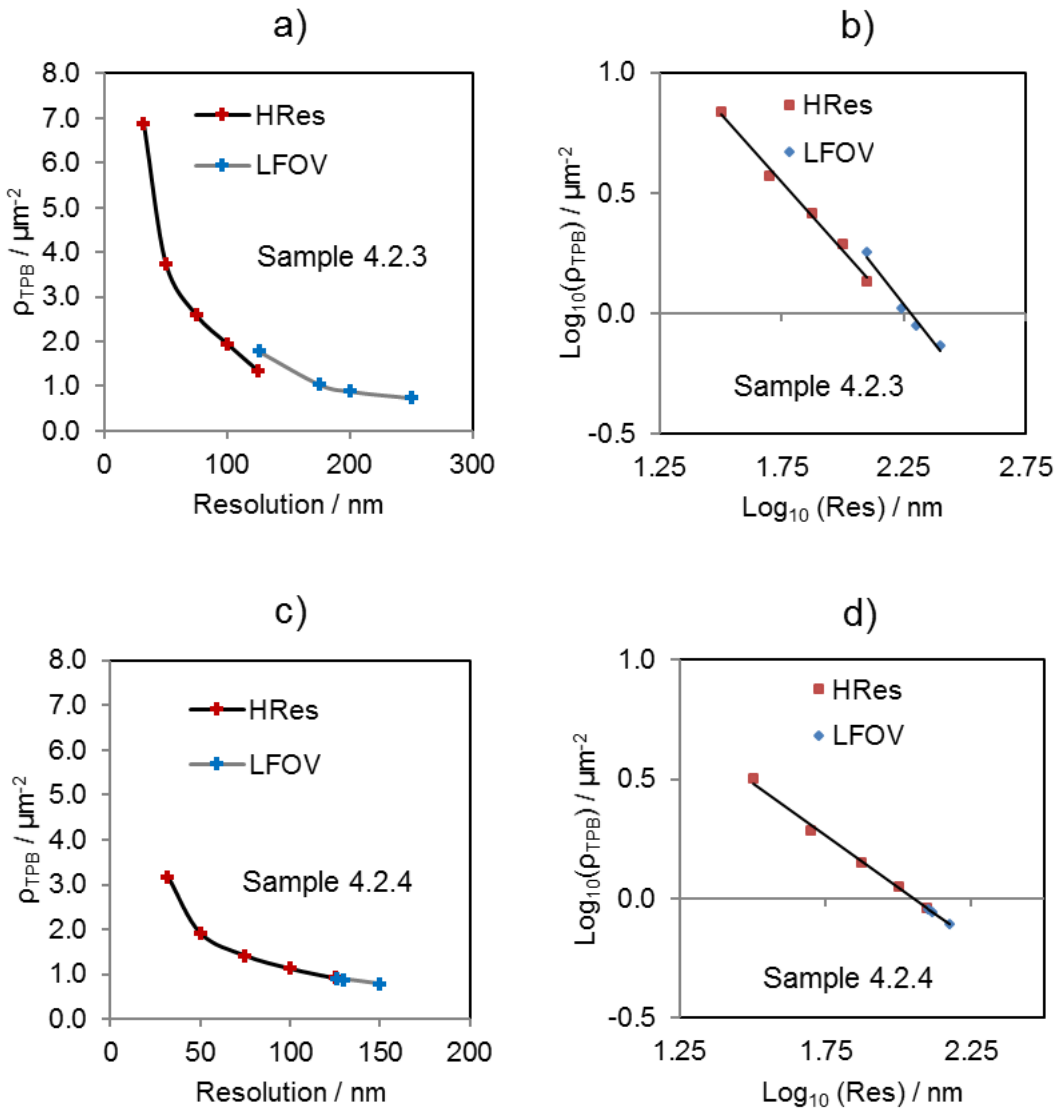

Figure 31 Inspecting the influence of voxel length when characterising the TPB within SOFC anodes by comparing two samples of differing Ni microstructure (S423 and S424): a) TPB density variation with resolution for sample S423, b) plotted on a log-log axes, with c) TPB density variation with resolution for sample S424, e) plotted on a log-log axes, with f) accompanying 32 nm resolution TPB map and roughness factors for the two imaging methods.

4.3.7. The Fractal Dimensions of the Total and Percolated TPB Sites

Finally the effects of resolution on the percentage of percolated reaction sites is inspected for a porous Ni-YSZ electrode using the LFOV technique. Again, the source of materials, sample preparation and X-ray imaging methods were identical to the previous two investigations. These data sets were also resampled in the same way as the previous study.

It is found that the percentage of reaction sites that are percolated remains relatively unchanged regardless of resolution: pTPB = 90 %. The fractal dimension and the linear scaling factor differ between percolated and total reaction sites however, as with the previous two samples (S423 and S424), both relationships display high linearity with coefficient of determination values of 1.00 to 2 d.p. The fractal information is presented in Table 15 along with the TPB density variation with resolution in Figure 32.

Table 15 Fractal properties for the total and percolated reaction site densities within a porous Ni-YSZ cermet anode obtained via LFOV nano-CT.

	Total	**Percolated**
Gradient, m	-1.20	-1.21
Fractal dimension, D	2.20	2.21
Linear scaling Factor, f	2.49	2.47
Coefficient of determination, R^2	1.00	1.00

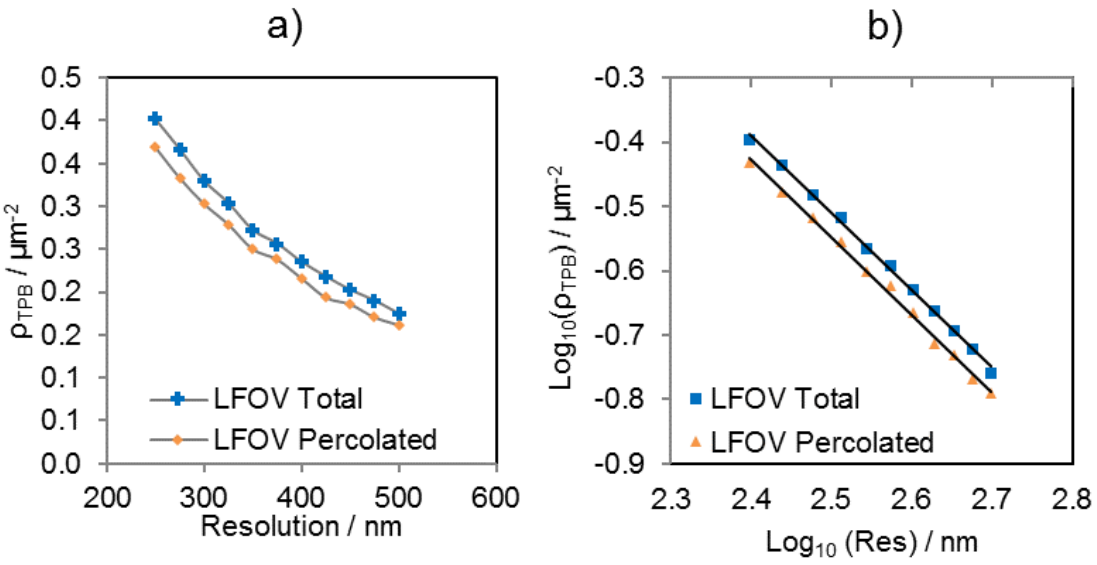

Figure 32 Inspecting the influence of voxel length when characterising the TPB within an SOFC anode sample (S425) by comparing the total and percolated reaction site densities: a) total and percolated TPB density variation with resolution obtained using LFOV, and b) total and percolated TPB density variation with resolution plotted on a log-log axes for the application of the Mandelbrot relationship.

4.3.8. Conclusions from Resolution and Fractal Studies of SOFCs

In conclusion, 3D characterisation can provide powerful insight into the causes for and effects of performance losses in electrochemical devices. X-ray CT has become prominently used as a characterisation technique in the non-destructive extraction of microstructural data. Many instruments exist and many more are being developed, resulting in a spectrum of resolution capabilities. In order to

inspect the effects of such variation in resolution on the properties obtained from electrochemical devices, several important properties have been extracted from a variety of SOFC anode materials as a case study. Predictions of the effective electrical conductivity are found to be significantly affected by resolution but resistances attributed to electron transport remain negligible compared to the transport of oxide ions. Moreover, the influence of resolution on the effective ionic conductivity is also considerable although the influence of temperature remains most prominent. The Mandelbrot relation has been used to inspect the fractal properties of the reaction sites within SOFC anodes characterised using X-ray CT. Fractal dimensions greater than unity are observed for all samples (S423 – S425) using all techniques; as a result it is concluded that reaction site densities characterised at different resolutions cannot be directly compared without the incorporation of fractal properties. The Ni particle size can influence the fractal properties of the TPB reaction site resulting in different fractal dimensions and linear scaling factors for different microstructures. Although varying between samples (S423 – S425), the fractal properties extracted from different techniques produces comparable results *i.e.* high magnification may be used to extrapolate apparent reaction site densities at lower resolutions. The degree of reaction site percolation may not be influenced by resolution but results in distinct fractal dimensions for the total and percolated TPB densities; the fractal properties of the percolated and isolated reaction sites may differ.

The influence of resolution on extracted metrics is not limited to SOFC but may apply across the field of X-ray characterisation. Furthermore, when comparing a variable from two or more datasets of differing resolutions the

variable of interest should be inspected for fractal properties before a direct comparison can be carried out. The extraction of fractal properties may not only improve the validity of instrument-to-instrument comparisons but also the accuracy of electrochemical simulations aiding in high-precision predictive modelling.

As discussed previously, the mechanisms that are responsible for the reduction of SOFC cell and stack performance are often 4D in nature, i.e. 3D microstructural features that develop over time. In order to observe the developments of microstructure with time, the sample cannot be destroyed during characterising (as in FIB-SEM) which historically has required the use of nano-CT at specialist synchrotron facilities. The following chapter section demonstrates methods for achieving 4D tomography of SOFC microstructures using lab-based X-ray instruments. Using a lab-based X-ray instrument, tomograms with sub-micron resolution were obtained between thermal cycling from the same ROI within an SOFC electrode as a demonstrated example. The intricate microstructural evolution captured within the material provide a model example of the capabilities of this technique in tracking challenging degradation mechanism.

4.4. Achieving 4D Tomography of SOFC Microstructures Using Lab-Based X-ray Instruments.

4.4.1. An Introduction to 4D Tomography

During fabrication the SOFC anode is deposited as a metal-oxide, typically nickel oxide, with the addition of zirconia- or ceria-based ceramic electrolyte particles. The metal-oxide is then reduced to its electrically conducting metallic form during the first operational cycle. So long as the anode remains in a reducing environment, free of impurities, the metal should remain metallic however, SOFCs are expected to experience many reduction and oxidation (REDOX) cycles throughout the lifetime of the stack due to fuel interruption, sealant damage and excessive fuel utilisation (31). Each REDOX cycle is accompanied by a microstructural change through the expansion of the metal during transition to metal oxide, along with a reduction in the electrode porosity. This microstructural cycling has been seen to be irreversible resulting in accumulated strain and cracking over the lifetime of the cell, gaining great interest in the microstructural research of SOFC degradation (31; 116).

Due to the intimate link between microstructure and electrochemical performance through microstructural metrics such as the TPB and specific surface area, the system degradation can be correlated to microstructural evolution via 4D studies, three spatial dimensions plus time. In order to better understand the microstructural evolutions which lead to, and result from, mechanisms such as thermal shock within the SOFC much work has been done on the characterisation of microstructures at cell-level. As discussed thoroughly within the literature review, in recent years the two popular methods for

microstructural characterisation have been FIB-SEM (48; 124; 125; 49) and X-ray CT (96; 62). FIB-SEM relies upon the destructive FIB milling of the sample between the collection of SEM images; therefore inherently does not allow the possibility of 4D studies. X-ray CT does not destroy the sample as the 3D microstructures are created through the combination of many radiograph projections, therefore enabling 4D studies. Applications that involve significant microstructural changes over a short period of time often require access to specialise synchrotron facilities due to their inherently higher flux and high-speed imaging capabilities (61). In recent years, due to significant advancements in instrument capabilities, lab-based X-ray nano-CT has emerged as a key technique, having the benefit of being able to obtain non-destructive 3D information with increased availability, allowing the collection of long-term 4D studies at resolutions competitive with specialist synchrotron facilities.

Many features that are attributed to electrochemical degradation are difficult to observe due to the length scale at which they occur; nanometre resolution is often required (59) which in turn often demands a Feret diameter in the order of tens of microns (115). Although this has been overcome by the use of advanced techniques such as FIB lift-out, the availability of such techniques can be limited and sometimes present inadequate durability (116). This has resulted in the use of quick, low-cost alternatives such as fast-set epoxies (96) despite the fact that techniques such as this offer minimal durability in operationally relevant environments, restricting analysis to room-temperature.

Presented here is the demonstration of a 4D tomography technique and subsequent analysis that can be achieved through the creation of mechanically

robust samples which allow repeated tomograms of the same ROI collected between exposures to high temperature environments. 3D information was reconstructed from an SOFC anode that was exposed to high temperatures: infrared (IR) laser heating of a Ni-YSZ anode electrode prepared via high-precision milling (88).

4.4.2. 4D Tomography Investigation Procedure

This study involves the investigation of a pre-fabricated cell; a planar, anode supported anode/electrolyte SOFC (Fuel Cell Materials, OH, USA) consisting of a 500 µm NiO-8YSZ cermet anode with a 10 µm 8YSZ ceramic electrolyte. A laser micro-machining technique (A Series/Compact Class 4 532 nm Laser Micromachining System, Oxford Lasers, Oxford, UK) as described by Bailey *et al.* (88) was used to remove a sample (S431) *ca.* 800 µm in diameter from the pre-fabricated cell and subsequently refined to *ca*. 10 µm in diameter using the laser lathe in preparation for nano X-ray CT imaging. The thermal treatment of the sample (S431) can be visualised in Figure 33. Firstly the sample (S431) was reduced within the tubular furnace described in the methodology (Section 3.3). This was done in a forming gas atmosphere: 4% H_2 in 96% N_2 with a flow-rate of 100 ml min^{-1} controlled using rotameters. This reduction was performed at 600 °C for a dwell duration of one hour and a thermal heating ramp rate of 5 °C min^{-1}; a relatively lower dwell temperature was employed here in order to minimise the sample's thermal history. An operational thermal cycle was then performed in forming gas to 750 °C at a heating rate of 20 °C min^{-1}. Once at temperature the

furnace elements were switched off without dwelling and allowed to cool passively to room temperature.

Laser heating was achieved by aligning the sample (S431), mounted in an X-ray imaging chuck, at the focus point of a High Performance Diode Class 4 980-999 nm laser (LIMO Lissotschenko Mikrooptik GmbH, Dortmund, Germany) as described in the methodology (Section 3.3) and subsequently heating in air by increasing the laser power from 0 – 3 W resulting in a ramp rate of 10 °C min^{-1} with a peak temperature of *ca.* 350 °C. Once 3 W was reached the power was held for a dwell time of 10 minutes before the laser was switched off and the sample (S431) was allowed to cool *via* natural convection, see Figure 33. This temperature profile was chosen for two reasons: firstly to observe the onset of oxidation; oxidation may be observed from temperatures as low as 200 °C (126), but secondly, gasket leakage is a primary cause of anode oxidation (31) and thermal gradients across cells have been observed on the order of hundreds of degrees (41). Therefore at an operating temperature of 750 °C it is conceivable that a temperature as low as 350 °C may be observed at the seal between the gasket and cell wall.

Four X-ray tomograms were collected from sample S431: one pre- and one post-reduction (points 1 and 2 in Figure 33) and one pre- and one post-re-oxidation (points 3 and 4 in Figure 33). All four tomography scans (D431 – D434) were collected using the Zeiss Xradia 810 Ultra in LFOV imaging mode as discussed in the methodology (Section 3.4). The scans (D431 – D434) were collected using 1101 radiograph projections at 60 second exposures each with a binning of 2 applied pre-reconstruction resulting in an isotropic voxel length of

127 nm for a FOV of 64 µm. By leaving sample S431 within the X-ray chuck during the laser-heated re-oxidation scans D433 and D434 could be directly compared by examining the exact same ROI.

Table 16 Experimental procedure for chapter section 4.4: achieving 4D tomography of SOFC microstructures using lab-based X-ray instruments.

Sample	Preparation and Scanning
S431	Pre-Fabricated anode-supported half-cell; 5 µm electrolyte on 500 µm anode; Laser Prepared: 800 µm pillar removed from bulk and refined to 10 µm; First CT in the LFOV of the Ultra; Reduced 800 °C 2 hrs in forming gas (4% H_2 in 96 % N_2); Second CT in the LFOV of the Ultra; Thermally cycled to 750 °C; Third CT in the LFOV of the Ultra; Laser-heated to 350 °C; Fourth CT in the LFOV of the Ultra

Table 17 Imaging conditions for chapter section 4.4: achieving 4D tomography of SOFC microstructures using lab-based X-ray instruments.

Sample	Investigation	Scan	Instrument	Projections	Exposure Time / s	Voxel Size / nm	FOV / µm
S431	I431 Thermal Stability	D431	Ultra LFOV	1101	60	127	64
		D432					
	I432 4D Proof of concept	D433					
		D434					

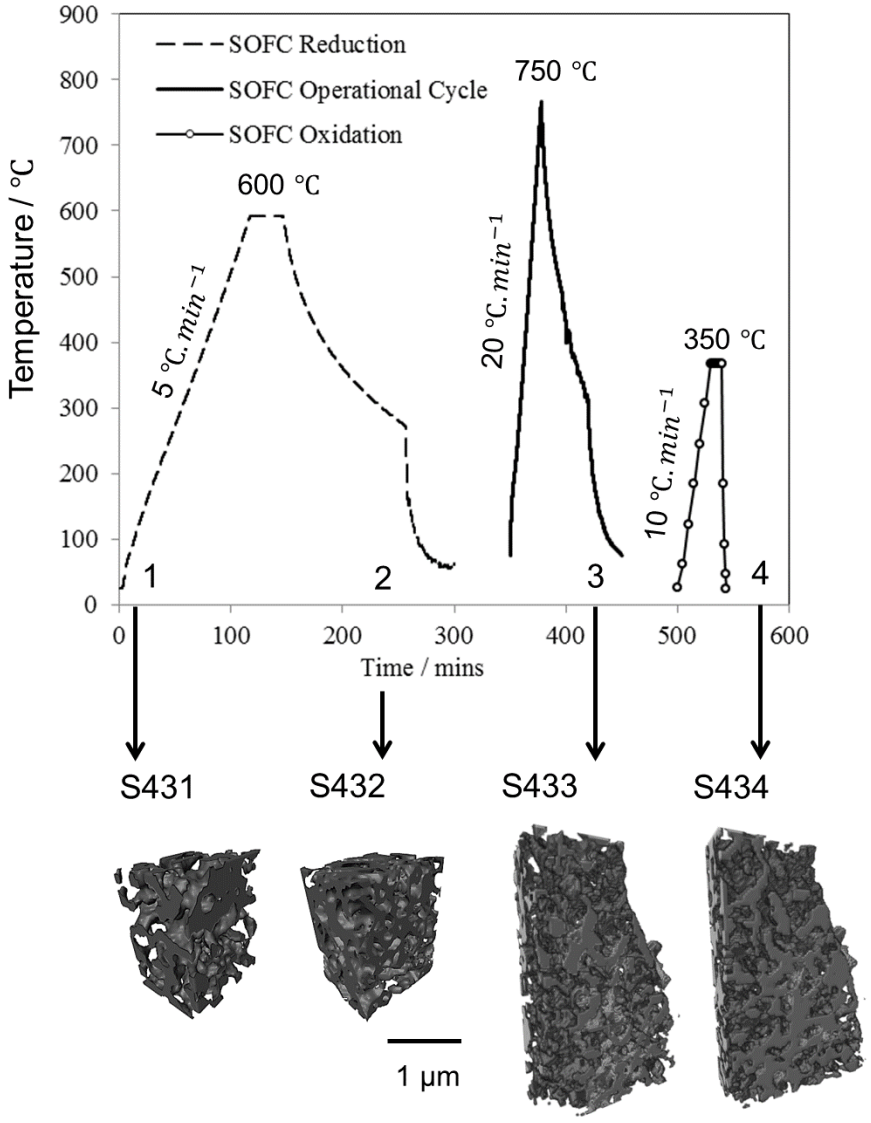

Figure 33 Temperature profiles for the SOFC sample S431 outlining the thermal treatments that each were exposed to before and after X-ray nano-CT imaging: the pristine sample (S431), after the tubular furnace reduction in a forming gas atmosphere (S432), after the operational thermal cycle (S433), and after the laser induced oxidation in an air atmosphere (S434).

4.4.3. Re-Oxidation of Ni-YSZ

The influence of heating a Ni-YSZ anode electrode in an oxidising environment was examined by use of 4D X-ray nano-CT. Firstly, by means of qualitative inspection, although the microstructure and distribution of the pore-phase network pre- and post-heating displayed respectively in Figure 34a and Figure 34b remains similar, a significant reduction in the total pore-phase volume fraction was observed after the thermal cycle. The extent of the porosity reduction was quantified and is presented in Figure 34c and also tabulated in Table 18. As expected, the volume content of the YSZ ceramic showed negligible change after the thermal cycle: -0.51 %. However, Ni metal is known to oxidise from as low as 200 °C (126), and, given the lack of a reducing agent in the local environment, the Ni would be expected to oxidise to NiO.

Table 18 Volumetric compositional data quantified using lab-based X-ray nano-CT from a Ni-YSZ anode electrode which was examined pre- and post-thermal cycling in an oxidative atmosphere to 350 °C using a laser heating gun (31).

	Pre	Post	Difference	
			Observed	Expected
Volume Analysed / μm^3	775.83	775.83	0.00	N/A
V_{Pore} / vol.%	44.56	31.48	-13.08	-16.56
V_{Metal} / vol.%	25.03	38.62	13.59	16.56
$V_{ceramic}$ / vol.%	30.41	29.89	-0.51	0.00
SV_{metal} / vol.%	45.15	56.37	11.22	13.00

Although the extent of the Ni oxidation would depend on many factors including the local oxygen partial pressure, microstructure, temperature, volume of Ni, *etc*., the alteration in the pore-phase volume, metal-phase volume and pore-metal specific interfacial surface area can give an indication into the amount of Ni that has been oxidised to NiO. A volumetric increase of 13.59 vol% was observed in the metal-phase after thermal cycling, resulting in a volumetric reduction of 13.08 vol% in the pore-phase. For an initial metal solid-volume (the volume only occupied by solid materials, *i.e.* Ni and YSZ), SV_{metal}, of 45.15 % the solid volume composition would be expected to increase *ca.* 13 % after complete oxidation. Moreover, an initial porosity of 44.56 % would be expected to reduce to *ca.* 28 % if fully oxidised (31). Hence both the change in metal-phase solid volume composition and the porosity observed here are close to what would be expected from previously presented literature but suggest sample S431 was not entirely oxidised during this cycle.

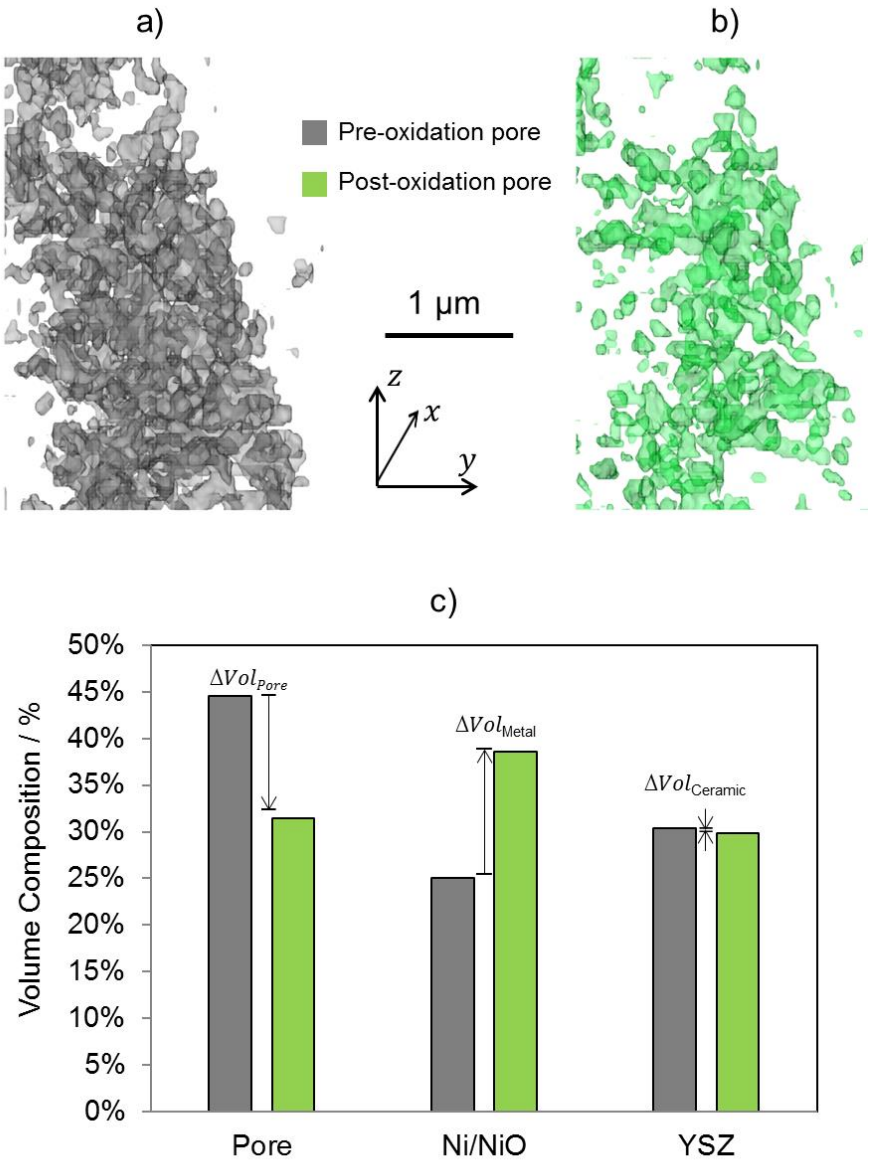

Figure 34 Oxidation of a Ni-YSZ SOFC anode electrode using a laser heating gun: 3D surface renders of the pore network from a) scan D433 pre-oxidation (grey) b) scan D434 post-oxidation (green), with c) accompanying volume composition for the three phases: pore, metal (Ni/NiO) and ceramic (YSZ).

4.4.4. Possible Electrochemical Implications of Oxidation

The alteration in the electrode composition can result in an unfavourable reduction in the TPB density, moreover, if oxidised the electrical conductivity of the metal can be expected to reduce by orders of magnitude (127; 30); resulting in not only a lower volumetric density of electrochemically active reaction sites but also greater Ohmic resistance in the electronic transport and a loss of catalytic activity. It is observed that pore-phase tortuosity-factor increased substantially after the thermal cycle, likely due to the metal-phase oxidising and obstructing, what were previously well connected pore networks. Although more tortuous, the pore network retained *ca.* 61 % percolation in the *x*-plane. A tabulated summary of the microstructural information can be found in Table 19.

Although the mechanisms for metal-oxide film growth are complex (126), an indication of the film thickness can be obtained by assuming the NiO film grows uniformly into the pore-phase from the metal-pore interface. The interfacial surface area of the metal-pore interface prior to thermal cycling is 838 μm^2, which is *ca.* 40 % of the total metal surface. Consequently, for a metal-phase volume increase of 106 μm^3 there would be a *ca.* 125 nm average film thickness as a result of the oxidation assuming isotropic growth; on average, the metal oxide film grew by one pixel on the metal surface after oxidation. While film thickness is below 100 nm, growth can be expected to proceed *via* logarithmic kinetics following a *Mott-Carbrera* mechanism whereby ions migrate through the oxide, driven by an electric field, however films thicker than 100 nm can be described by parabolic growth (31). The kinetics of this temperature profile would predict a film thickness of *ca.* 190 nm, although the parabolic rate constant is proportional

to the local partial pressure of oxygen to the power of a sixth (126). Given the increasingly tortuous pore network during oxidation the local partial pressure is likely to be affected, limiting kinetics, thus restricting film growth. An average film thickness of 125 nm is therefore acceptable for this temperature profile and is comparable to previous work studying NiO film growth within SOFC electrodes (116).

Table 19 A tabulated summary of the 4D nano X-ray nano-CT microstructural data quantified from a Ni-YSZ anode electrode which was examined pre- and post-thermal cycling in an oxidative atmosphere using a laser heating gun.

	Pre	**Post**	**Difference**
Tau Factor			
p_{pore} / vol.%	91.30	61.60	-29.70
τ_{pore} / no-units	5.90	31.60	25.70
TPB			
L_{TPB} / μm	2,995	1,715	-1,280
ρ_{TPB} / μm^{-2}	3.86	2.21	-1.65
Specific Surface Area			
A_{pore} / μm^{-1}	1.68	0.95	-0.73
A_{metal} / μm^{-1}	2.66	2.85	0.19
$A_{ceramic}$ / μm^{-1}	2.18	2.30	0.12
Specific Interfacial Surface Area			
$A_{metal-pore}$ / μm^{-1}	1.08	0.75	-0.33
$A_{metal-ceramic}$ / μm^{-1}	1.58	2.10	0.52
$A_{ceramic-pore}$ / μm^{-1}	0.60	0.20	-0.40

4.4.5. Conclusions from 4D Tomography

To conclude, a lab-based 4D X-ray nano-CT technique for the characterisation of thermally driven microstructural changes within SOFC materials has been demonstrated, microstructural evolutions triggered by thermal abuse were subsequently tracked and quantified. Within electrochemical devices the phase compositions, reaction site densities, tortuosity-factors and specific surface areas are amongst the most significant metrics in correlating structural data to electrochemical performance. The evolution of these metrics results in the degradation, and ultimately the failure of cells. Elevated temperatures are known to trigger such undesirable evolutions although, capturing the variation of these 3D metrics with time is challenging. This technique has been used to inspect the decline in porosity and reaction sites, and the increase in pore-phase tortuosity-factor during the oxidation of an SOFC anode.

Due to the limited availability of X-ray beams and precision sample preparation, materials statistics have until now been limited. However, through the use of sample preparation techniques such as this and readily accessible lab-based instruments, the author envisages the creation of large sample libraries that will improve the statistical confidence of materials characterisation. Moreover, the application of X-ray nano-CT is not limited to electrochemical devices; X-ray nano-CT has been vastly employed in the study of 3D microstructures within many materials. Furthermore, the application of image correlation techniques such as DVC and machine learning has enabled further information to be drawn from 4D tomographic studies. The work here demonstrates the first of many studies which will be carried out in the future of

lab-based 4D investigations spanning all areas of structural research and subsequent correlative analysis. Additionally, the robust nature of this technique may also be employed for other inspection methods such as X-ray and neutron diffraction, particularly where small sample sizes are required to achieve desired transmissions or extreme conditions are of interest. Utilising the non-destructive nature of X-ray nano-CT when conducting 4D studies to observe time-dependent mechanisms such as that which are responsible for degradation within electrochemical devices will lead to an improved fundamental understanding of the causes and effects which limit electrochemical device performance and lifetime.

4.5. Conclusions from Chapter Four

The performance of an SOFC at both cell and stack level hinges upon the density of percolated TPBs within the complex electrode microstructure as this is where the reaction site is thought to be located. However, the density and percolation of these sites is known to decrease with operation time due to multifaceted degradation mechanisms that occur across multiple length-scales. It is therefore of considerable interest to characterise these reaction sites in three- and four-dimensions and across a range of resolutions in order to better mitigate performance losses. This chapter discusses a method for the characterisation of TPBs using lab-based X-ray nano- and micro-CT, the influence of resolution and associated fractal dimensions when characterising across multiple length-scales, and how to achieve 4D tomography using lab-based X-ray instruments.

Firstly, TPB characterisation is demonstrated via two lab-based X-ray methods; nano-CT and micro-CT. Sufficient repeatability is ensured for the nano-CT through the analysis of composition verses the manufacturer's specifications for multiple samples across two length-scales: LFOV and HRes. Furthermore, confidence in the segmentation is confirmed by the comparison of theoretical greyscale values expected due to the attenuation properties of the cermet to the experimental greyscale values obtained from the reconstructed tomograms. Finally, the materials statistics were assessed with respect to the volume of sample analysed confirming stability of the extracted metrics for the features and length-scale of interest. Ensuring sufficient rigour of segmentation and statistics was extended to the use of micro-CT whereby greyscale-fiducials were employed

to provide additional confidence in segmentation, with the statistical representation was also assessed for several metrics.

Secondly, the influence of resolution when characterising SOFCs was assessed via four studies: the effective conductivity of Ni, the effective conductivity of YSZ, a comparison TPB variation within two different microstructures, and the comparison of percolated versus total TPBs. It was concluded that resolution can substantially influence SOFC metrics and the comparison of metrics extracted from an electrode microstructure i.e. the microstructure before and after aging, or, two microstructures obtained from the same manufacturing batch, can only be directly compared once inspected at the same resolution. Furthermore, the lower the resolution, the higher the likelihood that the actual TPB density value is underestimated due to the fractal nature of the microstructures. Therefore, with increasing resolution comes not only increasing precision, but also increasing accuracy.

Finally, a method for 4D characterisation using lab-based instruments is demonstrated via the reduction, thermal cycling and re-oxidation of an electrode microstructure. Firstly, the mechanical robustness is demonstrated by the repeat analysis of the same sample between exposures to severe temperature profiles, and secondly the exact same ROI is inspected allowing a direct comparison of the microstructure before and after re-oxidation of the Ni metal. This direct analysis allowed the comparison of experimental volume compositions from the tomograms to be compared to that which are expected due to the volume changes associated with the oxidation of Ni metal. Finally, metrics such as the

phase-percolation, tortuosity-factor, TPB and specific surface areas could be assessed in 4D.

This chapter introduces the techniques that have been developed in order to carry out the research that is reported in the following chapters. A large emphasis has been placed on the rigour in segmentation, materials statistics and general accuracy in the characterisation in order to ensure sufficient confidence in the results. The following chapters will now discuss the application of these methods through the investigation into specific SOFC degradation mechanisms.

Chapter Five: SOFC Degradation Results

5.1. Introduction to Chapter Five

An inability to withstand rapid thermal cycling remains a major challenge for SOFCs. For instance, delamination of the anode and electrolyte layers due to mismatch in the TEC of the constituent materials is a significant source of degradation. In an effort to combat this, the formation of cermet materials via the addition of the ceramic electrolyte to metal-based electrodes has become widely adopted in SOFC fabrication due to its benefits in maximizing TPB densities, while mitigating bulk expansion mismatch between electrode and electrolyte layers. However, performance losses attributed to thermal cycling continue to inhibit competitive entry to the mass-market due to complex degradation mechanisms that span multiple length scales from the crystal- to micro- to macrostructure. This work explores such degradation for operationally relevant thermal cycling conditions through a combination of X-ray CT and XRD techniques.

This chapter is divided into three length scales which sequentially examine the changes that can be associated with the macro-, micro- and crystal-structure with operational thermal cycling. To begin, macroscopic processes at the tens to hundreds of microns such as cell deformation, interfacial delamination and anode support layer cracking are studied using sub-micron resolution 4D X-ray CT. This is extended by the use of correlative techniques to expose the intricate developments with time. After establishing critical parameters in the operational profiles of SOFC at the macroscopic scale a detailed study of features on the order of single to tens of microns is carried out to examine developments within the cell microstructure to expose how the evolution of key metrics such as the

particle size, tortuosity-factor, percolation and TPB density may implicate electrochemical performance. Finally, this study concludes by exploring the changes in the crystal-structure within the Ni metal examining changes on the Angstrom scale. The influence on the ceramic choice on the thermo-mechanical properties of the cermet anode are assessed with thermal cycling, including the analysis of the non-linear expansion of Ni.

Sections of this work have been peer reviewed and are either published or in-press in the following journal articles: *Heenan, T.M., et al. 2017. ECS Transactions, 78 (1), pp.2317-2321; Heenan, T.M.M., et al., 2018. Journal of The Electrochemical Society, 165 (11), pp.F921-F931; Heenan, T.M.M., et al., 2018. Journal of The Electrochemical Society, 165 (11), pp.F932-F941; Heenan, T.M.M., et al., 2018.Solid State Ionics, 314, pp.156-164; Heenan, T.M.M., et al., 2018. Sustainable Energy and Fuels, in-press*.

5.2. Macroscopic Degradation Assessed Using X-ray CT

5.2.1. An Introduction to Macroscopic Degradation

Ni is a commonly employed anode material with 8 mol% YSZ ceramic as the electrolyte, forming Ni-YSZ as the cermet anode material. Bulk TEC values for Ni, Ni-YSZ and YSZ are approx. 16, 12 and 10 $\times 10^{-6}$ $^{o}C^{-1}$, respectively, through the temperature ranges typical of SOFC operation (128; 46; 129; 40). Evidently employing cermet anode materials does reduce the macroscopic TEC difference, although microscopically the disparity in TEC remains problematic (130; 131; 41; 45). Contact between the anode and electrolyte is imperative to allow the transport of O^{2-} ions from the reduction of oxygen at the cathode reaction sites,

thought the electrolyte to the oxidation with hydrogen forming water at the anode reaction sites i.e. delamination must be prevented in order to maintain electrochemical performance.

Although anode fabrication and characterisation methods are improving (132; 133; 134; 135) the reduction in the anode/electrolyte interfacial contact continues to impede performance (33; 136) and remains insufficiently understood. Furthermore, in order to find entry to the mass-market, portable SOFC applications will require rapid start-up and shut-down times to be comparable with competing technologies. In order to achieve this, high thermal ramp-rates must be employed which accelerate degradation and reduce cell lifetime. It is therefore of great importance to improve understanding of the mechanisms which lead to, and result from, electrolyte delamination as improved understanding will ultimately lead to enhanced mitigation strategies through intelligent cell designs and improved operation procedures.

The macrostructural evolution of two layers with different TECs exposed to thermal cycling is well understood and can be predicted by Timoshenko's model for a bi-material strip (137). The metal/ceramic and cermet/ceramic interactions have also been investigated extensively through a host of materials characterisation techniques (46; 45) postulating the initiation and propagation of cracking as observed by analogous studies (138) although, extended studies on the interfacial performance with operational cycling remain limited (139; 140; 141). This first study aims to expand the knowledge of the macroscopic implications of rapid thermal cycling on anode supported SOFCs.

5.2.2. Macroscopic X-ray CT Investigation Procedure

The cell investigated here was an anode supported, anode/electrolyte SOFC (Fuel Cell Materials, OH, USA) with a NiO - 8YSZ cermet anode and 8YSZ ceramic electrolyte, each ca. 500 and 10 μm in thickness, respectively. In order to collect 3D microstructures of sufficient resolution, a sample was extracted from the half-cell using an A Series/Compact Class 4 532 nm Laser Micromachining System (Oxford Lasers, Oxford, UK). First, a cylindrical sample with diameter ca. 800 μm was removed from the cell bulk and attached to an alumina tube using high-temperature cement, a technique which was developed and reported previously (Chapter 4 and (142; 143)), and finally refined to ca. 350 μm in diameter, this technique is also explored thoroughly elsewhere (88).

X-ray CT was conducted at two length scales through the use of micro- and nano-CT, as seen in Figure 35. Before conducting microstructural analysis, the metal within the anode cermet was reduced to Ni at 800 ºC in a forming gas atmosphere 4% H_2 96% N_2 held for two hours and allowed to cool via natural convection (Cycle 1 in Figure 36 a).

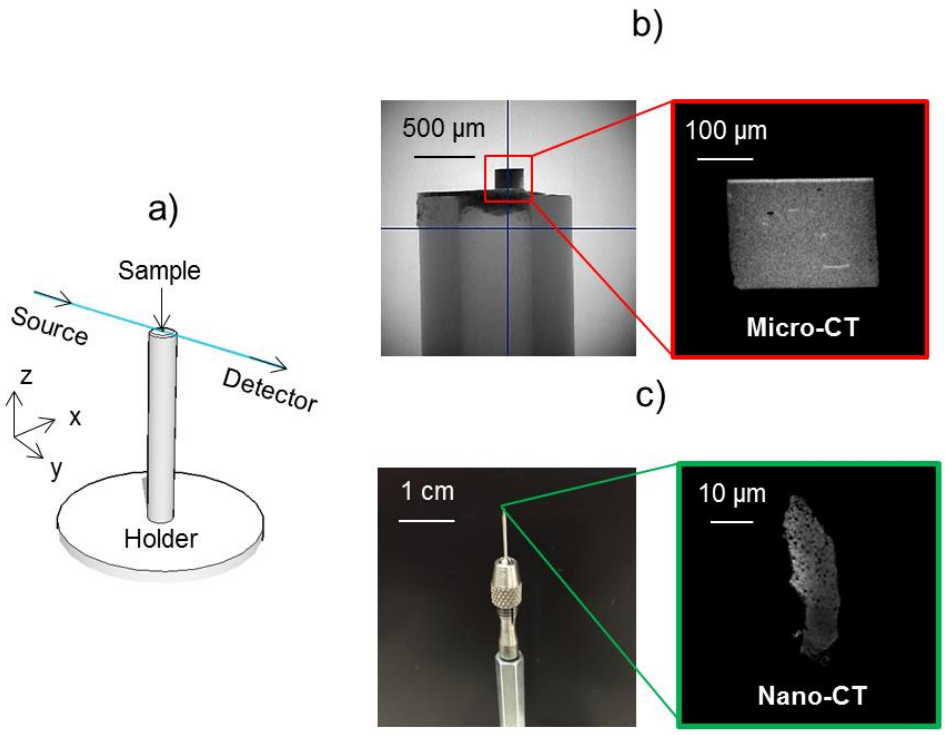

Figure 35 Multiple length-scale X-ray CT. a) Spatial orientation of the X-ray beam-path, b) low magnification radiograph of the sample and support-mount with accompanying reconstructed micro-CT ortho-slice and, c) photograph of the sample mounted for nano-CT with accompanying reconstructed nano-CT ortho-slice.

After reduction the Ni-8YSZ/8YSZ sample was sequentially exposed to thermal cycling (Cycles 2 – 15 in Figure 36 a). 3D microstructural information was obtained before and after each cycle using a lab-based 520 Versa micro-CT X-ray instrument (Zeiss Xradia 520 Versa, Carl Zeiss., CA, USA), with an isotropic pixel length of 395 nm and FOV of 384 µm (sample set-up is displayed in Figure 35 and the grey volume renders of each tomograms indicated by red arrows in

Figure 36c). Images were acquired with a 40× optical magnification and a binning of two. Thermal cycles were all conducted from room temperature to 750 ºC in a forming gas atmosphere although with each thermal cycle the heating ramp-rate was increased: 3, 10, 20 and 30 ºC.min^{-1} respectively. An accelerated stress test was then completed at 30 ºC.min^{-1} accumulating 15 total thermal cycles with tomograms collected every five thermal cycles.

Table 20 Experimental procedure for chapter section 5.2: macroscopic degradation: wall deformation, cell curvature, delamination and crack propagation.

Sample	Preparation
S511	Anode supported NiO-8YSZ/8YSZ half-cell ;Reduced 800 °C 2hrs in forming gas (4% H_2 in 96 % N_2); 800 µm sample removed using a laser lathe; Refined to 350 µm for X-ray micro-CT
S512	A 10 µm diameter sub-sample removed from sample S511 using laser lathe

On completion of the 15th thermal cycle a post-mortem analysis was conducted with use of a lab-based X-ray nano-CT instrument (Zeiss Xradia 810 Ultra, Carl Zeiss., CA, USA), with an isotropic pixel length of ca. 126 nm, (Figure 1b and 1c) with a FOV of ca. 64 µm. In order to collect this high-resolution post-mortem data the sample was reinserted into the micromachining system and a sub-sample, ca. 10 µm in diameter and 30 µm in height, was cut from the bulk for examination. The sample preparation, X-ray CT scanning parameters and thermal treatment conditions can be found in Table 20, Table 21 and Table 22.

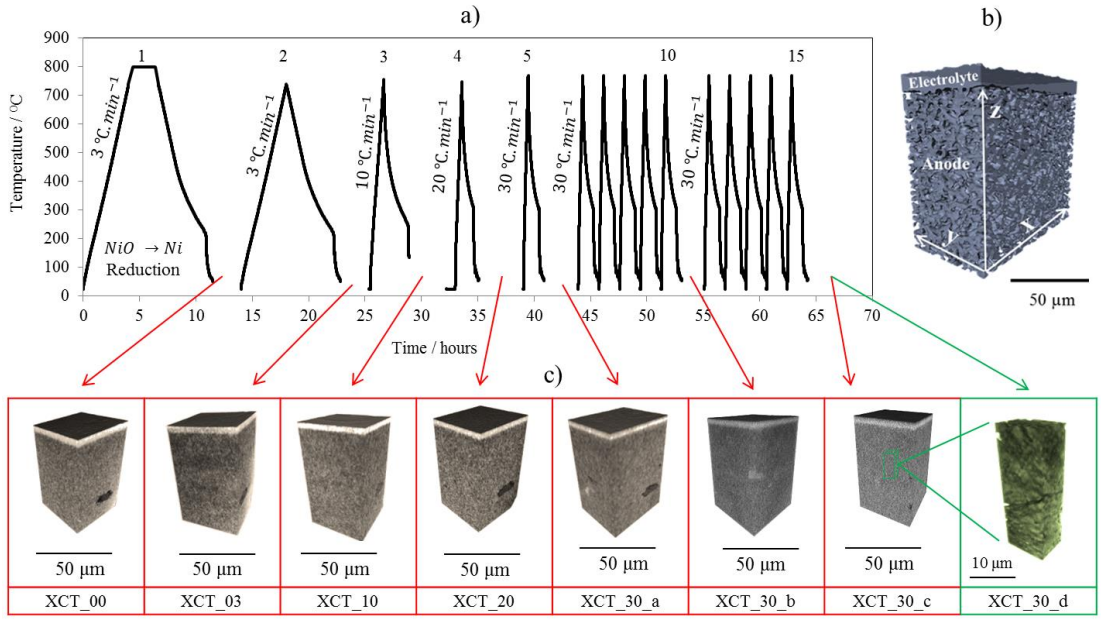

Figure 36 Furnace conditions for the thermal cycling of an anode supported SOFC examined via multiple length-scale X-ray CT. a) temperature profile with reference to when tomograms were collected, b) sample solid-volume surface rendering for reference of spatial orientations, and c) greyscale volume renders of sub-volumes taken from each tomogram. Throughout red and green respectively indicate micro- and nano-CT.

The cell deformation can be visualised by the schematics found in Figure 37. The figure references the orientation of the sample with respect to the x, y and z orthogonal planes and the location of sub-volumes for analysis from the cell-wall to cell-centre across the radius.

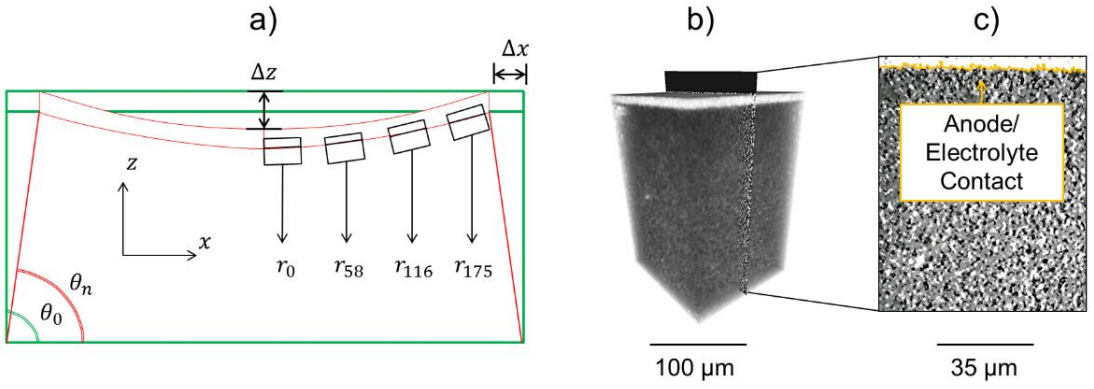

Figure 37 Geometric orientations for the quantification of the cell deformation: a) a schematic outlining the cell-wall angle (θ), horizontal (x) and vertical (z) cell displacement, b) a greyscale volume render of a sub-volume taken from the pristine sample at the centre of the cell, and c) a single slice from the same sub-volume with the anode-electrolyte contact area indicated in orange.

Table 21 Imaging conditions for chapter section 5.2: macroscopic degradation: wall deformation, cell curvature, delamination and crack propagation.

Sample	Investigation	Data	Instrument	Projections	Exposure Time / s	Voxel Size / nm	FOV / µm x µm
S511	I511 Implications of thermal ramp-rate on the cell macrostructure	D511	Versa 40X	2401	30	395	384 x 384
		D512					
		D513					
		D514					
		D515					
	I512 Implications of thermal cycle number on the cell macrostructure						
		D516					
		D517					
	I513 Multi-scale cracking within the anode support						
S512		D518	Ultra LFOV	1101	45	126	64 x 64

Table 22 Thermal cycling conditions for chapter section 5.2: macroscopic degradation: wall deformation, cell curvature, delamination and crack propagation.

Sample	Study	Data	Thermal cycling conditions prior to scan
S511	I511 Implications of thermal ramp-rate on the cell macrostructure	D511	Reduced 800 °C 2hrs in forming gas 3 °C min^{-1}
		D512	Cycled to 750 °C in forming gas 3 °C min^{-1}
		D513	Cycled to 750 °C in forming gas 10 °C min^{-1}
		D514	Cycled to 750 °C in forming gas 20 °C min^{-1}
		D515	Cycled to 750 °C in forming gas 30 °C min^{-1}
	I512 Implications of thermal cycle number on the cell macrostructure		
		D516	Cycled to 750 °C in forming gas 30 °C min^{-1} x5
		D517	Cycled to 750 °C in forming gas 30 °C min^{-1} x5
	I513 Multi-scale cracking within the anode support		
S512		D518	No additional cycling was conducted i.e. identical thermal history as data D517

5.2.3. Cell-Wall Contraction

Significant horizontal wall contraction is observed after thermal cycling (Figure 38 a and b), resulting in a horizontal displacement of 20.8 μm and contraction of the cell-wall by 7.5 º. Substantial vertical displacement is also observed after cycling, 6.6 μm (Figure 38 c and d), producing a curvature comparable to values reported previously (130) (Figure 39). The transition point for both the horizontal and vertical displacements occurs after the fifth thermal cycle in both orientations (Figure 40). The fifth thermal cycle is the first to exceed 20 °C/min. The relationship between structural performance and the thermal ramp-rate employed is well recognised: high thermal ramp-rates induce a higher degree of thermal shock and exacerbates thermal expansion mismatch between the constituent materials. However, the propagation of such shock is not well-known for real microstructures. Here it is observed that at low ramp-rate deformation is plastic but negligible, deforming less than 3 μm in both orientations, similarly, once high ramp rates are achieved deformation proceeds plastically but again no more than 3 μm. These two deformation developments are separated by a substantial deformation triggered by the fifth thermal cycle (Figure 40). This may indicate that a critical yield-point is irreversibly triggered once a sufficiently high thermal ramp-rate is exceeded, which in this case relates to rates above 20 °C min^{-1}.

Although the horizontal displacement is measured at the anode/electrolyte interface, the deformation of the cell support layer is also inspected through the quantification of the angle between the cell-wall and the cell face which would be in contact with the anode flow channels and current collector. The cell contraction angle, the angle by which the cell-wall changes with respect to the initial structure,

follows a similar profile (Figure 40 and Figure 41) to that of the horizontal and vertical displacements. However, the transition occurs more gradually suggesting that strain may not be uniform throughout the anode layers, this has been suggested by anode supported cells in previous literature (41). Quantification of the cell deformation is presented in Table 23.

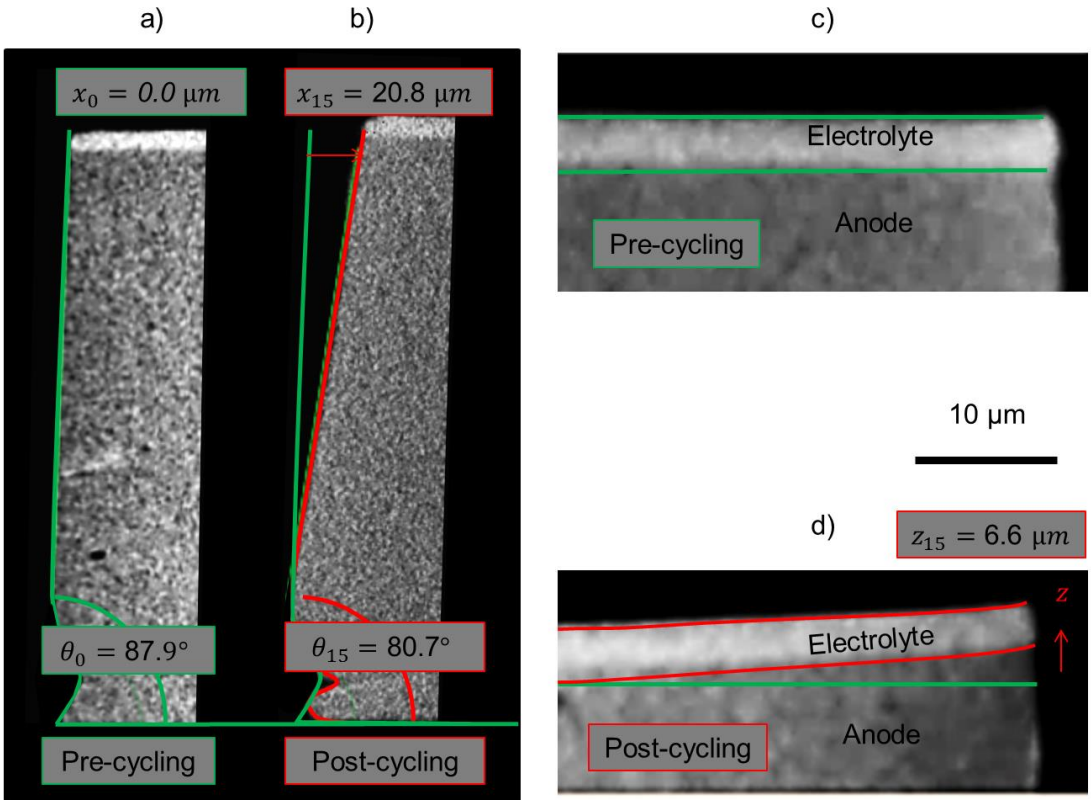

Figure 38 Deformations as a result of operational thermal cycling to 750 °C: X-ray tomogram ortho-slices in the x-z plane for cell displacement in the horizontal a) pre- and b) post-cycling, and vertical c) pre- and d) post-cycling.

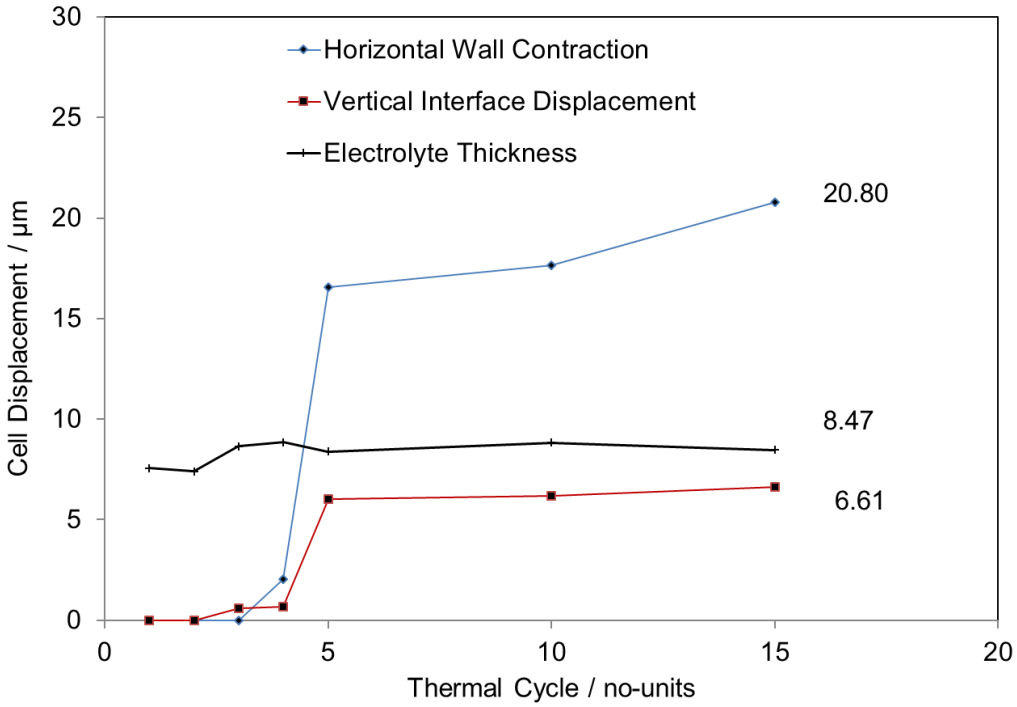

Figure 39 Deformations as a result of operational thermal cycling to 750 °C: horizontal and vertical cell displacement with accompanying electrolyte thickness.

Table 23 Cell deformations as a result of thermal cycling to 750 °C quantified by the cell wall angle, horizontal and vertical displacements.

Thermal Cycles / no-units	1	2	3	4	5	10	15
Thermal Ramp Rate / °C/min	3	3	10	20	30	30	30
Cell wall Angle / degrees	88.4	88.2	88.0	86.1	84.8	84.1	80.9
Cell Contraction / degrees	0.0	0.2	0.4	2.3	3.6	4.3	7.5
Horizontal displacement / µm	0.0	0.0	0.0	2.0	16.6	17.7	20.8
Vertical displacement / µm	0.0	0.0	0.6	0.7	6.0	6.2	6.6
Change in Horizontal displacement / µm	N/A	0.0	0.0	2.0	14.5	1.1	3.2
Change in Vertical displacement / µm	N/A	0.0	0.6	0.1	5.4	0.2	0.4

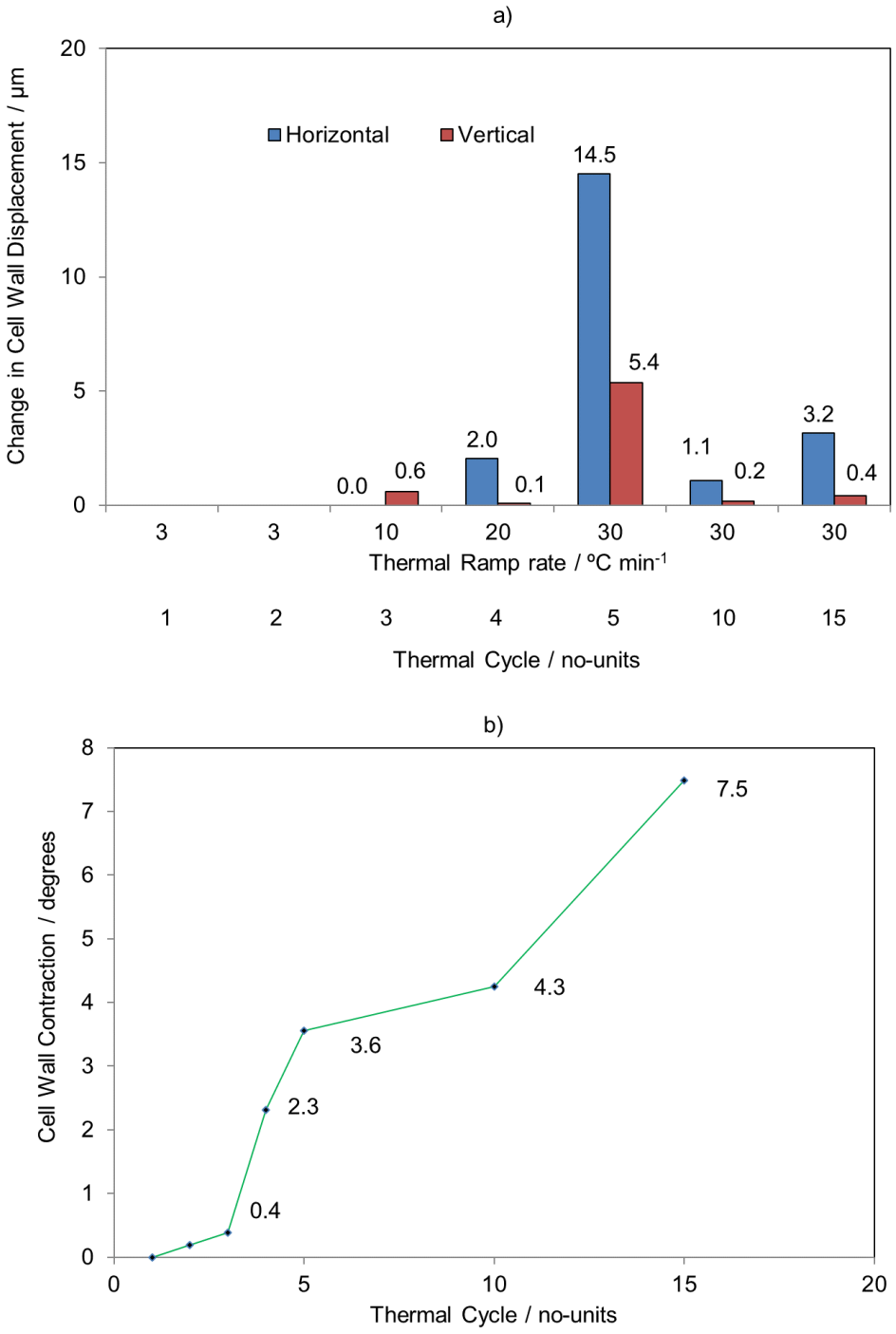

Figure 40 Deformations as a result of operational thermal cycling to 750 °C: a) change in horizontal and vertical cell displacement, and b) cell wall contraction angle with thermal cycling.

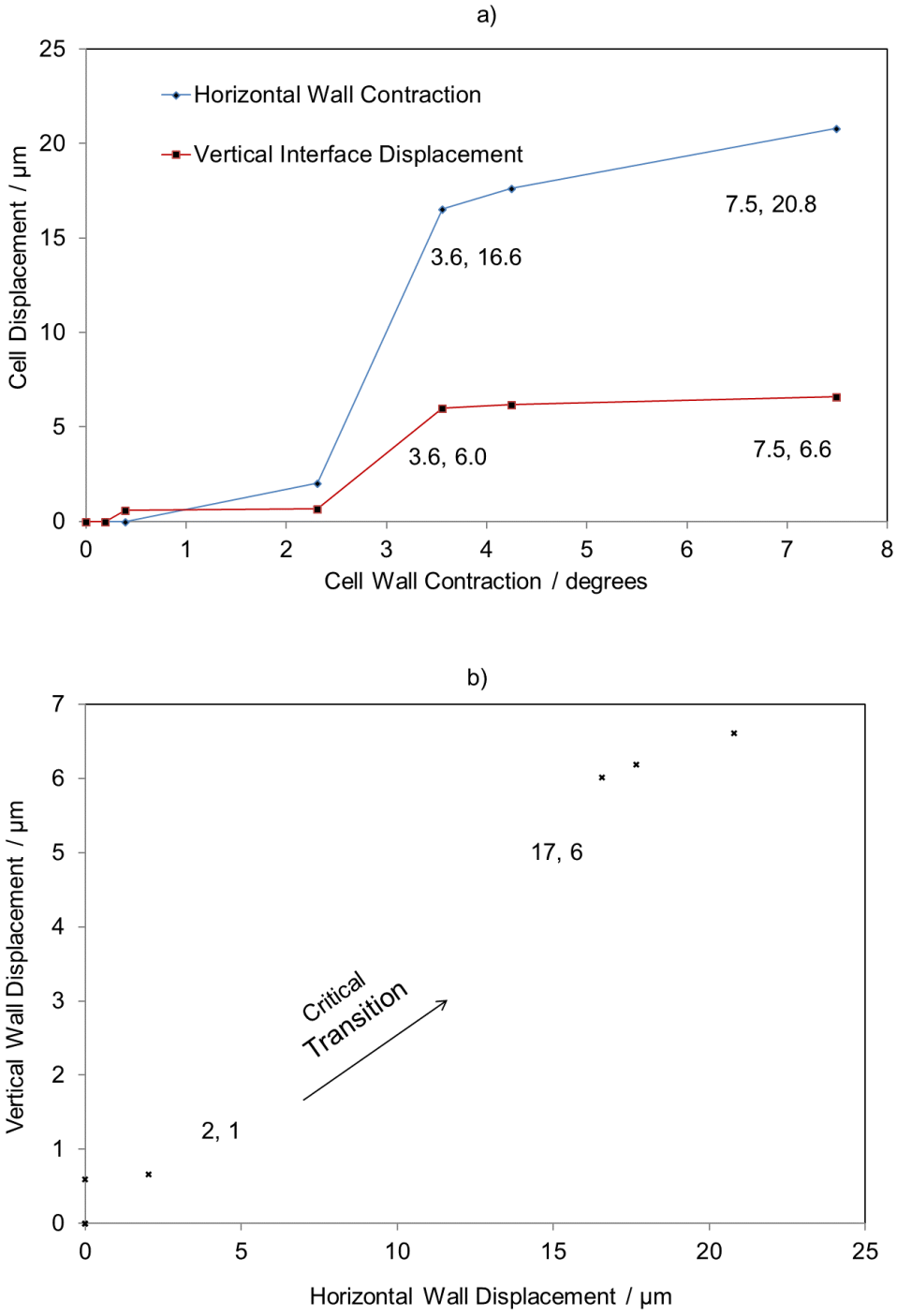

Figure 41 Deformations as a result of operational thermal cycling to 750 °C: a) horizontal and vertical cell displacement with respect to cell wall contraction angle, and b) the vertical versus horizontal cell displacement.

Negligible variation was observed in the electrolyte thickness across the cell radius. The electrolyte thickness was found to be relatively consistent with thermal cycling apart from the third, fourth and fifth cycles where the electrolyte thickness was recorded to increase by ca. 1 μm. These variations are very small with respect to the resolution off the datasets but large with respect to the electrolyte thickness and are presented consistently. This deviation is observed prior to the aforementioned critical yield point and may be a result of tension within the electrolyte caused by the electrolyte concaving upwards while being pulled downwards by the anode. This tension would be expected to accumulate before the severe cell curvature and contraction, at which point the electrolyte stress may relax as the anode and electrolyte delaminate. Delamination will be considered more thoroughly in the coming sections but this finding may be validated in future work using crystallographic information, as such techniques may provide further information on this tensile/compression mechanism but is considered beyond the scope of this macrostructure investigation.

5.2.4. Curvature and Delamination

The cell delamination is assessed by the loss of contact area between the anode and electrolyte layers, this is visualised in Figure 42. Inspecting the anode/electrolyte contact for each tomogram (Figure 44 d) it is clear that the contact decreases by a quasilinear trend until the thermal ramp-rate is no longer increased, at which point the contact reduces at a substantially reduced rate. This resulted in a contact reduction of 80 % after completion of the cycling profile, although 69 % of this was established during the first five cycles (Figure 44 e). Again, when inspected with respect to the cell-wall contraction (Figure 44 f) the decrease is more gradual, suggesting a non-uniform strain distribution within the cell. When compared to the cell wall displacements (Figure 44g) it is evident that the interfacial contact has reduced significantly (ca. 50 – 60 %) before the substantial cell deformation occurs. As mentioned in the previous section this would suggest that strain accumulates within the cell during thermal cycling until the critical yield transition occurs. The average volume-corrected anode/electrolyte contact area and reduction with respect to the initial interfacial contact is reported in Table 24.

Table 24 Average interfacial contact area volume corrected including the reduction in contact area with respect to the initial sample structure.

Thermal Cycles / no-units	**1**	**2**	**3**	**4**	**5**	**10**	**15**
Thermal Ramp Rate / °C min^{-1}	3	3	10	20	30	30	30
Average anode/electrolyte specific contact area / μm^{-1}	0.13	0.10	0.08	0.06	0.04	0.04	0.03
Reduction in contact area / %	0	27	43	54	69	70	80

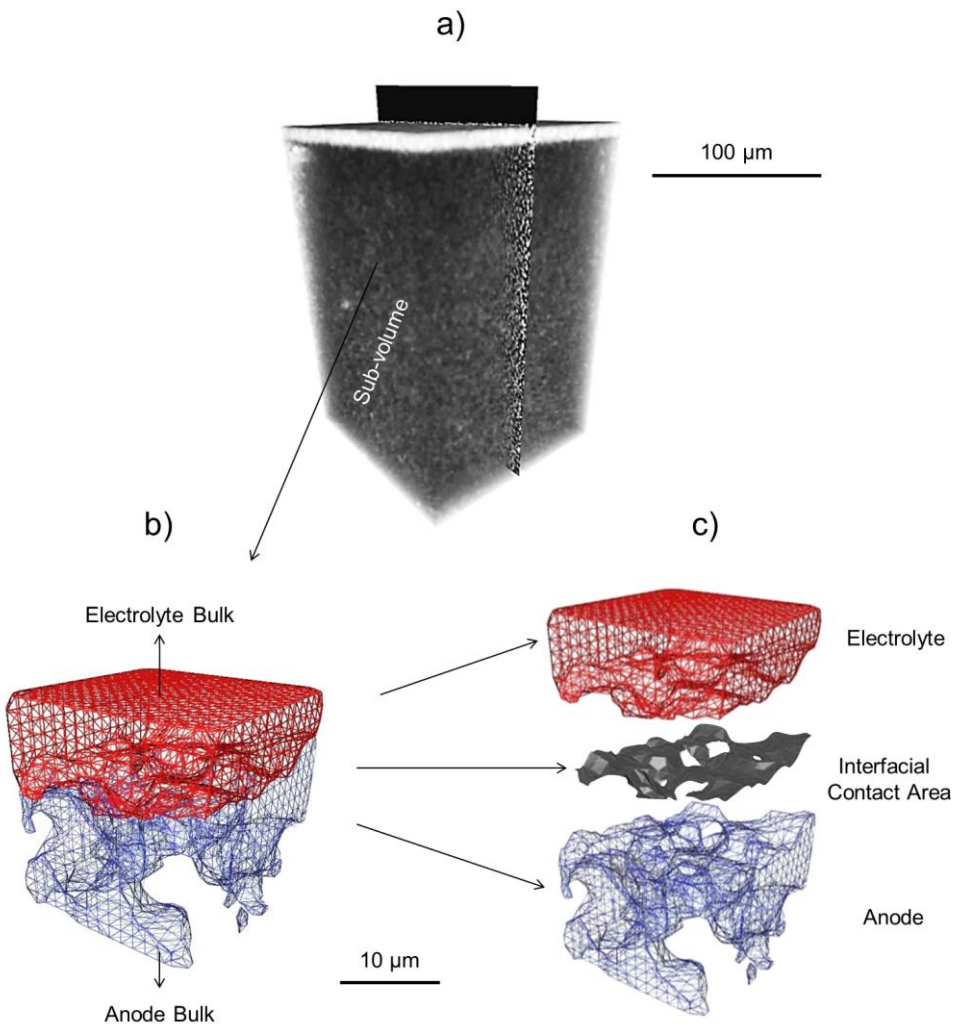

Figure 42 Interfacial contact between the anode and electrolyte assessed with thermal cycling: a) a greyscale volume render of a single 3D sub-volume from the first tomogram, b) a high-resolution surface generation, with c) exploded view of the anode (blue mesh)/electrolyte (red mesh) interface (grey surface).

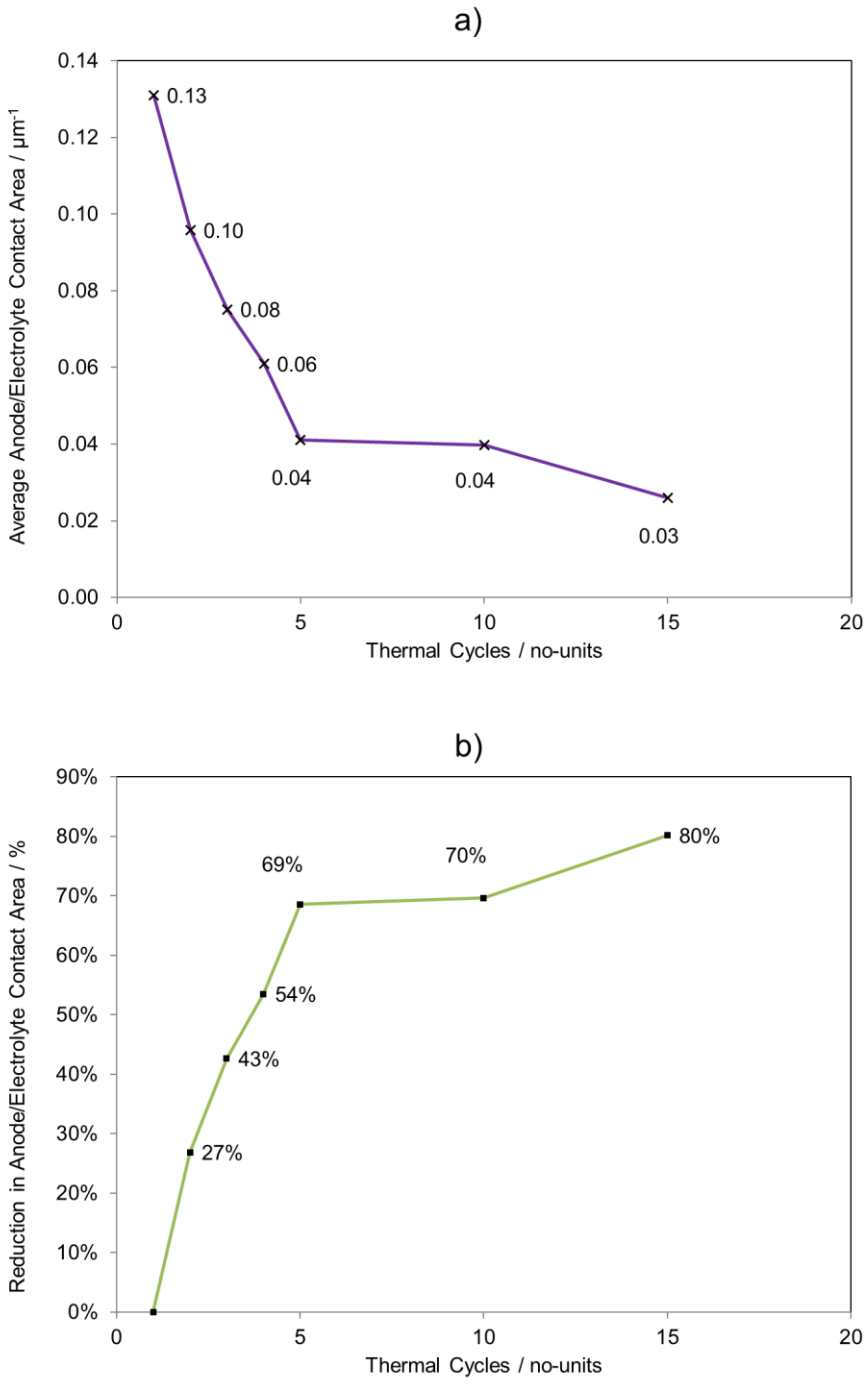

Figure 43 Interfacial contact between the anode and electrolyte assessed with thermal cycling: d) the average and e) reduction in the anode/electrolyte contact area, volume corrected and plotted with respect to the number of thermal cycles.

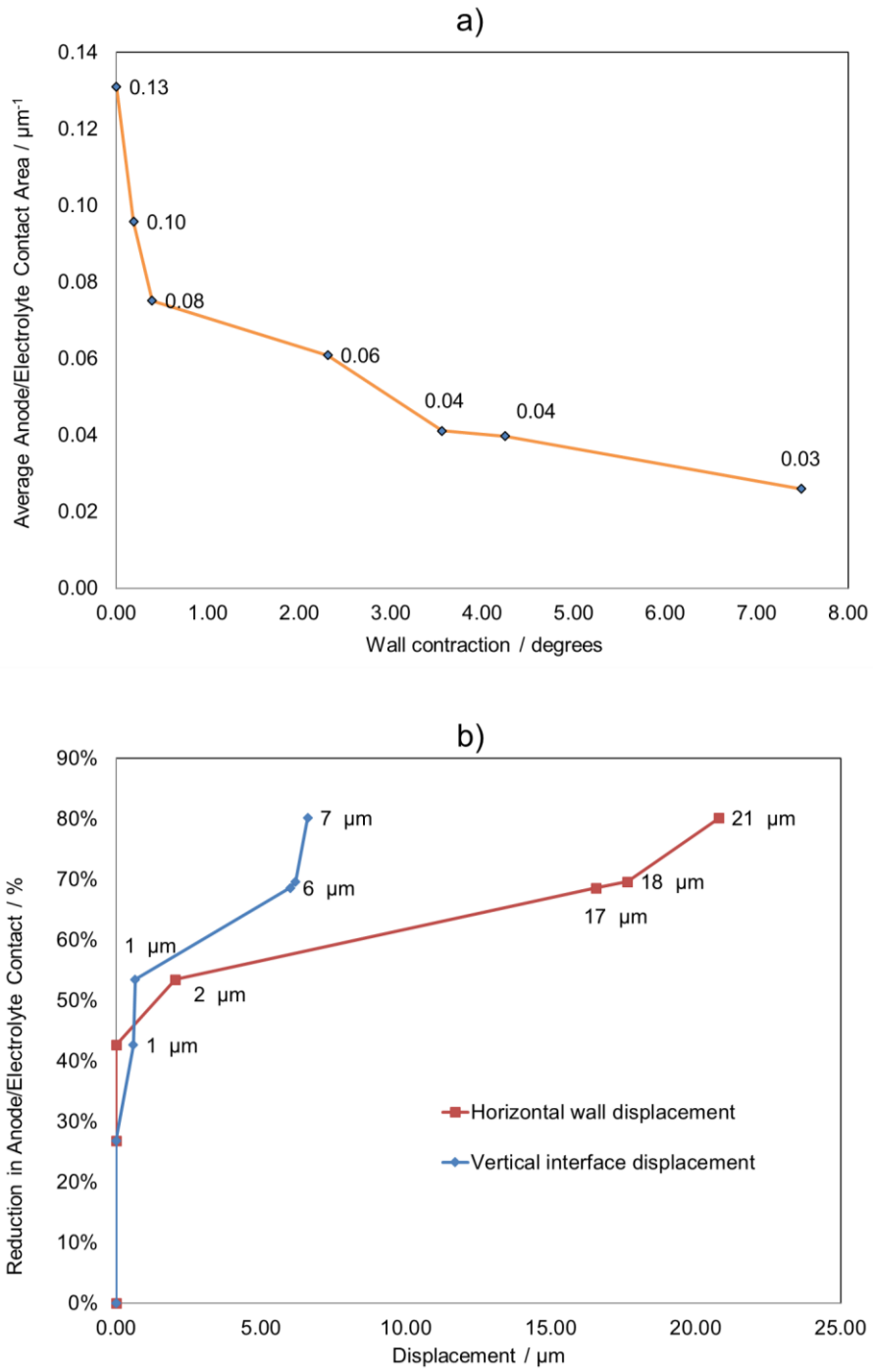

Figure 44 Interfacial contact between the anode and electrolyte assessed with thermal cycling: a) the variation in the anode/electrolyte contact area, volume corrected and plotted with respect to the cell-wall contraction angle, and b) the reduction in the anode/electrolyte contact area plotted with respect to the horizontal and vertical cell displacements.

5.2.5. Non-Uniform Degradation

As discussed, the average anode/electrolyte contact area is observed to reduce with thermal cycling although, the deformation observed in the form of electrolyte curvature and cell-wall contraction suggests non-uniform strain may be accumulating within the anode layers. Figure 45 displays the location of multiple sub-volumes which were extracted from each tomogram at four points along the cell radius from the centre to cell-wall, r_0, r_{58}, r_{116} and r_{175}, denoted as such according to the radial position: 0, 58, 116 and 175 µm.

Table 25 The reduction in the anode/electrolyte contact area with both radial position and thermal cycles calculated with respect to the centre of the initial tomogram.

Thermal Cycles / no-units	1	2	3	4	5	10	15
Radial Position = 0 µm	0%	25%	38%	49%	64%	64%	71%
Radial Position = 58 µm	4%	29%	44%	54%	70%	69%	81%
Radial Position = 116 µm	4%	31%	48%	58%	72%	74%	84%
Radial Position = 175 µm	7%	34%	49%	60%	74%	77%	87%

Inspecting the variation across the cell, there is a reduction in the interfacial contact area across the cell radius with increases with each thermal cycle (Figure 46); initially difference between the cell-centre and cell-wall is below 1 % but after cycling the difference rises to over 2 % (Figure 47). Again vertical displacement only occurs after substantial interfacial contact is lost; it is conceivable that until a certain degree of surface contact is lost the anode restrict the electrolyte from

displacing vertically. All of the data obtained from the local contact area and its variation with thermal cycling is displayed in Table 25.

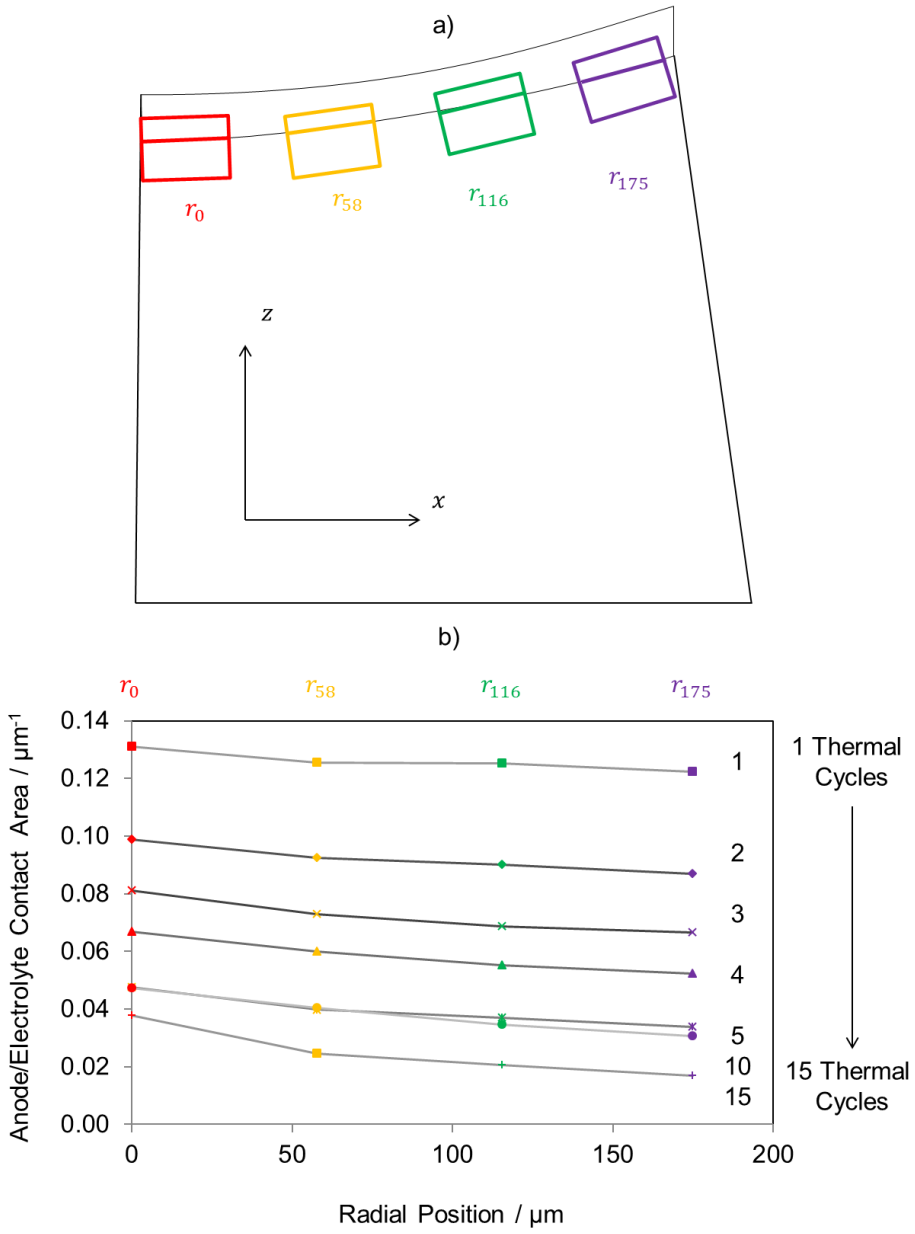

Figure 45 Radial variation in the anode/electrolyte interfacial contact area with thermal cycling: a) colour-coordinated spatial reference for the four sub-volumes removed from each tomogram, b) variation in the volume-corrected anode/electrolyte contact area plotted with respect to the radial position for each thermal cycle: 1, 2, 3, 4, 5, 10 and 15 cycles.

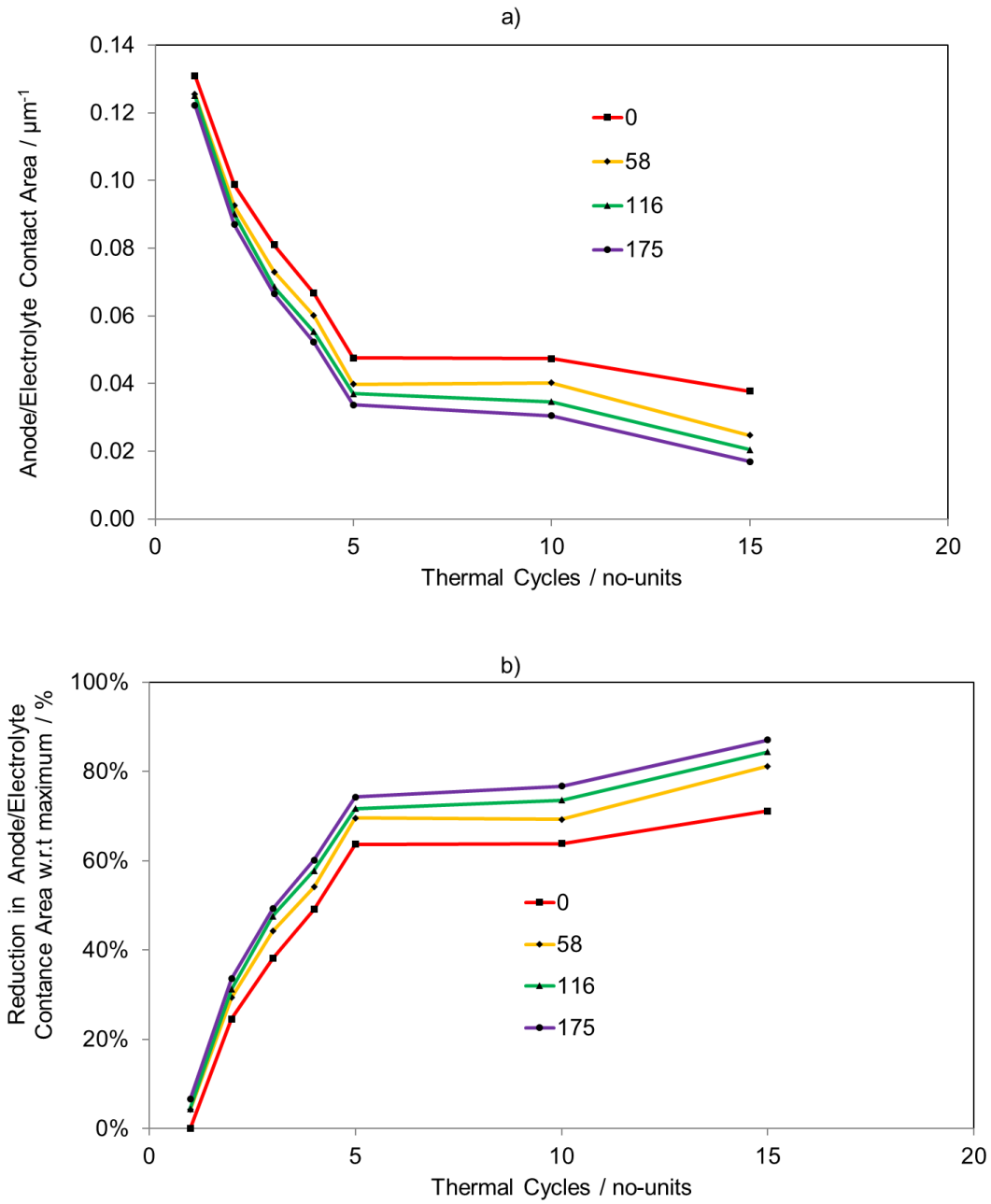

Figure 46 Radial variation in the anode/electrolyte interfacial contact area with thermal cycling: a) variation in the volume-corrected anode/electrolyte contact area plotted with respect to the number of thermal cycles, and b) the reduction in the anode/electrolyte contact area with respect to the maximum.

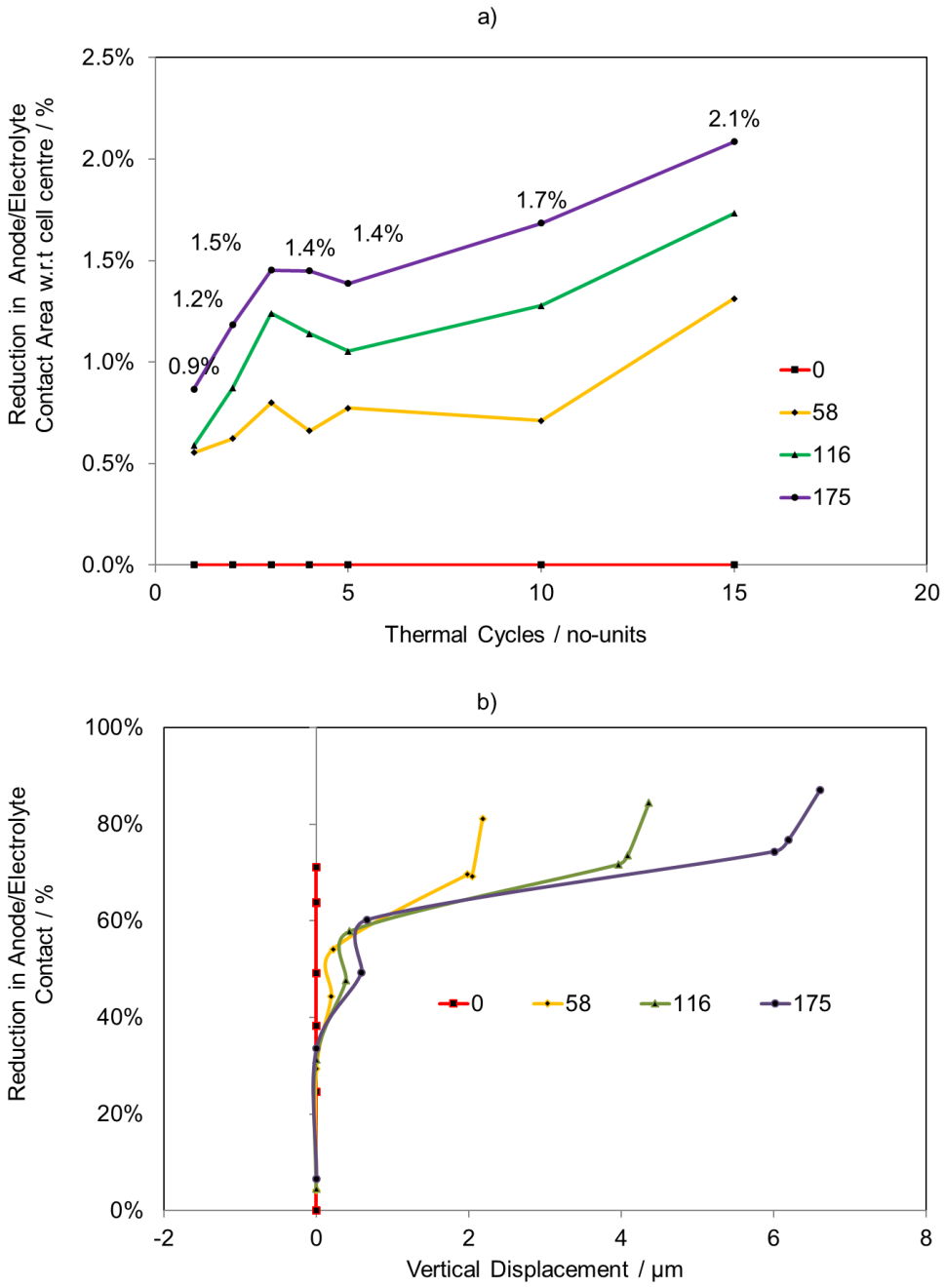

Figure 47 Radial variation in the anode/electrolyte interfacial contact area with thermal cycling: a) the reduction in interfacial contact with respect to the centre of the initial tomogram plotted against the number of thermal cycles, and b) the reduction in the interfacial contact plotted against the vertical displacement.

5.2.6. Anode Crack Propagation

The cell curvature is expected to induce tensile strain near the convex face and compressive strain near to the concaved face. In this set-up the anode would be expected to experience tensile strain, and the electrolyte compressive strain, both of which would be anticipated to increase with the accumulative curvature. Although compressive strain may be difficult to observe without crystallographic information, sufficient tensile strain may induce cracking which, if imaged with sufficient resolution like that which has been done here, may be mapped and quantified using X-ray CT.

Fracture mechanics are known to occur across multiple length scales through a wide range of mechanisms which are specific to the crack stimulus and the materials under investigation (144). The cracking within the anode is therefore mapped and quantified using both micro- and nano-CT allowing a multi-length scale comparison. Due to the trade-off between imaging resolution and FOV, multi-length scale CT is employed so that the cracks imaged by nano-CT increase the detectable size-range and are complemented by the cracks imaged by micro-CT which captures a more complete crack morphology (Figure 48). The crack-diameter histograms for the nano- and micro-CT tomograms follow a similar pattern; crack diameters cluster around 3 – 4 μm (Figure 49). A cluster also occurs at around 1 μm for the nano-CT, likely beyond the resolution limits of the micro-CT, and at 7 μm and 10 μm for the micro-CT, likely beyond the sample volume limits for nano-CT.

To inspect the mechanisms responsible for crack propagation several cracks are inspected individually. A general trend is observed that longer cracks

display a larger average crack diameter (Figure 49), although the local diameter decreases from the crack-opening to crack-tip regardless of crack length (Figure 50). Crack propagation can follow many complex mechanisms and although displaying a general decrease in crack diameter with crack length, the crack diameters also displayed significant undulation between regions of narrow and wide crack diameter, respectively due to bottlenecks and openings along the crack length. Fewer undulations are detected in the nano-CT due to the shorter crack lengths 10 – 15 μm compared to the micro-CT which are around double the length, 20 – 30 μm. Regardless of crack length, the gradient of the linear fitting remains on the same order of magnitude for all cracks, between -0.02 and -0.04 μm diameter per μm length. The crack properties for the six cracks inspected in detail are tabulated in Table 26.

Table 26 Crack properties for six cracks from the SOFC anode after thermal cycling collected from micro- and nano-CT macro- and microstructural post-mortem analyses.

	Micro 1	**Micro 2**	**Micro 3**	**Nano 1**	**Nano 2**	**Nano 3**
Crack Length / μm	30.0	25.0	22.0	17.0	11.0	11.0
Maximum Diameter / μm	6.6	5.0	3.7	0.6	0.6	0.5
Average Diameter / μm	2.8	2.3	2.1	0.3	0.5	0.3
Minimum Diameter / μm	1.1	0.8	1.1	0.1	0.1	0.1
Standard Diameter Deviation / no-units	1.2	1.1	0.6	0.1	0.1	0.1

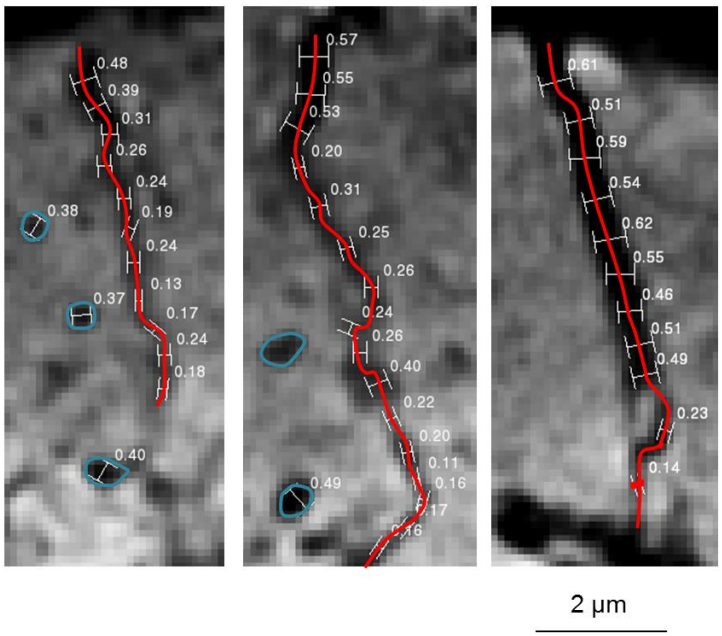

Figure 48 Mapping anode cracking across multiple length scales using micro- and nano-CT: three greyscale tomogram slices from the nano-CT, mapping cracks and their local diameters.

Although insight has been gained into the propagation of cracking within the anode all cracks which were detected were found within the anode bulk, away from the anode/electrolyte interface, therefore the implications of curvature-induced anode cracking may be minor until cracking propagates towards the functional layer. This lack of cracking near the interface is thought to be attributed to the strain distribution within the cell; the tensile strain within the anode will be maximised away from the convex of the interface. It was more difficult to apply confident spatial orientation to the nano-CT due to the sub-volume size; the nano-CT no longer had the electrolyte as a spatial reference therefore the orientation relative to working cell operation was difficult to obtain. However, all of the cracks detected within the micro-CT were dominated by propagation parallel to the

interface; i.e. cracks within the anode support layer typically propagated to the cell-wall rather than the interface, therefore even after propagation crack may not influence activity within the functional region of the anode. However, large cracking may influence the effective local gas diffusivities and the ability for current removal.

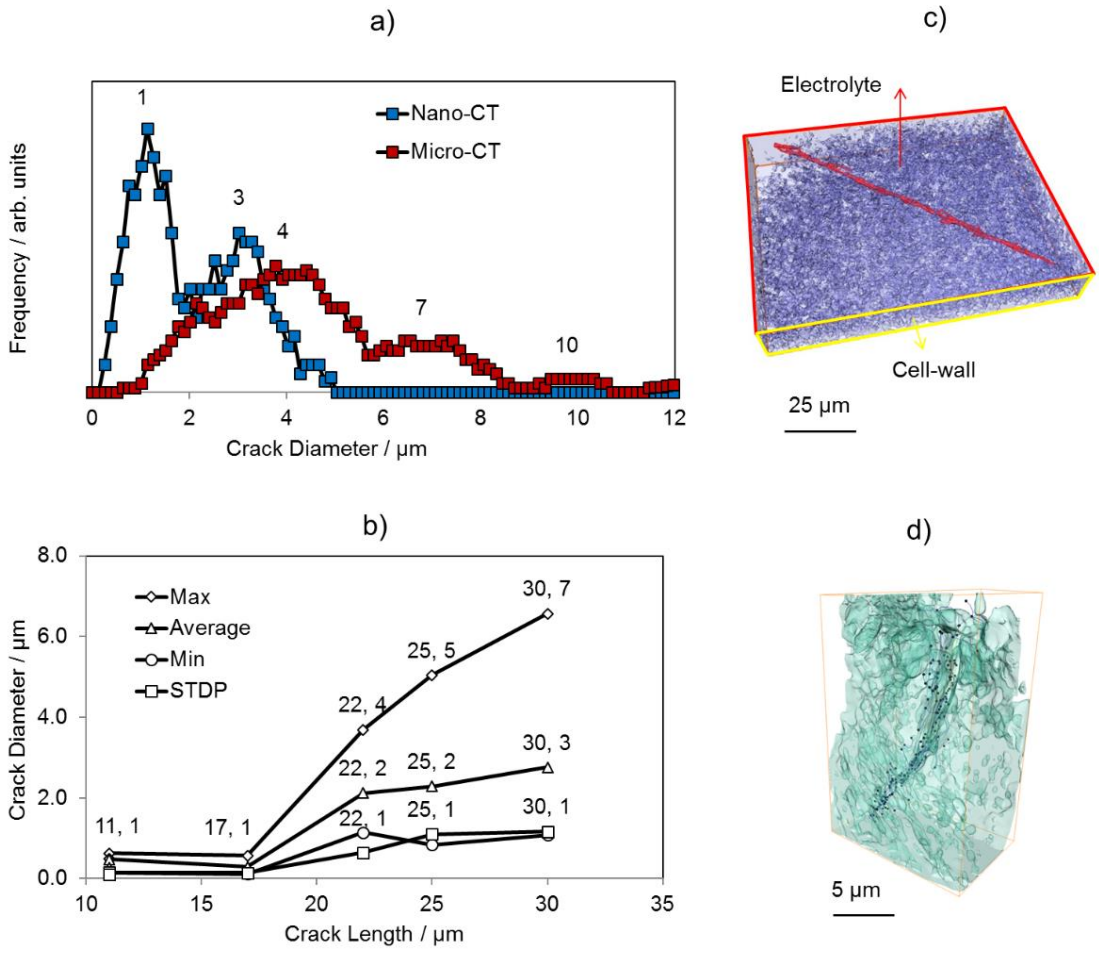

Figure 49 Mapping anode cracking across multiple length scales using micro- and nano-CT: a) crack diameter histogram for all detectable cracks, b) crack diameter plotted with respect to the observable crack length for seven individual cracks, c) micro-CT and d) nano-CT 3D surface generations from solid and crack phase segmentations.

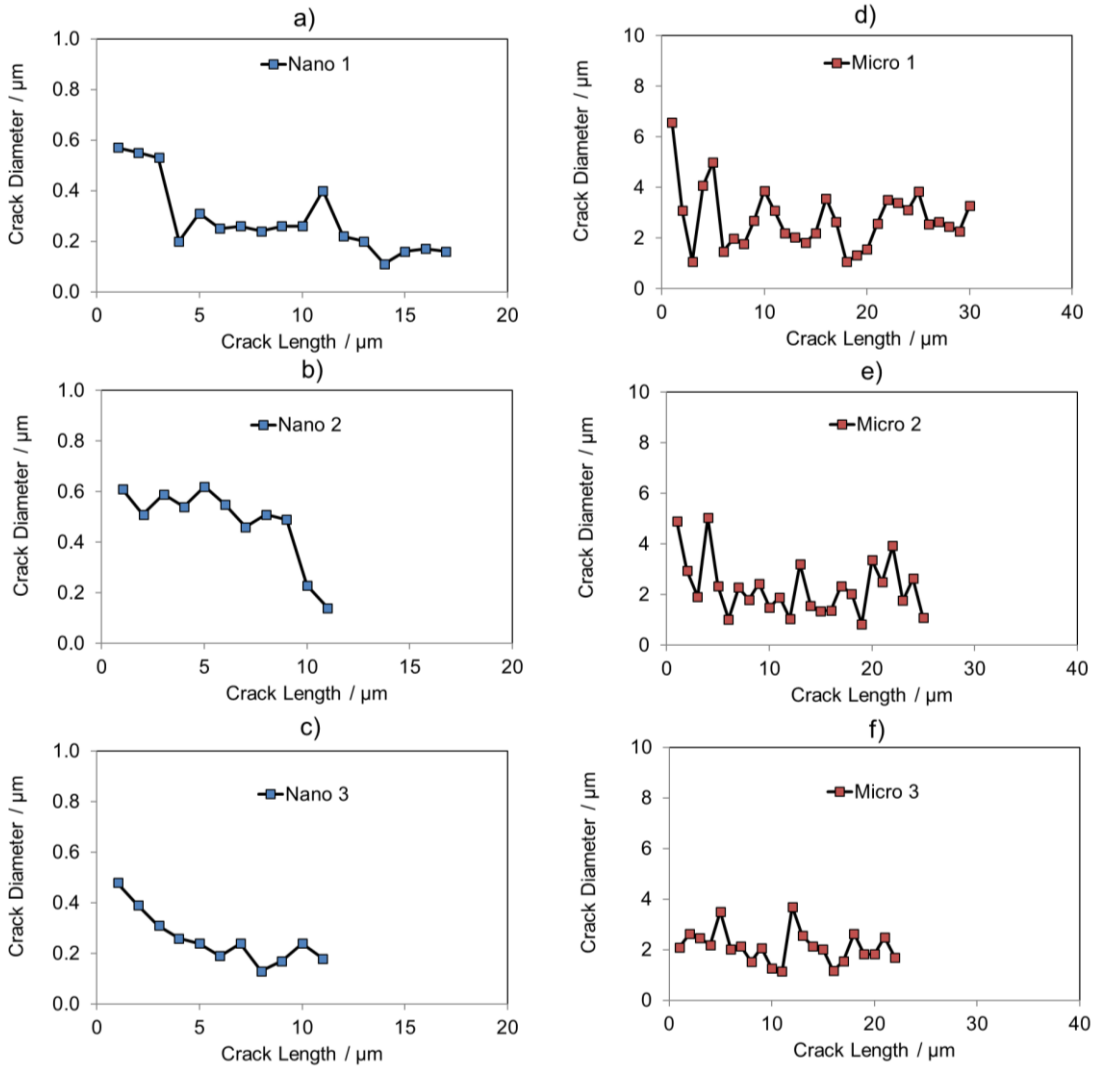

Figure 50 Mapping anode cracking across multiple length scales using micro- and nano-CT: Local diameter plotted with respect to crack length from the crack-opening to crack-tip for a – c) three nano-CT and d – f) three micro-CT cracks. Micro- and nano-CT are represented throughout by red and blue respectively.

5.2.7. Conclusions from Macrostructure Investigations

This work investigates the effects of thermal cycling on the anode/electrolyte contact area and its possible implications on electrochemical performance. With use of lab-based X-ray CT instruments, high-resolution macrostructural analyses of the same sample between exposures to operationally relevant thermal treatments has provided insight into the implications of rapid start-up times for planar anode-supported SOFCs.

It has been found that macroscopic deformation proceeds gradually with thermal ramping until a critical point is passed induced in this case through the use of rapid thermal ramp-rates, after which permanent deformation is observed in the form of a substantial curvature of the electrolyte at the interface and contraction of the cell-wall. Furthermore, cell-wall contraction angles suggest that the distribution within the anode layers may not be uniform possibly providing further mechanisms for performance loss. Microscopic interfacial contact between the anode and electrolyte decreases substantially after each thermal cycle but most considerably after the macroscopic deformation. Moreover, the anode contact varies across the radius of the cell whereby the contact is minimal at the cell wall and the deviation between the cell-centre and cell-wall increases with each thermal cycle, exacerbating the stress gradient. The tensile strain which the anode experiences during interfacial curvature may be responsible for anode cracking. Such cracks are expected to increase in diameter with increasing propagation length, possibly implicating phase percolation and macrostructural integrity although cracks have only been observed within the anode bulk and

parallel to the interface and therefore may not propagate towards the functional layer thus electrochemical implications may be minor.

5.3. Macro- and Microstructural Evolution Assessed using DVC

5.3.1. An Introduction to the Use of DVC for SOFC Studies

The use of 4D characterisation techniques are essential in performing accurate, longitudinal studies of phenomena that develop with time: for instance, observing different samples from an electrode's microstructure before and after degradation does not permit a direct comparison, which is essential in order to truly understand how these complex mechanisms progress. This is uniquely possible using techniques such as those described here.

A major advantage of 4D imaging lies in the correlative computations which can be applied to the macro- and microstructural data sets. Digital volume correlation (DVC) (105; 106; 67) compares two data sets from the exact same ROI before and after deformation. Correlation techniques (68) determine the displacement of features within the ROI after deformation producing 3D displacement and strain fields. Electrochemical devices have previously been explored with this technique (145; 107; 146) however, application has thus far been dominated by battery materials at coarser resolution. This section (5.3) of this work examines the evolution associated with the various thermal ramp-rates explored previously using DVC. Digital volume correlation (DVC) was computed and mapped using 'TomoWarp2', a Python-based open source software developed by Tudisco et al. (105). TomoWarp2 utilises correlation techniques such as those employed by Gates et al. (106), whereby the movement of features within a material are tracked and quantified. To track movements, two tomograms are required from the exact same ROI containing the 'initial' and 'deformed' structure. By locating the same feature within the initial and deformed structures

the displacement of said feature can be quantified. To do this, a local sub-volume is drawn which encloses the feature within the initial structure, a similar sub-volume is then drawn within the deformed structure and rastered throughout the volume until the feature is found.

To find the feature within the deformed volume, the brightness distribution functions of the initial and deformed volumes are compared and their difference is minimised. The degree of confidence in the location of the feature within the deformed volume is quantified in the form of a correlation coefficient (CC), whereby an optimum match in the brightness distribution functions would result in a CC value of 1. The various methods of calculating the CC values have been discussed and compared by Tong (68) although, confidence is typically only placed in displacement data which has obtained CC values above 0.97 (107).

5.3.2. DVC investigation procedure

DVC can be computationally intensive; therefore a sub-volume of the full diameter of the sample but half of the depth into the electrode, 350 µm × 350 µm × 100 µm, was removed from the same ROI within each tomogram for analysis. This significantly reduced the computation time (compared with the full tomographic volume) while maintaining a statistically representative volume that included information from both the anode/electrolyte interface and anode bulk. To conduct the DVC computations, first a regular grid of 3D nodes has to be defined according to the 'node spacing' over each tomogram. A 'correlation window' is then centred over each node for the correlation analysis and a 'search window' is defined to constrict the search for the displaced material within a local volume. The DVC computations within this work were performed with a node spacing of five, with search and correlation windows of fifteen and three, respectively. Previous analysis of these tomograms found the average Ni, YSZ and pore particle diameters to be 1.1 µm, 2.6 µm and 2.5 µm respectively (147). The DVC parameters were therefore chosen to sufficiently reflect these feature sizes. DVC computations were performed on the first five tomograms from scans D511 – D515 whereby the DVC analysis compared each tomogram to the tomogram collected immediately before it, i.e. D512 was compared with D511 etc. resulting in four data sets, a tabulated in Table 27 and visualised in Figure 51.

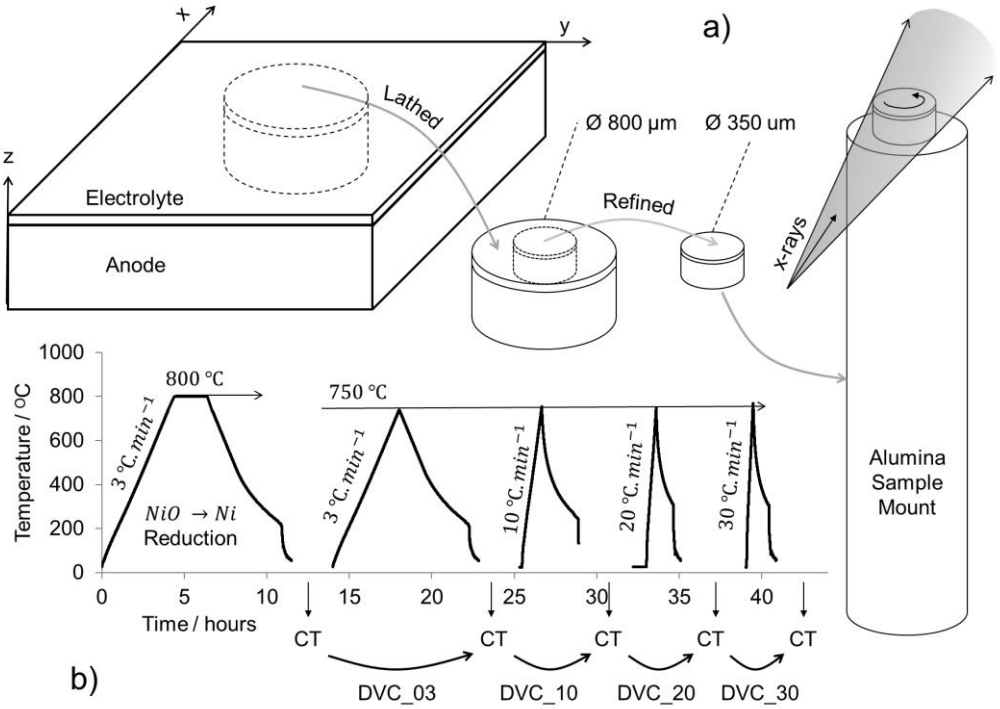

Figure 51 Experimental set-up for the correlation of lab-based X-ray tomograms using digital volume correlation: a) sample refinement and geometric set-up for X-ray characterisation and b) thermal profile with indication of the time at which the five tomograms and four DVC computations were conducted.

Table 27 DVC information for the analysis of operational start-up time within an anode supported SOFC.

X-rat CT Scan	Dataset	Thermal cycling conditions prior to scan
D511	N/A	Reduced 800 °C 2hrs in forming gas 3 °C min^{-1}
D512	DVC_03	Cycled to 750 °C in forming gas 3 °C min^{-1}
D513	DVC_10	Cycled to 750 °C in forming gas 10 °C min^{-1}
D514	DVC_20	Cycled to 750 °C in forming gas 20 °C min^{-1}
D515	DVC_30	Cycled to 750 °C in forming gas 30 °C min^{-1}

The minimum (CC_{Min}), average (CC_{Avg}) and maximum (CC_{Max}) correlation values for each of the four DVC computations are presented in Table 9. The CC_{Avg} value decreases after each thermal cycle, possibly due to the increased deformation to which the cell is subject, however the values remain sufficiently high throughout. Although CC_{Avg} provides an indication of the correlation quality as a bulk, the CC_{Min} and CC_{Max} are also presented so that the worst and best regions of displacement correlation can also be inspected. The lowest CC values were always found at the cell walls, which have previously been reported to deform substantially during thermal cycling (131), making correlation more challenging. All values away from the cell walls produced CC values above 0.97 therefore only the cell walls are omitted from the analysis.

Table 28 Minimum, average and maximum correlation coefficient values for the four DVC computations conducted on the tomograms obtained from a SOFC throughout operational thermal cycling, to 2 d.p.

	CC_{min}	CC_{avg}	CC_{max}
DVC_03	0.97	1.00	1.00
DVC_10	0.93	0.99	1.00
DVC_20	0.97	0.98	0.98
DVC_30	0.93	0.97	0.97

To visualise the displacement and strain data obtained from the DVC computations, Avizo Fire software (Avizo, Thermo Fisher Scientific, Waltham,

Massachusetts, U.S.) was employed to generate 3D displacement vector fields and strain volume renderings. Quantifications were achieved with use the of ImageJ (ImageJ, National Institute of Health, U.S.A) (91). Due to the periodic nature of the high ramp-rate strain map, the variation in strain is investigated across both the tangential and normal paths with respect to the strain wave propagation. To accomplish this, a strain map was extracted from the volume 350 μm in the normal length (x), 40 μm in the tangential length (y) and 5 μm in thickness (z), see Figure 51 for a geometric reference. The strain was then averaged vertically in z to reduce noise. The result was a single 2D map of strain whereby the strain variation in x and y could be decoupled and compared; seven line scans spaced evenly in parallel were collected across the normal and nine line scans again evenly spaced in parallel were collected across the wave tangent.

5.3.3. Degradation Trends and Initial Observations

Volume renderings and vector fields were employed to visualise the microstructural alterations that were tracked using DVC. Four strain and four displacement maps in the x-y view, are accompanied by two x-z views of the displacement at low and high ramp-rates in Figure 52 and Figure 53. The only visible reference point between all data-sets in the x-y orientation was the existence of a large heterogeneous region, indicated by blue arrows, where minimal evolution appeared throughout thermal cycling. Apart from this heterogeneous region, two distinct features were observed: microscopic clusters and macroscopic waves. By inspecting the volume perpendicular to the interface, via the x-z views, it is possible to assess the evolution near the interface and into the anode bulk. It is seen that, regardless of thermal ramp-rate, the largest evolutions were consistently seen within the anode functional layer towards the anode/electrolyte interface, indicated by the yellow arrows (Figure 54).

Low ramp-rates were dominated by cluster formations where material appeared to channel from different sources towards a common destination. The cluster density was seen to decrease with increasing ramp-rate accompanied by the introduction of a single strain-wave at moderate ramp-rates, indicated by dashed black arrows. At moderate ramp rates it was also observed that the clusters became significantly sparser and were scattered around large voids, as indicated by green arrows. At the highest thermal ramp-rate strain-waves completely dominated the structure and minimal clustering was observed, indicated by dashed red

arrows. Unlike the cluster formations which displayed localised microscopic features, the strain waves displayed macroscopic features that spanned the entire length of the sample. Moreover, hundreds of individual clusters were observed within the volume during low ramp-rates whereas, only nine distinct strain waves were observed after high-rate heating.

It is concluded that evolutions at low and high ramp-rates are dominated by the formation of microscopic clusters and macroscopic strain-waves respectively, with the greatest evolution occurring within the anode functional layer regardless of thermal ramp-rate. The channelling and wave propagation will now be investigated in closer detail.

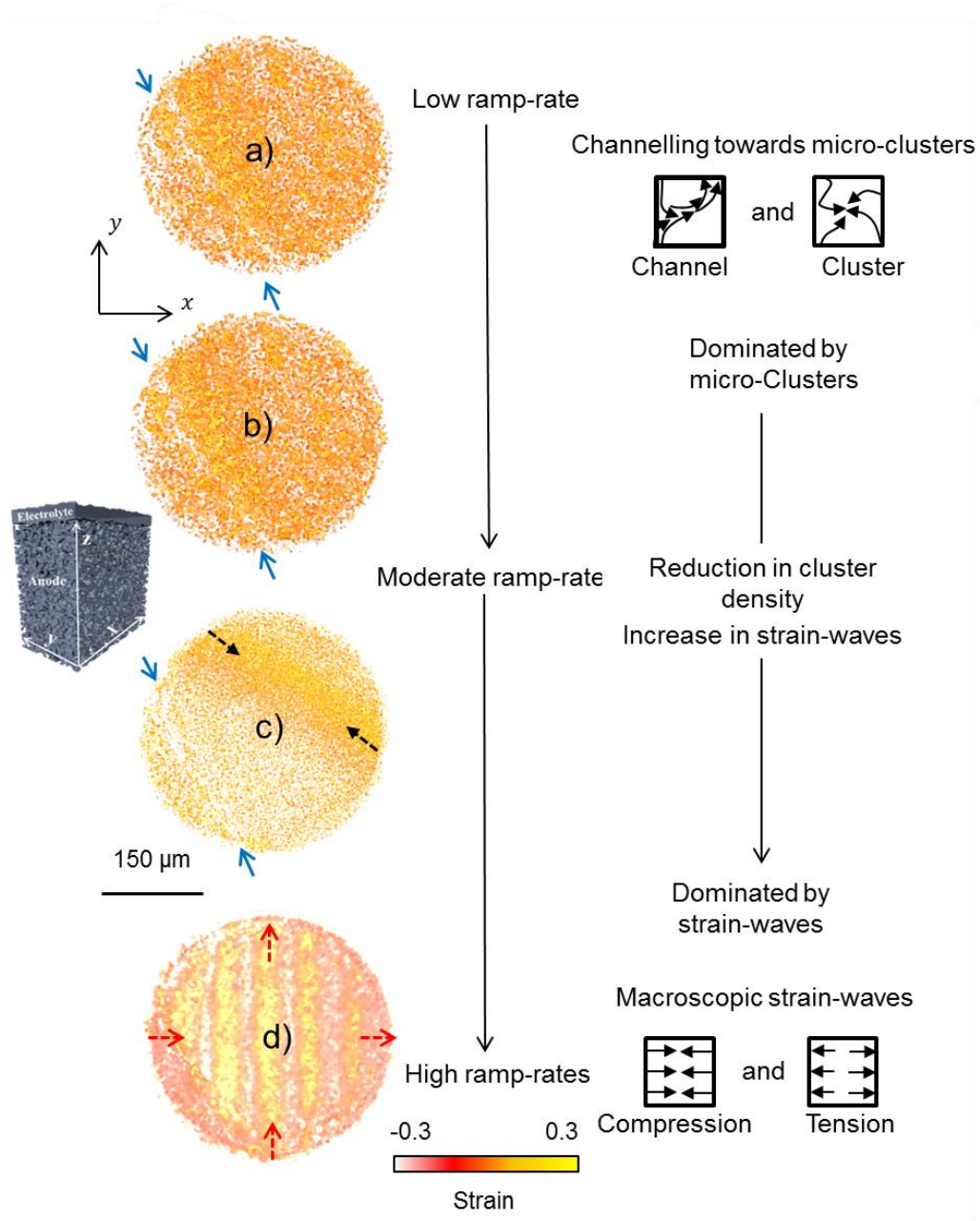

Figure 52 An overview of the workflow for data collection and analysis in the framework of the expected mechanisms of thermally induced degradation displayed as strain and displacement results from the four DVC computations conducted on an interfacial anode/electrolyte volume from an SOFC: x – y strain maps for a) 3 ºC min^{-1}, b) 10 ºC min^{-1}, c) 20 ºC min^{-1}, and d) 30 ºC min^{-1}.

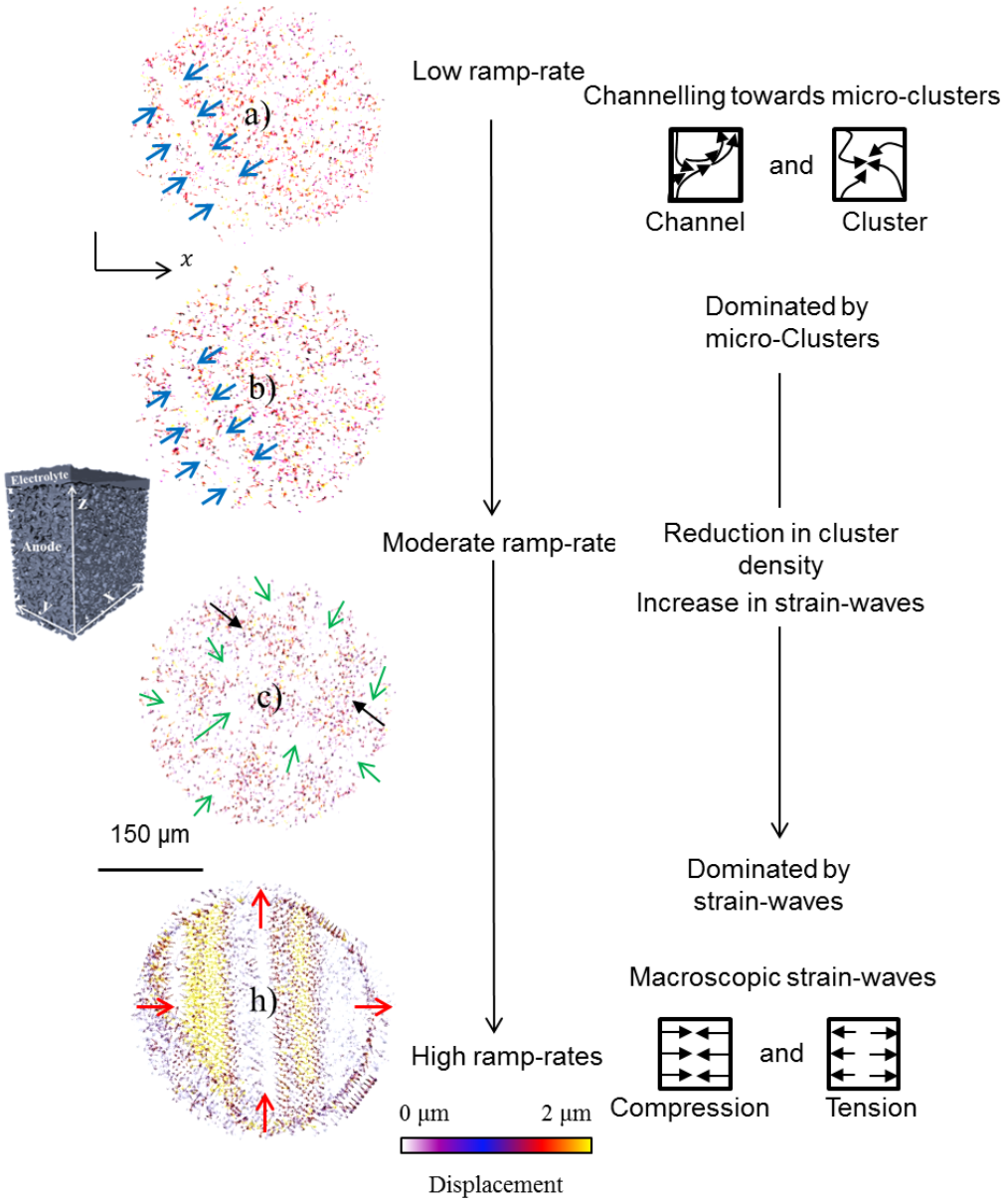

Figure 53 An overview of the workflow for data collection and analysis in the framework of the expected mechanisms of thermally induced degradation displayed as strain and displacement results from the four DVC computations conducted on an interfacial anode/electrolyte volume from an SOFC: x – y displacement maps for a) 3 ºC min^{-1} , b) 10 ºC min^{-1}, c) 20 ºC min^{-1}, and d) 30 ºC min^{-1}.

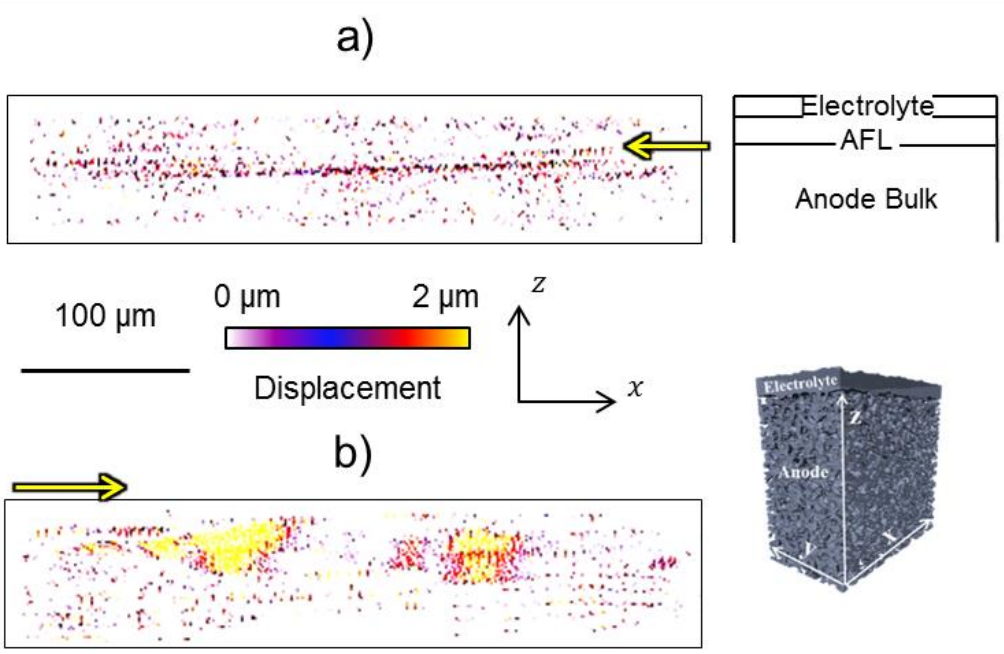

Figure 54 An overview of the workflow for data collection and analysis in the framework of the expected mechanisms of thermally induced degradation displayed as strain and displacement results from the four DVC computations conducted on an interfacial anode/electrolyte volume from an SOFC: x – z displacement maps for a) 3 ºC min^{-1} , and b) 30 ºC min^{-1}.

5.3.4. Low and High Ramp-Rate Degradation

Through inspection of the displacement maps for the low- and high ramp-rates under high magnification detail of the microscopic and macroscopic mechanisms was revealed. The low ramp-rate evolution which was dominated by micro-mechanisms such as channelling and clustering are displayed in Figure 55a and, the high ramp-rate evolution which was dominated by the macro-mechanisms such as the compression and tension strain-waves are displayed in Figure 55 b.

Within Figure 55b, red arrows have been added, on top of the black arrows which were generated by the DVC computation, to indicate the net movement of material. The low ramp-rate clusters were dispersed throughout the volume and were relatively homogenous in size; channels are ca. 1 μm in diameter and meander to lengths of 5 – 15 μm with the cluster region encompassed by a ca. 3 μm diameter. Unlike the clusters which were dispersed and meander in all directions, the strain-waves presented greater periodicity forming well-defined parallel waves throughout the structure. Regions of minimal displacement occurred within the centre of both the compression and tension bands. This stationary region was typically larger within the tensile band, approximately 4 – 5 μm, whereas the stationary regions within the compression bands were typically thinner, approx. 1 – 3 μm. The waves which connected the two bands are in the region of 5 – 8 μm in thickness. Although macroscopic in feature size, the waves were composed of many small displacements which were similar

in magnitude to the individual displacements that were responsible for the channel and cluster formations.

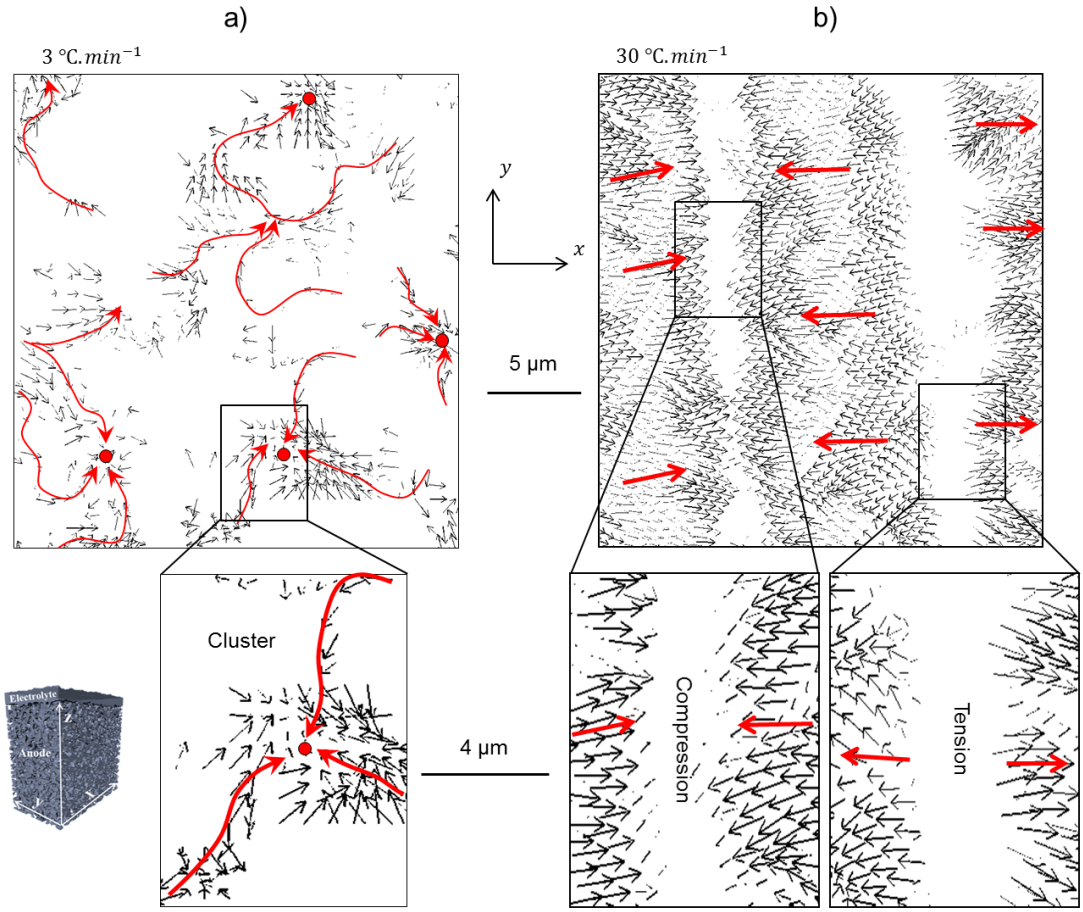

Figure 55 Displacements during high and low ramp-rates: a) x – y displacements displaying the micro-channelling towards micro-clusters during low ramp rates (3 ºC min^{-1}), and b) x – y displacements displaying tensile and compressive macroscopic strain-waves during high thermal ramp-rates (30 ºC min^{-1}).

It is concluded that the two features observed previously, microscopic clusters and macroscopic waves, formed and propagated through distinct mechanisms. The microscopic clusters were formed through the channelling of material from various locations to a common destination whereas the macroscopic waves propagated through compression and tension bands comprised of many small displacements aligned in the same orientation. These two mechanisms will now be investigated further in an effort to correlate the two distinct evolution mechanisms to degradation processes.

5.3.5. Microscopic Cluster Formations during Low Ramp-Rates

To better understand the processes responsible for the micro-channelling and the subsequent cluster formations, the cluster density was inspected at a macroscopic scale throughout the sample. Figure 56 displays five x-y vector slices obtained from the low ramp-rate displacement field. Using a lower magnification, the macroscopic trends can be observed i.e. higher or lower densities of clusters. Each dot on the on the extracted vector slices is a vector cluster and can be seen in magnified detail in Figure 56e. At the high resolution, each cluster displayed very similar characteristics, as discussed previously, see Figure 55 for finer detail. The macroscopic slices were extracted from the electrolyte through to the anode bulk in 5 μm increments. For simplicity, only the x and y components of the individual vectors are considered within each of the five slices but a 3D volume where the x, y and z components are all considered is presented for consideration in Figure 57.

Inspecting the vector slices, it is clear that the cluster density increases as the raster moves away from the electrolyte into the anode; there was a substantially higher evolution of material within the anode than the electrolyte. This is expected as YSZ should exhibit substantially higher microstructural stability throughout these operational profiles due to the higher melting temperature: Ni melts around 1452 ºC, whereas YSZ melts around 2700 ºC. Unlike the electrolyte which was purely ceramic, the anode contains Ni metal which is known to undergo sintering/coarsening processes at elevated temperatures (148) although; the microstructural

changes associated with sintering during thermal cycling are thought to be subtle (147).

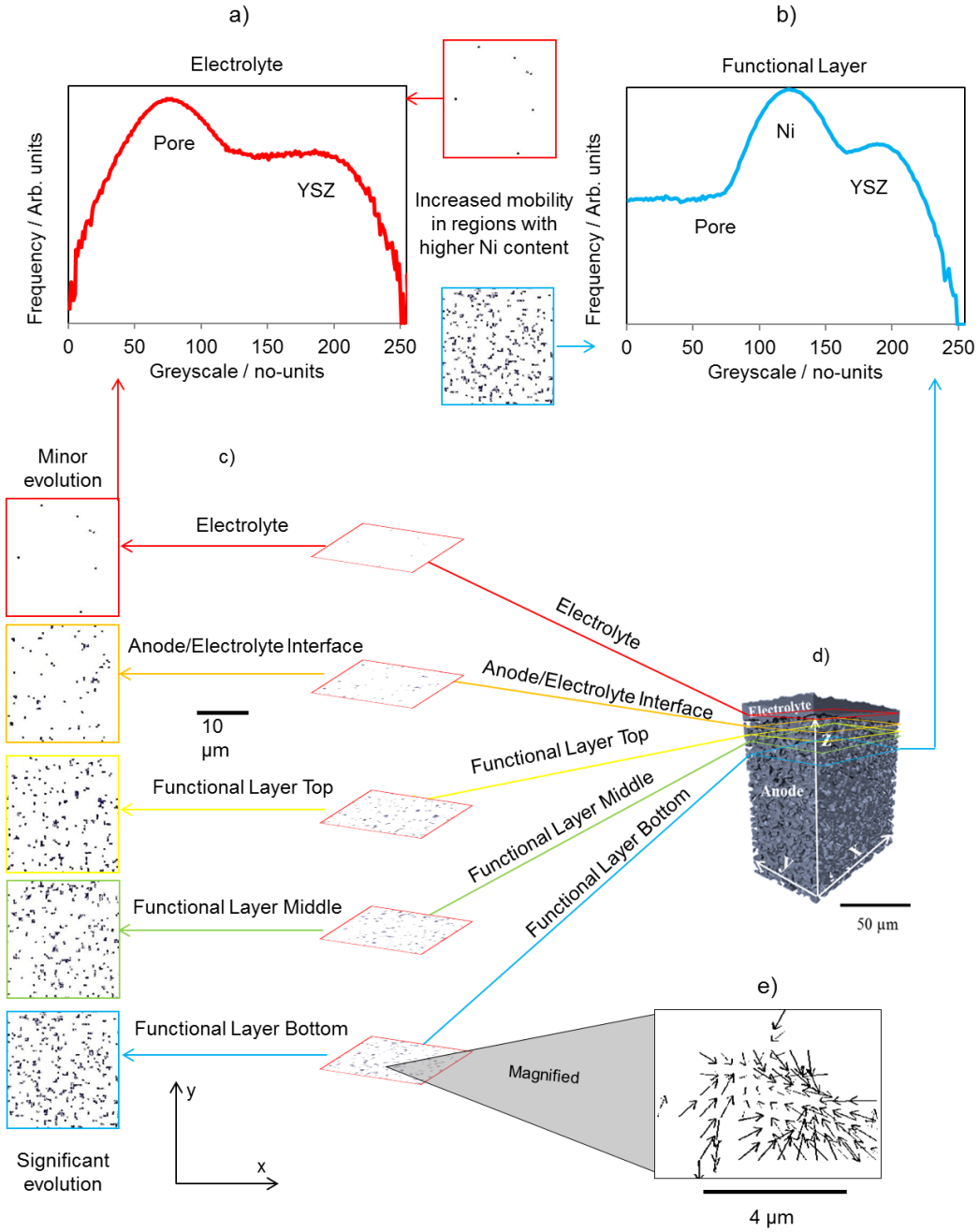

Figure 56 Correlating displacement through throughout the cell to the constituent materials: a) greyscale histograms for the ceramic and pore, and b) ceramic, pore and Ni from the electrolyte/pore interface and anode functional layer respectively, c) displacement vector slice raster from the electrolyte into the anode, with d) a geometric reference, and e) a magnified vector slice.

5.3.6. Correlating Displacement to Particular Materials

To determine whether Ni sintering may be responsible for the channel and cluster formations, the greyscale values responsible for the displacements were inspected to decouple the displacements of the constituent materials. To distinguish which displacements are responsible for which material, the greyscale values must first be assigned to each of the three phases: metal, ceramic and pore. To do this, two sub-volumes were extracted from the same ROI to accompany the five slices, one from the electrolyte/pore interface and one from the anode bulk. The former was positioned to ensure that only ceramic and pore phases were within the sub-volume whereas, the latter was positioned within the anode where all three phases were present. Greyscale histograms were then calculated for both sub-volumes and their profiles compared (Figure 56 a and b). The top sub-volume, containing ceramic and pore, produced a profile with only two shoulders/peaks, as expected due to only two phases being present. The bottom sub-volume, containing ceramic, pore and metal, produced a histogram profile with three distinct shoulders/peaks, two of which overlapped with the peaks from the top profile. These two peaks were then assumed to cover greyscale values for pore (dark greys/black) and ceramic (bright greys/white). The third peak positioned between the pore and ceramic was assumed to be associated with the Ni metal.

Now that the greyscale values could be associated with particular materials, vector slices were overlaid on top of the raw greyscale data in order to decouple the displacement of the constituent materials, as

displayed in a highly magnified image within Figure 57. From the overlaid images the displacement was directly correlated to greyscale values associated with the metal phase, greyscale values of approx. 100 – 160 from a 0 - 255 range in Figure 57 b. Moreover, the greyscale values associated with the ceramic were also inspected; negligible overlap was observed between the displacement vectors and the greyscale values associated with the ceramic concluding that insignificant displacement is attributed to the ceramic. Furthermore, the displacement trajectories were consistently affected by the border between the greyscale values associated with the metal and ceramic, suggesting that the ceramic may be responsible for the channelling mechanism.

In conclusion, the correlation of the greyscale values associated with the metal phase with the majority of the displacements observed during low ramp-rate cycling corroborates that the microscopic channelling and cluster formations may be due to the Ni mobility of the Ni metal while at elevated temperatures.

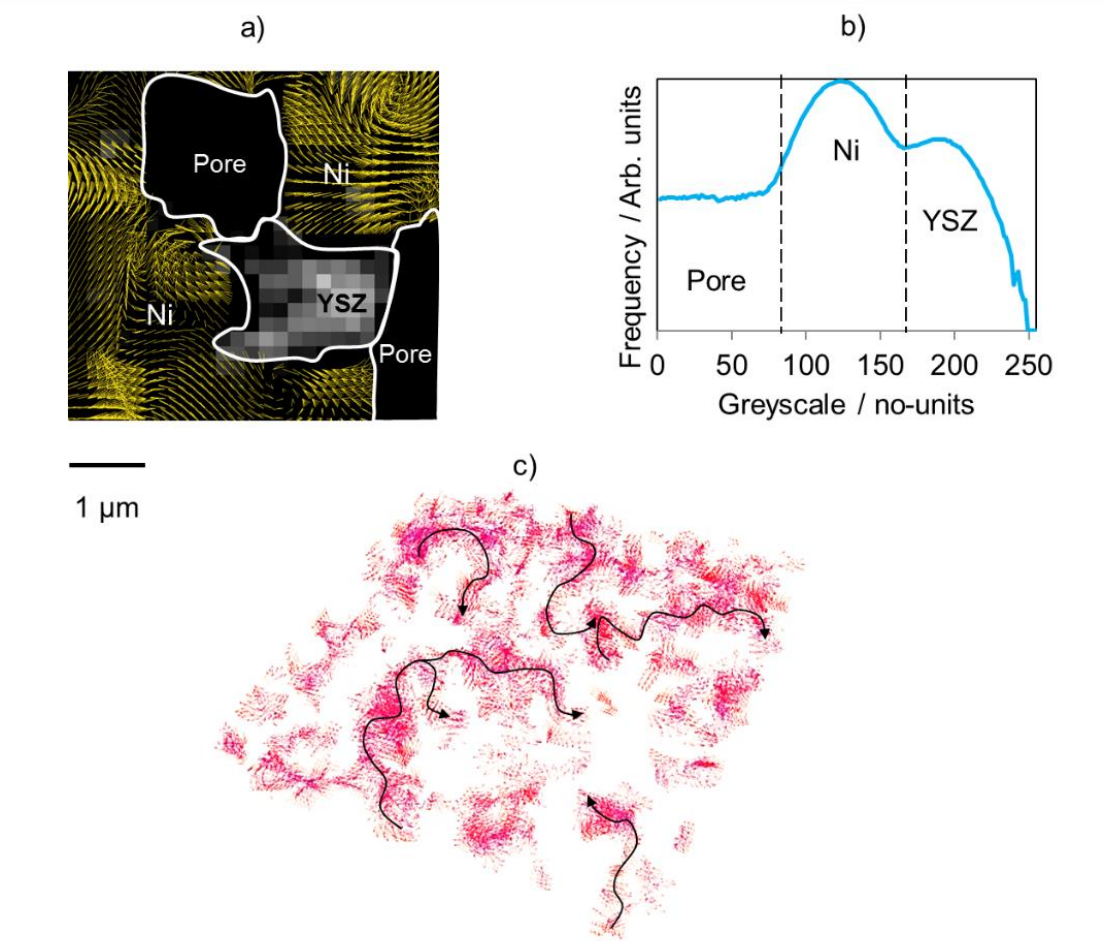

Figure 57 Correlating the displacement of Ni through micro-channelling and cluster formations through greyscale segmentation: a) magnified vector slice overlaid on top of the raw greyscale slice, with b) accompanying histogram outlined with greyscale thresholds for the three materials: pore, Ni and YSZ, and c) a 3D vector field from the anode with calculated vectors in red and annotated arrows in black.

5.3.7. Macroscopic Strain-Waves during High Ramp-Rates

To gain an understanding of the strain-wave propagation, the strain magnitude was inspected through both the normal and tangent of each strain wave, i.e. the normal inspects the variation between each wave and the tangent inspects the variation within each individual wave. Figure 58 displays the high ramp-rate strain field with the addition of seven line scans across the cell normal to the strain-wave propagation and nine line scans across the cell tangential to each of the individual waves. The tangential line scans were also separated into tension and compression fronts for analysis.

All seven line scans which were collected normal to the wave propagation, i.e. comparing each wave in turn, displayed very similar profiles; strain values undulated from peaks of tension to peaks of compression which decayed in magnitude from one cell-wall to the other, spanning approximately 350 μm. The tension and compression data are displayed separately in Table 29 and Table 30, respectively. An order of magnitude reduction in both the tension and compression peaks was observed across the cell; the tension peaks decayed from 0.283 to 0.053 and compression peaks decayed from -0.304 to -0.033.

Within the tables, the minimum, average, maximum, range, and standard deviation strain values calculated from the tangent, i.e. across each individual wave, are also presented. Undulation was observed across the wave tangents but far less than what was seen along the wave normal. For example, the tension ranged by a maximum of 0.01 across the tangent

whereas the tension ranged by a maximum of 0.24 across the normal. Consequently, the undulation across the tangent resulted in variation from high-compression to low-compression or high-tension to low-tension, as opposed to high-compression to high-tension across the normal. Furthermore, no decay profile was observed across the tangent, unlike the normal which decayed with a very similar profile for both the compression and tension peaks, visualised in Figure 58 c and e.

From the sixteen line scans taken across the strain waves which appeared during high thermal ramping, insight has been gained into the propagation profiles responsible for the strain variation throughout the cell. It is concluded that variations were observed within each of the strain waves in the form of minor undulations but the variation between waves was most considerable and decayed from one cell-wall to the other eventually reducing by an order of magnitude. However, unlike the microscopic channelling and cluster formations which are thought to be attributed to the sintering of the Ni metal, an extensively investigated mechanism (148), the mechanism responsible for the initiation of these strain waves is more elusive as no greyscale variation could be correlated to the compression-tension undulations. Nevertheless, non-linear strain distributions have been previously reported (41; 131). Previously, the strain was produced through thermal gradients which induced the ‘nearest–neighbour’ effect whereby contraction of the Ni units in a single direction enhanced strain. Unlike previous experiments, the thermal cycles explored in this work were conducted in highly isothermal environments; therefore, thermal gradients

are not thought to be responsible for the strain waves observed here although, as mentioned in the previous section, a large heterogeneous region was observed where minimal mobility occurred throughout thermal cycling. This region of the anode also contained a higher ceramic content which may have been responsible for exacerbating or even initiating the strain wave propagation. The presence of the constraining electrolyte layer is thought to preferentially distribute strain, inducing gradients analogous to work discussed by Clague et al. (45), but at a cell-level, as well as between individual particles. Cell walls were previously observed to deform during thermal cycling (131); a combination of the constriction during the wall deformation, the constraining electrolyte layer, and the existence of a large heterogeneous defect may have caused the rippling of strain throughout the anode. These mechanisms likely influence the probability of degradation and it has been previously reported that cell delamination (131) and loss of reaction sites can be expected (147).

Table 29 The maximum, average, minimum, range, and standard deviation of tension strain measurements obtained across the wave normal for each of the five wave fronts propagating in an SOFC sample after thermal cycling at high ramp-rates.

Location Along Normal	20 μm	88 μm	167 μm	245 μm	320 μm
Maximum Tension Along Tangent	0.283	0.119	0.080	0.066	0.053
Average Tension Along Tangent	0.230	0.083	0.047	0.048	0.026
Minimum Tension Along Tangent	0.187	0.031	0.017	0.014	-0.010
Tension Range Along Tangent	0.096	0.088	0.063	0.052	0.063
Standard deviation Along Tangent	0.092	0.055	0.031	0.027	0.027

Table 30 The minimum, average, maximum, range, and standard deviation of compression strain measurements obtained across the wave normal for each of the five wave fronts propagating in an SOFC sample after thermal cycling at high ramp-rates.

Location Along Normal	48 μm	119 μm	201 μm	279 μm
Minimum Compression Along Tangent	-0.121	-0.052	-0.036	0.017
Average Compression Along Tangent	-0.208	-0.105	-0.068	-0.010
Maximum Compression Along Tangent	-0.304	-0.154	-0.100	-0.033
Compression Range Along Tangent	0.183	0.102	0.064	0.050
Standard deviation Along Tangent	0.076	0.044	0.031	0.021

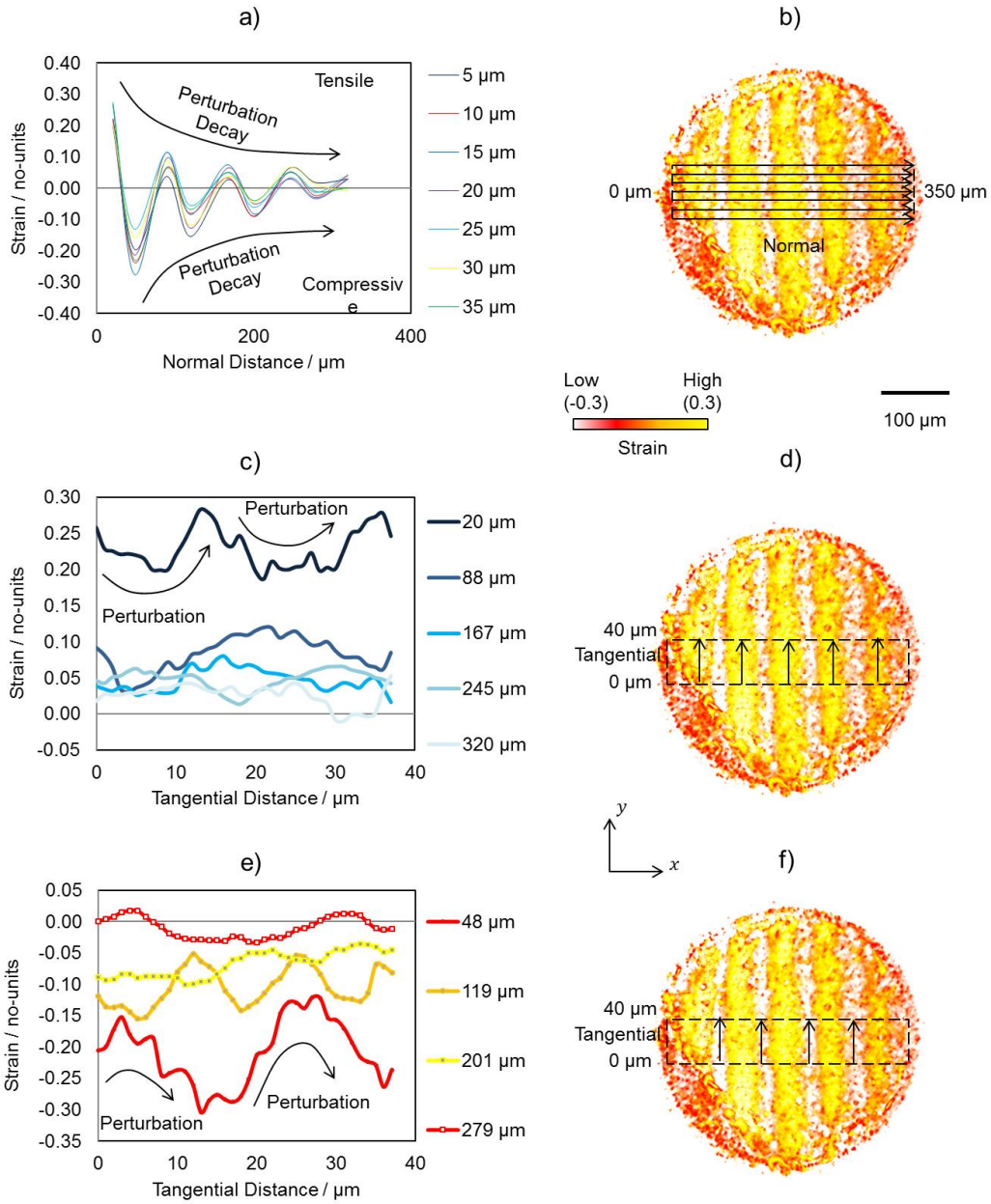

Figure 58 Strain-wave propagation in an SOFC exposed to high thermal ramp-rates: a) tensile and compressive strain decay across the cell observed from, b) seven line scans obtained normally to the wave propagation, c) perturbations across the five tensile wave fronts taken d) tangentially to each wave, e) perturbations across the four compression wave fronts taken f) normally to each wave.

5.3.8. Conclusions from DVC Investigations

The microstructure evolution within an SOFC has been tracked and quantified throughout operational thermal cycling using digital volume correlation techniques for the first time. The microstructural data was obtained from an anode/electrolyte interface using entirely lab-based X-ray CT instruments, achieving sub-micron resolutions. Each operational cycle was conducted at an increased thermal ramp-rate to emulate successively faster start-up times, a known cause of degradation in planar cells. The pre- and post-cycle microstructural data was then compared to track the movements of material within the ROI. Two distinct features were observed, the formation of clusters and waves.

Low ramp-rates were dominated by the formation of microscopic clusters which dispersed throughout the entire volume showing no unified orientation. The cluster density decreased considerably on increasing ramp-rate, their decline was accompanied by the introduction of macroscopic waves. At high ramp-rates macroscopic waves dominated the cell, propagating periodically throughout the cell in a well-organised pattern. After high-resolution inspection, the microscopic clusters were determined to form through the micro-channelling of material from various locations to a common destination. These channels and clusters were then correlated to the greyscale values attributed to the Ni metal, which is known to undergo sintering mechanisms at elevated temperatures. By inspecting the boundaries between the metal and ceramic greyscale values, it was seen that the ceramic backbone appears to cause the channelling of the metal;

Ni gains its mobility from the high temperature and its propensity to minimise its surface/interfacial energy and was channelled by the ceramic skeleton, likely inhibiting mobility effects. It is also suspected that the decrease in the cluster density that accompanied the increased ramp rate was likely due to the reduced time at temperature i.e. the degree of sintering is a function of the amount of time at a certain temp, rising to temperature faster results in less time at elevated temperatures and therefore less sintering. The high-resolution inspection of the macroscopic waves found that the propagation occurred through the formation of tension and compression fronts which decayed in magnitude across the cell. The waves were composed of many small displacements all aligned in the same orientation either pulling towards or away from one another, respectively causing the compressive and tensile strains. The waves and accompanying decay profiles are thought to be triggered by a combination of the cell-wall deformation and the existence of a large heterogeneous defect.

The two mechanisms observed here: micro-channelling with cluster formation and strain wave propagation, are also expected to affect the electrochemical performance as well as the mechanical properties of the cell. Ni mobility during channelling and cluster formation can improve percolation; however, it may also reduce the amount of reaction sites due to loss of Ni-YSZ contact area triggered by metal sintering and expansion mismatch. Strain waves may result in cracking and delamination of the constituent layers, such as the anode from the electrolyte. Tomography-

based analysis which has been reported prior to this work supports both of these hypotheses (147; 131).

Considering the wider application and future of the field of SOFC research, 4D techniques will enable microstructural design and tailored operational profiles. For instance, one microstructural design may electrochemically outperform another, at the expense of mechanical integrity or long term durability. If applied correctly, the techniques such as those that are discussed will enable enhanced cell microstructures to be fabricated, and improved operational profiles to be employed, ultimately leading to extended cell lifetimes.

This work is the first report of DVC computations applied to an SOFC exposed to high temperatures achieving sub-micron resolutions using entirely lab-based X-ray CT instruments. Furthermore, thermally driven degradation is not limited to electrochemical devices therefore this work will provide as an example of the advanced characterisation studies which are now possible using lab-based X-ray CT.

5.4. Microscopic Degradation Assessed Using X-ray CT

5.4.1. An Introduction to Microscopic Degradation

The previous two sections discuss the macroscopic degradation that has been observed within an anode supported SOFC, also touching upon the microscopic structural evolutions associated with Ni mobility that is constrained be the ceramic backbone. There are many metrics that can be extracted from microstructures of SOFCs as discussed previously (Chapters 2 and 3) that can be employed to access the electrochemical performance of the cell. Particularly, the composition, tortuosity-factor, percolation, particle size, surface area, particle-particle contact area, and TPB density are all such metrics of interest. The following section will therefore explore these microstructural changes within the same sample that was explored in the previous sections (5.2 and 5.3).

5.4.2. Microscopic X-ray CT Investigation Procedure

The previous section of this chapter (Section 5.1) explored the macroscopic degradation within the cell through the analysis of X-ray CT tomograms collected throughout several operational thermal cycles. It was found that after reaching a critical thermal ramp-rate a mechanical yield point was reached causing significant microstructural deformation. However, understanding degradation required a multi-length-scale approach as demonstrated through the X-ray micro- and nano-CT characterisation of the anode support layer cracking. Therefore this section will investigate the same sample but with focus on the cell microstructure (rather than macrostructure), examining the particle-particle interactions prior to the critical transition after high ramp-rate cycling. For clarity the sample and scans explored within this section are tabulated in Table 31 and Table 32.

Table 31 Imaging conditions for chapter section 5.4: Microscopic Degradation: Exploring the variations in the Tortuosity-factor, phase-percolation, surface area, interfacial contact and TPB density.

Sample	Study	Data	Instrument	Projections	Exposure Time / s	Voxel Size / nm	FOV / µm x µm
S511	I521 Implications of thermal ramp-rate on the cell microstructure	D511	Versa 40X	2401	30	395	384 x 384
		D512					
		D513					
		D514					
		D515					

Table 32 Thermal cycling conditions for chapter section 5.4: Microscopic Degradation: Exploring the variations in the Tortuosity-factor, phase-percolation, surface area, interfacial contact and TPB density.

Sample	Study	Data	Thermal cycling conditions prior to scan
S511	I521 Implications of thermal ramp-rate on the cell microstructure	D511	Reduced 800 °C 2hrs in forming gas 3 °C min^{-1}
		D512	Cycled to 750 °C in forming gas 3 °C min^{-1}
		D513	Cycled to 750 °C in forming gas 10 °C min^{-1}
		D514	Cycled to 750 °C in forming gas 20 °C min^{-1}
		D515	Cycled to 750 °C in forming gas 30 °C min^{-1}

5.4.3. Compositional Variation

The pore, metal and ceramic networks are displayed in Figure 59 with accompanying local volume fractions presented slice-by-slice for the three phases in Figure 60 (calculated via methods discussed in Chapter 3). The bulk composition values presented here are typical of an SOFC anode: 0.35:0.28:0.37 for $\overline{\varphi}_{\mathrm{Ni}}:\overline{\varphi}_{\mathrm{YSZ}}:\overline{\varphi}_{\mathrm{Pore}}$ (96; 48). Furthermore, minimal change is seen in the composition of the anode throughout the thermal cycling: on average, the ceramic increased by 0.5 vol% whereas the Ni and pore decreased and increased by 3.4 vol% and 2.9 vol% respectively. The variation in the ceramic content is negligible as expected due to the stability of YSZ within these conditions. The compositional changes within the Ni and pore volume fractions are slightly larger and may be explained by the mobility of Ni at elevated temperatures; Ni may leave/enter the ROI to/from the external volume. However, variations remain minor and may also be due to the sensitivity of the segmentation. Therefore it is concluded that, under a sufficiently reducing atmosphere, the anode composition remains relatively unchanged throughout several operational thermal cycles when evaluated at this length scale.

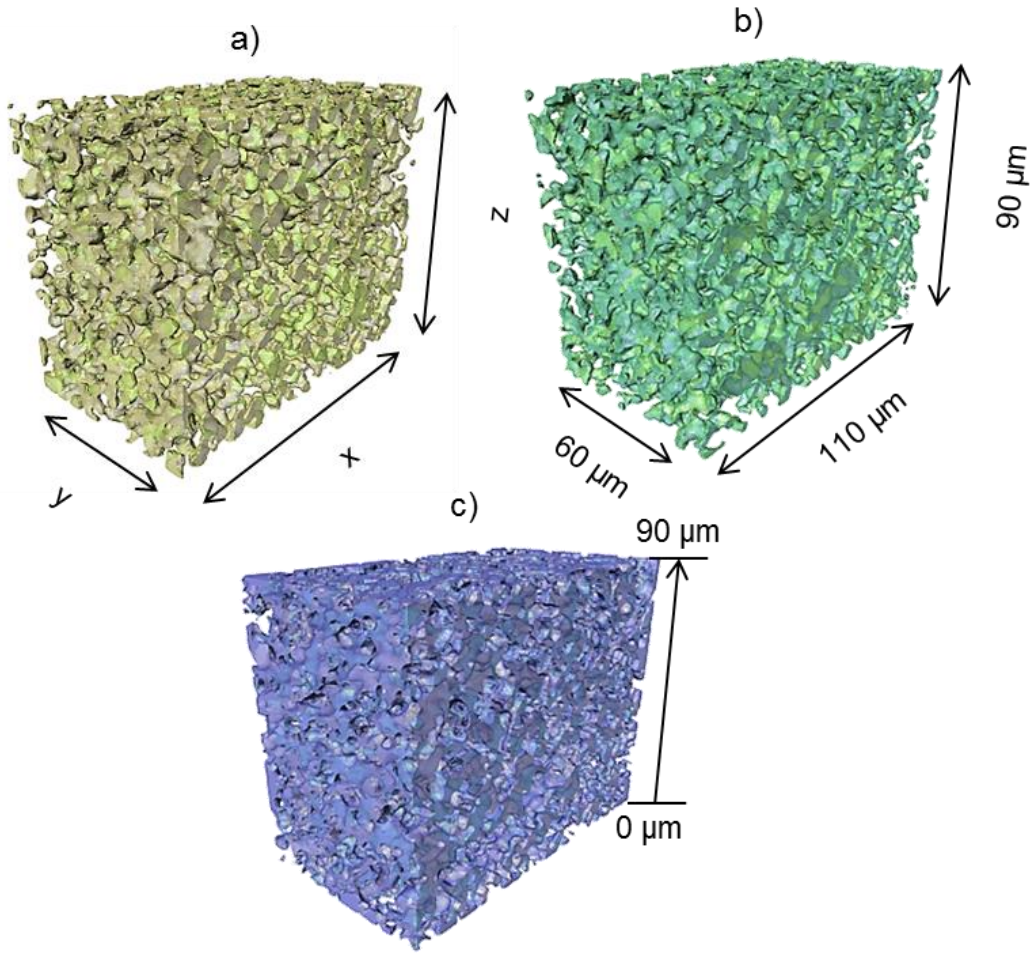

Figure 59 The three-phase segmentation of a Ni-YSZ SOFC anode using X-ray micro-CT: a) pore, b) Ni and c) YSZ 3D phase volumes.

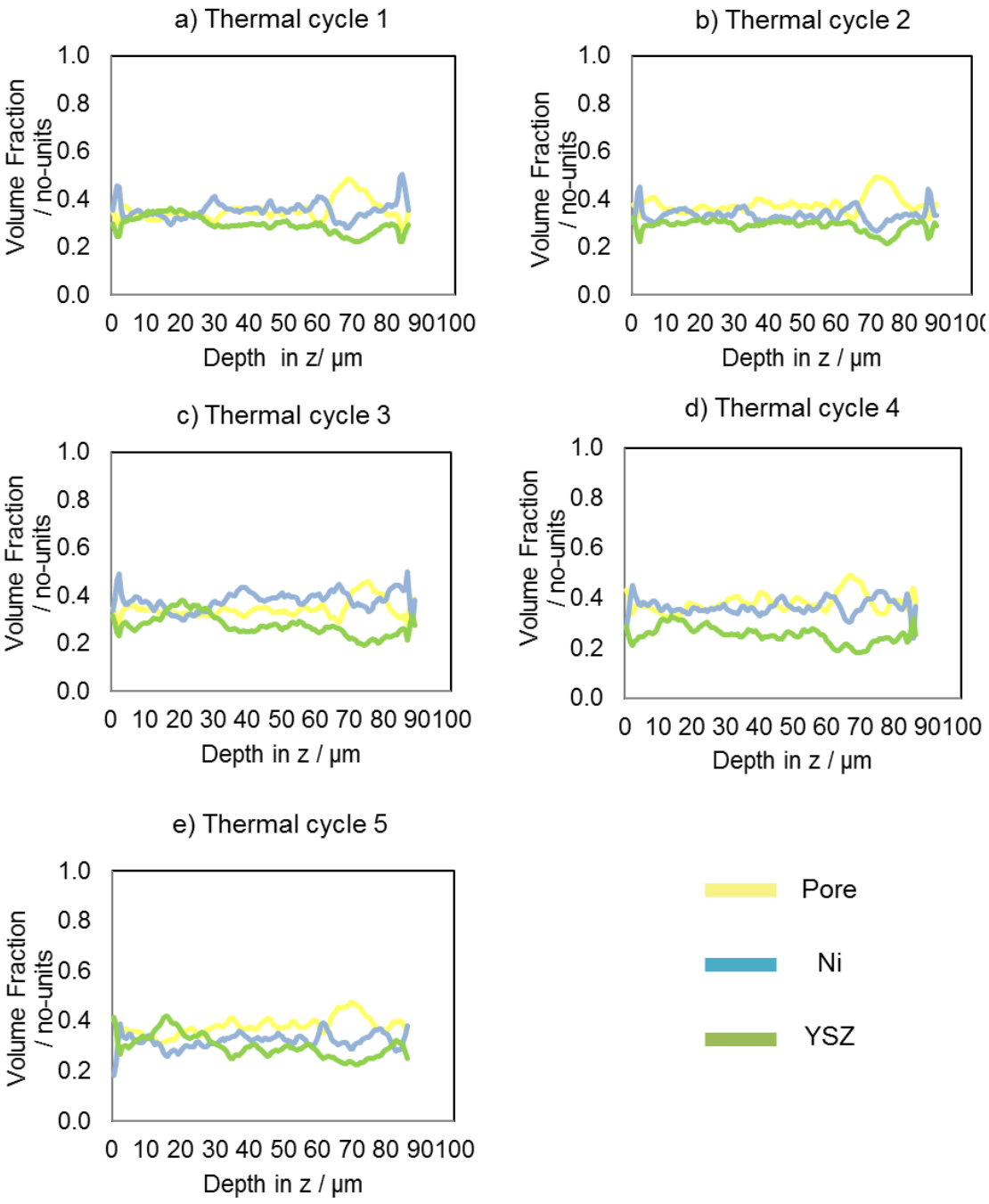

Figure 60 The three-phase segmentation of a Ni-YSZ SOFC anode using X-ray micro-CT: a – e) the slice-by-slice compositional volume fraction for the three phases for respective thermal cycles 1 – 5.

5.4.4. Tortuosity-Factor and Percolation

The metal, ceramic and pore tortuosity-factors and percolation percentages in the three orientations are presented in Figure 61 and Figure 62 respectively and are tabulated in Table 33, Table 34 and Table 35. The tortuosity-factor values and phase percolation percentages found here are comparable to that which have been presented in the literature previously and are typical of SOFC anodes (57; 149).

The average tortuosity-factor values for Ni and YSZ remain relatively constant throughout the operational thermal cycling: $\Delta\overline{\tau}_{\mathrm{Ni}} = +0.02$ and $\Delta\overline{\tau}_{\mathrm{YSZ}} = -0.49$. However, the pore-phase tortuosity-factor reduces substantially $\Delta\overline{\tau}_{\mathrm{Pore}} = -3.68$, accompanied by a ca. 4 % increase in percolation. The Ni and YSZ percolation percentages remain high (above 97 %) throughout. The majority of the reduction in the pore-phase τ occurs after the first thermal cycle; the pore-phase tortuosity-factor reduction after the first cycle is $\Delta\overline{\tau}_{\mathrm{Pore}} = -3.35$, ca. 91 % of the total reduction after cycling. The alterations in the pore-phase may be explained by Ni mobility during the first low-ramp thermal cycle; further investigation with the use of advanced computational techniques such as digital volume correlation (DVC) (105) may confirm this but is beyond the scope of this work.

Table 33 Tortuosity-factor values for Ni, YSZ and pore phases within an SOFC anode throughout five operational thermal cycles and in the three spatial orientations: x, y and z and presented to 2 d.p.

Thermal Cycles	Tortuosity-Factor in x / no-units			Tortuosity-Factor in y / no-units			Tortuosity-Factor in z / no-units		
	Ni	YSZ	Pore	Ni	YSZ	Pore	Ni	YSZ	Pore
1	3.09	4.28	6.01	3.55	5.67	8.41	3.21	4.27	5.79
2	3.51	4.29	3.01	4.24	6.05	4.00	3.42	4.55	3.17
3	2.57	4.72	3.5	2.73	6.66	4.25	2.75	5.76	4.01
4	2.90	5.93	3.2	3.05	7.27	3.46	2.81	5.47	2.99
5	2.98	3.27	2.63	3.64	5.51	3.68	3.27	3.97	2.88

Table 34 Percentage percolation values for Ni, YSZ and pore phases within an SOFC anode throughout five operational thermal cycles and in the three spatial orientations: x, y and z and presented to 1 d.p.

Thermal Cycles	Percolation in x /%			Percolation in y /%			Percolation in z /%		
	Ni	YSZ	Pore	Ni	YSZ	Pore	Ni	YSZ	Pore
1	98.8	98.6	95.2	98.8	98.6	95.2	98.8	98.6	95.2
2	98.3	98.7	99.6	98.3	98.7	99.6	98.3	98.7	99.6
3	99.2	98.6	99.2	99.2	98.6	99.2	99.2	98.6	99.2
4	99.1	97.7	99.8	99.1	97.7	99.8	99.1	97.7	99.8
5	99.2	99.1	99.8	99.2	99.1	99.8	99.2	99.1	99.8

Considering the different orientations, all phases were percolated to a similar degree in all directions. However, larger tortuosity-factor values were consistently observed in the y-plane, particularly in the ceramic and pore. This suggests that parallel to the interface, there may be non-uniformities in perpendicular directions. This is contrary to what would be expected in a homogenous cell; directions x and y would be assumed arbitrary in a spatially-homogenous microstructure, whereas z is often graded intentionally in order to supply favourable microstructures at different distances from the anode/electrolyte interface such as the anode functional (AFL) and support layers (ASL), spatial variation can also occur due to inertia affects during fabrication processing, e.g. gravity. This could arise as a result of artefacts in the reconstruction, or errors within the segmentation; however, the discrepancy between the x and y planes is consistent for all five thermal cycles and because the sample was removed from the X-ray chuck for each thermal cycle the likelihood of an x-y bias in the creation of acquisition/reconstruction artefacts is very low; moreover, although the same greyscale fiducial technique (as discussed in Chapter 4) was applied to all datasets, each dataset was segmented independently, improving confidence in the consistency of the results. Therefore, inhomogeneity between the x and y planes suggests the existence of microstructural defects, possibly introduced during fabrication.

Ultimately only minor variation is observed in the Ni and YSZ tortuosity-factor values and percolation percentages throughout thermal cycling, and the same is observed within the pore-phase after stabilising during low ramp-rates.

However consistent differences between the orthogonal directions within the anode suggest non-uniformities parallel to the interface.

Table 35 Tortuosity-factor and percolation values for Ni, YSZ and pore phases within an SOFC anode throughout five operational thermal cycles averaged in the three spatial orientations: x, y and z and presented to 2 d.p.

Thermal Cycles	Average Percolation / %			Average Tortuosity-Factor / no-units		
	Ni	YSZ	Pore	Ni	YSZ	Pore
1	98.8	98.6	95.2	3.28	4.74	6.74
2	98.3	98.7	99.6	3.72	4.96	3.39
3	99.2	98.6	99.2	2.68	5.71	3.92
4	99.1	97.7	99.8	2.92	6.22	3.22
5	99.2	99.1	99.8	3.30	4.25	3.06

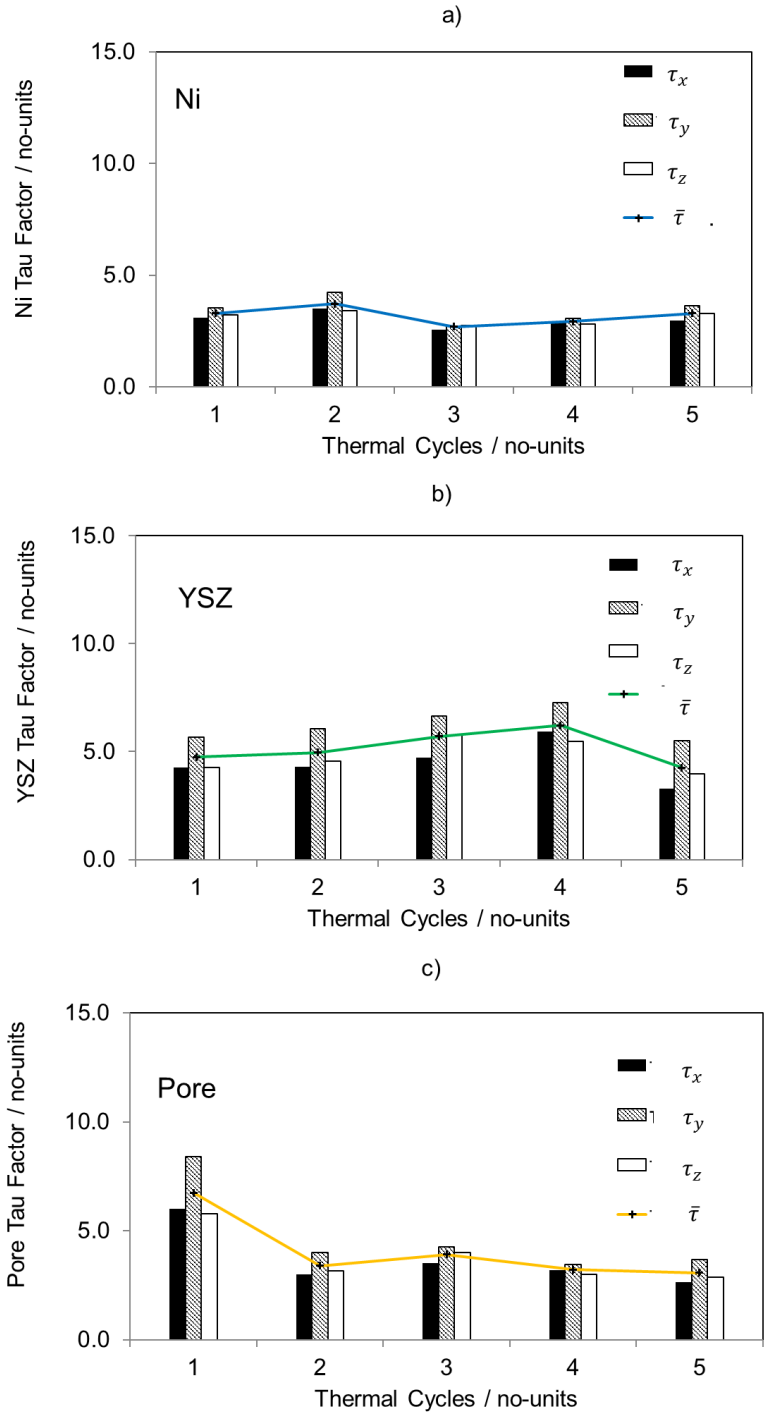

Figure 61 Tortuosity-factors for the three phases (Ni, YSZ and pore), in the three orientations (x, y and z), for the five thermal cycles: a) Ni, b) YSZ and c) pore with average values plotted as lines across each bar chart.

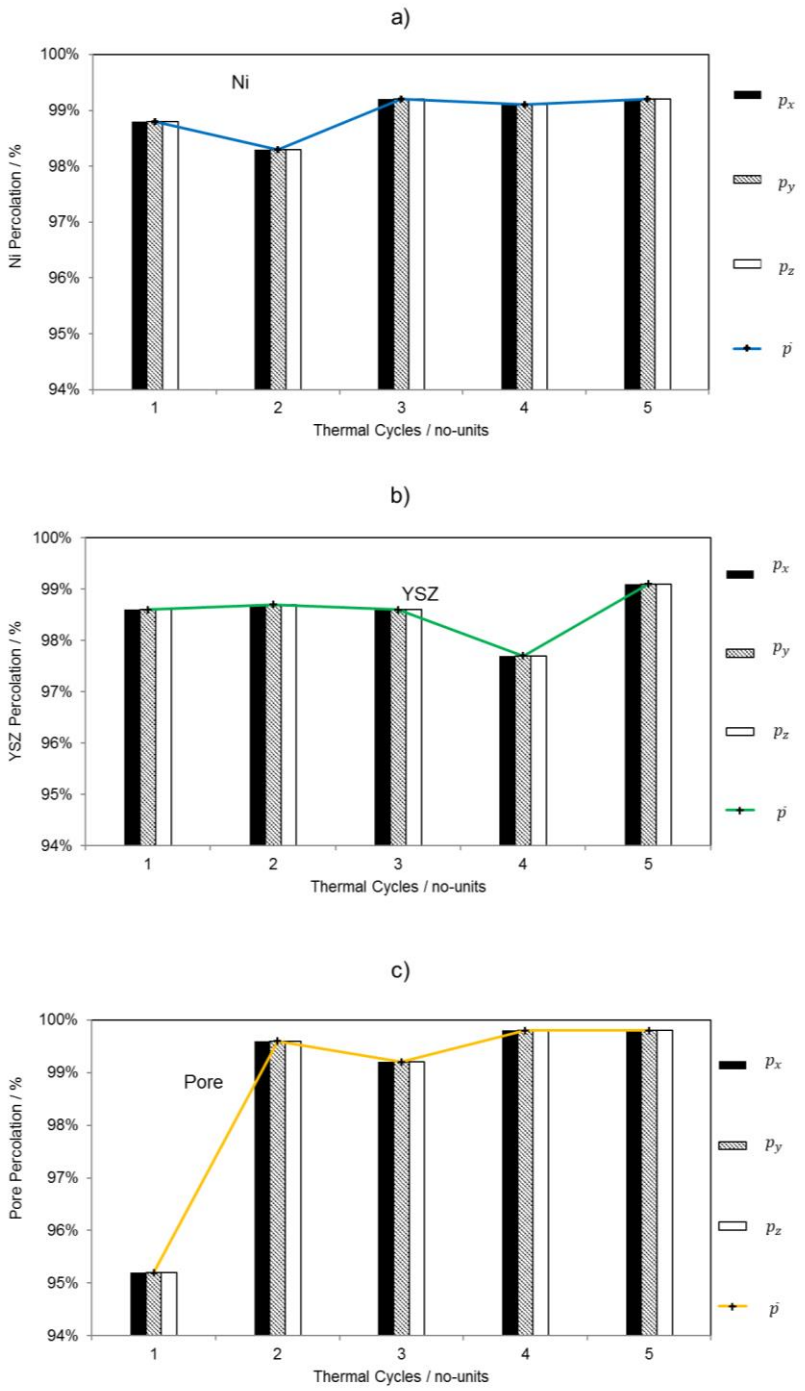

Figure 62 Percolation percentages for the three phases (Ni, YSZ and pore), in the three orientations (x, y and z), for the five thermal cycles: a) Ni, b) YSZ and c) pore with average values plotted as lines across each bar chart.

5.4.5. Particle Size

The particle Feret diameters for each of the three phases are presented in Figure 63 and are tabulated in Table 36. Particle size histograms indicate that Ni particles have a small range of diameters and are also relatively small in size but remain characteristic of an SOFC microstructure (150; 57) , throughout cycling the average Ni diameter ranges from $\overline{\varphi}_{\mathrm{Ni}} = 1.00$ µm to 1.14 µm. Whereas, the pore and ceramic particles present larger, but similar, diameters throughout, ranging from $\overline{\varphi}_{\mathrm{pore}} = 2.36$ µm to 2.55 µm and $\overline{\varphi}_{\mathrm{YSZ}} = 2.48$ µm to 2.61 µm, respectively.

Inspecting the variation in the percentage of Ni particles smaller than 1.5, 3.0, 5.0 and 8.0 µm with each thermal cycle (Table 36 and Figure 63), it is concluded that there is a reduction in the percentage of smaller particles, a relatively consistent percentage of medium particles and a subtle increase in the percentage of large particles; the rate of growth of large Ni particles (ca. 0.1 %) is an order of magnitude lower than the rate of loss of small Ni particles (ca. 1.0 %), Figure 64. This is quite typical of sintering mechanisms because it requires several smaller particles to combine in order to form larger particles; therefore there will inherently be fewer large particles created during sintering, compared to the number of small particles removed. Smaller particles also have a larger area-to-volume ratio which results in a higher system energy and lower stability. Although the Ni particles are observed to sinter, the ramp-rate appears to have a negligible effect on the degree of coarsening due to the relatively short periods at temperature (under 10 hours), compared to long operational dwell times which are often quoted in the thousands of hours. During long-term operation

considerable agglomeration of the Ni particles is expected to occur; the average Ni particle diameter can be expected to grow with a logarithmic profile during operation (151; 152). However, YSZ, which has a significantly higher melting temperature, would be expected to demonstrate more stable structural properties, such as particle diameter; Figure 63 confirms the greater stability of YSZ with thermal cycling; a 14 % change in diameter is observed within the Ni, whereas only a 5 % change within the YSZ.

Table 36 The average particle Feret diameter for Ni, YSZ and pore after each thermal cycle with units of microns.

Material	Thermal Cycles / no units				
	1	2	3	4	5
Ni	1.00	1.03	1.06	1.04	1.14
YSZ	2.48	2.49	2.61	2.57	2.60
Pore	2.55	2.43	2.54	2.40	2.36

Table 37 The percentage of total Ni particles from an SOFC anode with Feret diameters of 1.5, 3.0, 5.0 or 8.0 μm for each thermal cycle.

Feret Diameter	Thermal Cycles				
	1	2	3	4	5
1.5 μm	41.5 %	40.6 %	39.5 %	40.5 %	36.0 %
3.0 μm	10.5 %	8.1 %	7.6 %	7.6 %	6.9 %
5.0 μm	3.1 %	2.7 %	3.0 %	2.6 %	3.1 %
8.0 μm	0.7 %	0.7 %	1.0 %	0.8 %	1.1 %

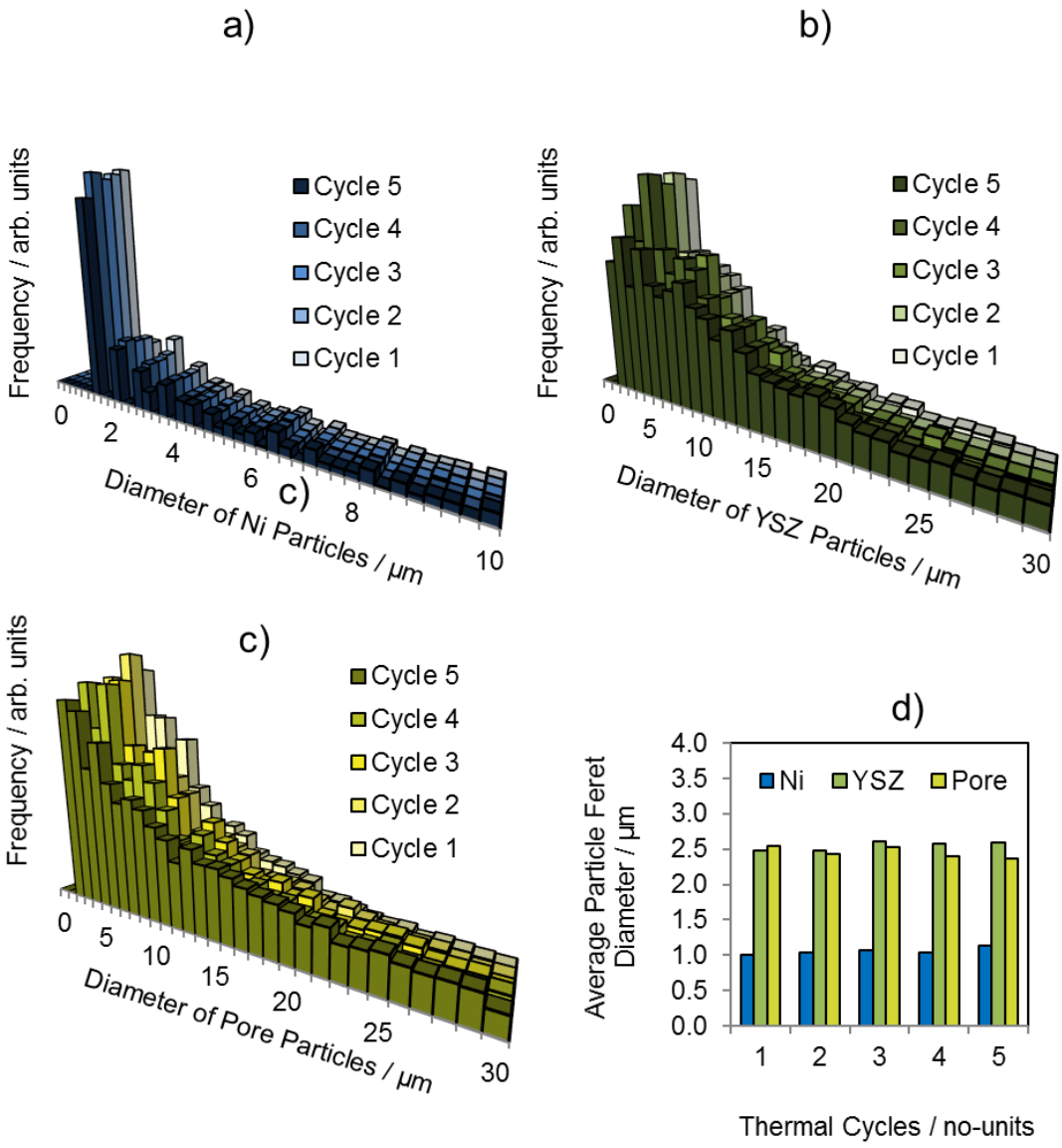

Figure 63 Particle size analysis of the Ni (blue), YSZ (green) and pore (yellow) with each thermal cycle: histograms of the particle Feret diameters for a) Ni, b) YSZ and c) pore, d) the average particle size with thermal cycling.

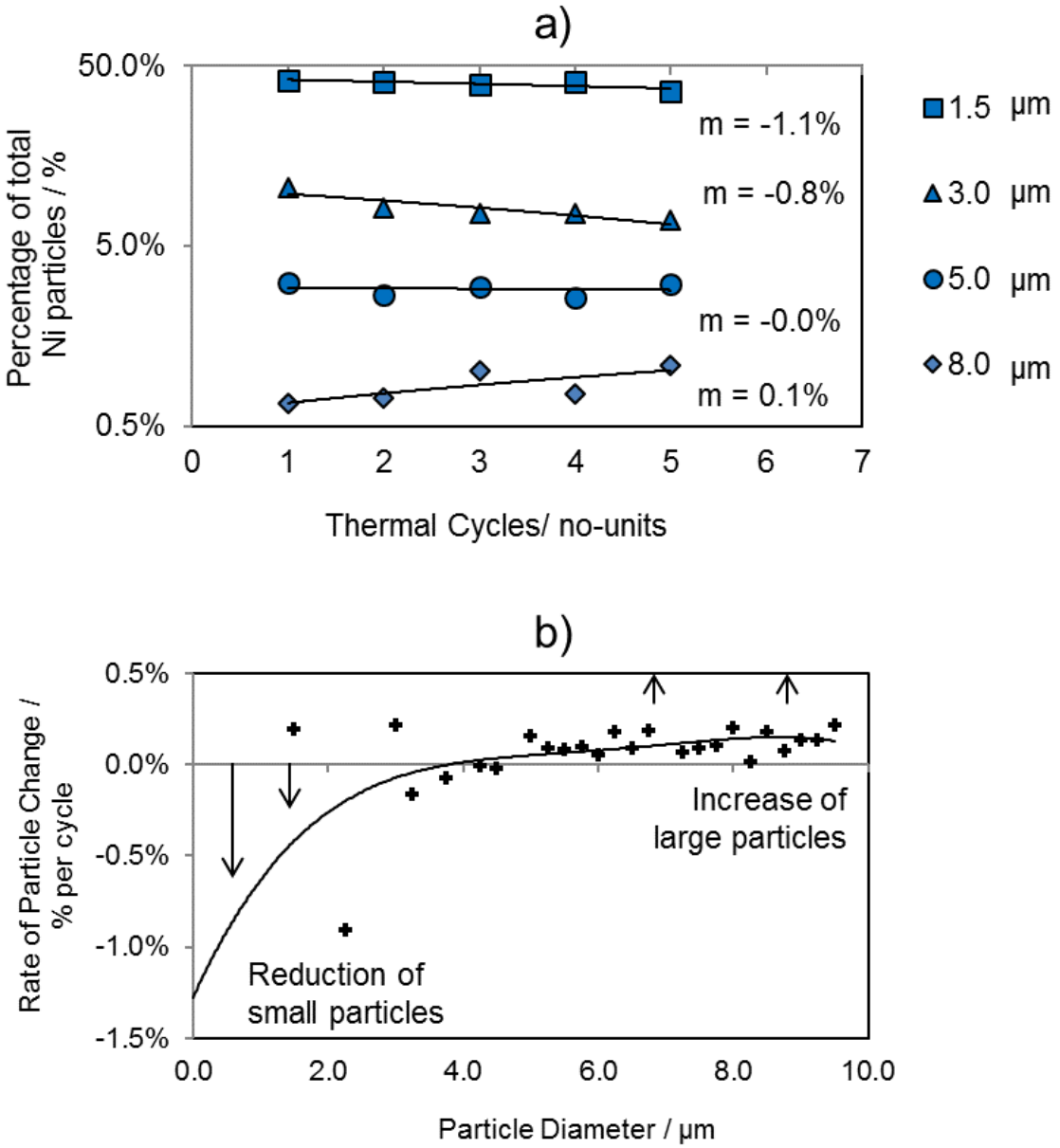

Figure 64 Particle size analysis: a) the percentage of Ni particles between 1.5 – 10 µm with the rate of change with thermal cycling indicated by the gradients 'm' and b) m plotted for a range of particle sizes from 1.5 – 10 µm.

5.4.6. Volume-Specific Surface Area and Interfacial Contact

The volume specific surface areas for the three phases and their volume specific interfacial contact areas are presented in Figure 65. It can be seen that there is a general reduction in particle surface area with thermal cycling; the total surface area after one cycle $\overline{A}_{total}$ = 3.79 μm^{-1} whereas after cycling this reduces to $\overline{A}_{total}$ = 3.10 μm^{-1}. Ni consistently presents the largest specific surface areas ranging from $\overline{A}_{Ni}$ = 1.79 μm^{-1} to 1.37 μm^{-1} likely due to the smaller particle size, but comparable to values presented in literature previously (150). While the large particles of pore and YSZ range from $\overline{A}_{pore}$ = 1.18 μm^{-1} to 0.93 μm^{-1} and $\overline{A}_{YSZ}$ = 1.05 μm^{-1} to 0.80 μm^{-1}.

Inspecting the particle-particle volume specific contact area it can be seen that the ceramic and pore share significantly less contact area than the metal and ceramic and, the metal and pore. The ceramic and pore contact area ranges from 0.24 μm^{-1} to 0.18 μm^{-1}, whereas the metal and ceramic, and metal and pore range from 0.81 μm^{-1} to 0.62 μm^{-1} and 0.85 μm^{-1} to 0.76 μm^{-1}, respectively. The ceramic-pore and metal-pore contact is relatively consistent throughout the thermal cycling, reducing by only 0.06 μm^{-1} and 0.09 μm^{-1}, respectively. Whereas although initially similar to values presented in the literature (28), the metal-ceramic contact reduces by 0.19 μm^{-1}, over triple the ceramic-pore losses and double the metal-pore losses.

It is possible that there are two mechanisms responsible for the reduction in Ni-YSZ contact during thermal cycling: firstly, grain growth leads to Ni diffusing

into the metal bulk, with a general loss of Ni surface area observed as it agglomerates, and secondly, the mismatch in the Ni and YSZ thermal expansion results in deformation consistent with Timoshenko's model (137). The microscopic implications of thermal expansion mismatch between single parties, have been explored elsewhere (45; 46). Moreover, as discussed previously, the agglomeration effects observed here during operational cycling are minor compared to operational dwelling, suggesting TEC mismatch is the dominant mechanism responsible for degradation during cycling.

Finally, the delamination of the metal can be quantified by the reduction of the Ni surface which is in contact with the ceramic. The Ni-YSZ contact reduces by approximately 5 % after the five thermal cycles. However, although delamination occurs consistently after each thermal cycle the degree of delamination appears to not be affected by the thermal ramp rate; a similar magnitude of metal-ceramic delamination is observed after each thermal cycle, a reduction of approximately 1 % per cycle.

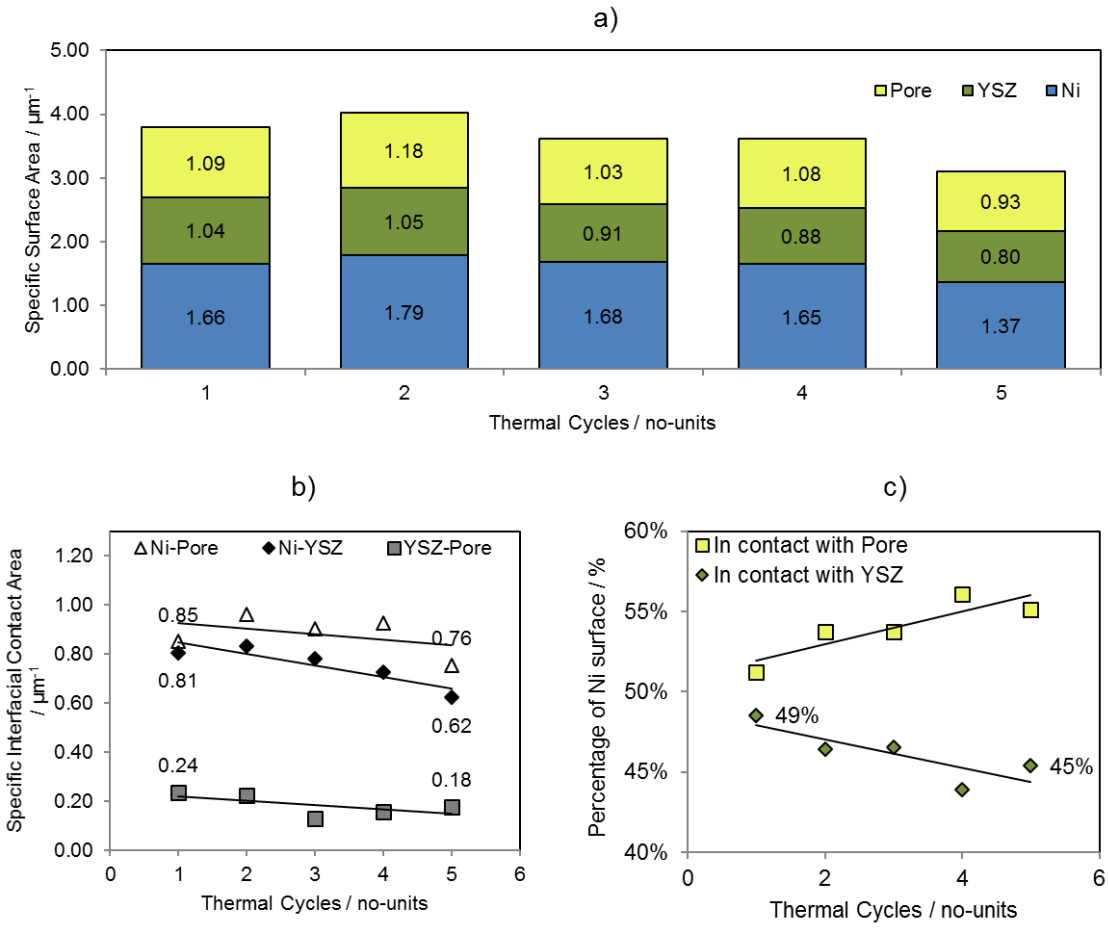

Figure 65 The specific surface and interfacial contact areas for the three phases with thermal cycling: a) the specific surface area for each phase, b) the interfacial contact between the three phases and, c) the change in the percentage of the Ni surface which is in contact with either YSZ or pore.

5.4.7. Reduction of the Bulk TPB Density

Figure 66 displays the TPB map for the same ROI throughout operational thermal cycling. From a purely qualitative inspection of Figure 66 a, it is clear that there is a reduction in the ρ_{TPB} throughout the sample, confirmed quantitatively in Figure 66 b; the reaction site density reduces from 0.93 μm^{-2} to 0.57 μm^{-2} after five thermal cycles, a reduction of ca. - 0.07 μm^{-2} per thermal cycle. Deviations between $\bar{\rho}_{TPB}$ values obtained from TauFactor and MATLAB were negligible throughout, under 1 %.

The TPB percolation was also extracted for each thermal cycle; the first thermal cycle delivered a TPB percolation of 88 %, which increased substantially after the following thermal cycle and remained consistent until the final cycle, at around 92 %. As speculated previously, although the sintering of Ni particles is subtle during operational start-up and shut-down this may provide sufficient mobility to reduce the number of restricted and tortuous pore networks, increasing the population of percolated TPB reaction sites. Values quoted within the literature for the $\bar{\rho}_{TPB}$ and p_{TPB} can be varied; $\bar{\rho}_{TPB}$ values are typically reported to be between 1 – 10 μm^{-2} (96; 61; 150; 57), whereas p_{TPB} percentages can vary between 50 – 90 % (61; 57). Therefore this anode is on the lower end of the reported TPB values compared to the literature but it has also been found that there is a dependency on the resolution (97), therefore direct comparisons to literature values obtained using a different resolution cannot be applied.

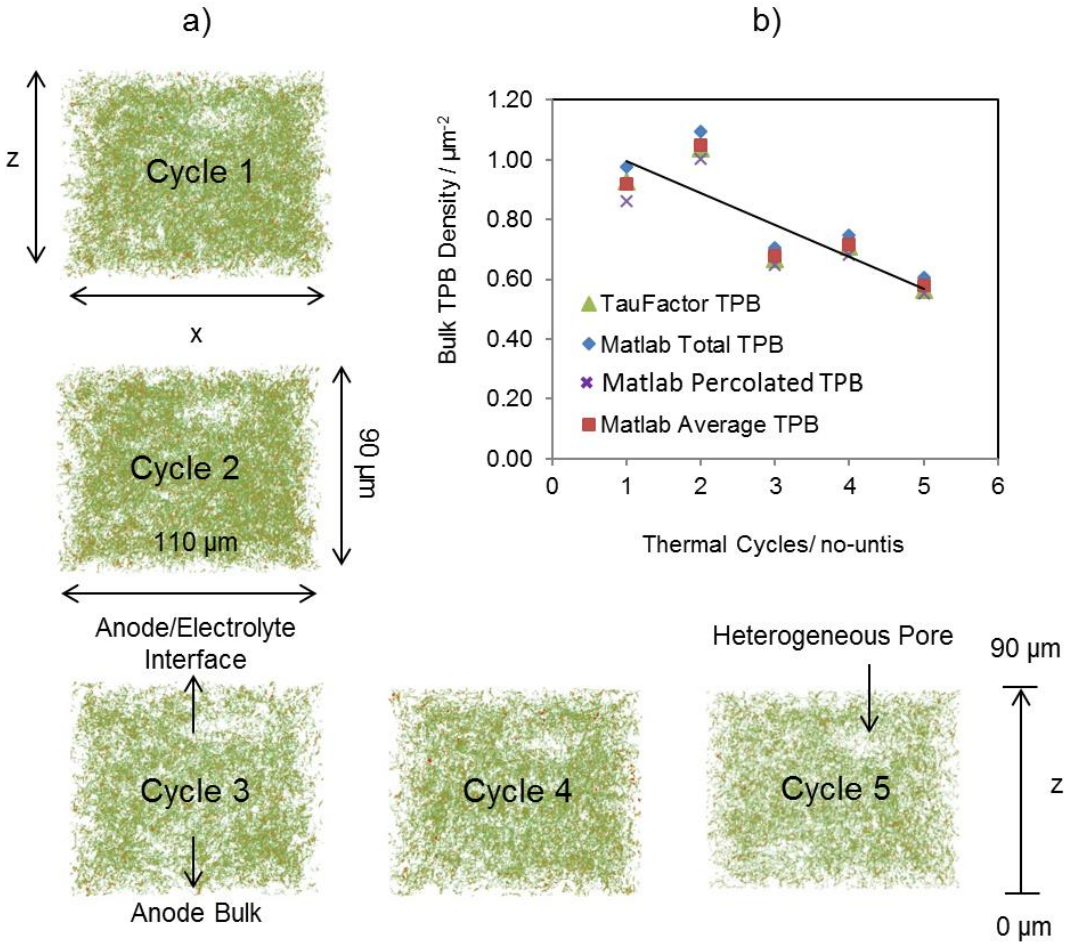

Figure 66 Mapping the triple-phase boundaries within an SOFC anode with thermal cycling: a) the TPB maps for the five thermal cycles, and b) the bulk TPB value within the ROI, with each thermal cycle from several techniques (28; 89)

5.4.8. Spatial Variation of the TPB Density

Another mechanism which is observed is that the TPB density is consistently highest towards the electrolyte, even after thermal cycling. This is demonstrated in Figure 67 where the TPB density was calculated and mapped for the entire volume, then considered on a slice-by-slice basis through the z-plane (as discussed in Chapter 3). This is likely due to an anode functional layer deposited during fabrication. Although, the region of peak TPB density not only reduced in magnitude but also broadens and retracts away from the interface into the bulk. This suggests that the electrochemical reaction site density increases inhomogeneity during cycling, reducing the distinction between the functional and bulk anode layers. Literature has previously reported the reduction of reaction sites near the anode/electrolyte interface along with the retraction of the reaction zone (151).

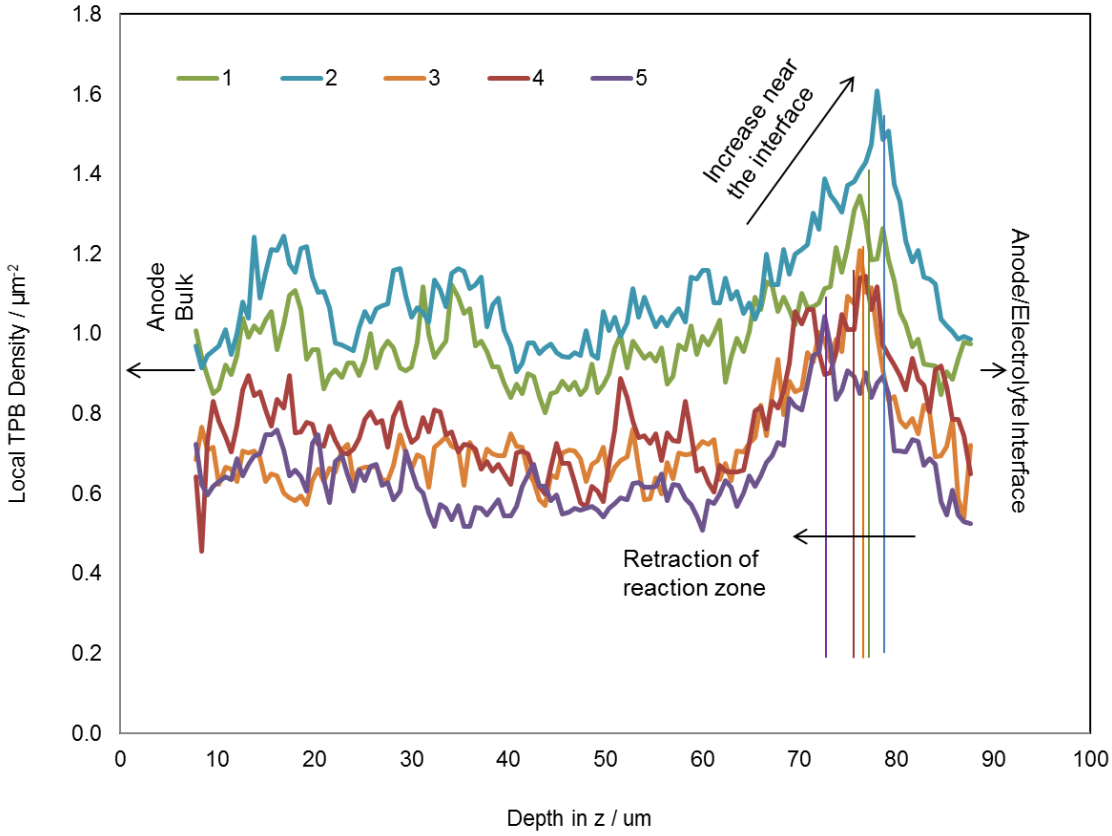

Figure 67 Mapping the triple-phase boundaries within an SOFC anode with thermal cycling: the local TPB value for each thermal cycle.

5.4.9. Identifying the Causes for the Reduction in TPB Density

To inspect the mechanisms responsible for the reduction in the TPB density with thermal cycling Figure 68 displays the first (black) and last (red) TPB density data collected from the SOFC anode for a slice-by-slice comparison. As discussed within the previous section (5.4.8) the TPB density presents a reduction throughout the entire volume, but retains a similar line profile that peaks towards the anode/electrolyte interface; however, this peak is observed to retract into the anode after cycling. This plot can now be used as a reference in order to compare the changes in the extracted metrics such as composition, interfacial particle contact and particle size to the reduction in TPB density.

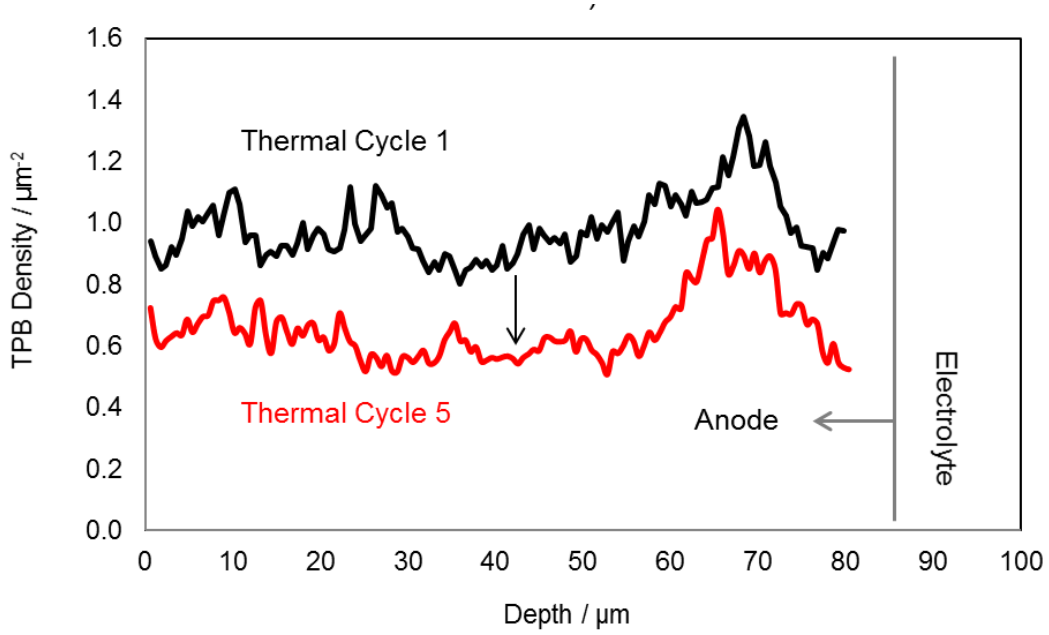

Figure 68 A direct slice-by-slice comparison of an SOFC anode before and after thermal cycling inspecting the reduction in the TPB density.

The compositional data displays minimal change after cycling for all three phases, inherently retaining very similar line profiles, Figure 67. Whereas the TPB density displays a net reduction throughout the sample, Figure 68. This consistency in composition suggests that compositional variation, triggered by thermal cycling have a negligible effect on TPB density.

In order to inspect the influence of sintering effects on the reduction in the TPB density, Figure 70 displays the reduction in the number of parties smaller than 1 µm in diameter with respect to the location within the cell. Overlaid on this plot is the reduction in TPB density, *i.e*. the difference between the black and red lines plotted in Figure 68, also plotted with respect to the location within the cell, ca. 90 µm is the location of the anode/electrolyte interface and 0 µm is towards the anode bulk. The figure broadly displays a similar trend for the reduction in small particles and reduction in TPB density, however, significantly disparities are also presented; although an increased loss of TPB density can typically be seen in regions where there is also an increased loss of small particles, and vice-versa, several regions present the opposite; significant reduction in the number of small particles not accompanies by a substantial reduction in TPB density. This suggests that, although agglomeration effects may influence TPB density loss, during operational thermal cycling, i.e. ramping to/from temperature rather than dwelling at operating temperature, agglomeration effects are likely insignificant compared to another, more dominant mechanism(s).

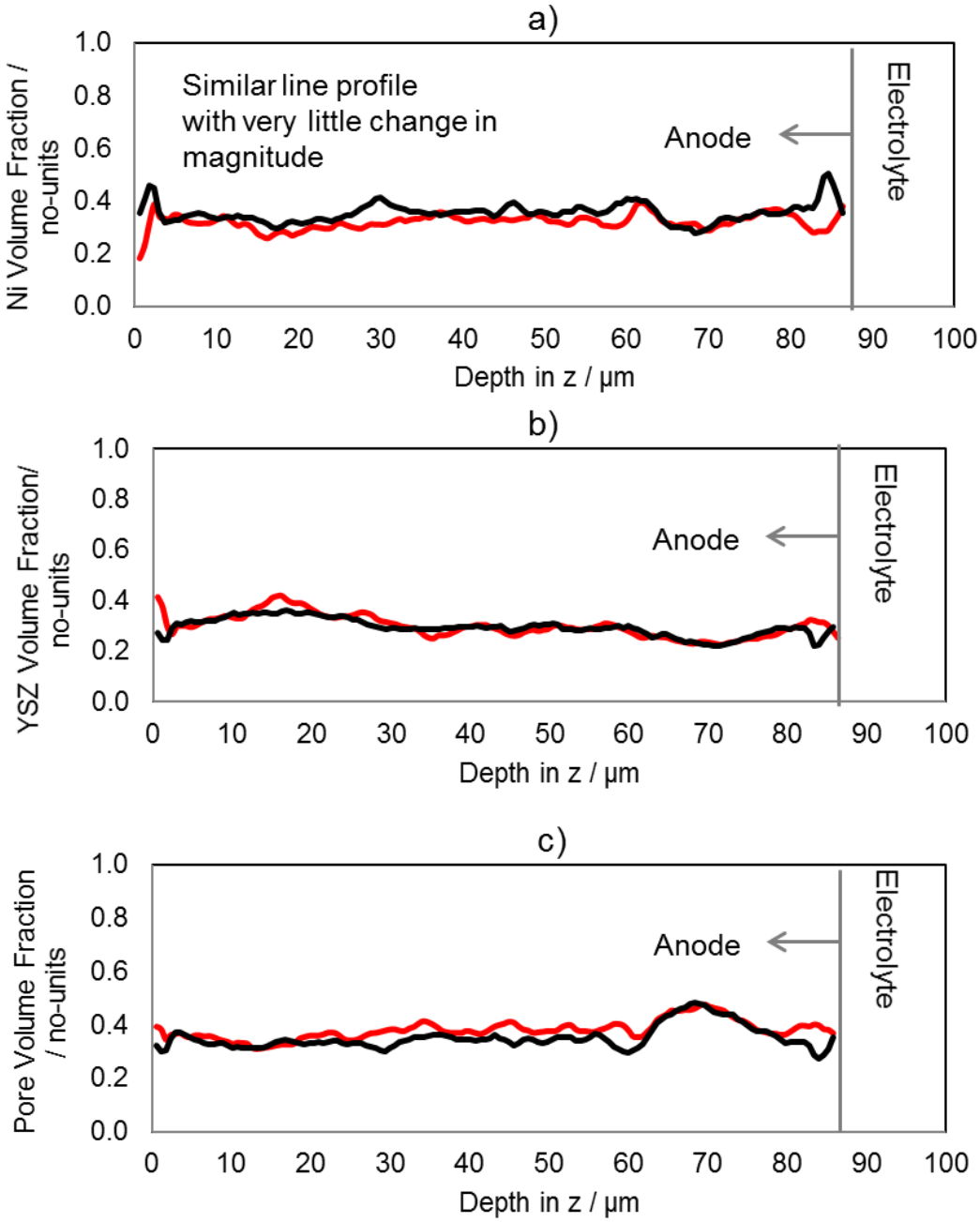

Figure 69 A direct slice-by-slice comparison of an SOFC anode before and after thermal cycling inspecting the reduction in the composition.

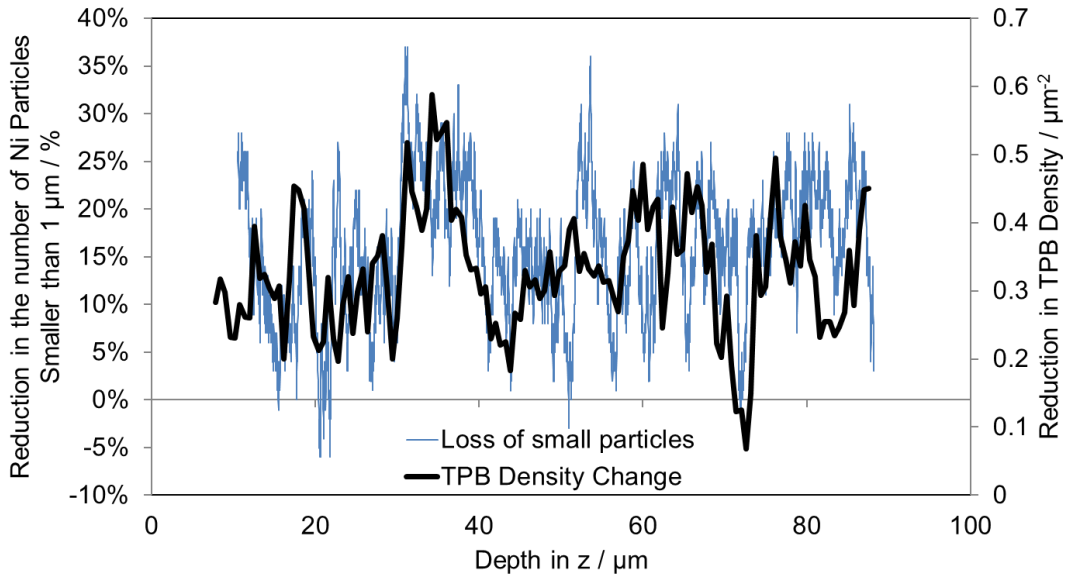

Figure 70 Correlating the sintering effects to the reduction in the TPB density: primary y-axes displays the reduction in the number of Ni particles smaller than 1 µm and the secondary y-axes displays the reduction in the TPB density both plotted with respect to the electrode depth (ca. 90 µm is the location of the anode/electrolyte interface).

One such mechanism may be the particle-particle delamination. Therefore to explore this, the same plot as Figure 70 was produced but for the reduction in Ni-YSZ specific surface contact (Figure 71). Unlike the agglomeration profile in Figure 70, the particle delamination profile in Figure 71 displays a significantly closer profile to the TPB density reduction; generally, regions of substantial particle-particle delamination are accompanied by signification TPB loss. This suggests that delamination affects may be more dominant than that of

agglomeration during operational thermal cycling. This has been previously predicted with the use of advanced computational models based upon morphological operations applied to X-ray CT data of tubular SOFC anodes (28).

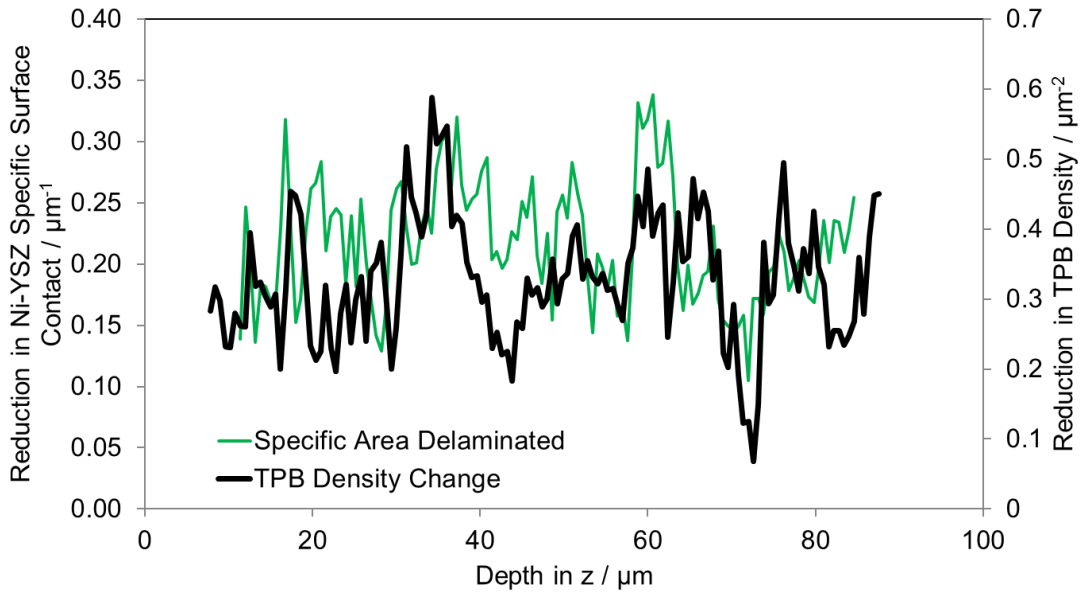

Figure 71 Correlating the reduction in the specific interfacial contact area to the reduction in the TPB density: primary y-axes displays the reduction in the specific interfacial contact area between Ni and YSZ , and the secondary y-axes displays the reduction in the TPB density both plotted with respect to the electrode depth (ca. 90 µm is the location of the anode/electrolyte interface).

In order to decouple the influence of the sintering and delamination, the reduction in the number of small particles and the reduction in the Ni-YSZ specific surface contact are both plotted with respect to the loss of TPB density in Figure 72 and

Figure 73 respectively. By doing so it is revealed that there is a fairly neutral correlation between the degree of agglomeration; a linear line of best fit has a gradient near zero, horizontal. Furthermore, there is significant scattering, i.e. low correlation, particularly for regions of significant agglomeration.

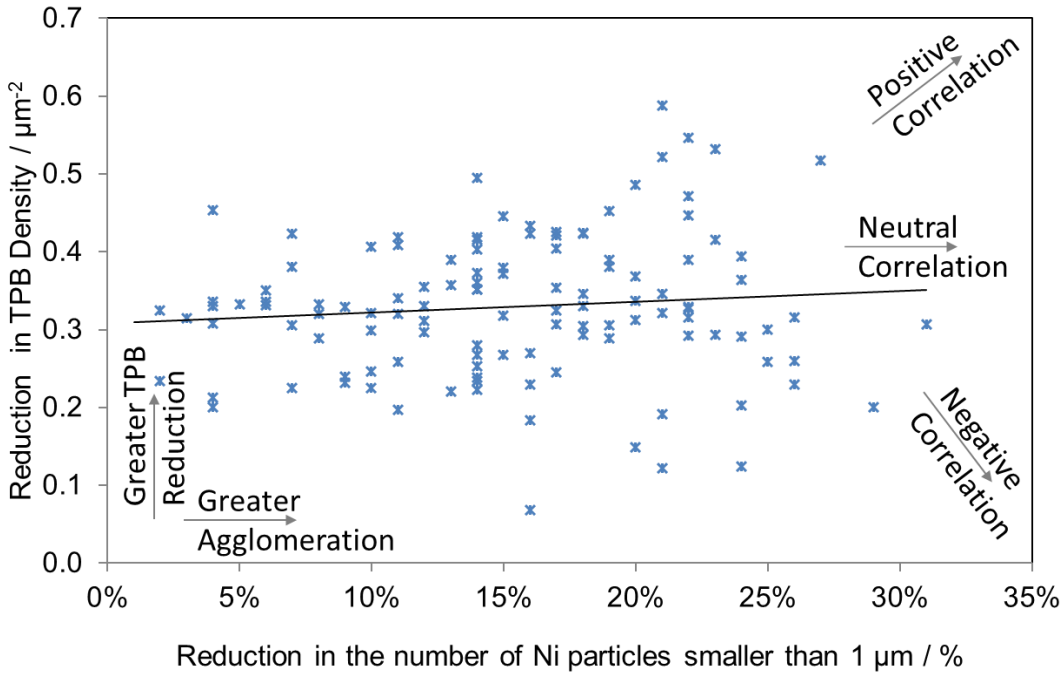

Figure 72 Correlating sintering effects to the reduction in the TPB density: the reduction in the number of small particles plotted against the reduction in the TPB density.

Considering the effects of delamination, from Figure 73 it is clear that the degree of delamination is more influential on the loss of TPB density than the degree of sintering as the linear line of best fit has a gradient above zero. Similar to Figure 72, there is also a degree of scattering (poor correlation) observed in Figure 73.

However, unlike Figure 72, the degree of scattering in Figure 73 does not change significantly with increasing delamination.

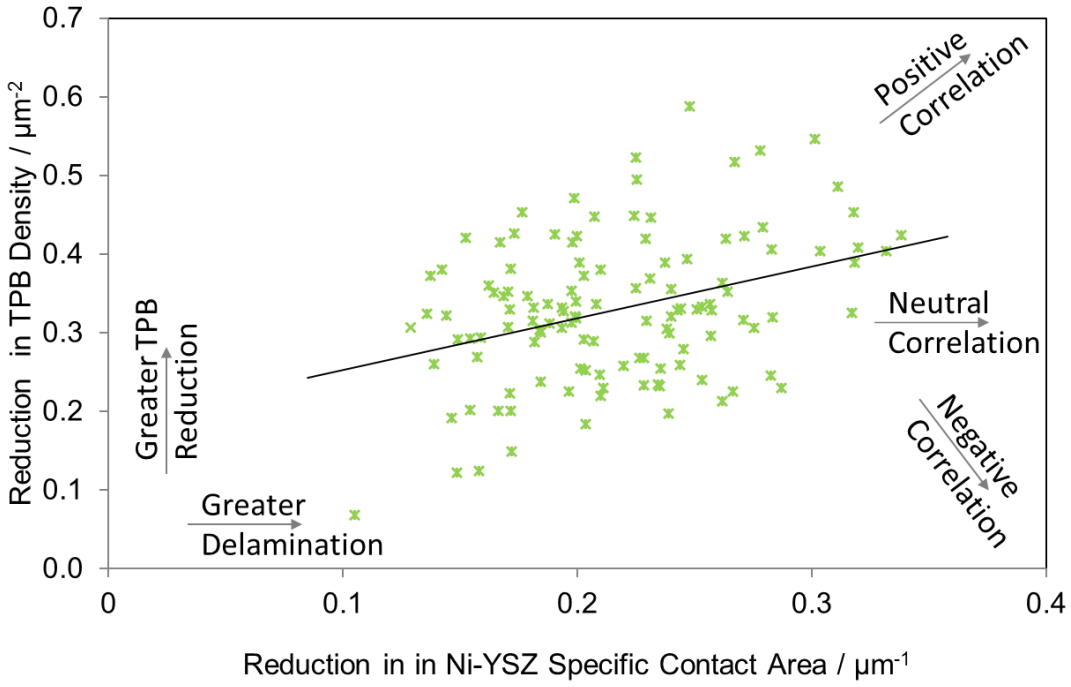

Figure 73 Correlating delamination effects to the reduction in the TPB density: the reduction in the Ni-YSZ particle-particle contact plotted against the reduction in the TPB density.

These two figures confirm the complexity of the degradation responsible for TPB loss during operational start-up and shut-down. Here, delamination is found to be the dominant mechanisms for TPB loss; however, as sintering effects become more severe during long-duration operational dwelling, this may reverse as the population of small particles diminishes.

5.4.10. Control Variables and Scope for Future Work

To examine the effects of operational start-up time, the peak operating temperature, dwelling time at operating temperature and thermal cooling rates were kept consistent. Future studies may investigate the effects of the peak operating temperature, dwell time at operating temperature and thermal cooling rates but these results suggest that the thermal heating-rate does not have a significant effect on the interaction between Ni and YSZ particles at a microscopic scale whereas, the number of thermal cycles does appear to influence the degree of delamination and should therefore be minimised. However, two points should be considered before reducing the number of thermal cycles: firstly, reducing the number of thermal cycles may increase the duration at temperature, possibly intensifying what are currently insignificant agglomeration effects, secondly the macroscopic implications of high ramp-rates may be more prominent i.e. delamination of the electrolyte from the anode (153).

5.4.11. Conclusions from Microstructure Investigations

This work concludes a two-part study on thermally induced macro- and microstructural degradation within SOFCs. The properties which are thought to influence the electrochemical performance within SOFC anodes have been quantified and monitored for the same ROI throughout the operational thermal cycling of a Ni-YSZ cermet anode sample from an anode-supported SOFC.

Through the use of the electrolyte and surrounding space as greyscale-fiducial references each dataset was segmented with sufficient confidence for comparison. It is seen that the compositional volume fractions follow very similar profiles within the anode throughout thermal cycling, with the ceramic content deviating by negligible amounts and minor variation in the Ni and pore composition possibly being attributed to the mobility of Ni at elevated temperatures. Alignment of the sample produced a direct comparison between datasets allowing the correlation of degradation mechanisms to prominent microstructural metrics such as particle size, tortuosity-factor, percolation and surface area. The reduction in the number of small Ni particles is observed with thermal cycling; although, the sintering effects are minimal compared to the long-duration operational dwelling. Substantial reduction is observed in the pore-phase tortuosity-factor after a low ramp-rate thermal cycle, accompanied by a significant 4 % increase in percolation. This evolution is attributed to the Ni mobility due to a longer duration at temperature. Although the tortuosity-factor values in the x- and z-planes displayed very similar values for all datasets, consistent deviation is observed in the y-plane suggesting non-uniform degradation mechanisms parallel to the anode/electrolyte interface, possibly due

to a fabrication defect. The delamination of the Ni and YSZ appears to be independent of the thermal ramp rate; a similar magnitude of approximately 1 % reduction of the Ni-YSZ contact surface area is observed after each thermal cycle. Finally the effects Ni sintering and Ni-YSZ delamination on the loss of TPB density are assessed on a slice-by-slice basis; both mechanisms correlate closely with the loss in electrochemical performance but for operational thermal cycling, delamination proves more detrimental to electrochemical performance.

As discussed previously, similar to how the degradation of this cell spanned multiple length scales, the crystal-structure within the Ni lattice is also expected to demonstrate changes with degradation therefore the following section will explore the crystallographic information that is obtained from Ni-based SOFC anodes materials with operational thermal cycling.

5.5. Crystallographic Degradation Assessed Using XRD

5.5.1. An Introduction to Crystallographic Degradation

Although the crystallography of pure Ni is well-understood (34; 35; 36; 37; 38; 39; 40) the influence of ceramic addition has been the subject of increased research in recent years and still requires further understanding (41; 33; 74; 154; 155; 156). For instance, non-uniform thermal expansion within SOFCs is a known cause of unfavourable strain distribution (41; 33) therefore, the location and cause of any non-linear expansion is of interest in mitigating mechanical degradation in the form of delamination and cracking, and the subsequent loss in electrochemical performance. The Curie point is the temperature that is thermodynamically sufficient to disrupt dipole alignments causing a magnetic transition from ferromagnetism to paramagnetism. This transition results in a well-documented non-linearity in the Ni thermal expansion coefficient (TEC) understood (34; 35; 36; 37; 38; 39; 40); although, the temperature at which metals are able to exhibit ferromagnetism is thought to be sensitive to the level of strain to that the material is subjected to (157), and correlation has also been observed between the sintering conditions and the Néel temperature (158).

Studies using macroscopic techniques such as dilatometry have suggested that bulk non-linearity is suppressed to insignificant values by the addition of the supporting ceramic backbone (40). However, the microscopic interactions between the metal and ceramic phases (at the TPB) are thought to be of great thermo-mechanical importance (45) and it has been suggested by techniques such as thermal mechanical analysis (TMA) that the non-linear expansion of the metallic phase may remain regardless of the presence of the

ceramic (129). This has been demonstrated in the previous section of this chapter (Section 5.2) where the TPB density was observed to decrease with thermal cycling even before substantial macroscopic degradation could be observed in the macrostructure. Furthermore, long-duration operation can cause undesirable agglomeration further reducing the TPB density (130; 159). Ni is also known to undergo thermally driven deformation (TDD) in the form of mechanical creep observed through lattice hysteresis during thermal cycling, thought to be attributable to temperature-triggered stress relaxation due to lattice distortions and imperfections held in residual stress within the metal (41). Improved understanding of these mechanisms is required.

5.5.2. XRD Investigation Procedure

This section investigates three commonly employed SOFC anode materials examined via synchrotron powder XRD: Ni (Novamet Specialty Products Corp, Lebanon), Ni-YSZ (Fuel Cell Materials, OH, USA) and Ni-GDC (Fuel Cell Materials, OH, USA). The zirconia powder was supplied with 8 mol% yttria content, 8YSZ, and the ceria powder was supplied with 10 mol% gadolinia doping, 10GDC. Both cermet materials, Ni-YSZ and Ni-GDC, were supplied with a 60:40 composition of metal to ceramic by weight, and the ceramic-free powder is supplied at 99.6 % purity with the residual volume consisting of 3000 ppm oxygen, 800 ppm iron, 30 ppm carbon and 30 ppm sulphur.

Initially, powders were formed into cylindrical pellets by iso-static pressing as discussed in the methodology (Section 3.2) and subsequently sintered at 1200 ºC for 2.5 Hours in air. The pellets were then reduced in forming gas (4 % H_2 in 96 % N_2) for 2 hours at 800 ºC; reduction of NiO to Ni was confirmed with Raman spectroscopy, see Figure 74 a. The reduced pellets were then ground into powders using diamond files and inserted into open-ended quartz capillary tubes, 10 cm in length with internal diameter of 580 µm.

Crystallographic investigations were conducted at the X04SA-MS beamline (108) (Swiss Light Source, Paul Scherrer Institute, Switzerland). The samples within the capillary tubes were inserted into a goniometer head (HUBER Diffraktionstechnik GmbH & Co. KG, Germany) via a brass button seal, and positioned perpendicular to the X-ray beam with a hot-air blower was placed below the capillary tube, coincident with the X-ray beam, in order to collect XRD patterns at elevated temperatures. To increase the accuracy of temperature

recordings a thin, high precision thermocouple (ca. 250 µm in diameter) was inserted into the capillary, until coincident with the horizontal X-ray beam and vertical hot-air blower. Further information on this characterisation method can be found in the methodology (Sections 3.3 and 3.7).

To prevent oxidation of the samples, premixed gas (5 % H_2 in 95 % N_2) was passed over the sample at a continuous rate of 25 mL min^{-1}. All XRD patterns were collected at two theta angles from -60º to +60º at 26 keV (0.4788 Å) using a MYTHEN II (microstrip system for time-resolved experiments) detector covering 120º with over 60,000 channels on a double layer for a 0.0036º intrinsic resolution (microstrip system for time-resolved experiments) at an exposure of 60 seconds per detector.

For reference, XRD patterns of the empty capillary were collected for all temperatures. A background removal was also applied to all patterns before extracting lattice parameters of interest (160). Ni and NiO peak intensities are compared in Figure 74 b to confirm no re-oxidation of the Ni during thermal cycling, one thermal ramp is presented here but this was conducted for all data sets. A corrected Ni-YSZ pattern is displayed in Figure 75 a with Ni peak locations compared to a reference for several crystallographic indices displayed in Figure 75 b (41). Very minor deviations were observed achieving a coefficient of determination close to unity $R^2 = 0.998$.

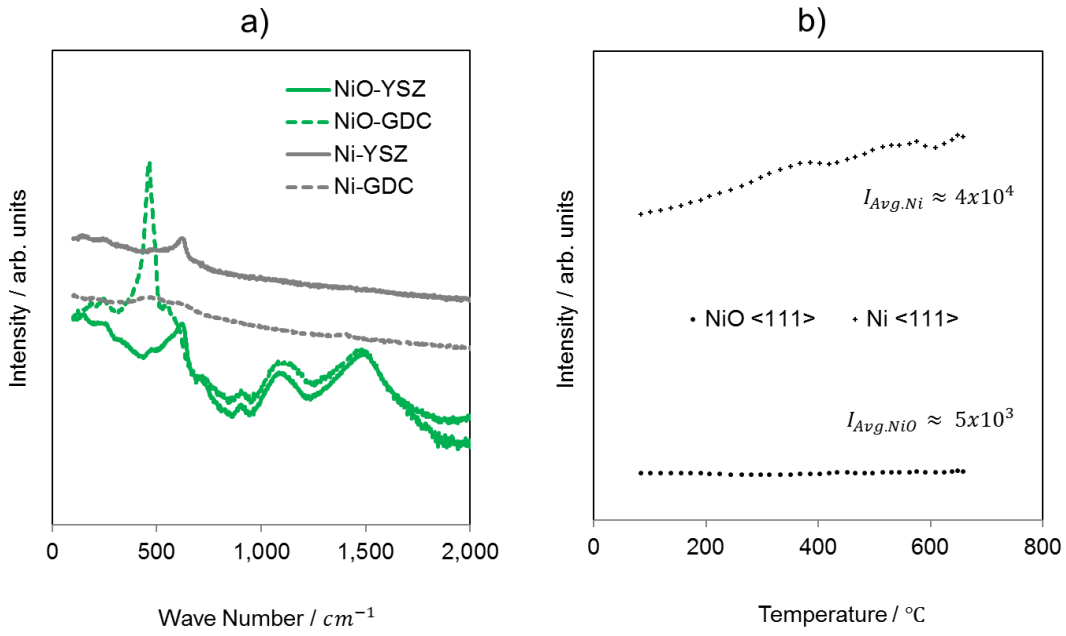

Figure 74 Ensuring sample quality during fabrication and during thermal cycling for Ni-YSZ and Ni-GDC: a) pre- and post-reduction Raman pattern, and b) Ni and NiO peak intensities plotted with respect to temperature.

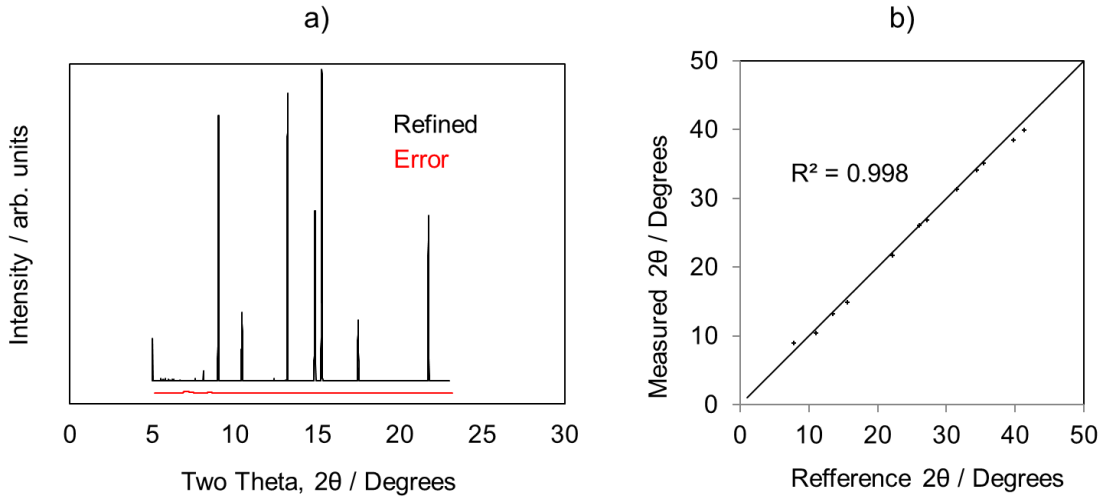

Figure 75 Confirmation of XRD data quality: (a) corrected pattern from a Ni-YSZ XRD, and (b) Ni peak locations with comparison to a reference for several crystallographic orientations with coefficient of determination R^2 = 0.9998 (41).

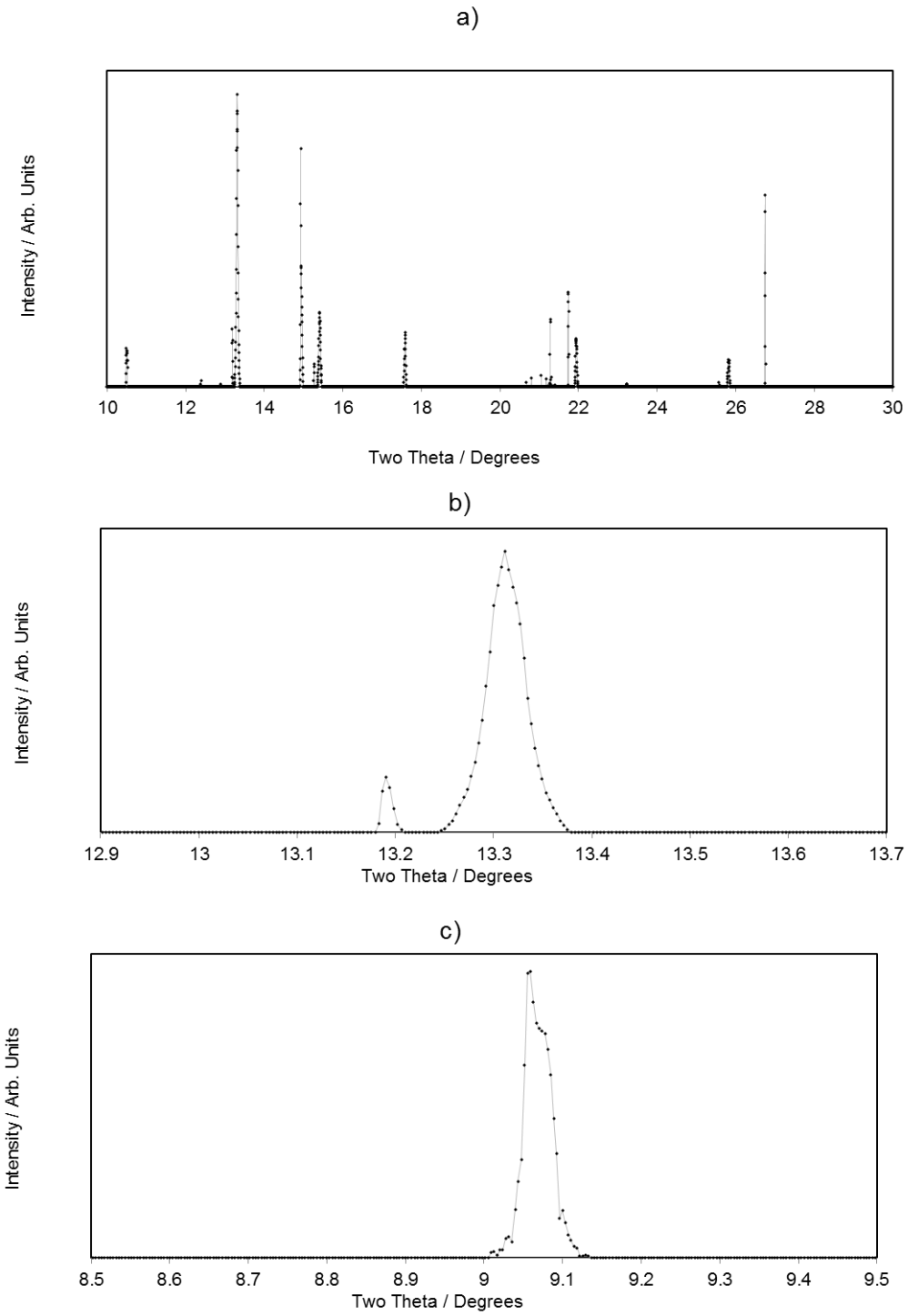

Figure 76 Raw diffraction patterns collected from a Ni-YSZ powder sample.

Firstly, XRD patterns were collected through both heating and cooling during one thermal cycle for each of the three materials: Ni, Ni-YSZ and Ni-GDC. Patterns were collected continuously resulting in one pattern every two minutes at a ramp rate of ca. 10 ºC min^{-1} from ca. 100 ºC to 650 ºC and back to 100 ºC; equating to ca. 2 hours of data acquisition per sample. These data sets were collected to inspect hysteresis and non-linearity in the Ni phase. Further XRD patterns were collected from fresh samples over an additional thermal cycle for the Curie transition ca. 250 ºC to 550 ºC for the three materials using a reduced ramp-rate of 5 ºC min^{-1}.

Extended thermal cycling was then conducted on a Ni-YSZ sample. One thermal cycle was conducted at ca. 10 ºC min^{-1}, followed by four additional thermal cycles at an accelerated stress-test rate of ca. 60 ºC min^{-1}. For these high ramp rates, data were collected only at 100 ºC and 600 ºC, i.e. no data was collected during thermal ramping. Temperature was held constant during data collection to allow enough dwell time for thermal equilibrium to be reached, ca. 25 mins. Sample preparation, data acquisition and thermal cycling information can be found in Table 38, Table 39 and Table 40.

The lattice parameters, thermal strains and thermal stresses for three orientations of Ni: <111>, <200> and <220> were obtained sequentially from the thermal cycle of each material: Ni, Ni-YSZ and Ni-GDC. It is important to consider multiple orientations because, unless oxidized, Ni should retain a face-centred cubic (FCC) structure throughout each data acquisition, i.e. independent of ceramic addition, resulting in an isotropic expansion and contraction with temperature change although, it has been previously proven that this is not

necessarily the case for non-isothermal environments (73). Therefore by examining these three families of Miller indices, as visualized in Figure 77, any non-isotropic effects of ceramic addition can be examined.

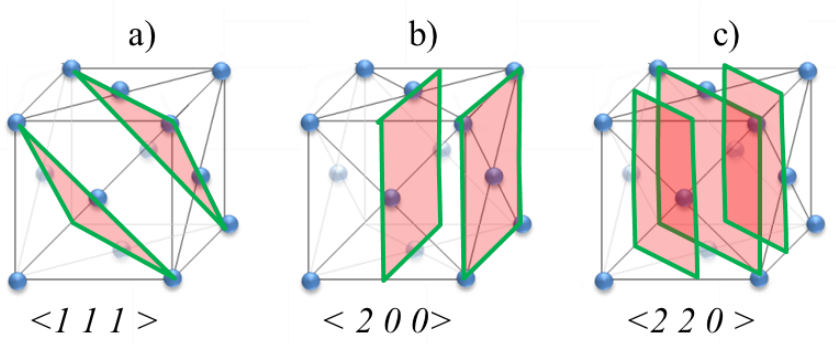

Figure 77 Three families of Miller indices for the crystallographic investigations of Ni metal using XRD.

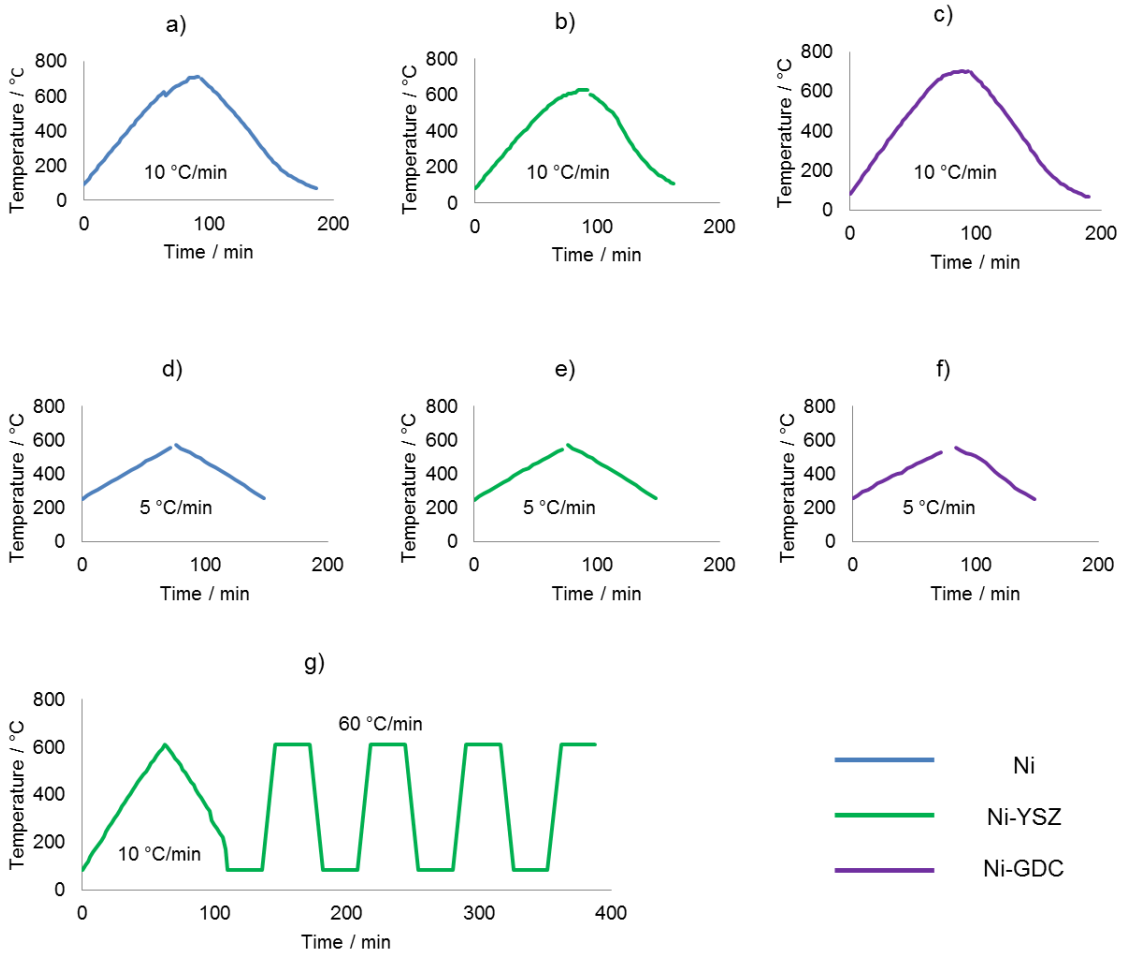

Figure 78 Thermal cycling profiles for the synchrotron XRD experiments: a – c) single thermal cycle to operating temperature at 10 °C min^{-1}, d – f) single thermal cycle through the Curie point of Ni, and g) accelerated stress test on a Ni-YSZ sample, 10 °C min^{-1} for the first cycle followed by 60 °C min^{-1} for the four following that. Throughout blue, green and purple correspond to Ni, Ni-YSZ and Ni-GDC respectively.

Table 38 Experimental procedure for chapter section 5.5: Crystallographic Degradation: Influence of ceramic choice, non-linear expansion and stress-test cycling.

Sample	Preparation
All	Powder pressed into pellets; Sintered 1200 °C 2.5 hrs in air; Reduced 800 °C 2 hrs in forming gas (4% H_2 in 96 % N_2); Filed into powder using a diamond file Inserted into separate capillaries with; 580 µm internal diameter 10 cm in length
S531	Capillary filled with Ni powder
S532	Capillary filled with Ni-YSZ powder
S533	Capillary filled with Ni-GDC powder
S534	Capillary filled with Ni powder
S535	Capillary filled with Ni-YSZ powder
S536	Capillary filled with Ni-GDC powder
S537	Capillary filled with Ni-YSZ powder

Table 39 Data collection conditions for chapter section 5.5: Crystallographic Degradation: Influence of ceramic choice, non-linear expansion and stress-test cycling.

Sample	Study	Data	Instrument	Exposure Time / s	Intrinsic Resolution / deg
S531	I531 Single Thermal Cycle of SOFC anode materials	D531	X04SA-MS Beamline	60 per detector	0.0036º
S532		D532			
S533		D533			
S534	I532 Inspecting the Curie transition temperature	D534			
S535		D535			
S536		D536			
S537	I533 Ni-YSZ accelerated stress-test	D537			

Table 40 Thermal cycling conditions for chapter section 5.5: Crystallographic Degradation: Influence of ceramic choice, non-linear expansion and stress-test cycling.

Sample	Study	Data	Thermal cycling conditions during data acquisition
S531	I531	D531	One thermal cycle per sample
S532	Single Thermal Cycle of	D532	Thermally cycled from 100 ºC to 650 ºC
S533	SOFC anode materials	D533	Ramp-rate at 10 ºC min^{-1}
S534	I532	D534	One thermal cycle per sample
S535	Inspecting the Curie	D535	Thermally cycled from 250 ºC to 550 ºC
S536	transition temperature	D536	Ramp-rate at 5 ºC min^{-1}
S537	I533 Ni-YSZ accelerated stress-test	D537	One thermal cycle from 100 ºC to 600 ºC Ramp-rate at 10 ºC min^{-1} No dwell at temperature Four cycles from 100 ºC to 600 ºC Ramp-rate at 60 ºC min^{-1} 25 min dwell at temperature per cycle

5.5.3. The Influence of Ceramic Addition to Ni Expansion

The lattice parameters, thermal strain and thermal stress for three orientations of Ni: <111>, <200> and <220>, are obtained from the thermal cycle of each material: Ni, Ni-YSZ and Ni-GDC. The lattice parameters display close similarity with those presented previously (34; 35; 36; 37; 38; 39; 40), and the thermal stress, calculated using the Young's modulus values reported by Pihlatie et al. (128), also show good agreement with related work (41).

First, we consider the ceramic-free Ni sample, and examine the crystallographic information obtained from Ni without the influence of a constraining ceramic skeleton (Figure 79, Figure 80 and Figure 81). The lattice expansion and contraction patterns display very similar values for heating and cooling, as do the three crystallographic orientations; suggesting that an FCC structure is maintained throughout the temperature range examined. Non-linearity and subtle hysteresis is seen near the Curie temperature of Ni, c.a. 354 ºC, but with the exception of the Curie temperature distortion, the resulting strain variation displays a near-linear trend with the lattice parameters returning to a very similar value after the thermal cycle to that which was seen before thermal ramping, 3.525 Å.

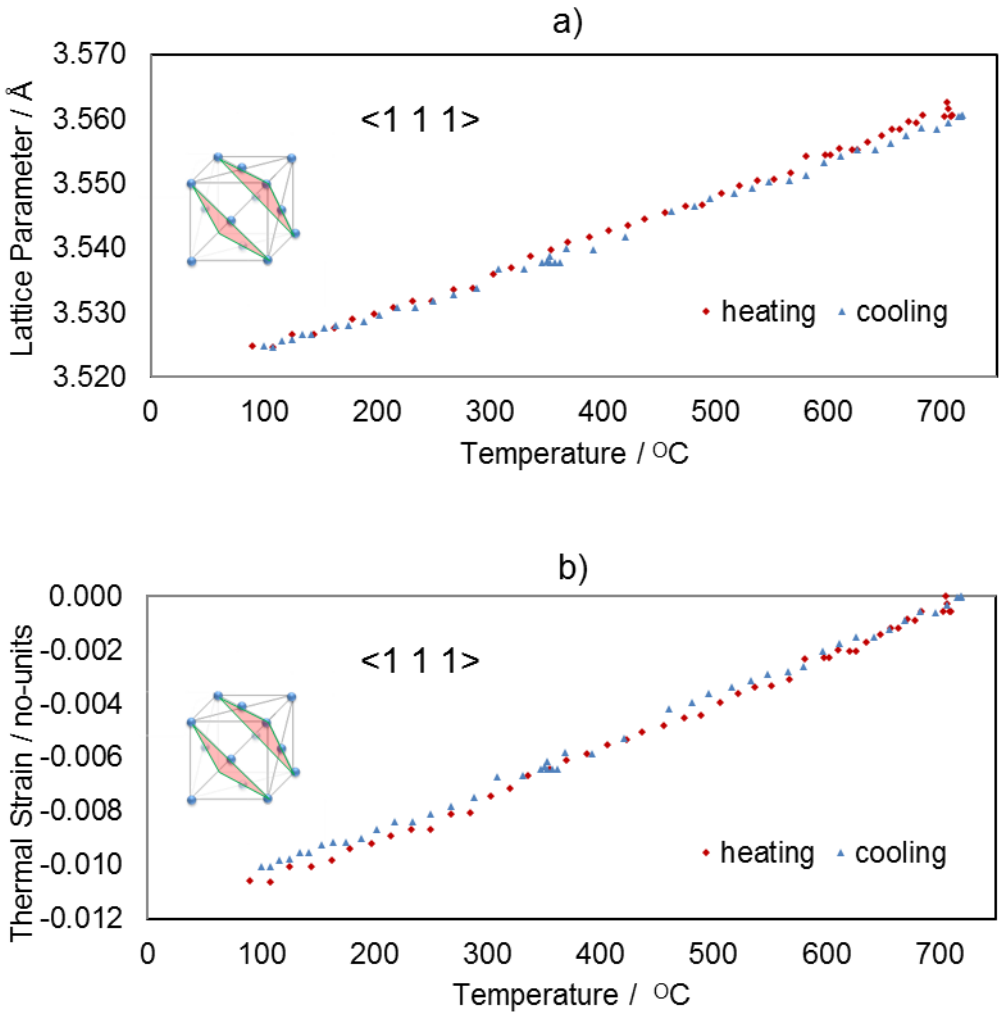

Figure 79 Crystallographic information obtaining from Ni within ceramic-free Ni for the <111> using synchrotron powder XRD at 26 keV: a) lattice and, b) strain variation with temperature.

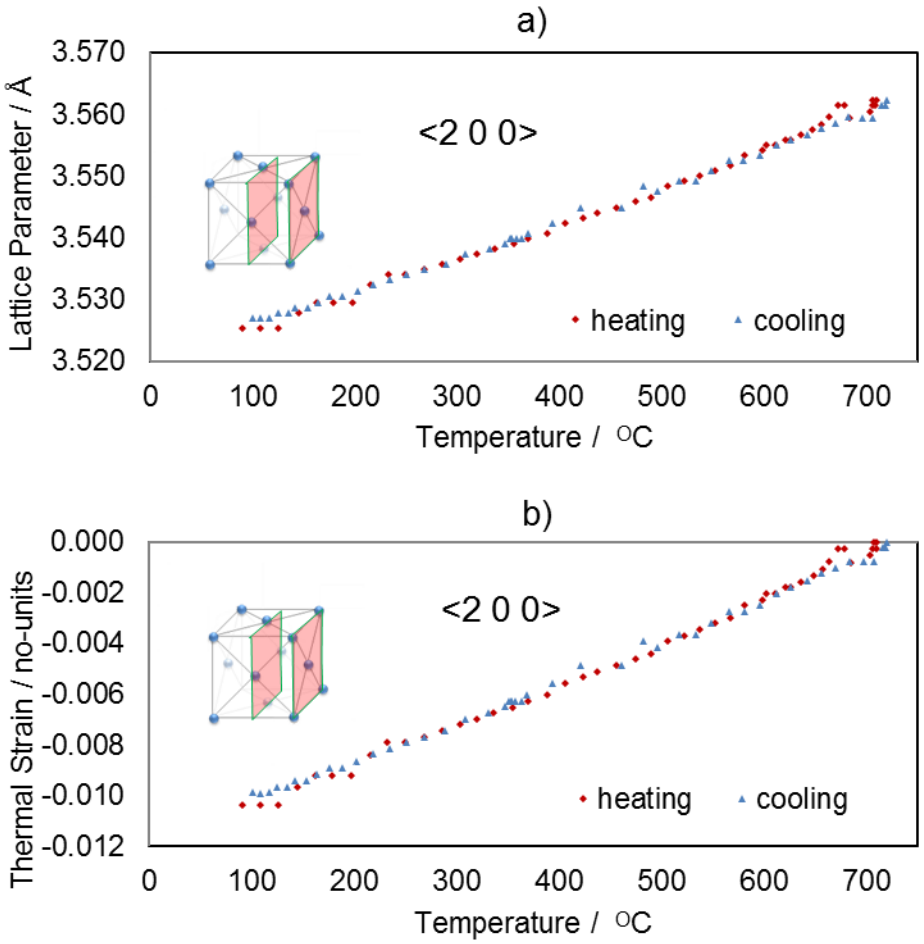

Figure 80 Crystallographic information obtaining from Ni within ceramic-free Ni for the <200> using synchrotron powder XRD at 26 keV: a) lattice, and, b) strain variation with temperature.

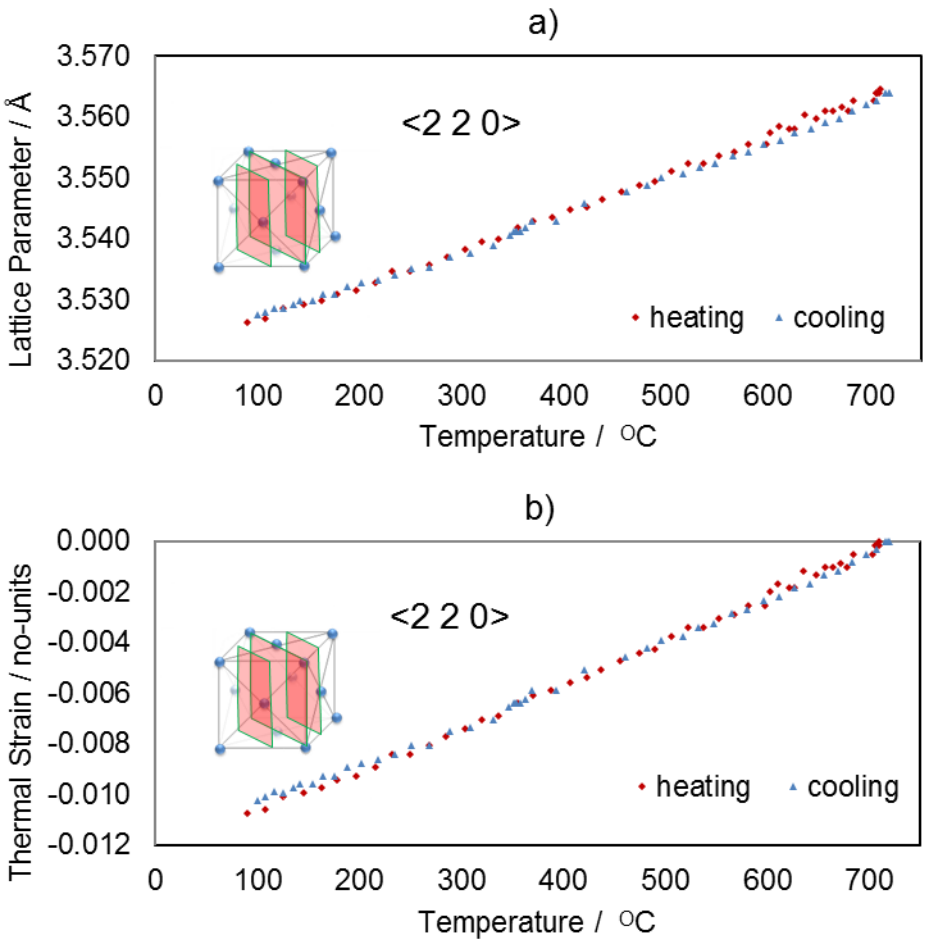

Figure 81 Crystallographic information obtaining from Ni within ceramic-free Ni for the <220> using synchrotron powder XRD at 26 keV: a) lattice and, b) strain variation with temperature.

Secondly, we examine the Ni lattice expansion within a composite material of Ni and YSZ (Figure 82, Figure 83 and Figure 84). Similarity in the lattice patterns for the three orientations again suggests a FCC structure is maintained throughout the temperature range examined. Non-linearity and hysteresis is again seen near the Curie temperature of Ni although within the cermet material the hysteresis appears to extend to temperatures above the Curie point. This is possibly a result of the interaction between the metal and ceramic during this transition; ceramic materials have previously been reported to influence the Ni expansion causing deviation from linearity (161). Away from the Curie temperature the resulting strain variation again displays relatively linear expansion and contraction with the lattice parameters returning to a similar value after the thermal cycle to that which was seen in the ceramic-free sample.

Thirdly, crystallographic information of Ni is examined within the Ni-GDC cermet (Figure 85, Figure 86 and Figure 87). Away from the Curie point, relatively linear strain is observed, but notable deviation is observed between the three lattice orientations, particularly about the Curie point and at the highest temperatures examined. Furthermore, large hysteresis looping is seen, primarily within the <111> orientation, although the lattice parameters observed after the single thermal cycle are similar to that seen in both the YSZ cermet and ceramic-free samples.

The Ni lattice parameters displayed here present near-elastic cycling in all three samples; the room-temperature lattice parameters before and after thermal cycling deviate in insignificant amounts over a single cycle. However, it is conceivable that what is considered negligible deviation over a single thermal

cycle could accumulate to significant amounts over prolonged operational cycling. Moreover, undesirable expansion in the form of non-linearities may result in an increased population of dislocations within the crystalline structure. It is therefore important to understand the effects of ceramic addition to the metal lattice dynamics about any non-linear expansion.

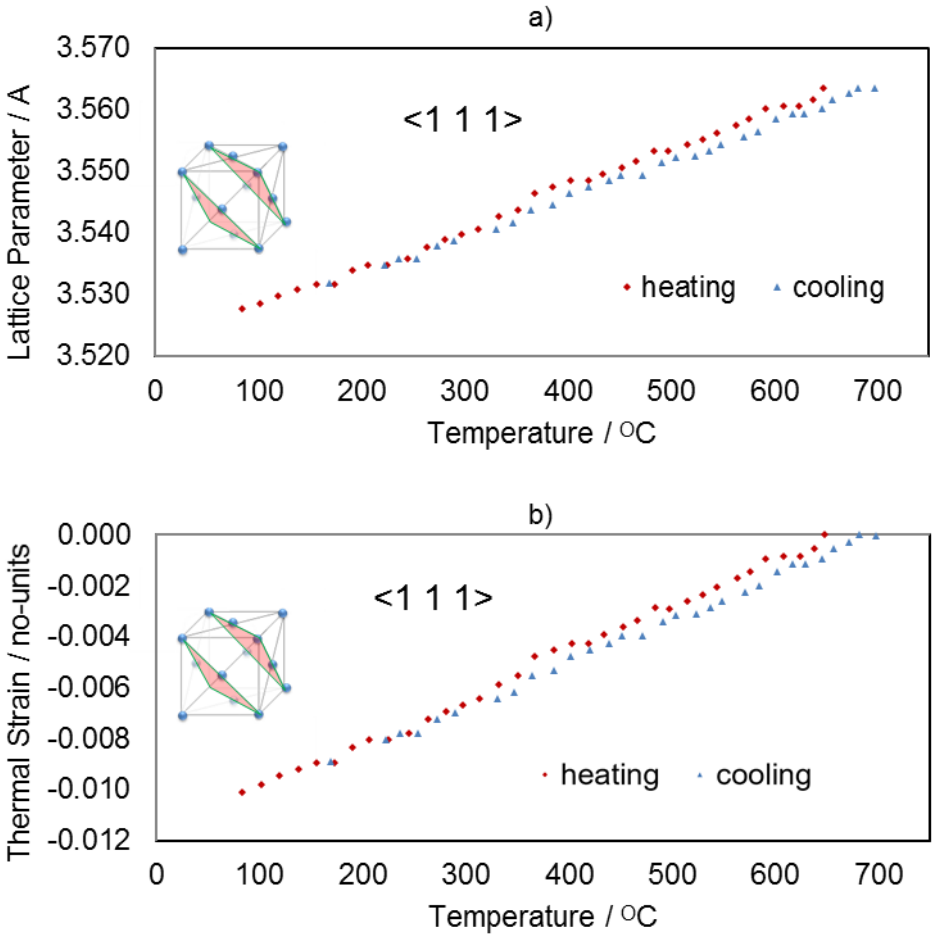

Figure 82 Crystallographic information obtaining from Ni within Ni-YSZ for the <111> using synchrotron powder XRD at 26 keV: a) lattice and, b) strain variation with temperature.

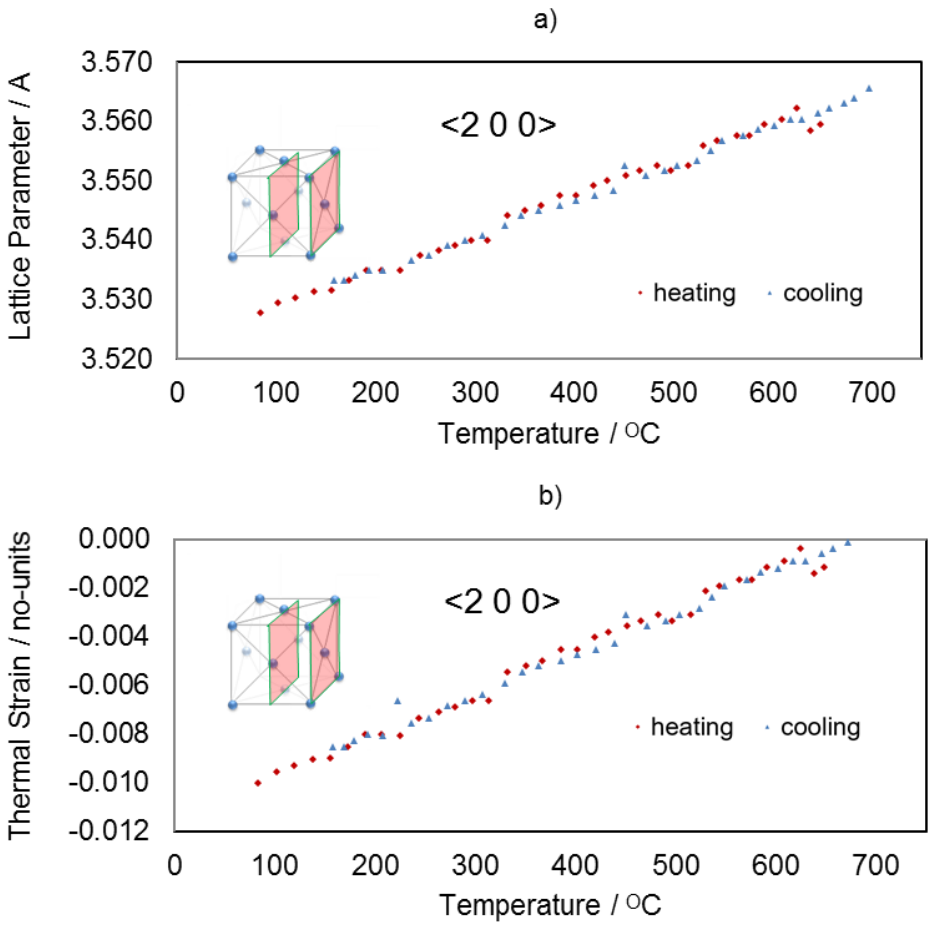

Figure 83 Crystallographic information obtaining from Ni within Ni-YSZ for the <200> using synchrotron powder XRD at 26 keV: a) lattice and, b) strain variation with temperature.

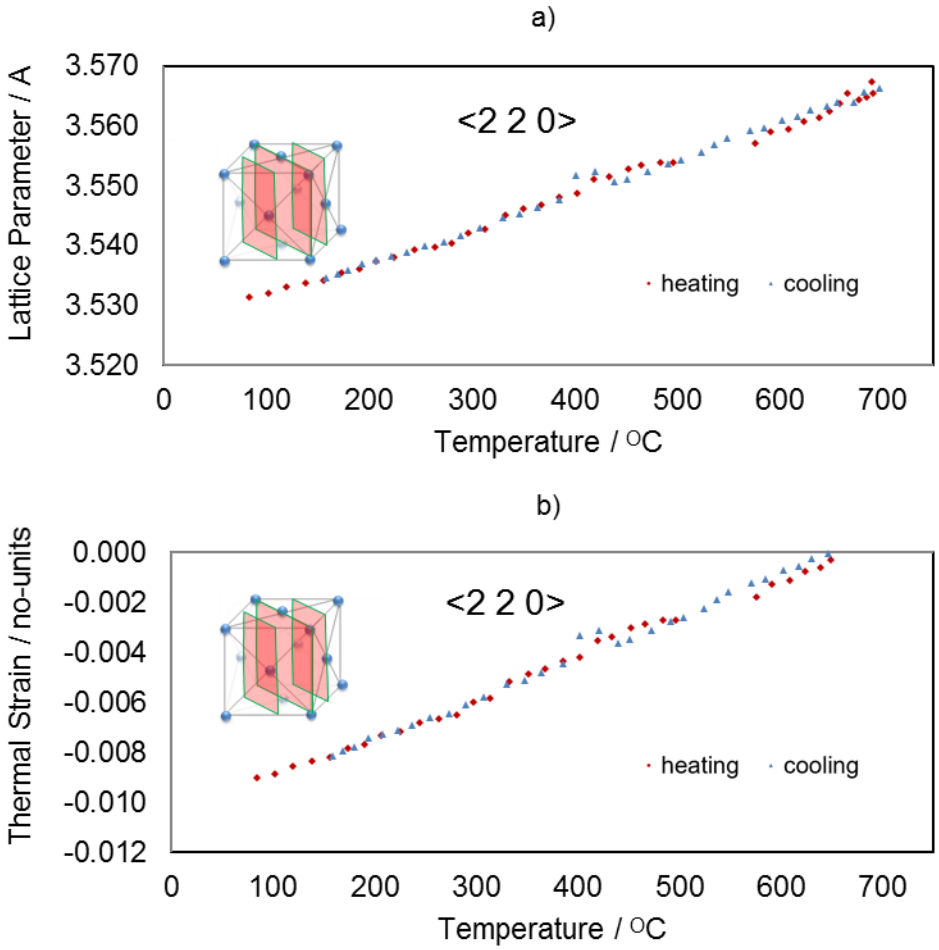

Figure 84 Crystallographic information obtaining from Ni within Ni-YSZ for the <220> using synchrotron powder XRD at 26 keV: a) lattice and, b) strain variation with temperature.

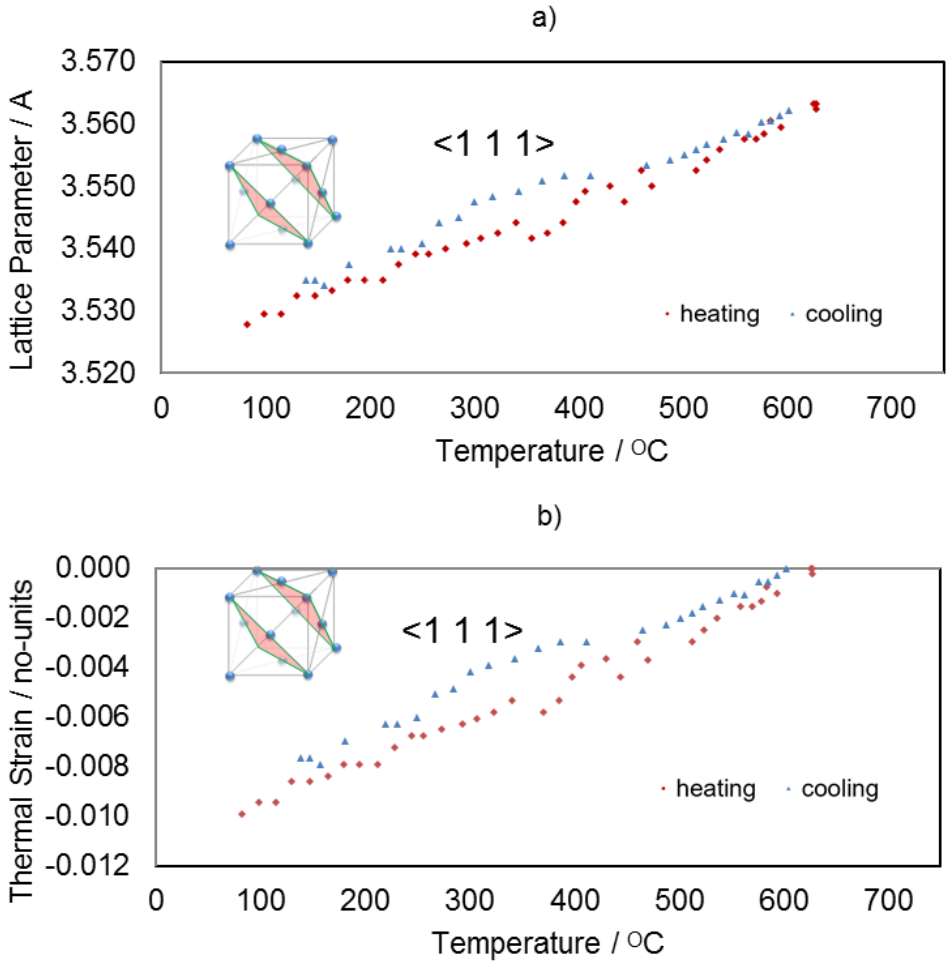

Figure 85 Crystallographic information obtaining from Ni within Ni-GDC for the <111> using synchrotron powder XRD at 26 keV: a) lattice and, b) strain variation with temperature.

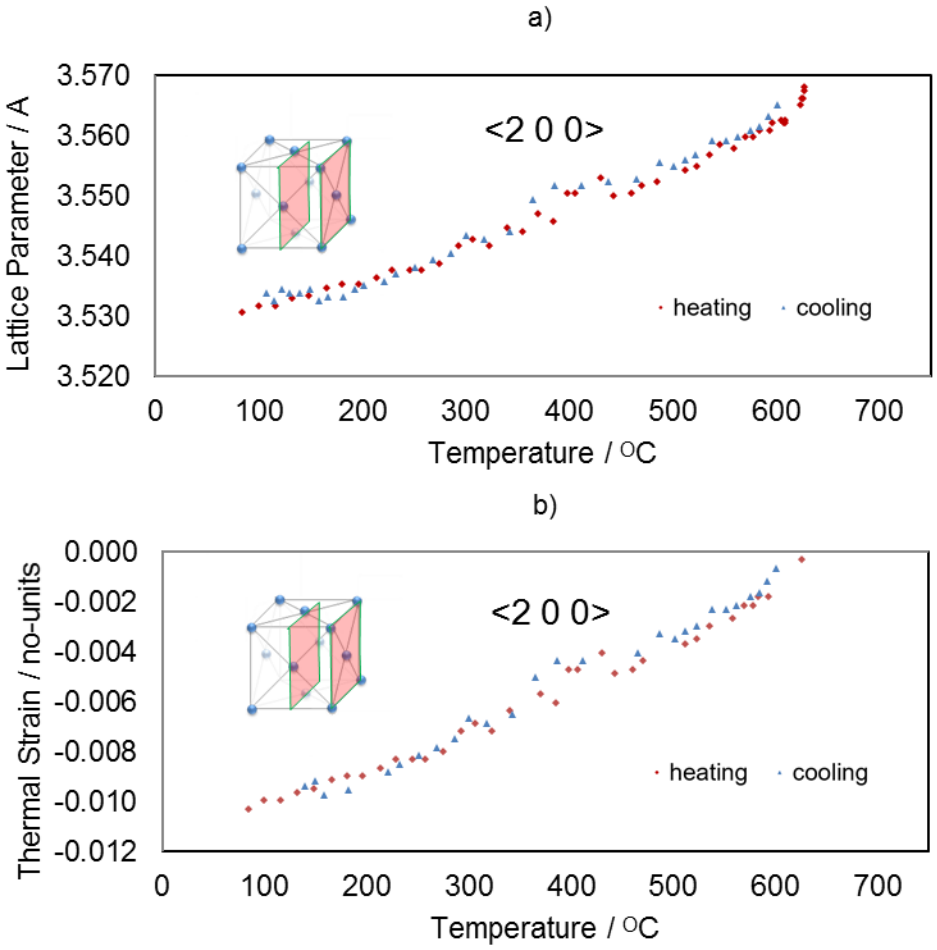

Figure 86 Crystallographic information obtaining from Ni within Ni-GDC for the <200> using synchrotron powder XRD at 26 keV: a) lattice and, b) strain variation with temperature.

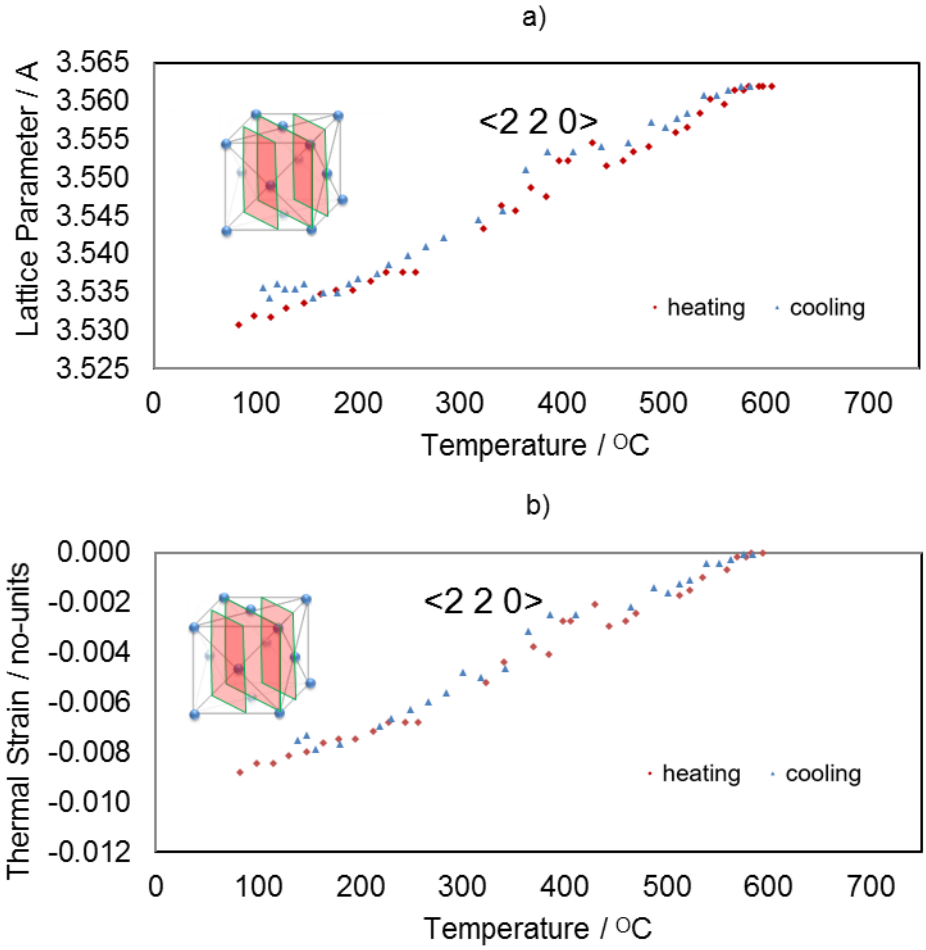

Figure 87 Crystallographic information obtaining from Ni within Ni-GDC for the <220> using synchrotron powder XRD at 26 keV: a) lattice and, b) strain variation with temperature.

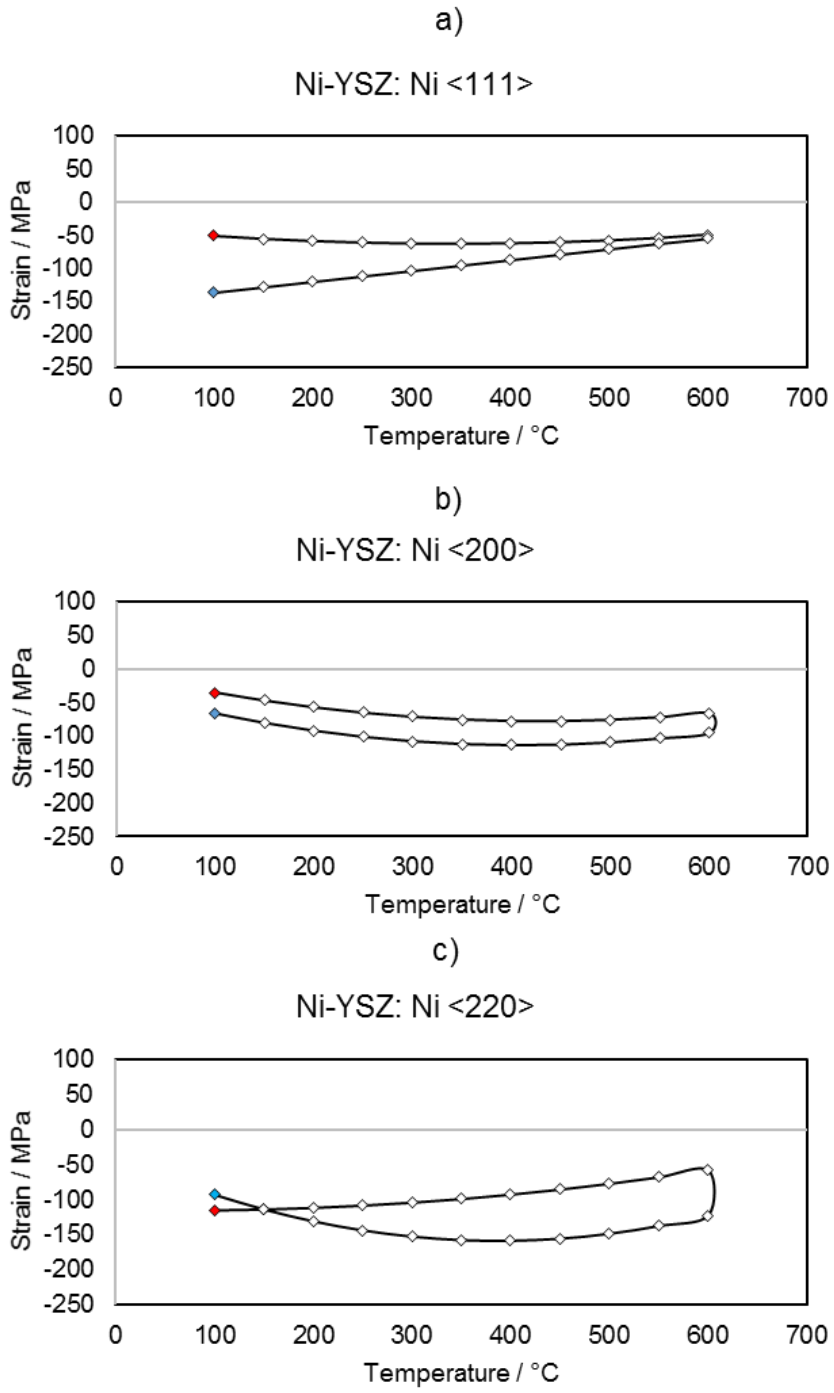

Figure 88 Crystallographic information obtaining from Ni within Ni-GDC for the <200> using synchrotron powder XRD at 26 keV: a) lattice and, b) strain variation with temperature.

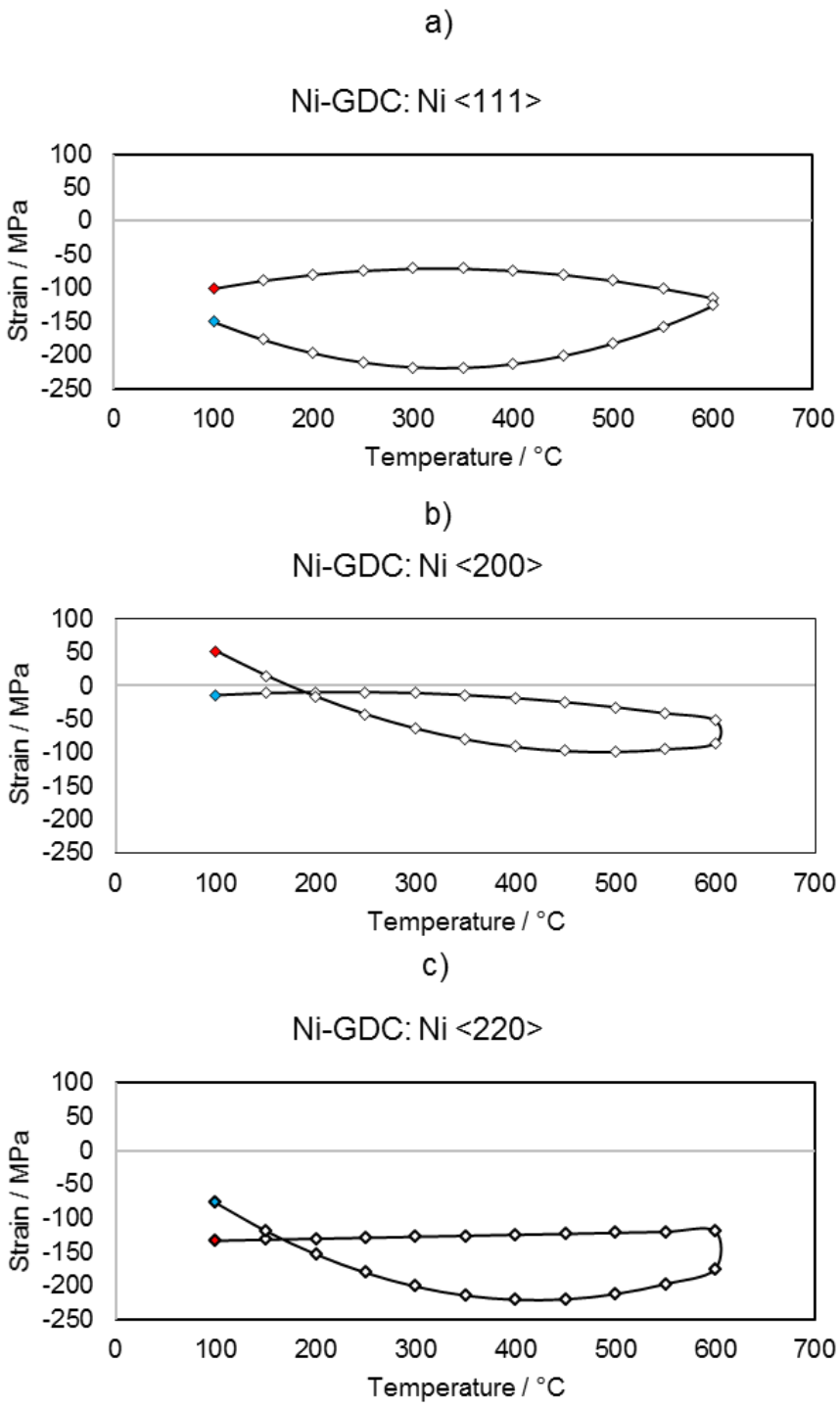

Figure 89 Crystallographic information obtaining from Ni within Ni-GDC for the <200> using synchrotron powder XRD at 26 keV: a) lattice and, b) strain variation with temperature.

As discussed, although the Ni lattice parameters return to nearly the same value after cycling for each of the three samples, hysteresis and non-linear expansion is observed during cycling and the degree of deviation from an ideal, linear thermal expansion cycle is suspected to be influenced by the ceramic choice. To examine this the thermal stress has been explored for the Ni metal within the two cermet materials corrected for the thermal stress of the ceramic-free Ni, i.e. the thermal stress of the ceramic-free Ni subtracted from the stress of the Ni within the cermet material at each temperature; the stress for each orientation can be seen in Figure 87 and Figure 88 for Ni-YSZ and Ni-GDC, respectively. Within the figures, the red and blue nodes indicate the start and end of the thermal cycles.

Although the state of the Ni stress returns to nearly the same value after thermal cycling, there remains a consistent difference in all orientations which, as speculated, may become more prominent if allowed to accumulate over serval thermal cycles. Furthermore, the variation of stress during heating and cooling exhibit smooth but different and non-linear trends; i.e. the stress experienced within the Ni during heating and cooling is not the same. Moreover, the difference in profiles between the three orientations is consistent between the two samples, suggesting that although a FCC structure may be maintained before and after cycling, during operation the Ni unit cell may experience non-uniform stress, distorting the FCC structure.

5.5.4. Non-Linear Ni Expansion

The thermal expansion coefficient (TEC) variation about the Curie point, 354 ºC (162), for the <111>, <200> and <220> orientation of Ni within ceramic-free Ni are displayed in Figure 90. These three orientations are then collectively compared with several reference sources (34; 37; 38; 39; 40) and in presented in Figure 91. The magnitude of the non-linear Ni peak (TEC_{peak}) and the temperature where the peak is located (T_{peak}) are displayed in Table 41 for all three orientations. Comparative data from XRD (35) and dilatometry (40) experiments from the literature are also presented. For the ceramic-free sample it can be seen that the values for both T_{peak} and TEC_{peak} present close similarity to values that have been reported in literature.

Table 41 Temperature and magnitude of the non-linear thermal expansion coefficient peak on passing the Ni Curie point for three Ni orientations within ceramic-free Ni respect to three references.

Sample	T_{peak} / ºC	TEC_{peak} / x10^{-6} ºC^{-1}	Reference
Ni <111>	354	18.1	Measured
Ni <200>	351	17.8	Measured
Ni <220>	351	18.0	Measured
Ni <111>	354	17.7	(35)
Ni <111>	355	18.8	(34)
Ni Dilatometry	350	17.5	(40)

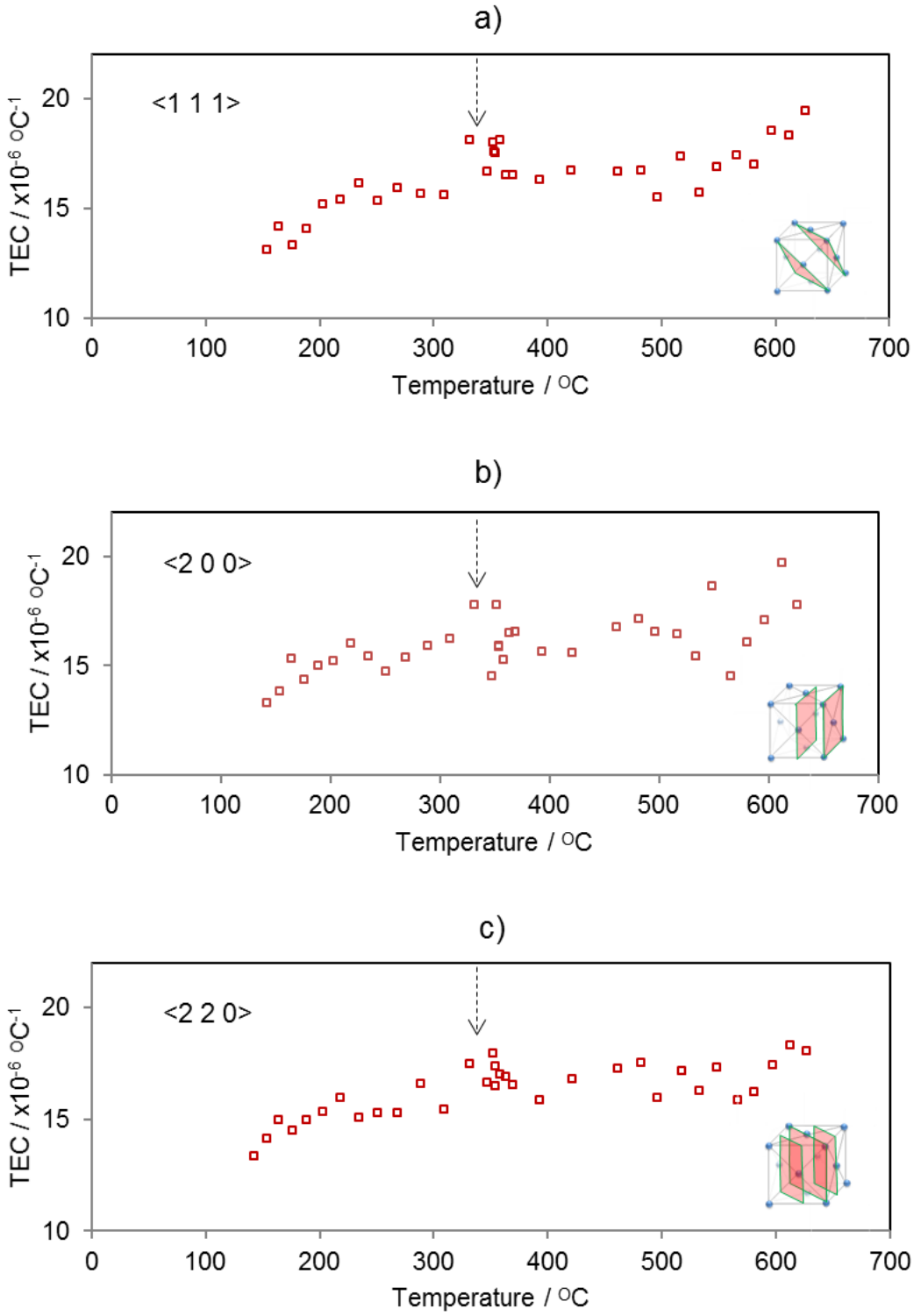

Figure 90 Non-linear thermal expansion coefficient for Ni on passing the Curie point: three orientations of Ni (a) <111>, (b) <200> and (c) <220>.

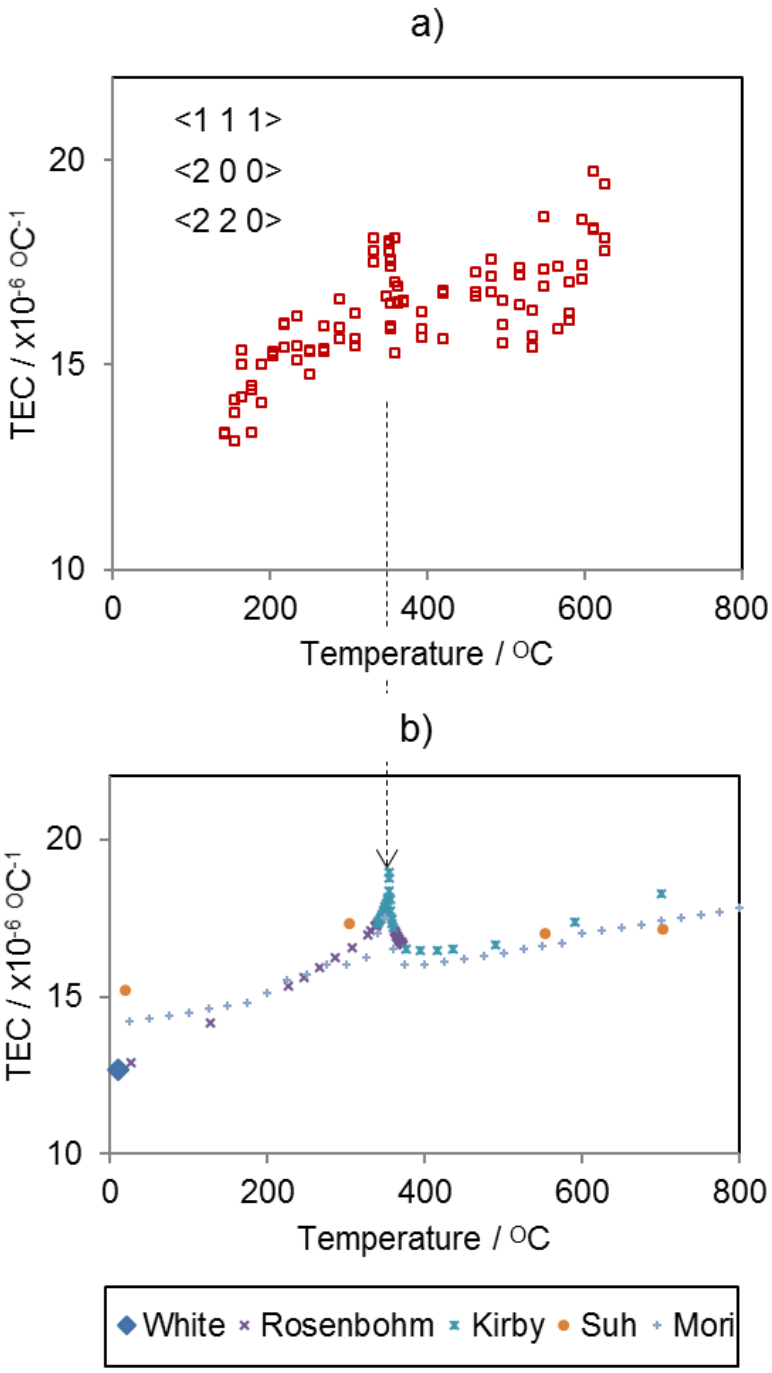

Figure 91 Non-linear thermal expansion coefficient for Ni on passing the Curie point: three orientations of Ni <111>, <200> and <220>, a) collectively compared to b) several references (162; 163; 164; 165; 40).

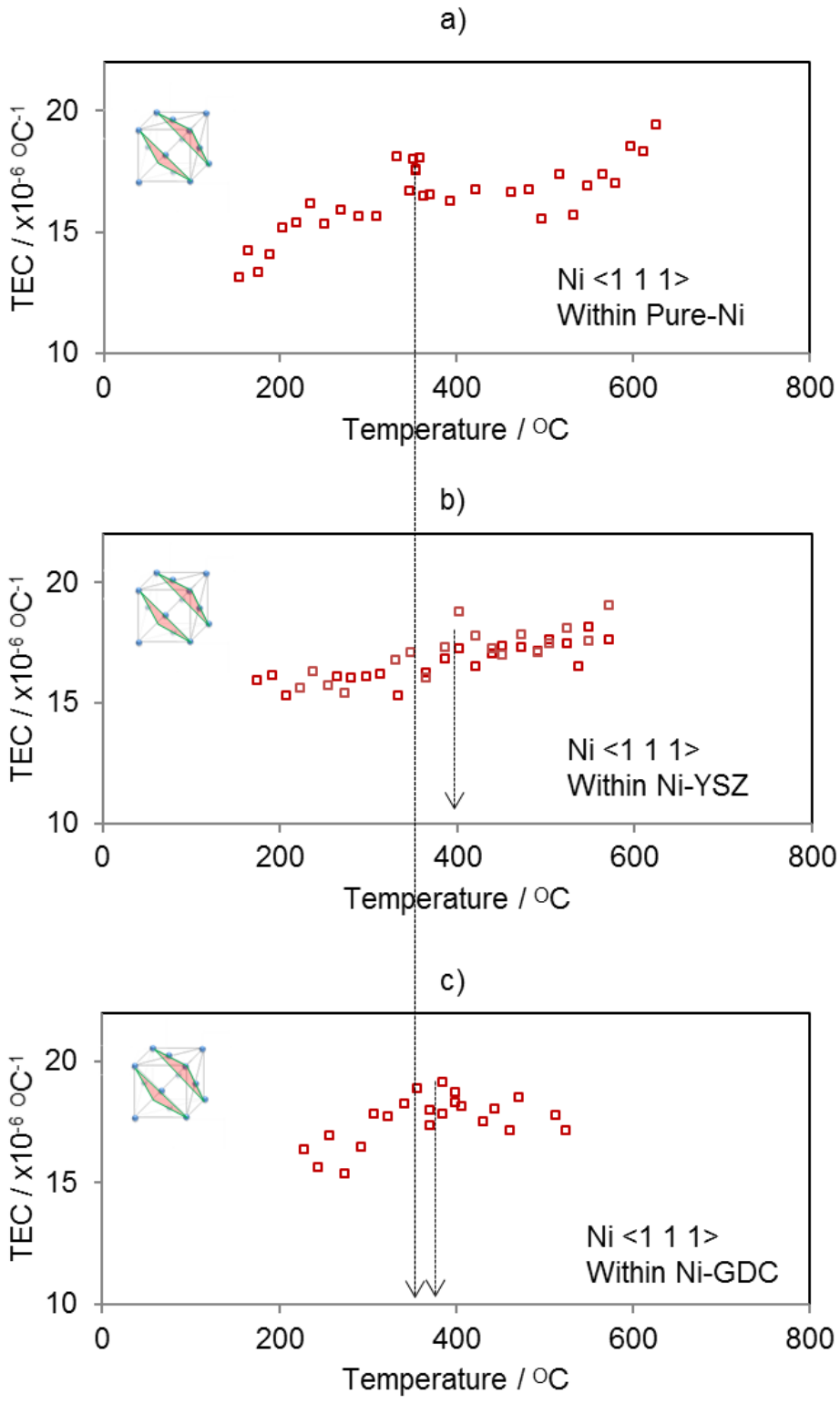

Figure 92 Non-linear thermal expansion coefficient for Ni on passing the Curie point: a comparison of Ni <111> within a) Ni, b) Ni-YSZ and c) Ni-GDC.

Previous dilatometry studies conducted on Ni and Ni-YSZ have reported bulk suppression of TEC non-linearity through the addition of a constraining ceramic backbone. Mori et al. presented a 5 $x10^{-6}$ $^{o}C^{-1}$ reduction in the bulk Ni-YSZ material TEC near the Curie temperature, resulting in greatly increased linearity of thermal expansion for Ni-YSZ compared to Ni alone. Unlike XRD, techniques such as dilatometry are limited to providing only macroscopic bulk effects resulting in limited information regarding the constituent materials at the microscopic/crystallographic level. Here, the TEC of Ni was examined for cermet materials Ni-YSZ and Ni-GDC as well as metallic Ni, from 250 ºC to 550 ºC to understand the effects of ceramic addition on the T_{peak} location and TEC_{peak} magnitude. The comparison of the Ni <111> orientation within Ni, Ni-YSZ and Ni-GDC is presented in Figure 92.

Table 42 presents the T_{peak} location and TEC_{peak} magnitude for the Ni <111> orientation for the ceramic-free Ni, and the two ceramic containing cermet materials. We observe that whilst macroscopically the ceramic addition may constrain the Ni expansion enough to overcome any non-linear TEC behaviour (40), non-linearity in the Ni crystallography remains and ceramic addition does not suppress non-linear crystallographic Ni expansion.

Table 42 Temperature and magnitude of the non-linear thermal expansion coefficient peak on passing the Ni Curie point for one Ni orientations <111> within three materials: Ni, Ni-YSZ and Ni-GDC.

Material	T_{peak} / ºC	TEC_{peak} / x10^{-6} ºC^{-1}
Ni	354	18.1
Ni-GDC	385	19.2
Ni-YSZ	402	18.8

The Ni lattice parameter increases with increasing temperature and the temperature at which the non-linear Ni thermal expansion peak occurs is shifted to a higher temperature for cermet materials (Figure 92). Thus the lattice parameter immediately preceding the non-linear expansion, i.e. the onset lattice parameter, is higher in cermet materials than that which is observed in pure metal (Figure 90 and Figure 91). Therefore it should be noted that the magnitude of the thermal expansion peak within cermet materials can be expected to be higher than that of pure Ni, an increase possibly attributed to the higher onset lattice parameter. The reason why the expansion peak is not observed with techniques such as dilatometry (40) is likely due to the macroscopic stiffness that suppresses large expansion. However, because these materials are porous, stress relaxation is thought to occur at microscopic length scales within the Ni phase via expansion into neighbouring pores (45; 166; 167; 46) and consequently the non-linear expansion can still be observed for crystallographic studies.

The temperature at which non-linearity is observed, $T_{peak,}$ shifts within the cermet materials; the Ni Curie transition is reported at 354 ºC by several sources (163; 164; 165) which agrees closely with the ceramic-free Ni data, but a shift of ca. 30 ºC and 50 ºC is observed for Ni-GDC and Ni-YSZ, respectively. We hypothesize two possible mechanisms contributing to the peak shift: mechanical rigidity of the ceramic backbone and the altered population of crystallographic dislocations. Firstly, the mechanical stiffness may increase the energy required to cause the Ni restructuring due to the constraining backbone which mechanically restricts expansion; the mechanical constraint caused by the ceramic backbone is thought to be of great importance particularly at the metal-ceramic interface (45; 167; 46); the magnitude of this constraint being a function of the Young's modulus of the ceramic. Secondly, the ceramic addition may alter the dislocation density within the metal favouring ferromagnetism; it has been suggested that lattice distortions associated with crystallographic dislocations promote the emergence of ferromagnetism (158).

A reduced ramp-rate during the Curie transition may allow for the dissipation of undesirable thermal shock experienced due to the non-linear expansion, by prolonging the opportunity for the Ni phase to relax into the porous phase and alleviating interfacial stress peaks. This may possibly be beneficial in the design of thermal control systems for SOFCs operating under conditions where high ramp rates are anticipated.

5.5.5. Accelerated Stress Testing For Ni-YSZ

Finally, the lattice parameters with accompanying thermal strain and stress are presented for an accelerated stress test (AST) using the Ni-YSZ material, as displayed in Figure 93 a – c. Data was acquired for one full thermal cycle at a ramp rate of ca. 10 ºC min $^{-1}$ followed by data acquisition only at low (100 ºC) and high (600 ºC) temperatures with sequential cycling at an accelerated rate of ca. 60 ºC min $^{-1}$. ASTs such as this allows for the analysis of residual stress relaxation and thermally induced shock both observed in the form of TDD over the course of many cycles providing an insight into real-life, long-term thermal operation that would otherwise be very time intensive.

For each thermal cycle, the sample was held at the low temperature while several patterns were collected (see Figure 93 a at 100 – 120 mins), the lattice parameter for these acquisitions was then averaged (see Figure 93 g, Cycle 1). This process was repeated for the high-temperature acquisitions, then for each thermal cycle in turn, resulting in a variation in the five high (Figure 93 d) and five low (Figure 93 g) lattice parameters with respect to the number of thermal cycles. These values were then used to calculate the thermal strain variation with respect to the initial high-temperature lattice parameter (Figure 93 e and h), and the thermal stress calculated from the results (Figure 93).

Table 43 Low temperature crystallographic data for the Ni <111> orientation from a Ni-YSZ sample exposed to five thermal cycles with strain and stress calculated with respect to the initial thermal cycle.

Cycle	Lattice / Å	Strain / x10^{-3} no-units	Stress / MPa
1	3.525	-9.9	-704
2	3.526	-9.7	-690
3	3.527	-9.3	-666
4	3.529	-8.9	-638
5	3.530	-8.6	-613

Table 44 High temperature crystallographic data for the Ni <111> orientation from a Ni-YSZ sample exposed to five thermal cycles with strain and stress calculated with respect to the initial thermal cycle.

Cycle	Lattice / Å	Strain / x10^{-3} no-units	Stress / MPa
1	3.560	0.0	0
2	3.561	0.2	9
3	3.562	0.5	30
4	3.563	0.7	45
5	3.564	1.0	63

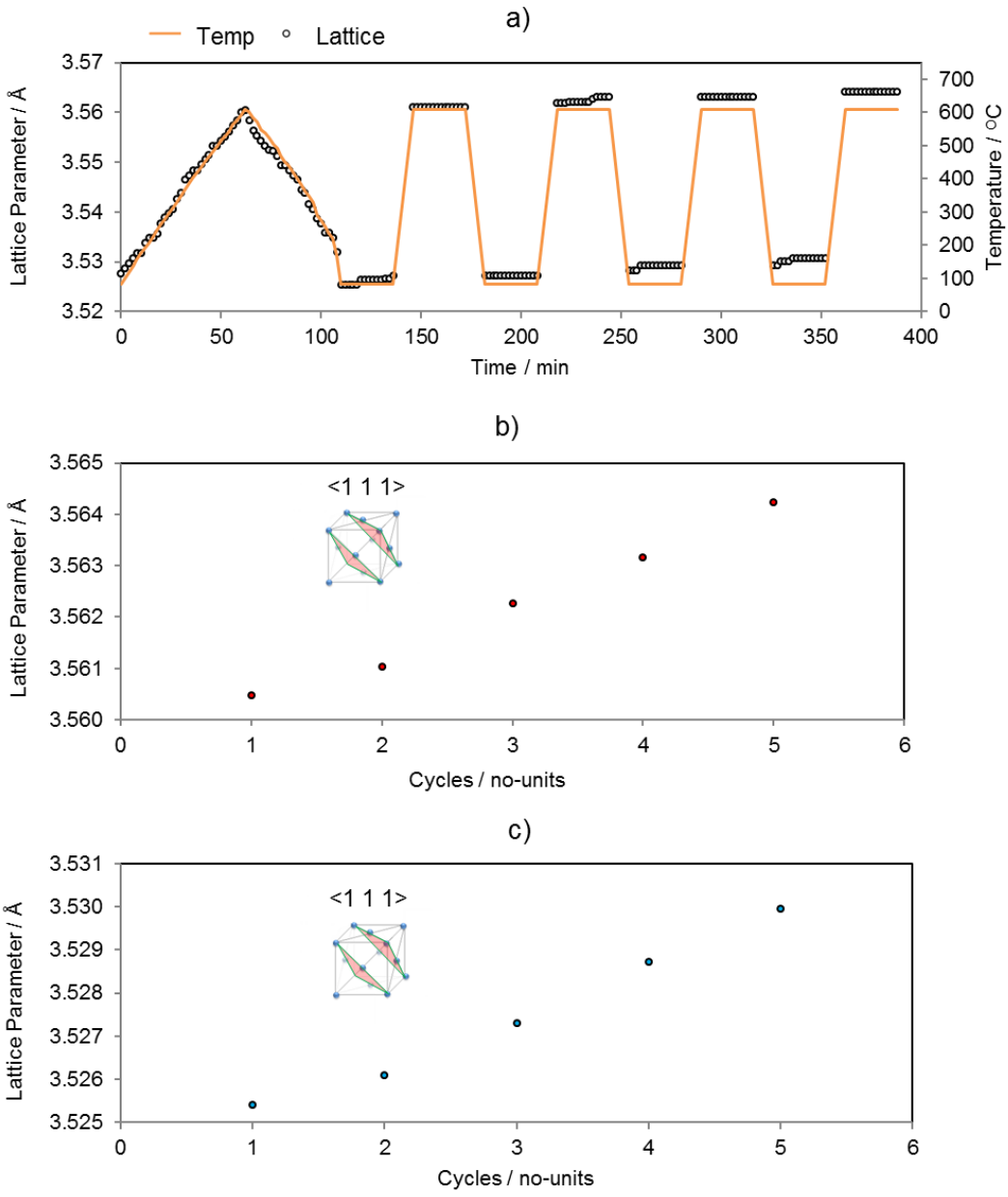

Figure 93 Thermal cycling of Ni-YSZ powder examining the variation of the <111> lattice parameter within Ni for five thermal cycles from low temperature (100 ºC) to operating temperature (650 ºC) in a forming gas environment: a) all lattice data, b) high-temperature lattice, and c) low-temperature lattice variation with thermal cycles.

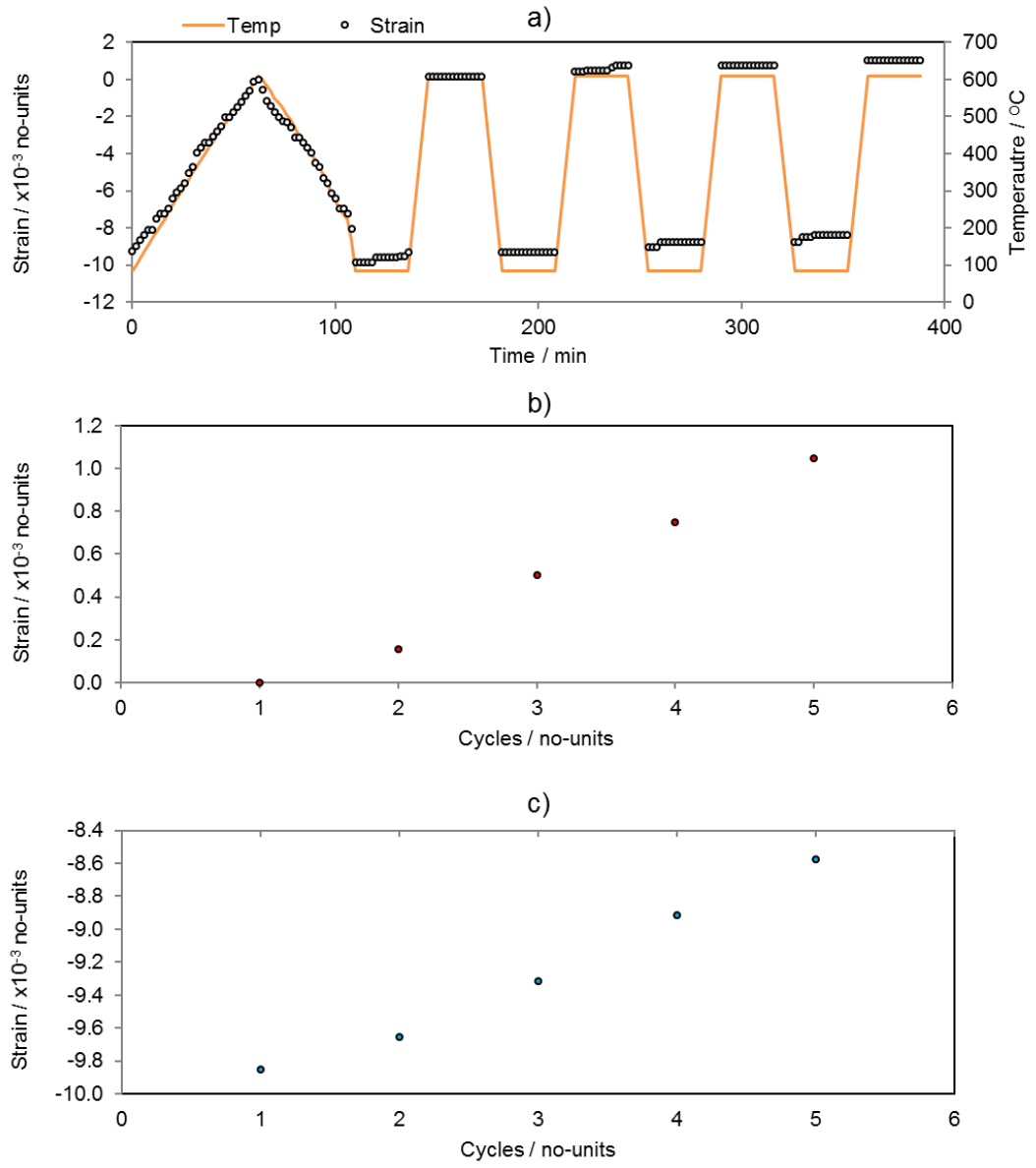

Figure 94 Thermal cycling of Ni-YSZ powder examining the variation of the <111> lattice parameter within Ni for five thermal cycles from low temperature (100 ºC) to operating temperature (650 ºC) in a forming gas environment: a) all strain data, b) high-temperature strain, and c) low-temperature strain variation with thermal cycles.

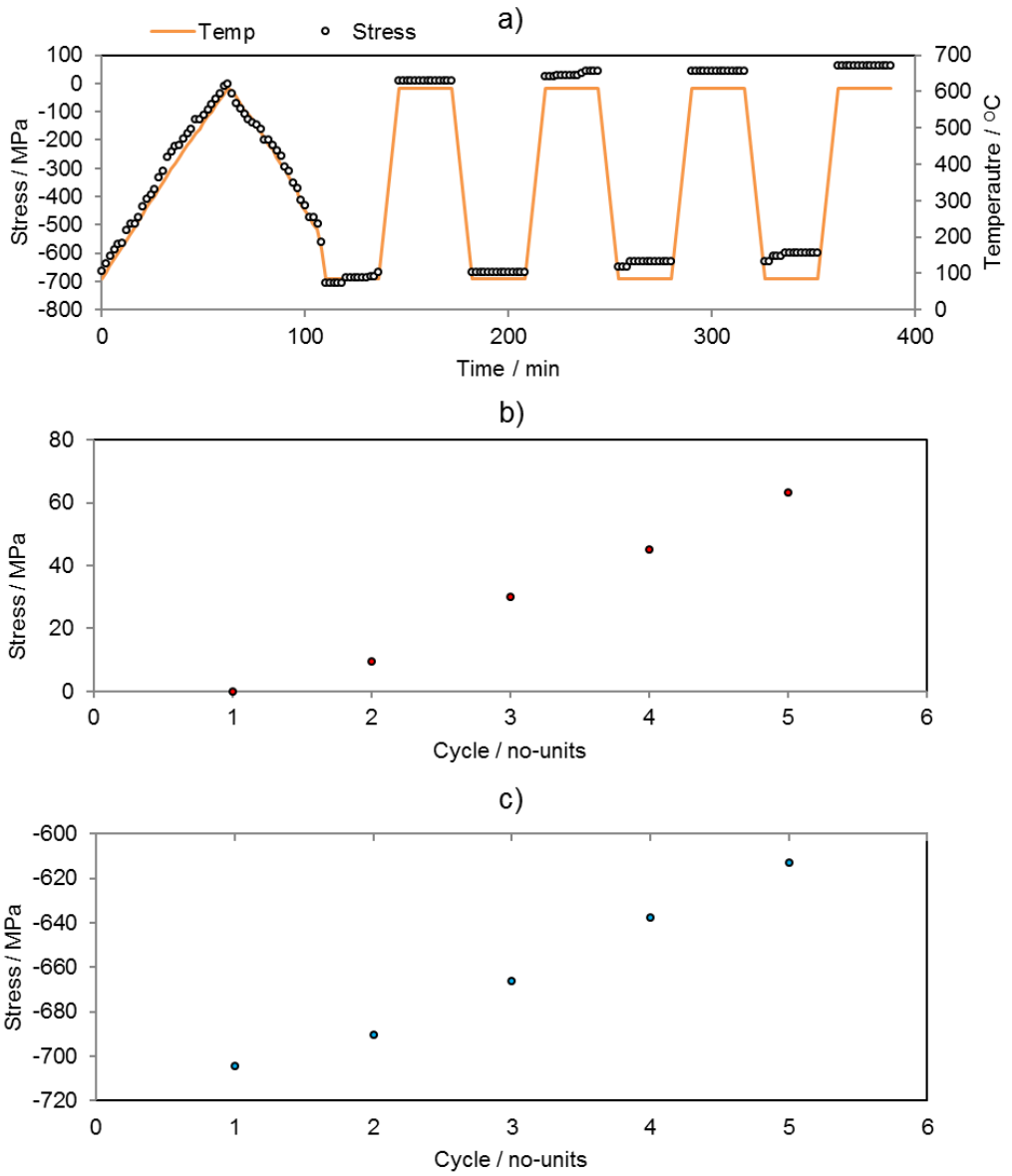

Figure 95 Thermal cycling of Ni-YSZ powder examining the variation of the <111> lattice parameter within Ni for five thermal cycles from low temperature (100 ºC) to operating temperature (650 ºC) in a forming gas environment: a) all stress data, b) high-temperature stress, and c) low-temperature stress variation with thermal cycles.

TDD is seen in both the high and low-temperature lattice parameters; the lattice parameters are seen to increase with thermal cycling, resulting in a positive shift for strain and stress with respect to the initial thermal cycle. Marginally more creep is seen in the low temperature (Table 43) parameters than that observed at high temperatures (Table 44), possibly due to increased mobility at high temperatures resulting in greater relief of residual stresses on heating compared to cooling. This is examined more closely in Table 45 by the quantification of the thermally driven deformation into TDD values from both the low (3.525 Å) and high (3.560 Å) temperature lattice parameters. Although both high and low temperature TDD correlate positively with increasing number of thermal cycles, the TDD_{LT} and TDD_{HT} values display a locally divergent path; the high-temperature deformation follows a near-linear increase with each thermal cycle, whereas the low-temperature deformation shows consistently greater deformation with each thermal cycle which accelerates non-linearly, particularly after the third thermal cycle. The locally divergent deformation is quantified by the difference in the high- and low-temperature deformation (ΔTDD), also displayed in Table 45.

The TDD observed here, suggests that the Ni is either provided an insufficient time to relax residual stresses, is experiencing mechanical degradation due to accelerated thermal shock, or a combination of the two processes. Firstly, unlike high-temperature thermal cycling (ca. 1000 ºC), lower temperature cycling (ca. 600 ºC) may require several thermal cycles or extended dwell times at operational temperatures before residual stresses can be relieved. Given the infrequency of thermal cycles in stationary CHP applications, extended

dwell times at lower temperatures may allow sufficient time for residual stress relaxation, although, higher frequency operational cycling may require many cycles before residual stresses are relieved from the materials. Secondly, it is conceivable that the high thermal ramp-rates induce tensile stress within the Ni phase due to the difference in the Ni and YSZ thermal expansion coefficients, likely observed more notably in cooling due to the higher stress-state. Finally, a combination of relaxation and thermally induced shock would support the divergent paths of the high and low temperature deformations.

Table 45 Thermally driven deformation of the Ni <111> lattice parameter within Ni-YSZ quantified with respect to increasing thermal cycles from the low (3.525 Å) and high (3.560 Å) temperature lattice parameters with deformation difference defined as their difference.

Cycle	TDD_{LT} / no-units	TDD_{HT} / no-units	ΔTDD / no-units
1	0.000%	0.000%	0.0000%
2	0.028%	0.028%	0.0003%
3	0.057%	0.056%	0.0006%
4	0.113%	0.084%	0.0291%
5	0.142%	0.112%	0.0294%

5.5.6. Conclusions from Crystal-Structure Investigations

In this chapter section, the influence of ceramic addition on thermo-mechanical performance was examined for two cermet materials with comparison to a ceramic-free metal sample. Crystallographic information suggests that the effects of ceramic addition to the expansion of the FCC structure of Ni in isothermal environments are minor over a single thermal cycle. Nevertheless, over the lifetime of an SOFC the anode is expected to withstand multiple thermal cycles. Therefore, techniques such as accelerated stress testing should be employed to understand the accumulative effects of operational cycling.

AST revealed that lower temperature operation, i.e. 600 ºC rather than higher 1000 ºC, results in deformation of the lattice parameters at both, low and high temperatures, likely due to a combination of two mechanisms: shock-induced tensile stress and delayed relaxation hysteresis. Furthermore, the high and low temperature deformation has been found to be divergent resulting in a greater relative deformation in the cold lattice parameters than that observed at high temperature. A likely contributor to the thermally driven degradation on operational start-up and shut-down is the non-linear TEC peak found at the Curie temperature. Until now, macroscopic studies have understood that the ceramic backbones suppress the non-linear expansion of the Ni phase resulting in a subdual of the peak. However, this work demonstrates that the non-linearity remains within the crystallographic structure although shifted to a higher temperature, a temperature that is dependent upon the ceramic employed.

5.6. Conclusions from Chapter Five

Degradation of the electrochemical performance of SOFCs continue to inhibit entry to the mass-market. Particularly, issues during operation start-up and shut-down triggered by differences in the expansion of the constituent materials causes structural changes that span multiple length scales from the crystal-, to micro-, to macrostructure. As a result, the cascade of degradation processes that occur are complex and require a host of instruments in order to be characterised. In this chapter SOFC degradation has been investigated with a focus on the operational thermal cycling of the anode and electrolyte layers, which are known to be mostly problematic during start-up and shut-down. To do this, a range of X-ray characterisation techniques including micro- and nano-CT, and point XRD have been employed using a mixture of lab- and synchrotron-based instruments.

To begin, macroscopic features are studied for a range of start-up times and operational cycles. Sub-micron X-ray micro-CT revealed that rapid thermal cycling may induce significant cell-wall contraction, electrolyte concaving and curvature may induce delamination. These mechanisms are thought to reduce interfacial contact between the anode and electrolyte, and trigger tensile-induced stress within the anode support layer that may facilitate cracking that spans multiple length scale. These macroscopic mechanisms exhibited a dependency upon the thermal ramp-rate, prompting additional investigation. To examine this relationship a computation correlation method, DVC, was employed to track macro- and microstructural changes between datasets exposing microscopic channelling and cluster formation that was correlated to Ni mobility during low ramp-rates. This clustering was formed through the development of multiple

channels through to be triggered by the inhibition of sintering attributed to the constraining ceramic skeleton. Finally, at high ramp-rates macroscopic strain-waves propagate in periodic compression-tension undulations and appear to initiate at a macrostructural defect. From these macroscopic investigations it would be recommended that defects in fabrication should be avoided in order to minimise the effects of high thermal ramp-rates during rapid operational start-up times.

As discussed, these mechanisms are known to occur across multiple length scales, therefore a multi-length scale characterisation approach was required, examining from the macro- into the microstructure. At the microscale, the particle-particle interactions could be inspected, as a result the TPB reaction site density could be mapped quantified. It was found that the TPB density reduces after thermal cycle even at low ramp-rates, as does the interfacial surface area between Ni and YSZ particles. Furthermore, sintering of the Ni is known to be an issue during long-duration operation, and DVC investigations had suggested Ni mobility during lower ramp-rates. So in order to inspect this, the particle size of the Ni metal was quantified for each cycle, however, compared to long-duration operation, the Ni particle grow after thermal clinging remained negligible. As a result, the Ni-YSZ delamination is concluded to be a prominent cause of electrochemical performance losses as the dominant cause for TPB density reduction during start-up and shut-down.

Finally, the degradation was explored again in finer detail by examining the crystal-structure within the Ni metal and the influence of the ceramic additional on the metal structure. It was found that the effects of ceramic addition to the

expansion of the cubic structure of Ni in isothermal environments are minor over a single thermal cycle for both zirconia- and ceria-based ceramics. However, the ceramic choice did influence the thermal expansion non-linearity on passing the Ni Curie temperature which, contrary to previous literature, is not suppressed through ceramic addition, instead it is shifted to a higher temperature, a temperature that is dependent upon the ceramic employed. Lastly, accelerated stress tests revealed that lower temperature operation, i.e. 600 ºC rather than higher 1000 ºC, results in deformation of the lattice parameters at both, low and high temperatures, likely due to a combination of two mechanisms: shock-induced tensile stress and delayed relaxation hysteresis. Moreover, this high and low temperature deformation has been found to be divergent resulting in a greater relative deformation in the cold lattice parameters.

This chapter explores the multi-length scale characterisation capabilities that are possible for examining SOFC degradation. Several prominent mechanisms responsible for performance losses have been elucidated using a host of methods. These results are intended to inform the field of SOFC research and commercialisation of potential pitfalls from manufacturing to operation in order to improve competitiveness within the mass-market.

Chapter Six: Conclusions

6.1. Introduction to Chapter Six

This thesis has introduced the fundamental principles of the SOFC, its limitations and the current state of the literature available for SOFC research. This was assimilated in order to develop techniques to characterise features of interest in SOFC performance loss. These techniques were subsequently applied to carry out a series of investigations into SOFC degradation. This final chapter will summarise the findings of this work, the means by which it has been disseminated and provide an outlook of the potential future research in the field of SOFC degradation.

6.2. Thesis Conclusions

Motivations are shifting towards low-carbon alternatives for energy conversion as a result of depleting fuel stores and increasing pollution levels. A promising electrochemical device is the SOFC which boasts fast reaction kinetics for a range of fuels without the requirement of an expensive platinum catalyst. Moreover, SOFC are also highly scalable allowing versatility in application from single- to mega-watt installations. Fuel versatility and favourable reaction kinetics are achieved by operating at high temperatures; however, these temperatures cause degradation of the cell structure and, as a result, the electrochemical performance deteriorates during start-up, operation and shut-down. In its most simple form the SOFC can be described by two electrodes separated by an electrolyte but connected via an external circuit. Complex microstructures have been developed for the cell electrodes in an effort to inhibit degradation mechanisms in order to maintain competitive performances during long-duration

operation. The anode is typically Ni-based with the addition of the ceramic electrolyte to form a porous cermet material. The reaction site is thought to be located at the boundary between the three constituent phases within the electrode: metal, ceramic and pore, as these phases allow the transport of the species involved in the reactions: electrons, ions and gaseous reactants/products. The addition of the ceramic creates a mechanical skeleton that is intended to impede sintering, reduce macroscopic thermal expansion mismatch and increase the volumetric reaction site density. Yet, the Ni remains susceptible to sintering, oxidation, delamination and poisoning from fuel impurities. A multitude of characterisation studies have been reported in the literature, aimed at improving our understanding of these complex structures and their ability, or inability, to produce high-performance cells capable of sufficiently supressing degradation. The chronological development of characterisation methods has progressed primarily through the improvement of dimensional and resolution capabilities. The former began as 2D SEM imaging, progressing to 3D FIB-SEM, 3D X-ray CT and finally 4D X-ray CT. The latter has resulted in facilities capable of characterising 3D structures with nanoscale detail using lab-based instruments. This thesis employs a host of characterisation methods than span multiple dimensions and length scales in order to study the effects of thermal cycling on the degradation of SOFC structures.

Lab-based characterisation methods are developed and demonstrated to enable extensive studies of SOFC structures to be conducted using CT. Firstly three-phase segmentation and subsequent TPB characterisation is demonstrated across multiple length-scales from the nano- to microscale. This is

the first report of TPB quantification using X-rays without the requirement of specialist synchrotron facilities. After observing discrepancies between the extract same ROI characterised using different resolutions the influence of voxel size was inspected. As a result, it was concluded that metrics characterised at different X-ray CT resolutions cannot necessarily be directly compared; to compare data of different resolutions, a correction factor should be applied; and consequently, resolution analysis may deliver higher accuracy electrochemical models. Degradation mechanisms result in the structure developing over time; consequently, 4D methods are required in order to obtain a thorough depiction of the structural developments. Therefore a lab-based 4D nano-CT technique compatible with high temperatures has been developed and demonstrated, whereby an identical ROI was inspected within an electrode material between thermal treatments. Consequently, the application of this method for a case-study intended to emulate a gasket failure indicated that metal oxide film growth in SOFCs can increase the pore-phase tortuosity-factor.

These methods were then applied in order to conduct a multi-length-scale analysis of thermally driven degradation within SOFC structures from the macro- to micro- to crystal-structure for operationally relevant conditions. Beginning at the macro-structure, the effects of thermal cycling effects were investigated with sub-micron resolution X-ray CT, observing that rapid thermal cycling may induce significant cell-wall contraction and electrolyte concaving.

Delamination of the electrolyte from the anode support may occur as a result of the cell curvature, reducing interfacial contact thus increasing the electrochemical impedance. This concaving likely produces tensile stress within

the anode inducing and facilitating anode cracking, however, cracking was observed far from the reaction zone, so the implications of anode support-layer cracking on the electrochemical performance may be dwarfed by contact resistances associated with the electrolyte delamination.

To inspect these developments further, correlative DVC techniques were applied to study the evolution of the macro- and micro-structure with time. The microscopic cluster formation was correlated to Ni mobility during low ramp-rates with the inhibition of sintering in the form of material being channelled, that is attributed to the restricting ceramic skeleton. High ramp-rates demonstrated significant degradation observed in the form of macroscopic, defect-induced strain-waves that propagate in periodic compression-tension undulations though to originate at a structural defect consisting of increased localised ceramic content.

Expanding this investigation from the macro- to microscale revealed that the TPB density and interfacial surface area between Ni and YSZ particles reduces after each thermal cycle even at low ramp-rates, the Ni particles also grow via agglomeration mechanisms after each thermal cycle but by negligible amounts compared to long-duration operation. Consequently, the Ni-YSZ delamination is concluded to be a prominent cause of electrochemical performance loss through the reduction in the volumetric TPB density.

Advancing further through this multi-length-scale problem, the crystal-structure is examined using synchrotron XRD. The effects of ceramic addition to the expansion of the cubic structure of Ni in isothermal environments were concluded to be minor over a single thermal cycle; whereas, accelerated stress

tests revealed that lower temperature operation, i.e. 600 ºC rather than higher 1000 ºC, results in deformation of the lattice parameters at both, low and high temperatures, likely due to a combination of two mechanisms: shock-induced tensile stress and delayed relaxation hysteresis. Moreover, this high and low temperature deformation was found to be divergent resulting in a greater relative deformation in the cold lattice parameters.

Finally, the thermal expansion non-linearity on passing the Ni Curie temperature was found to not be suppressed by ceramic addition; however, it is shifted to a higher temperature, a temperature that appears to be dependent upon the ceramic employed. A list of all samples prepared, data collected and investigation carried out for this thesis can be found in the appendix.

In conclusion, this thesis has explored the limitations of SOFCs through the development of new preparation methods and characterisation techniques, and their application in investigating the effects of operational cycling of Ni-based SOFC anode materials. Structural characterisation across multiple length scales has exposed several degradation mechanism with what are concluded to be varying degrees of influence on the electrochemical performance.

Mechanisms such as the electrolyte curvature and detachment from the anode at the macroscale, delamination of the metal and ceramic particles at the microscale, and diverging hysteresis between the hot and cold lattice parameters are all thought to contribute to electrochemical performance losses and occur as a result of thermally driven degradation primarily as a cause of either rapid start-up times or repeated operational cycling.

In order to translate this to real-world applications, one can consider how these findings may be employed to optimise the operational thermal profiles for SOFC units. It is widely accepted that low ramp-rates deliver lower thermal shock; however, work presented her suggests that low ramp-rates (3 ºC min-1) may stimulate agglomeration of the Ni metal analogous to dwelling at operational temperature. Although agglomeration effects during time spent ramping to operating temperature are considerably less severe than long-duration operational dwelling and may even be beneficial through improved material connectivity. Nevertheless, raising the thermal ramp-rate to 10 ºC min-1 or even as high as 20 ºC min-1, i.e. reducing the start-up time by an order of magnitude from hundreds to tens of minuets, demonstrated no critical macroscopic failure, minimal Ni mobility and an equivalent degree of particle-particle delamination. Whereas high thermal ramp-rates, i.e. 30 – 60 ºC min-1, presented critical structural failure across all length scales. As a result, it may be concluded that lower ramp-rates may not necessarily be best but there is certainly an upper limit on the rates that can be employed, and for this cell geometry rates between 10 – 20 ºC min-1 may be optimal for operational start-up even when rapid power delivery is not a necessity.

It should also be noted that non-linear thermal expansion i.e. when passing the Curie temperature, may be particularly damaging to the structural integrity of the cell. A reduced thermal ramp-rate purely when passing this transition may extend the lifetime of the cell, i.e. a single ramp-rate may not be optimal for the entire operational start-up time. The apparent dependence of the Curie transition temperature on the ceramic modulus also suggests that less brittle ceramics may

yield more durable cells, or at least reduced Ni strain during cycling. As a result, ceria-based cells may be favourable from a mechanical perspective for operations that require frequent thermal cycling. However, macro- and microstructural investigations, analogous to those presented here on zirconia-based materials, should be conducted on ceria-based cells to explore this.

Consequently thermal profiles for operational start-up have complex repercussions, and a *one size fits all* approach cannot be applied if optimising for applications which intend to be commercially competitive. Nevertheless, the methods presented here may be applied to optimise the start-up profiles for any cell geometry or material configuration.

6.3. Dissemination and Awards

This work has been disseminated through several journal papers, front covers and conference talks both nationally and internationally. A full list of authored papers can be found in the appendix.

The techniques developed here are not for the exclusive use on the study of SOFCs; as a result, the author has engaged in several collaborative projects spanning from low-temperature fuel cell fabrication to lithium-ion battery safety in failure. These collaborations have resulted in work with many UK universities and also international institutions such as the European Synchrotron Radiation Facility (ESRF, Grenoble, France), The Paul Scherrer Institute (PSI, Villigen, Switzerland), Argonne National Labs (ANL, Lemont, USA), the National Aeronautics and Space Administration (NASA, Houston, USA) and the National Renewable Energy Labs (NREL, Colorado, USA).

Dissemination comes in the form of many outlets in order to reach as large an audience as possible; and the author co-led a public engagement group focussing on fuel cell engagmentent for over two years. The author also organised and ran an early career conference funded by the Science and Technology Facilities Council (STFC).

This work has been awarded for its merits, including a conference award for the presentation at the Hydrogen Fuel Cell Technical Conference, Birmingham, and The A. J. V. Underwood Exhibition Award for the most promising research student pursuing a research degree in the Department of Chemical Engineering at UCL.

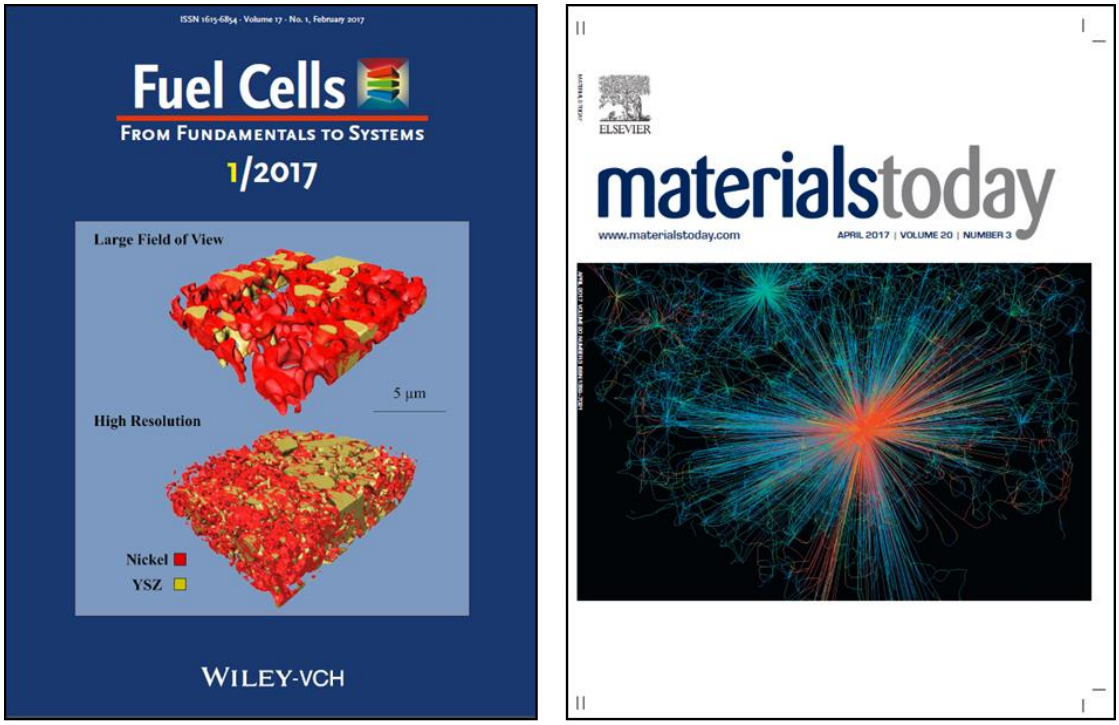

Figure 96 Journal Covers published by the author, left: Fuel Cells, and right: Materials Today.

6.4. Future Work

Although significant advancements have been presented in this work, a considerable amount of work on the optimisation of SOFC operation remains; however, the author envisages three prominent routes that future research will be directed in as a result of this thesis: innovative characterisation technique developments, advanced multi-scale modelling of highly complex systems, and prominent degradation processes beyond thermal shock e.g. such as REDOX and Ni-poisoning.

Firstly, although absorption-based transmission CT, such as the work presented here, can provide significant information about the macro- and microstructure of the cell, no crystallographic information can be obtained unless a diffraction detector is employed. Moreover, although the greyscale can be correlated to the element or compound within the voxel, all material within the voxel is averaged making elemental mapping non-trivial, often requiring confirmation from a complimentary technique. Therefore, analogous to how studies have developed from 2D, to 3D, to 4D, future studies may develop from 4D studies with a single characterisation mode, to the application of multiple complimentary methods applied in unison. Particularly, maintaining the ability to spatially resolve information with time, XRD-CT and XRF-CT may become prominent in future work.

Secondly, computational models are improving at a significant rate due to several factors including but not limited to: higher processing powers, improved algorithms and more detailed input parameters achieved from characterisation studies such as those presented in this thesis. With the enormous data libraries

that are accumulating from characterisation studies models are becoming increasingly more accurate and precise but many factors can still be incorporated to further improve real-world accuracy; for instance, to the author's knowledge no thermomechanical model exist in the literature that accounts for the Curie transition of Ni during operational thermal cycling. By combining data characterised from real structures with complex models, predictions can be made that closely reflect real-world applications.

Thirdly, SOFCs are expect to withstand many REDOX cycled during operation. This can occur if a cell gasket fails, during overutilization of the fuel or if oxygen is in the fuel-stream. Although being a well-known issue, literature on the implications of such chemical cycling on the cell structure remains limited, and is often limited to a single technique of characterisation i.e. SEM or X-ray CT. Future studies may benefit from combining multiple complimentary techniques as discussed above, and investigate operating cells near the gasket or at the inlet after fuel-stream failure. Similar studies may also be applied to carbon deposition, sulphur poisoning and other chemical issues.

6.5. Conclusions from Chapter Six

This thesis has explored the principles of SOFC technology, current limitations and characterisation methods. These methods have then bee further developed through several proof-of-concept studies, then employed across multiple length scales via macro- micro- and crystal structure degradation investigations. These results have been disseminated through journal publications conference talks and public engagement. Although this thesis demonstrates several successful studies into SOFC degradation, scope remains for future studies to further expand our understanding of these complex mechanisms using analogous investigation procedures and methods.

Chapter Seven: Appendices

Figure 97 Total list of samples discussed within the thesis.

Sample	Preparation and Scanning
S411	Powders pressed into pellets; Sintered 1200 °C 2.5 hrs in air; Reduced 800 °C 2hrs in forming gas (4% H_2 in 96 % N_2); Four samples prepared using a scalpel, each scanned in HRes & LFOV of the Ultra
S412	
S413	
S414	
S415	Pre-Fabricated anode-supported half-cell; 5 µm electrolyte on 500 µm anode; Reduced 800 °C 2 hrs in forming gas (4% H_2 in 96 % N_2); Laser Prepared: 800 µm pillar removed from bulk and refined to 350 µm; One sample scanned in the Versa at 40X magnification
S421	Ni powder pressed into pellets; Sintered 1200 °C 2.5 hrs in air; Reduced 800 °C 2hrs in forming gas (4% H_2 in 96 % N_2); One sample prepared using a scalpel; First CT conducted in the Versa at 20X magnification; Second CT conducted in the Versa at 40X magnification
S422	Ni-YSZ powder pressed into pellets; Sintered 1200 °C 2.5 hrs in air; Reduced 800 °C 2hrs in forming gas (4% H_2 in 96 % N_2); Prepared using a scalpel; Four samples prepared using a scalpel; Three samples imaged in both the LFOV and HRes of the Ultra and the last sample imaged only in the Ultra LFOV
S423	
S424	
S425	
S431	Pre-Fabricated anode-supported half-cell; 5 µm electrolyte on 500 µm anode; Laser Prepared: 800 µm pillar removed from bulk and refined to 10 µm; First CT in the LFOV of the Ultra; Reduced 800 °C 2 hrs in forming gas (4% H_2 in 96 % N_2) Second CT in the LFOV of the Ultra; Thermally cycled to 750 °C; Third CT in the LFOV of the Ultra; Laser-heated to 350 °C; Fourth CT in the LFOV of the Ultra
S511	Anode supported NiO-8YSZ/8YSZ half-cell; Reduced 800 °C 2hrs in forming gas (4% H_2 in 96 % N_2); 800 µm sample removed using a laser lathe; Refined to 350 µm for X-ray micro-CT

Figure 98 continued Total list of samples discussed within the thesis.

Sample	Preparation and Scanning
S512	A 10 µm diameter sub-sample removed from sample S511 using laser lathe
S511	Anode supported NiO-8YSZ/8YSZ half-cell; Reduced 800 °C 2hrs in forming gas (4% H_2 in 96 % N_2); 800 µm sample removed using a laser lathe; Refined to 350 µm for X-ray micro-CT
S531 to S537	Powder pressed into pellets; Sintered 1200 °C 2.5 hrs in air; Reduced 800 °C 2 hrs in forming gas (4% H_2 in 96 % N_2); Filed into powder using a diamond file; Inserted into separate capillaries with 580 µm internal diameter 10 cm in length
S531	Capillary filled with Ni powder
S532	Capillary filled with Ni-YSZ powder
S533	Capillary filled with Ni-GDC powder
S534	Capillary filled with Ni powder
S535	Capillary filled with Ni-YSZ powder
S536	Capillary filled with Ni-GDC powder
S537	Capillary filled with Ni-YSZ powder

Figure 99 Total list of the characterisation parameters for every sample.

Sample	Investigation	Scan	Instrument	Projections	Exposure Time / s	Resolution / nm or deg	FOV / µm
S411	I412	D411	Ultra LFOV	1101	45	127 nm	64 x 64
S411	I412	D412	Ultra HRes	1501	65	33 nm	16 x 16
S412	I412	D413	Ultra LFOV	1101	45	127 nm	64 x 64
S412	I412	D414	Ultra HRes	1501	65	33 nm	16 x 16
S413	I412	D415	Ultra LFOV	1101	45	127 nm	64 x 64
S413	I412	D416	Ultra HRes	1501	65	33 nm	16 x 16
S414	I412	D417	Ultra LFOV	1101	45	127 nm	64 x 64
S414	I412	D418	Ultra HRes	1501	65	33 nm	16 x 16
S415	I412	D419	Versa 40X	2401	30	395 nm	384 x 384
S421	I421	D421	Versa 20X	2401	30	800 nm	768 x 768
S421	I421	D422	Versa 40X	2401	30	400 nm	384 x 384
S422	I422	D423	Ultra HRes	1501	65	32 nm	16 x 16
S422	I422	D424	Ultra LFOV	1101	45	130 nm	64 x 64
S423	I423	D425	Ultra HRes	1501	65	32 nm	16 x 16
S423	I423	D426	Ultra LFOV	1101	45	130 nm	64 x 64
S424	I423	D427	Ultra HRes	1501	65	32 nm	16 x 16
S424	I423	D428	Ultra LFOV	1101	45	130 nm	64 x 64
S425	I424	D429	Ultra LFOV	1101	45	130 nm	64 x 64
S431	I431	D431	Ultra LFOV	1101	60	127 nm	64 x 64
S431	I431	D432	Ultra LFOV	1101	60	127 nm	64 x 64
S431	I432	D433	Ultra LFOV	1101	60	127 nm	64 x 64
S431	I432	D434	Ultra LFOV	1101	60	127 nm	64 x 64

Figure 100 continued Total list of the characterisation parameters for every sample.

Sample	Investigation	Scan	Instrument	Projections	Exposure Time / s	Resolution / nm or deg	FOV / µm
S511	I511	D511	Versa 40X	2401	30	395 nm	384 x 384
S511	I511	D512	Versa 40X	2401	30	395 nm	384 x 384
S511	I511	D513	Versa 40X	2401	30	395 nm	384 x 384
S511	I511	D514	Versa 40X	2401	30	395 nm	384 x 384
S511	I511 and I512	D515	Versa 40X	2401	30	395 nm	384 x 384
S511	I512	D516	Versa 40X	2401	30	395 nm	384 x 384
S511	I512 and I513	D517	Versa 40X	2401	30	395 nm	384 x 384
S512	I513	D518	Ultra LFOV	1101	45	126 nm	64 x 64
S511	I521	D511	Versa 40X	2401	30	395 nm	384 x 384
S511	I521	D512	Versa 40X	2401	30	395 nm	384 x 384
S511	I521	D513	Versa 40X	2401	30	395 nm	384 x 384
S511	I521	D514	Versa 40X	2401	30	395 nm	384 x 384
S511	I521	D515	Versa 40X	2401	30	395 nm	384 x 384
S531	I531	D531	X04SA-MS	N/A	60*	0.0036º	N/A
S532	I531	D532	X04SA-MS	N/A	60*	0.0036º	N/A
S533	I531	D533	X04SA-MS	N/A	60*	0.0036º	N/A
S534	I532	D534	X04SA-MS	N/A	60*	0.0036º	N/A
S535	I532	D535	X04SA-MS	N/A	60*	0.0036º	N/A
S536	I532	D536	X04SA-MS	N/A	60*	0.0036º	N/A
S537	I533	D537	X04SA-MS	N/A	60*	0.0036º	N/A

* per detector for two detectors

Below is a list of each investigation conducted within this thesis with the associated chapter section from chapter 4.

4.1. Establishing a Method for the Characterisation of TPBs in SOFC Electrodes Using Lab-Based X-ray CT

- I411 Characterisation of TPBs in SOFC Electrodes Using X-ray Nano-CT
- I412 Characterisation of TPBs in SOFC Electrodes Using X-ray Micro-CT

4.2. Inspecting the Influence of Resolution and Associated Fractal Dimensions When Characterising SOFCs.

- I421 Inspecting the Influence of Resolution on Ni Conductivity
- I422 Inspecting the Influence of Resolution on YSZ conductivity
- I423 Inspecting the Influence of Resolution TPB compared for two structures
- I424 Inspecting the Influence of Resolution on the TPB Percolation

4.3. Achieving 4D Tomography of SOFC Microstructures Using Lab-Based X-ray Instruments.

- I431 Achieving sufficient Thermal Stability
- I432 Demonstrating 4D Proof of concept

Below is a list of each investigation conducted within this thesis with the associated chapter section from chapter 5.

5.1. Macroscopic Degradation: Wall Deformation, Cell Curvature, Delamination and Crack Propagation.

I511 Implications of thermal ramp-rate on the cell macrostructure

I512 Implications of thermal cycle number on the cell macrostructure

I513 Multi-scale cracking within the anode support

5.2. Microscopic Degradation: Exploring the variations in the Tortuosity-factor, phase-percolation, surface area, interfacial contact and TPB density.

I521 Implications of thermal ramp-rate on the cell microstructure

5.3. Crystallographic Degradation: Influence of ceramic choice, non-linear expansion and stress-test cycling.

I531 Single Thermal Cycle of SOFC anode materials

I532 Inspecting the Curie transition temperature

I533 Ni-YSZ accelerated stress-test

Below is a full list of all authored journal publications, including transactions, special issues, full publications and journal covers. These are also listed within the references.

1. **Heenan, T. M. M**., Lu, X., Iacoviello, F., Robinson, J.B., Brett, D.J.L. and Shearing, P.R., 2018. Thermally Driven SOFC Degradation in 4D: Part I. Microscale. Journal of The Electrochemical Society, 165(11), pp.F921-F931.
2. **Heenan, T. M. M**., Lu, X., Robinson, J.B., Iacoviello, F., Brett, D.J.L. and Shearing, P.R., 2018. Thermally Driven SOFC Degradation in 4D: Part II. Macroscale. Journal of The Electrochemical Society, 165(11), pp.F932-F941.Fractal
3. **Heenan, T. M. M**., Lu, X., Finegan, D. P., Robinson, J.B., Iacoviello, F., Bailey, J., Brett, D.J.L. and Shearing, P.R., 2018. Structural Evolutions within a Solid Oxide Fuel Cell Tracked Using Sub-Micron Digital Volume Correlation. Sustainable Energy and Fuels, in-press.
4. **Heenan, T. M. M**., D. P. Finegan, Bernhard Tjaden, Xuekun Lu, Francesco Iacoviello, Jason Millichamp, Dan JL Brett, and Paul R. Shearing. 4D nano-tomography of electrochemical energy devices using lab-based X-ray imaging. Nano Energy 47 (2018): 556-565.
5. **Heenan, T. M. M**., Robinson, J.B., Lu, X., Tjaden, B., Cervellino, A., Bailey, J., Brett, D.J.L. and Shearing, P.R., 2018. Understanding the thermo-mechanical behaviour of solid oxide fuel cell anodes using synchrotron X-ray diffraction. Solid State Ionics, 314, pp.156-164.

6. **Heenan, T. M. M.,** Robinson, J.B., Lu, X., Bailey, J., Brett, D. J. L., and Shearing, P. R. Analysing the mechanical performance of solid oxide fuel cells at interfacial anode/electrolyte regions using sub-micron resolution 3D X-ray computed tomography. ECS Transactions 78, no. 1 (2017): 2317-2321.
7. **Heenan, T. M. M**., D. J. L. Brett, and P. R. Shearing. Mapping electrochemical activity in solid oxide fuel cells X-ray nano computed tomography of heterogeneous microstructures. Materials Today 20, no. 3 (2017): 155-156.
8. **Heenan, T. M. M**., D. J. L. Brett, and P. R. Shearing. Mapping electrochemical activity in solid oxide fuel cells X-ray nano computed tomography of heterogeneous microstructures. Materials Today Journal Cover, (2017).
9. **Heenan, T. M. M.**, Josh J. Bailey, Xuekun Lu, James B. Robinson, Francesco Iacoviello, Donal P. Finegan, D. J. L. Brett, and P. R. Shearing. Three-Phase Segmentation of Solid Oxide Fuel Cell Anode Materials Using Lab Based X-ray Nano-Computed Tomography. Fuel Cells 17, no. 1 (2017): 75-82.
10. **Heenan, T. M. M.**, Josh J. Bailey, Xuekun Lu, James B. Robinson, Francesco Iacoviello, Donal P. Finegan, D. J. L. Brett, and P. R. Shearing. Three-Phase Segmentation of Solid Oxide Fuel Cell Anode Materials Using Lab Based X-ray Nano-Computed Tomography. Fuel Cells Journal Cover (2017).
11. **Heenan, T. M. M**., D. J. L. Brett, and P. R. Shearing. X-ray attenuation properties of commonly employed solid oxide fuel cell materials. Journal of Physics, vol. 849, no. 1, p. 012017. IOP Publishing, 2017.
12. Robinson, J.B., **Heenan, T.M.M,** Jervis, J.R., Tan, C., Kendrick, E., Brett, D.J. and Shearing, P.R., 2018. Multiscale tomographic analysis of the thermal failure of Na-Ion batteries. Journal of Power Sources, 400, pp.360-368.

13. Tan, C., **Heenan, T.M.M.**, Ziesche, R.F., Daemi, S.R., Hack, J., Maier, M., Marathe, S., Rau, C., Brett, D.J. and Shearing, P.R., 2018. Four-Dimensional Studies of Morphology Evolution in Lithium-Sulfur Batteries. ACS Applied Energy Materials.
14. Hack, J., **Heenan T. M. M.,** Iacoviello F., Mansor N., Meyer Q., Shearing P., Brandon N., and Brett D. J. L.. A Structure and Durability Comparison of Membrane Electrode Assembly Fabrication Methods: Self-Assembled Versus Hot-Pressed. Journal of The Electrochemical Society 165, no. 6 (2018): F3045-F3052.
15. Lu, X., **Heenan, T.M.M,** Bailey, J.J., Li, T., Li, K., Brett, D.J. and Shearing, P.R., 2017. Correlation between triple phase boundary and the microstructure of Solid Oxide Fuel Cell anodes: The role of composition, porosity and Ni densification. Journal of Power Sources, 365, pp.210-219.
16. Bailey, J.J., **Heenan, T.M.M.,** Finegan, D.P., Lu, X., Daemi, S.R., Iacoviello, F., Backeberg, N.R., Taiwo, O.O., Brett, D.J.L., Atkinson, A. and Shearing, P.R., 2017. Laser-preparation of geometrically optimised samples for X-ray nano-CT. Journal of microscopy, 267(3), pp.384-396.
17. Tan, C., **Heenan, T.M.M.**, Ziesche, R.F., Daemi, S.R., Hack, J., Maier, M., Marathe, S., Rau, C., Brett, D.J. and Shearing, P.R., 2018. Four-dimensional studies of morphology evolution in lithium–sulfur batteries. ACS Applied Energy Materials, 1(9), pp.5090-5100.
18. Usseglio-Viretta F. L. E., Colclasure A., Mistry A., Yao K.P.C., Pouraghajan F., Finegan D.P., **Heenan T.M.M**, Abraham D.P., Mukherjee P.P., Wheeler D.R., Shearing P.R., Cooper S., Smith K., Resolving the Discrepancy in

Tortuosity Factor Estimation for Li-ion Battery Electrodes through Micro-Macro Modeling and Experiment, The Electrochemical Society, (2018), in-press.

19. Finegan D.P., Walker W., Darst J., Jervis R., **Heenan T.M.M.**, Hack J., Rack A., Shearing P.R., Keyser M., Darcy E. Li-ion battery failure: Linking external risks to internal events, Power Sources Conference Proceedings, Denver, 2018.
20. Robinson, J.B., Finegan, D.P., **Heenan, T.M.M**., Smith, K., Kendrick, E., Brett, D.J. and Shearing, P.R., 2018. Microstructural Analysis of the Effects of Thermal Runaway on Li-Ion and Na-Ion Battery Electrodes. Journal of Electrochemical Energy Conversion and Storage, 15(1), p.011010.
21. Tan, C., Daemi, S., Taiwo, O., **Heenan, T.M.M.,** Brett, D. and Shearing, P., 2018. Evolution of Electrochemical Cell Designs for In-Situ and Operando 3D Characterization. Materials, 11(11), p.2157.
22. Lu, X., Li, T., Bertei, A., Cho, J., **Heenan, T. M.M.,** Rabuni, M., Li, K., Brett, D. and Shearing, P., 2018. The Application of Hierarchical Structures in Energy Devices: New Insights into the Design of Solid Oxide Fuel Cells with Enhanced Mass Transport. Energy & Environmental Science.
23. Finegan, D.P., Darcy E., Keyser M., Tjaden B., **Heenan T.M.M**, Jervis R., Bailey J. Vo N.T., Magdysyuk O.V., Drakopoulos M., Michiel M. Di., Rack A., Hinds G., Brett D.J.L., Shearing P.R. Identifying the Cause of Rupture of Li-Ion Batteries during Thermal Runaway. Advanced Science 5, no. 1 (2018): 1700369.

24. 21. Finegan, D.P., Darcy E., Keyser M., Tjaden B., **Heenan T.M.M**, Jervis R., Bailey J. Vo N.T., Magdysyuk O.V., Drakopoulos M., Michiel M. Di., Rack A., Hinds G., Brett D.J.L., Shearing P.R. Identifying the Cause of Rupture of Li-Ion Batteries during Thermal Runaway. Advanced ScienceJournal Cover, (2017).
25. Taiwo, O. O., Paz-García, J.M., Hall S.A., **Heenan T.M.M**, Finegan D.P., Mokso R., Villanueva-Pérez P., Patera A., Brett D.J.L, and Shearing P.R. Microstructural degradation of silicon electrodes during lithiation observed via operando X-ray tomographic imaging. Journal of Power Sources 342 (2017): 904-912.
26. Finegan, D. P., Tjaden B., **Heenan T.M.M**, Jervis R., Michiel M. Di., Rack A., Hinds G., Brett DJL, and Shearing P.R. Tracking internal temperature and structural dynamics during nail penetration of lithium-ion cells. Journal of The Electrochemical Society 164, no. 13 (2017): A3285-A3291.
27. Lu, X., Li T., Taiwo O. O., Bailey J., **Heenan T.M.M**., Li K., Brett D. J. L., and Shearing P. R.. Study of the tortuosity factors at multi-scale for a novel-structured SOFC anode. In Journal of Physics: Conference Series, vol. 849, no. 1, p. 012020. IOP Publishing, 2017.
28. Finegan, D.P., Darcy, E., Keyser, M., Tjaden, B., **Heenan, T.M.M.,** Jervis, R., Bailey, J.J., Malik, R., Vo, N.T., Magdysyuk, O.V. and Atwood, R., 2017. Characterising thermal runaway within lithium-ion cells by inducing and monitoring internal short circuits. Energy & Environmental Science, 10(6), pp.1377-1388.

29. Finegan, D.P., Darcy, E., Keyser, M., Tjaden, B., **Heenan, T.M.M.,** Jervis, R., Bailey, J.J., Malik, R., Vo, N.T., Magdysyuk, O.V. and Atwood, R.,. Characterising thermal runaway within lithium-ion cells by inducing and monitoring internal short circuits. Energy & Environmental Science, Journal Cover, (2017).
30. Jervis, R., Brown L.D., Neville T.P., Millichamp J., Finegan D.P., **Heenan T.M.M.,** Brett D.J.L., and Shearing P.R.. Design of a miniature flow cell for in situ X-ray imaging of redox flow batteries. Journal of Physics D: Applied Physics 49, no. 43 (2016): 434002.
31. Robinson, J. B., Brown L.D., Jervis R., Taiwo, O.O., **Heenan T.M.M.,** Millichamp, J., Mason, T.J., Neville T.P., Clague R., Eastwood D.S., Reinhard C., Lee P. D. , Brett D. J.L., Shearing P.R. Investigating the effect of thermal gradients on stress in solid oxide fuel cell anodes using combined synchrotron radiation and thermal imaging. Journal of Power Sources 288 (2015): 473-481.

Chapter Eight: References

1. *The Paris Agreement.* Jayaraman, T. and Kanitkar, T. 2016, Economic and Political Weekly, p. 51(3).

2. *Next-Generation Batteries.* Chou, S.L. and Dou, S.X. 2017, Advanced Materials, p. 29(48).

3. *Redox flow batteries for energy storage: a technology review. .* Ye, R., Henkensmeier, D., Yoon, S.J., Huang, Z., Kim, D.K., Chang, Z., Kim, S. and Chen, R. 2018, Journal of Electrochemical Energy Conversion and Storage, pp. 15(1), p.010801.

4. *A review of durability test protocols of the proton exchange membrane fuel cells for vehicle. .* Chen, H., Song, Z., Zhao, X., Zhang, T., Pei, P. and Liang, C.,. 2018, Applied Energy, pp. 224, pp.289-299.

5. *Review of energy storage systems for electric vehicle applications: Issues and challenges. .* Hannan, M.A., Hoque, M.M., Mohamed, A. and Ayob, A.,. 2017, Renewable and Sustainable Energy Reviews, pp. 69, pp.771-789.

6. *Social acceptance of renewable energy sources: A review of contingent valuation applications.* Stigka, E.K., Paravantis, J.A. and Mihalakakou, G.K.,. 2014, Renewable and Sustainable Energy Reviews, pp. 32, pp.100-106.

7. *Grid-scale energy storage applications in renewable energy integration: A survey. .* Castillo, A. and Gayme, D.F. 2014, Energy Conversion and Management, pp. 87, pp.885-894.

8. Singhal, S.C. and Kendall, K.,. *High-temperature solid oxide fuel cells: fundamentals, design and applications.* s.l. : Elsevier, 2003.

9. Brandon, N.,. *Solid Oxide Fuel Cell Lifetime and Reliability: Critical Challenges in Fuel Cells.* s.l. : Academic Press, 2017.

10. *Fundamental mechanisms involved in the degradation of nickel–yttria stabilized zirconia (Ni–YSZ) anode during solid oxide fuel cells operation: a review. .* Khan, M.S., Lee, S.B., Song, R.H., Lee, J.W., Lim, T.H. and Park, S.J.,. 2016, Ceramics International, pp. 42(1), pp.35-48.

11. *Progress in material selection for solid oxide fuel cell technology: A review. .* Mahato, N., Banerjee, A., Gupta, A., Omar, S. and Balani, K.,. 2015, Progress in Materials Science, pp. 72, pp.141-337.

12. *High-Performance, Anode-Supported, Microtubular SOFC Prepared from Single-Step-Fabricated, Dual-Layer Hollow Fibers.* Othman, M.H.D., Droushiotis, N., Wu, Z., Kelsall, G. and Li, K. 2011, Advanced Materials, pp. 23(21), pp.2480-2483.

13. *Combined solid oxide fuel cell and gas turbine systems for efficient power and heat generation.* Palsson, J., Selimovic, A. and Sjunnesson, L. 2000, Journal of power sources, pp. 86(1-2), pp.442-448.

14. *A review of integration strategies for solid oxide fuel cells. .* Zhang, X., Chan, S.H., Li, G., Ho, H.K., Li, J. and Feng, Z. 2010, Journal of Power Sources, pp. 195(3), pp.685-702.

15. *WR Grove and the fuel cell.* Thomas, J.M.,. 2012, pp. Philosophical Magazine, 92(31), pp.3757-3765.

16. Hoogers, G. *Fuel cell technology handbook.* s.l. : CRC press, 2002.

17. *SOFC technology development at Rolls-Royce.* Gardner, F.J., Day, M.J., Brandon, N.P., Pashley, M.N. and Cassidy, M. 2000, Journal of Power Sources, pp. 86(1-2), pp.122-129.

18. Energy, Bloom. [Online] https://www.bloomenergy.com/.

19. *Solid oxide fuel cells for stationary, mobile, and military applications.* Singhal, S.C. 2002, Solid State Ionics, pp. 152, pp.405-410.

20. *Application of solid oxide fuel cell technology for power generation—A review.* Choudhury, A., Chandra, H. and Arora, A. 2013, Renewable and Sustainable Energy Reviews, pp. 20, pp.430-442.

21. *Mapping electrochemical activity in solid oxide fuel cells.* Heenan, T. M. M., Brett, D.J.L. and Shearing, P.R. 2017, Materials Today, pp. 20(3), pp.155-156.

22. *Transport properties of solid oxide electrolyte ceramics: a brief review. .* Kharton, V.V., Marques, F.M.B. and Atkinson, A. 2004, Solid State Ionics, pp. 174(1-4), pp.135-149.

23. *Towards intelligent engineering of SOFC electrodes: a review of advanced microstructural characterisation techniques.* Shearing, P. R., Brett D. J. L. , Brandon, N. P. 2010, International Materials Reviews, pp. 55, 347 – 363.

24. *A review on the status of anode materials for solid oxide fuel cells. .* Zhu, W.Z. and Deevi, S.C. 2003, Materials Science and Engineering: A, pp. 362(1-2), pp.228-239.

25. *Cathode materials for solid oxide fuel cells: a review.* Sun, C., Hui, R. and Roller, J. 2010, Journal of Solid State Electrochemistry, pp. 14(7), pp.1125-1144.

26. *Microstructural analysis of a solid oxide fuel cell anode using focused ion beam techniques coupled with electrochemical simulation.* Shearing, P., R., Cai, Q., Golbert, J.I., Yufit, V., Adjiman, C.S., Brandon, N.P. 15, s.l. : Journal of Power Sources, 2010, Journal of Power Sources, Vol. 195, pp. 195(5), pp. 4804-4810. pp 4804-4810.

27. *Computation of TPB length, surface area and pore size from numerical reconstruction of composite solid oxide fuel cell electrodes. .* Kenney, B., Valdmanis, M., Baker, C., Pharoah, J.G. and Karan, K. 2009, Journal of Power Sources, pp. 189(2), pp.1051-1059.

28. *Correlation between triple phase boundary and the microstructure of Solid Oxide Fuel Cell anodes: The role of composition, porosity and Ni densification. .* Lu, X., Heenan, T.M., Bailey, J.J., Li, T., Li, K., Brett, D.J. and Shearing, P.R. 2017, Journal of Power Sources, pp. 365, pp.210-219.

29. *Fundamental mechanisms involved in the degradation of nickel–yttria stabilized zirconia (Ni–YSZ) anode during solid oxide fuel cells operation: a review.* Khan, M.S., Lee, S.B., Song, R.H., Lee, J.W., Lim, T.H. and Park, S.J. 2016, Ceramics International, pp. 42(1), pp.35-48.

30. *Electrical properties of NiO. .* Morin, F.J.,. 1954, Physical Review, pp. 93(6), p.1199.

31. *Redox Cycling of Ni-Based Solid Oxide Fuel Cell Anodes: A Review.* Sarantaridis, D. and Atkinson, A.,. 2007, Fuel cells, pp. 7(3), pp.246-258.

32. *SOFC system operating strategies for mobile applications. .* Holtappels, P., Mehling, H., Roehlich, S., Liebermann, S.S. and Stimming, U. 2005, Fuel Cells, pp. 5(4), pp.499-508.

33. *An analysis of contact problems in solid oxide fuel cell stacks arising from differences in thermal expansion coefficients.* Blum, L.,. 2017, Electrochimica Acta, pp. 223, pp.100-108.

34. *Thermal expansion of magnetic metals at low temperatures.* White, G. K.,. 1965, Proc. Phys. Soc., pp. 86, 159.

35. *Low temperature thermal expansion of some metallic alloys.* Clark, A. F. ,. 1968, Cryogenics, pp. 8(5), pp. 282 – 289.

36. *Totskii, E. E., Teplofiz. Vys. 1964, Temp. , pp. 2, 205 .*

37. Über eine einrichtung zur photographischen aufzeichnung der linearenwärmeausdehnungvonmetallen. Ausdehnungskoeffizient von kupfer und nickel. Rosenbohm, E.,. 1938, Physica, pp. 5, 385.

38. Kirby, ,R. K.,. American Institute of Physics Handbook, . New York : 2nd ed., McGraw-Hill, pp. 4-64., 1963.

39. High temperature thermal expansion of six metallic elements measured by dilatation method and X - ray diffraction,. K. Suh, H. Ohta, Y. Waseda,. s.l. : Journal of Material Science, 23, 757 - 760, (, 1988, Journal of Material Science, , pp. 23, 757 - 760.

40. Thermal Expansion of Nickel-Zirconia Anodes in Solid Oxide Fuel Cells during Fabrication and Operation. Mori, M., Yamamoto, T., Itoh, H., Inaba, H. and Tagawa, H.,. 1998, Journal of the Electrochemical Society, pp. 145(4), pp.1374-1381.

41. Investigating the effect of thermal gradients on stress in solid oxide fuel cell anodes using combined synchrotron radiation and thermal imaging. . Robinson, J.B., Brown, L.D., Jervis, R., Taiwo, O.O., Heenan, T.M., Millichamp, J., Mason, T.J., Neville, T.P., Clague, R., Eastwood, D.S. and Reinhard, C., Lee, P., Brett, D., Shearing, P.,. 2015, Journal of Power Sources, pp. 288, pp.473-481.

42. Strong metal support interactions of infiltrated Ni with TiO2 in a porous YSZ anode matrix-A possible method for Ni-stabilization. . Singh, C.A., Bansal, L., Tiwari, P. and Krishnan, V.V.,. 2009, ECS Transactions, pp. 25(2), pp.1897-1904.

43. Observing the microstructural evolution of Ni-Yttria-stabilized zirconia solid oxide fuel cell anodes. . Kennouche, D., Chen-Wiegart, Y.C.K., Yakal-Kremski, K.J., Wang, J., Gibbs, J.W., Voorhees, P.W. and Barnett, S.A.,. 2016, Acta Materialia, pp. 103, pp.204-210.

44. Advances, aging mechanisms and lifetime in solid-oxide fuel cells. Tu, H. and Stimming, U.,. 2004, Journal of power sources, pp. 127(1-2), pp.284-293.

45. Stress analysis of solid oxide fuel cell anode microstructure reconstructed from focused ion beam tomography. Clague, R., Shearing, P.R., Lee, P.D., Zhang, Z., Brett, D.J.L., Marquis, A.J. and Brandon, N.P. 2011, Journal of Power Sources, pp. 196(21), pp.901.

46. Three dimensional stress analysis of solid oxide fuel cell anode micro structure. Celik, S., Ibrahimoglu, B., Toros, S. and Mat, M.D.,. 2014, International Journal of Hydrogen Energy, pp. 39(33), pp.19119-19131.

47. Three-dimensional microstructural imaging of sulfur poisoning-induced degradation in a Ni-YSZ anode of solid oxide fuel cells. Harris, W.M., Lombardo, J.J., Nelson, G.J., Lai, B., Wang, S., Vila-Comamala, J., Liu, M., Liu, M. and Chiu, W.K.,. 2014, Scientific reports, pp. 4, p.5246.

48. Three-dimensional reconstruction of a solid-oxide fuel-cell anode. . Wilson, J.R., Kobsiriphat, W., Mendoza, R., Chen, H.Y., Hiller, J.M., Miller, D.J., Thornton, K., Voorhees, P.W., Adler, S.B. and Barnett, S.A.,. 2006, Nature materials, pp. 5(7), p.541.

49. Quantification of SOFC anode microstructure based on dual beam FIB-SEM technique. . Iwai, H., Shikazono, N., Matsui, T., Teshima, H., Kishimoto, M., Kishida, R., Hayashi, D., Matsuzaki, K., Kanno, D., Saito, M. and Muroyama, H. 210, Journal of Power Sources, pp. 195(4), pp.955-961.

50. Effect of Ni content in SOFC Ni-YSZ cermets: A three-dimensional study by FIB-SEM tomography. . Vivet, N., Chupin, S., Estrade, E., Richard, A., Bonnamy,

S., Rochais, D. and Bruneton, E. 2011, Journal of Power Sources, pp. 196(23), pp.9989-9997.

51. Reconstruction of porous electrodes by FIB/SEM for detailed microstructure modeling. . Joos, J., Carraro, T., Weber, A. and Ivers-Tiffée, E. 2011, Journal of Power Sources, pp. 196(17), pp.7302-7307.

52. Quantitative three-dimensional microstructure of a solid oxide fuel cell cathode. . Wilson, J.R., Duong, A.T., Gameiro, M., Chen, H.Y., Thornton, K., Mumm, D.R. and Barnett, S.A. 2009, Electrochemistry Communications, pp. 11(5), pp.1052-1056.

53. Evaluation of SOFC anode polarization simulation using three-dimensional microstructures reconstructed by FIB tomography. Kanno, D., Shikazono, N., Takagi, N., Matsuzaki, K. and Kasagi, N. 2011, Electrochimica Acta, pp. 56(11), pp.4015-4021.

54. Numerical assessment of SOFC anode polarization based on three-dimensional model microstructure reconstructed from FIB-SEM images. Shikazono, N., Kanno, D., Matsuzaki, K., Teshima, H., Sumino, S. and Kasagi, N. 2010, Journal of The Electrochemical Society, pp. 157(5), pp.B665-B672.

55. 3D reconstruction of SOFC anodes using a focused ion beam lift-out technique. Shearing, P. R., Golbert, J., Chater, R.J. and Brandon, N.P. 2009, Chemical Engineering Science, pp. 64(17), pp.3928-3933.

56. X-ray nano computerised tomography of SOFC electrodes using a focused ion beam sample-preparation technique. . Shearing, P.R., Gelb, J. and Brandon, N.P. 2010, Journal of the European Ceramic Society, pp. 30(8), pp.1809-1814.

57. Three-dimensional reconstruction and analysis of an entire solid oxide fuel cell by full-field transmission X-ray microscopy. Cronin, J.S., Chen-Wiegart, Y.C.K., Wang, J. and Barnett, S.A. 2013, Journal of Power Sources, pp. 233, pp.174-179.

58. Comparison of SOFC cathode microstructure quantified using X-ray nanotomography and focused ion beam–scanning electron microscopy. . Nelson, G.J., Harris, W.M., Lombardo, J.J., Izzo Jr, J.R., Chiu, W.K., Tanasini, P., Cantoni, M., Comninellis, C., Andrews, J.C., Liu, Y. and Pianetta, P. 2011, Electrochemistry Communications, pp. 13(6), pp.586-589.

59. Analysis of the three-dimensional microstructure of a solid-oxide fuel cell anode using nano X-ray tomography. Guan, Y., Li, W., Gong, Y., Liu, G., Zhang, X., Chen, J., Gelb, J., Yun, W., Xiong, Y., Tian, Y. and Wang, H. 2011, Journal of Power Sources, pp. 196(4), pp.1915-1919.

60. 3D Non-destructive morphological analysis of a solid oxide fuel cell anode using full-field X-ray nano-tomography. . Chen-Wiegart, Y.C.K., Cronin, J.S., Yuan, Q., Yakal-Kremski, K.J., Barnett, S.A. and Wang, J. 2012, Journal of Power Sources, pp. 218, pp.348-351.

61. Analysis of triple phase contact in Ni–YSZ microstructures using non-destructive X-ray tomography with synchrotron radiation. Shearing, P.R., Gelb,

J., Yi, J., Lee, W.K., Drakopolous, M. and Brandon, N.P. 2010, Electrochemistry Communications, pp. 12(8), pp.1021-1024.

62. Nondestructive reconstruction and analysis of SOFC anodes using X-ray computed tomography at sub-50 nm resolution. . Izzo, J.R., Joshi, A.S., Grew, K.N., Chiu, W.K., Tkachuk, A., Wang, S.H. and Yun, W. 2008, Journal of the Electrochemical Society, pp. 155(5), pp.B504-B508.

63. Effect of Ni content on the morphological evolution of Ni-YSZ solid oxide fuel cell electrodes. Chen-Wiegart, Y.C.K., Kennouche, D., Scott Cronin, J., Barnett, S.A. and Wang, J. 2016, Applied Physics Letters, pp. 108(8), p.083903.

64. Using synchrotron X-ray nano-CT to characterize SOFC electrode microstructures in three-dimensions at operating temperature. . Shearing, P.R., Bradley, R.S., Gelb, J., Lee, S.N., Atkinson, A., Withers, P.J. and Brandon, N.P. 2011, Electrochemical and Solid-State Letters, pp. 14(10), pp.B117-B120.

65. Exploring microstructural changes associated with oxidation in Ni–YSZ SOFC electrodes using high resolution X-ray computed tomography. Shearing, P. R. , Bradley, R.S., Gelb, J., Tariq, F., Withers, P.J. and Brandon, N.P. 2012, Solid State Ionics, pp. 216, pp.69-72.

66. Microscopic techniques for analysis of ceramic fuel cells. . Jouttijärvi, S., Asghar, M.I. and Lund, P.D.,. 2018, Wiley Interdisciplinary Reviews: Energy and Environment.

67. Digital volume correlation: three-dimensional strain mapping using X-ray tomography. Bay, B.K., Smith, T.S., Fyhrie, D.P. and Saad, M.,. s.l. :

Experimental mechanics, 1999, Experimental mechanics,, Vols. 39(3),, pp. pp.217-226.

68. An evaluation of digital image correlation criteria for strain mapping applications. Tong, W. s.l. : Strain , 2005, Strain, Vol. 41(4), pp. pp.167-175.

69. Determination of global and local residual stresses in SOFC by X-ray diffraction. . Villanova, J., Sicardy, O., Fortunier, R., Micha, J.S. and Bleuet, P.,. 2010, Nuclear Instruments and Methods in PhysicsResearch Section B: Beam Interactions with Materials and Atoms, pp. 268(3-4), pp.282-286.

70. Mechanical characterization of SOFC/SOEC cells. Wei, J., Osipova, T., Malzbender, J. and Krüger, M. 2018, Ceramics International.

71. Improvement on durability and thermal cycle performance for solid oxide fuel cell stack with external manifold structure. . Yang, J., Yan, D., Huang, W., Li, J., Pu, J., Chi, B. and Jian, L. 2018, Energy, pp. 149, pp.903-913.

72. Mechanism of chromium poisoning the conventional cathode material for solid oxide fuel cells. . Zhang, X., Yu, G., Zeng, S., Parbey, J., Xiao, S., Li, B., Li, T. and Andersson, M. 2018, Journal of Power Sources, pp. 381, pp.26-29.

73. A novel high-temperature furnace for combined in situ synchrotron X-ray diffraction and infrared thermal imaging to investigate the effects of thermal gradients upon the structure of ceramic materials. . Robinson, J.B., Brown, L.D., Jervis, R., Taiwo, O.O., Millichamp, J., Mason, T.J., Neville, T.P., Eastwood, D.S., Reinhard, C., Lee, P.D. and Brett, D.J., Shearing, P. R.,. 2014, Journal of synchrotron radiation, pp. 21(5), pp.1134-1139.

74. Changes of internal stress in solid-oxide fuel cell during red-ox cycle evaluated by in situ measurement with synchrotron radiation. . Sumi, H., Ukai, K., Yokoyama, M., Mizutani, Y., Doi, Y., Machiya, S., Akiniwa, Y. and Tanaka, K.,. 68-74, s.l. : Journal of Fuel Cell Science and Technology, 2006, Changes of internal stress in solid-oxide fuel cell during red-ox cycle evaluated by in situ measurement with synchrotron radiation. , Vol. 3(1), pp. 3(1), pp.68-74.

75. In situ synchrotron measurement of internal stresses in solid-oxide fuel cell during red-ox cycle. In Materials Science Forum (Vol. 571, pp. 339-344). . Tanaka, K., Akiniwa, Y., Kimura, H., Ukai, K., Yokayama, M. and Mizutani, Y.,. 2008, Trans Tech Publications.

76. Multiscale measurements of residual strains in a stabilized zirconia layer. Villanova, J., Maurice, C., Micha, J.S., Bleuet, P., Sicardy, O. and Fortunier, R. 2012, Journal of Applied Crystallography, pp. 45(5), pp.926-935.

77. Tables of X-ray mass attenuation coefficients and mass energy-absorption coefficients 1 keV to 20 MeV for elements Z= 1 to 92 and 48 additional substances of dosimetric interest (No. PB--95-220539/XAB; NISTIR--5632). Hubbell, J.H. and Seltzer, S.M.,. s.l. : National Inst. of Standards and Technology-PL, Gaithersburg, MD (United States). , 1995, National Inst. of Standards and Technology-PL, Gaithersburg, MD (United States). .

78. Winick, H. and Doniach, S. Synchrotron radiation research. s.l. : Springer Science & Business Media, 2012.

79. Synchrotron radiation. Akademia Nauk SSSR, Moskovskoie Obshchestvo Ispytatelei prirody. Sektsia Fiziki. Sokolov, A.A. and Ternov, I.M.,. 1966, Sinkhrotron Radiation, Nauka Eds., Moscow,, p. 228 pp.

80. Principles and applications of zone plate X-ray microscopes. . Howells, M., Jacobsen, C., Warwick, T. and Van den Bos, A.,. 2007, In Science of microscopy, Springer New York., pp. pp. 835-926.

81. Charge-coupled device area X-ray detectors. . Gruner, S.M., Tate, M.W. and Eikenberry, E.F. 2002, Review of Scientific Instruments, pp. 73(8), pp.2815-2842.

82. X-ray interactions: photoabsorption, scattering, transmission, and reflection at E=50-30000 eV, Z=1-92. B.L. Henke, E.M. Gullikson, and J.C. Davis. 1993, Atomic Data and Nuclear Data Tables Vol. 54 (no.2), pp. pp.181-342 .

83. Van Grieken, R. and Markowicz, A.,. Handbook of X-ray Spectrometry. s.l. : CRC Press, 2001.

84. Early history of X rays. Beam Line. Assmus, A.,. 1995. , pp. 25(2), pp.10-24.

85. Why do commercial CT scanners still employ traditional, filtered back-projection for image reconstruction? Pan, X., Sidky, E.Y. and Vannier, M. 2009, Inverse problems, pp. 25(12), p.123009.

86. TOMCAT: A beamline for TOmographic Microscopy and Coherent rAdiology experimenTs. Stampanoni, M., Groso, A., Isenegger, A., Mikuljan, G., Chen, Q., Meister, D., Lange, M., Betemps, R., Henein, S. and Abela, R.,. 2007, AIP Conference.

87. X-ray computed tomography in Zernike phase contrast mode at 8 keV with 50-nm resolution using Cu rotating anode X-ray source. . Tkachuk, A., Duewer, F., Cui, H., Feser, M., Wang, S. and Yun, W.,. 2007, Zeitschrift für Kristallographie-Crystalline Materials, 222(11/2007), , pp. pp.650-655.

88. Laser-preparation of geometrically optimised samples for X-ray nano-CT. . Bailey, J.J., Heenan, T.M.M., Finegan, D.P., Lu, X., Daemi, S.R., Iacoviello, F., Backeberg, N.R., Taiwo, O.O., Brett, D.J.L., Atkinson, A. and Shearing, P.R.,. 2017, Journal of microscopy, pp. 267(3), pp.384-396.

89. TauFactor: An open-source application for calculating tortuosity factors from tomographic data. Cooper, S.J., Bertei, A., Shearing, P.R., Kilner, J.A. and Brandon, N.P.,. 2016, SoftwareX, pp. 5, pp.203-210.

90. Microstructural modeling of solid oxide fuel cell anodes. Golbert, J., Adjiman, C.S. and Brandon, N.P. 2008, Industrial & Engineering Chemistry Research, pp. 47(20), pp.7693-7699.

91. NIH Image to ImageJ: 25 years of image analysis. . Schneider, C.A., Rasband, W.S. and Eliceiri, K.W.,. 2012, Nature methods, pp. 9(7), pp.671-675.

92. On tortuosity and the tortuosity factor in flow and diffusion through porous media. . Epstein, N.,. 1989, Chemical Engineering Science, pp. 44(3): p. 777-779.

93. Segmentation of color fundus images of the human retina: Detection of the optic disc and the vascular tree using morphological techniques. . Walter, T. and

Klein, J.C. 2001, International Symposium on Medical Data Analysis , pp. pp. 282-287.

94. Distance-ordered homotopic thinning: a skeletonization algorithm for 3D digital images. Pudney, C. 1998, Computer Vision and Image Understanding, pp. 72(3), pp.404-413.

95. Comparison of three-dimensional analysis and stereological techniques for quantifying lithium-ion battery electrode microstructures. . Taiwo, O.O., Finegan, D.P., Eastwood, D.S., Fife, J.L., Brown, L.D., Darr, J.A., Lee, P.D., Brett, D.J. and Shearing, P.R.,. 2016, Journal of microscopy, pp. 263(3), pp.280-292.

96. Three-Phase Segmentation of Solid Oxide Fuel Cell Anode Materials Using Lab Based X-ray Nano-Computed Tomography. . Heenan, T.M.M., Bailey, J.J., Lu, X., Robinson, J.B., Iacoviello, F., Finegan, D.P., Brett, D.J.L. and Shearing, P.R., 2017. Three-Phase Segmentation of Solid Oxide Fuel Cell Anode Materials Using Lab Based X-ray Nano-Computed Tomography. Fuel Cells, 17(1. 2017, Fuel Cells, pp. 17(1), pp.75-82.

97. The fractal nature of the three-phase boundary: A heuristic approach to the degradation of nanostructured solid oxide fuel cell anodes. . Bertei, A., Ruiz-Trejo, E., Kareh, K., Yufit, V., Wang, X., Tariq, F. and Brandon, N.P.,. 2017, Nano Energy , pp. 38, pp.526-536.

98. How long is the coast of Britain? Statistical self-similarity and fractional dimension. . Mandelbrot, B.,. 1967, Science, pp. 156(3775), pp.636-638.

99. Fractal character of fracture surfaces of metals. Mandelbrot, B.B., Passoja, D.E. and Paullay, A.J.,. 1984, Nature, pp. 308(5961), p.721.

100. Characterization of pore-fracture networks and their evolution at various measurement scales in coal samples using X-ray μCT and a Fractal method. Zhou, H.W., Zhong, J.C., Ren, W.G., Wang, X.Y. and Yi, H.Y.,. 2018, International Journal of Coal Geology, Vols. 189, , pp. pp. 35-49.

101. Fractal assembly of micrometre-scale DNA origami arrays with arbitrary patterns. . Tikhomirov, G., Petersen, P. and Qian, L.,. 2017, Nature, pp. 552(7683), p.67.

102. Fractal stream chemistry and its implications for contaminant transport in catchments. . Kirchner, J.W., Feng, X. and Neal, C.,. 2000, Nature, pp. 403(6769), p.524.

103. Fractal structure in the volumetric contrast enhancement of malignant gliomas as a marker of oxidative metabolic pathway gene expression. . Miller, K.J., Berendsen, S., Seute, T., Yeom, K., Gephardt, M.H., Grant, G.A. and Robe, P.A.,. 2017, Translational Cancer Research.

104. Characterisation of Solid Oxide Fuel Cell Ni–8YSZ substrate by synchrotron X-ray nano-tomography: from 3D reconstruction to microstructure quantification. J. Laurencin, R. Quey, G. Delette, H. Suhonen, P. Cloetens, P. Bleuet,. 2012, Journal of Power Sources, pp. 198, 182 – 189.

105. TomoWarp2: a local digital volume correlation code. Tudisco, E., Andò, E., Cailletaud, R. and Hall, S.A. 2017, SoftwareX, Vols. 6, , pp. pp.267-270.

106. Towards high performance digital volume correlation. Gates, M., Lambros, J. and Heath, M.T. 2011, Experimental Mechanics, pp. 51(4), pp.491-507.

107. Quantifying Bulk Electrode Strain and Material Displacement within Lithium Batteries via High-Speed Operando Tomography and Digital Volume Correlation. . Finegan, D.P., Tudisco, E., Scheel, M., Robinson, J.B., Taiwo, O.O., Eastwood, D.S., Lee, P.D., Di Michiel, M., Bay, B., Hall, S.A. and Hinds, G., P. R. Shearing. 2016, Advanced Science, p. 3(3).

108. The materials science beamline upgrade at the Swiss Light Source. . Willmott, P.R., Meister, D., Leake, S.J., Lange, M., Bergamaschi, A., Böge, M., Calvi, M., Cancellieri, C., Casati, N., Cervellino, A. and Chen, Q.,. 2013, Journal of synchrotron radiation, pp. 20(5), pp.667-682.

109. Nickel–Zirconia Anode Degradation and Triple Phase Boundary Quantification from Microstructural Analysis. A. Faes, A. Hessler-Wyser, D. Presvytes, C. G. Vaynas, J. Van herle,. 2009, Fuel Cells, pp. 6, 841 – 851.

110. Modelling the effects of measured anode triple-phase boundary densities on the performance of micro-tubular hollow fiber SOFCs. U. Doraswami, P. Shearing, N. Droushiotis, K. Li, N. P. Brandon, G. H. Kelsall,. 2011, Solid State Ionics, pp. 192, 494 – 500.

111. Designing an optimal 3D microstructure for three-phase solid oxide fuel cell anodes with maximal active triple phase boundary length (TPBL). M. M. Sebdani, M. Baniassadi, J. Jamali, M. Ahadiparast, K. Abrinia, M. Safdari,. 2015, Journal of Hydrogen Energy, pp. 40, 15585 – 15596.

112. 3D reconstruction of SOFC anodes using a focused ion beam lift-out technique. . Shearing, P.R., Golbert, J., Chater, R.J. and Brandon, N.P. 2009, Chemical Engineering Science, pp. 64(17), pp.3928-3933.

113. 3D Microstructural characterization of a solid oxide fuel cell anode reconstructed by focused ion beam tomography. N. Vivet, S. Chupin, E. Estrade, T. Piquero, P.L. Pommier, D. Rochais, E. Bruneton,. 2011, Journal of Power Sources, pp. 2011, 196, 7541 – 7549.

114. Non invasive, multiscale 3D X-Ray characterization of porous functional composites and membranes, with resolution from MM to sub 50 NM. Lau, Y. S. H., C. Wilson, F. Garzon, H. Chang, A. Tkachuk, M. Feser,. 2009, Journal of Physics: Conference Series,, pp. 152, 12 – 59.

115. X-ray nano computerised tomography of SOFC electrodes using a focused ion beam sample-preparation technique. Shearing, P.,R., Gelb, J. and Brandon, N.P. 2010, Journal of the European Ceramic Society, pp. 30(8), pp.1809-1814.

116. Exploring microstructural changes associated with oxidation in Ni–YSZ SOFC electrodes using high resolution X-ray computed tomography. . Shearing, P.R., Bradley, R.S., Gelb, J., Tariq, F., Withers, P.J. and Brandon, N.P. 2012, Solid State Ionics, pp. 216, pp.69-72.

117. FuelCellMaterials. Nickel Oxide – YSZ anode Powder for General Applications. [Online] http://FuelCellmaterials.com.

118. Quantitative characterization of SOFC nickel-YSZ anode microstructure degradation based on focused-ion-beam 3D-reconstruction technique. Jiao, Z.,

Shikazono, N. and Kasagi, N. 2012, Journal of The Electrochemical Society, pp. 159(3), pp.B285-B291.

119. Representative elementary volume estimation for porosity, moisture saturation, and air-water interfacial areas in unsaturated porous media: Data quality implications. Costanza-Robinson, M.S., Estabrook, B.D. and Fouhey, D.F. 2011, Water Resources Research, p. 47(7).

120. The effect of fractal surface roughness on diffusion and reaction in porous catalysts–from fundamentals to practical applications. . Coppens, M.O. 1999, Catalysis Today, pp. 53(2), pp.225-243.

121. Tortuosity in electrochemical devices: a review of calculation approaches. Tjaden, B., Brett, D.J. and Shearing, P.R.,. 2018, International Materials Reviews, pp. 63(2), pp.47-67.

122. The Application of Hierarchical Structures in Energy Devices: New Insights into the Design of Solid Oxide Fuel Cells with Enhanced Mass Transport . Lu, X., Li, T., Bertei, A., Cho, J., Heenan, T., Rabuni, M., Li, K., Brett, D. and Shearing, P., R.,. 2018, Energy & Environmental Science.

123. A review on micro-level modeling of solid oxide fuel cells. Timurkutluk, B. and Mat, M.D.,. 2016, International Journal of Hydrogen Energy, pp. 41(23), pp.9968-9981.

124. Nanoscale chemical mapping of Li-ion battery cathode material by FIB-SEM and TOF-SIMS multi-modal microscopy. . Sui, T., Song, B., Dluhos, J., Lu, L. and Korsunsky, A.M.,. 2015, Nano Energy, pp. 17, pp.254-260.

125. Morphology of nanoporous carbon-binder domains in Li-ion batteries—A FIB-SEM study. Vierrath, S., Zielke, L., Moroni, R., Mondon, A., Wheeler, D.R., Zengerle, R. and Thiele, S.,. 2015, Electrochemistry Communications, pp. 60, pp.176-179. .

126. On the Mechanism of Low-Temperature Oxidation (23°–450° C) of Polycrystalline Nickel. Graham, M.J. and Cohen, M. 7, 879-882, s.l. : J. Electrochem. Soc., 1972, Journal of the Electrochemical Society, Vols. 119, , pp. 119(7), pp.879-882.

127. High-pressure and high-temperature electrical resistivity of ferromagnetic transition metals: Nickel and iron. Yousuf, M., Sahu, P.C. and Rajan, K.G. 1986, Physical Review B, pp. 34(11), p.8086.

128. Mechanical properties of NiO/Ni–YSZ composites depending on temperature, porosity and redox cycling. Pihlatie, M., Kaiser, A. and Mogensen, M.,. 2009, Journal of the European Ceramic Society, pp. 29(9), pp.1657-1664.

129. Thermophysical properties of YSZ and Ni-YSZ as a function of temperature and porosity. Radovic, M., Lara-Curzio, E., Trejo, R.M., Wang, H. and Porter, W.D.,. 2009, Advances in Solid Oxide Fuel Cells II: Ceramic Engineering and Science Proceedings, Cocoa Beach, pp. Volume 27, (4), p.79.

130. Residual stress and thermal cycling of planar solid oxide fuel cells. Atkinson, A. and Sun, B. 2007, Materials Science and Technology, pp. 23(10), pp.1135-1143.

131. Thermally Driven SOFC Degradation in 4D: Part II. Macroscale. Heenan, T.M.M., Lu, X., Robinson, J., Iacoviello, F., Brett, J. L. B., Shearing, P.R.,. 2018, Journal of The Electrochemical Society,, pp. 165(11), pp.F932-F941.

132. A high-performance cathode for the next generation of solid-oxide fuel cells. Shao, Z. and Haile, S.M.,. 2004, Nature, pp. 431(7005), pp.170-173.

133. Configurational and electrical behavior of Ni-YSZ cermet with novel microstructure for solid oxide fuel cell anodes. . Itoh, H., Yamamoto, T., Mori, M., Horita, T., Sakai, N., Yokokawa, H. and Dokiya, M.,. 1997, Journal of the Electrochemical Society, pp. 144(2), ppp. 641-646.

134. Lu, X., Li, T., Taiwo, O.O., Bailey, J., Heenan, T., Li, K., Brett, D.J.L. and Shearing, P.R.,. 2017,, In Journal of Physics: Conference Series,, pp. Vol. 849, No. 1, p. 012020,.

135. A redox-stable efficient anode for solid-oxide fuel cells. Tao, S. and Irvine, J.T.,. 2003, Nature materials, pp. 2(5), pp.320-323.

136. The degradation of SOFC electrodes. Hsiao, Y.C. and Selman, J.R.,. 1997, Solid State Ionics, pp. 98(1), pp.33-38.

137. Analysis of bi-metal thermostats. Timoshenko, S.,. 1925, JOSA, pp. 11(3), pp.233-255.

138. Effect of hydration and crack orientation on crack-tip strain, crack opening displacement and crack-tip shielding in elephant dentin. Lu, X., Rawson, S.D. and Withers, P.J.,. 2018, Dental Materials.

139. 3D phase mapping of solid oxide fuel cell YSZ/Ni cermet at the nanoscale by holographic X-ray nanotomography. Julie, V., Jérôme, L., Peter, C., Pierre, B., Gérard, D., Heikki, S. and François, U.V.,. 2013, Journal of Power Sources, pp. 243, pp.841-849.

140. Characterisation of Solid Oxide Fuel Cell Ni–8YSZ substrate by synchrotron X-ray nano-tomography: from 3D reconstruction to microstructure quantification. Laurencin, J., Quey, R., Delette, G., Suhonen, H., Cloetens, P. and Bleuet, P. 2012, Journal of Power Sources, pp. 198, pp. 182 - 189.

141. A numerical tool to estimate SOFC mechanical degradation: case of the planar cell configuration. . Laurencin, J., Delette, G., Lefebvre-Joud, F. and Dupeux, M.,. 2008, Journal of the European Ceramic Society, pp. 28(9), pp.1857-1869.

142. Analyzing the Mechanical Performance of Solid Oxide Fuel Cells at Interfacial Anode/Electrolyte Regions Using Sub-Micron Resolution 3D X-Ray Computed Tomography. Heenan, T.M., Robinson, J.B., Lu, X., Bailey, J.J., Brett, D.J. and Shearing, P.R.,. 2017, ECS Transactions , pp. 78(1), pp. 2317 - 2321.

143. 4D nano-tomography of electrochemical energy devices using lab-based X-ray imaging. Heenan, T.M.M., Finegan, D.P., Tjaden, B., Lu, X., Iacoviello, F., Millichamp, J., Brett, D.J. and Shearing, P.R.,. 2018, Nano Energy, pp. 47, pp.556-565.

144. Fracture mechanics by three-dimensional crack-tip synchrotron X-ray microscopy. . Withers, P.J. 2015, Phil. Trans. R. Soc. A, pp. 373(2036), p.20130157.

145. Lithium-induced dilation mapping in a lithium-ion batttery electrode by 3D X-ray microscopy and digital volume correlation . Eastwood, D.S., Yufit, V., Gelb, J., Gu, A., Bradley, R.S., Harris, S.J., Brett, D.J., Brandon, N.P., Lee, P.D., Withers, P.J. and Shearing, P.R.,. 2014, Advanced Energy Materials, p. 4(4).

146. Investigation of cycling-induced microstructural degradation in silicon-based electrodes in lithium-ion batteries using X-ray nanotomography. Paz-Garcia, J.M., Taiwo, O.O., Tudisco, E., Finegan, D.P., Shearing, P.R., Brett, D.J.L. and Hall, S.A.,. 2016, , Journal of Power Sources, , pp. 320, pp.196-203.

147. Thermally Driven SOFC Degradation in 4D: Part I. Microscale. Heenan, T.M.M., Lu, X., Iacoviello, F., Robinson, J., Brett, J. L. B., Shearing, P.R.,. 2018, , Journal of The Electrochemical Society, , pp. 165(11), pp.F921-F931.

148. intering behavior of Ni/Y2O3-ZrO2cermet electrodes of solid oxide fuel cells. Jiang, S.P.,. 2003,, Journal of materials science, , pp. 38(18), pp.3775-3782.

149. Study of the tortuosity factors at multi-scale for a novel-structured SOFC anode. . Lu, X., Li, T., Taiwo, O.O., Bailey, J., Heenan, T., Li, K., Brett, D.J.L. and Shearing, P.R.,. 2017, Journal of Physics: Conference Series, pp. Vol. 849, No. 1, p. 012020.

150. Quantitative analysis of micro structural and conductivity evolution of Ni-YSZ anodes during thermal cycling based on nano-computed tomography. . Guan, Y.,

Gong, Y., Li, W., Gelb, J., Zhang, L., Liu, G., Zhang, X., Song, X., Xia, C., Xiong, Y. and Wang, H. 2011, Journal of Power Sources, pp. 196(24), pp.10601-10605.

151. Nickel Depletion and Agglomeration in SOFC Anodes During Long-Term Operation. . Zekri, A., Herbrig, K., Knipper, M., Parisi, J. and Plaggenborg, T.,. 2017, Fuel Cells, pp. 17(3), pp.359-366.

152. Microstructure and electrical conductivity of nanocrystalline nickel-and nickel oxide/gadolinia-doped ceria thin films. . Muecke, U.P., Graf, S., Rhyner, U. and Gauckler, L.J.,. 2008, Acta Materialia, pp. 56(4), pp.677-687.

153. Fundamental mechanisms limiting solid oxide fuel cell durability. . Yokokawa, H., Tu, H., Iwanschitz, B. and Mai, A. 2008, Journal of Power Sources, pp. 182(2), pp.400-412.

154. Yttria-stabilized zirconia (YSZ) supported Ni–Co alloys (precursor of SOFC anodes) as catalysts for the steam reforming of ethanol. . Resini, C., Delgado, M.C.H., Presto, S., Alemany, L.J., RiaNi, P., Marazza, R., Ramis, G. and Busca, G.,. 2008, Journal of Hydrogen Energy, pp. 33(12), pp. 2580-2588.

155. Thermal stress analysis of a planar SOFC stack. . Lin, C.K., Chen, T.T., Chyou, Y.P. and Chiang, L.K.,. 2007, Journal of Power Sources, pp. 164(1), pp.238-251. .

156. Thermo-electrochemical and thermal stress analysis for an anode-supported SOFC cell. . Chiang, L.K., Liu, H.C., Shiu, Y.H., Lee, C.H. and Lee, R.Y.,. 2008, Renewable Energy, , pp. 33(12), pp.2580-2588. .

157. Onset of room temperature ferromagnetism by plastic deformation in three paramagnetic pure metals. . Cepeda-Jiménez, C.M., Hernando, A., Barandiarán, J.M. and Pérez-Prado, M.T.,. 2016. , Scripta Materialia, , pp. 118, pp. 41-45.

158. Evolution of structure and magnetic properties with annealing temperature in nanoscale high-energy-milled nickel ferrite. . Šepelák, V., Baabe, D., Mienert, D., Schultze, D., Krumeich, F., Litterst, F.J. and Becker, K.D.,. 2003., Journal of Magnetism and Magnetic Materials , pp. 257(2), pp. 377-386.

159. Anode microstructural change upon long-term operation for the cathode-supported tubular-type SOFC. Matsui, T., Kim, J.Y., Muroyama, H., Shimazu, M., Abe, T., Miyao, M. and Eguchi, K.,. 2012. , Solid State Ionics,, pp. 225, pp.50-54.

160. Chromatogram baseline estimation and denoising using sparsity (BEADS). . Ning, X., Selesnick, I.W. and Duval, L. 2014, Chemometrics and Intelligent Laboratory Systems, pp. 139, pp.156-167.

161. Impedance of SOFC electrodes: A review and a comprehensive case study on the impedance of LSM: YSZ cathodes. . Nielsen, J. and Hjelm, J.,. 2014. , Electrochimica Acta, , pp. 115, pp.31-45.

162. Über eine einrichtung zur photographischen aufzeichnung der linearenwärmeausdehnungvonmetallen. Ausdehnungskoeffizient von kupfer und nickel. . Rosenbohm, V.E.,. 1938, Physica, , pp. 5, pp. 385 – 398.

163. Low temperature thermal expansion of some metallic alloys. . Clark, A.F.,. 1968., Cryogenics,, pp. 8(5), pp. 282 – 289.

164. High-temperature thermal expansion of six metallic elements measured by dilatation method and X-ray diffraction. Suh, I.K., Ohta, H. and Waseda, Y.,. 1988. , Journal of Materials Science,, pp. 23(2), pp. 757 – 760.

165. R. K. Kirby, in American Institute of Physics Handbook, 2nd ed.,. McGraw-Hill, New York, 1963, pp. pp. 4 – 64.

166. Effects of anode porosity on thermal stress and failure probability of planar solid oxide fuel cell with bonded compliant seal. Luo, Yun, et al. 2016, International Journal of Hydrogen Energy , pp. 41.18: 7464-7474.

167. 3D imaging and quantification of interfaces in SOFC anodes. Tariq, F., Kishimoto, M., Yufit, V., Cui, G., Somalu, M. and Brandon, N.P.,. 2014, Journal of the European Ceramic Society, , pp. 34(15), pp.3755-3761.

168. Analysis of bi-metal thermostats. Timoshenko, S. 1925, JOSA, pp. 11(3), pp.233-255.

169. An evaluation of digital image correlation criteria for strain mapping applications. Tong, W. 2005, Strain, Vols. 41(4), , pp. pp.167-175.

170. TomoWarp2: a local digital volume correlation code. Tudisco, E., Andò, E., Cailletaud, R. and Hall, S.A.,. 2017, SoftwareX, Vols. 6, , pp. pp.267-270.

171. Characterization of pore-fracture networks and their evolution at various measurement scales in coal samples using X-ray μCT and a Fractal method. Zhou, H.W., Zhong, J.C., Ren, W.G., Wang, X.Y. and Yi, H.Y.,. 2018, International Journal of Coal Geology, Vols. 189,, pp. pp. 35-49.

172. Heenan, T. M. M., Lu, X., Iacoviello, F., Robinson, J.B., Brett, D.J.L. and Shearing, P.R., 2018. Thermally Driven SOFC Degradation in 4D: Part I. Microscale. Journal of The Electrochemical Society, 165(11), pp.F921-F931.

173. Heenan, T. M. M., Lu, X., Robinson, J.B., Iacoviello, F., Brett, D.J.L. and Shearing, P.R., 2018. Thermally Driven SOFC Degradation in 4D: Part II. Macroscale. Journal of The Electrochemical Society, 165(11), pp.F932-F941.Fractal

174. Heenan, T. M. M., Lu, X., Finegan, D. P., Robinson, J.B., Iacoviello, F., Bailey, J., Brett, D.J.L. and Shearing, P.R., 2018. Structural Evolutions within a Solid Oxide Fuel Cell Tracked Using Sub-Micron Digital Volume Correlation. Sustainable Energy and Fuels, in-press.

175. Heenan, T. M. M., D. P. Finegan, Bernhard Tjaden, Xuekun Lu, Francesco Iacoviello, Jason Millichamp, Dan JL Brett, and Paul R. Shearing. 4D nano-tomography of electrochemical energy devices using lab-based X-ray imaging. Nano Energy 47 (2018): 556-565.

176. Heenan, T. M. M., Robinson, J.B., Lu, X., Tjaden, B., Cervellino, A., Bailey, J., Brett, D.J.L. and Shearing, P.R., 2018. Understanding the thermo-mechanical behaviour of solid oxide fuel cell anodes using synchrotron X-ray diffraction. Solid State Ionics, 314, pp.156-164.

177. Heenan, T. M. M., Robinson, J.B., Lu, X., Bailey, J., Brett, D. J. L., and Shearing, P. R. Analysing the mechanical performance of solid oxide fuel cells at interfacial anode/electrolyte regions using sub-micron resolution 3D X-ray computed tomography. ECS Transactions 78, no. 1 (2017): 2317-2321.

178. Heenan, T. M. M., D. J. L. Brett, and P. R. Shearing. Mapping electrochemical activity in solid oxide fuel cells X-ray nano computed tomography of heterogeneous microstructures. Materials Today 20, no. 3 (2017): 155-156.

179. Heenan, T. M. M., D. J. L. Brett, and P. R. Shearing. Mapping electrochemical activity in solid oxide fuel cells X-ray nano computed tomography of heterogeneous microstructures. Materials Today Journal Cover, (2017).

180. Heenan, T. M. M., Josh J. Bailey, Xuekun Lu, James B. Robinson, Francesco Iacoviello, Donal P. Finegan, D. J. L. Brett, and P. R. Shearing. Three-Phase Segmentation of Solid Oxide Fuel Cell Anode Materials Using Lab Based X-ray Nano-Computed Tomography. Fuel Cells 17, no. 1 (2017): 75-82.

181. Heenan, T. M. M., Josh J. Bailey, Xuekun Lu, James B. Robinson, Francesco Iacoviello, Donal P. Finegan, D. J. L. Brett, and P. R. Shearing. Three-Phase Segmentation of Solid Oxide Fuel Cell Anode Materials Using Lab Based X-ray Nano-Computed Tomography. Fuel Cells Journal Cover (2017).

182. Heenan, T. M. M., D. J. L. Brett, and P. R. Shearing. X-ray attenuation properties of commonly employed solid oxide fuel cell materials. Journal of Physics, vol. 849, no. 1, p. 012017. IOP Publishing, 2017.

183. Robinson, J.B., Heenan, T.M.M, Jervis, J.R., Tan, C., Kendrick, E., Brett, D.J. and Shearing, P.R., 2018. Multiscale tomographic analysis of the thermal failure of Na-Ion batteries. Journal of Power Sources, 400, pp.360-368.

184. Tan, C., Heenan, T.M.M., Ziesche, R.F., Daemi, S.R., Hack, J., Maier, M., Marathe, S., Rau, C., Brett, D.J. and Shearing, P.R., 2018. Four-Dimensional Studies of Morphology Evolution in Lithium-Sulfur Batteries. ACS Applied Energy Materials.

185. Hack, J., Heenan T. M. M., Iacoviello F., Mansor N., Meyer Q., Shearing P., Brandon N., and Brett D. J. L.. A Structure and Durability Comparison of Membrane Electrode Assembly Fabrication Methods: Self-Assembled Versus Hot-Pressed. Journal of The Electrochemical Society 165, no. 6 (2018): F3045-F3052.

186. Lu, X., Heenan, T.M.M, Bailey, J.J., Li, T., Li, K., Brett, D.J. and Shearing, P.R., 2017. Correlation between triple phase boundary and the microstructure of Solid Oxide Fuel Cell anodes: The role of composition, porosity and Ni densification. Journal of Power Sources, 365, pp.210-219.

187. Bailey, J.J., Heenan, T.M.M., Finegan, D.P., Lu, X., Daemi, S.R., Iacoviello, F., Backeberg, N.R., Taiwo, O.O., Brett, D.J.L., Atkinson, A. and Shearing, P.R., 2017. Laser-preparation of geometrically optimised samples for X-ray nano-CT. Journal of microscopy, 267(3), pp.384-396.

188. Tan, C., Heenan, T.M.M., Ziesche, R.F., Daemi, S.R., Hack, J., Maier, M., Marathe, S., Rau, C., Brett, D.J. and Shearing, P.R., 2018. Four-dimensional studies of morphology evolution in lithium–sulfur batteries. ACS Applied Energy Materials, 1(9), pp.5090-5100.

189. Usseglio-Viretta F. L. E., Colclasure A., Mistry A., Yao K.P.C., Pouraghajan F., Finegan D.P., Heenan T.M.M, Abraham D.P., Mukherjee P.P., Wheeler D.R., Shearing P.R., Cooper S., Smith K., Resolving the

Discrepancy in Tortuosity Factor Estimation for Li-ion Battery Electrodes through Micro-Macro Modeling and Experiment, The Electrochemical Society, (2018), in-press.

190. Finegan D.P., Walker W., Darst J., Jervis R., Heenan T.M.M., Hack J., Rack A., Shearing P.R., Keyser M., Darcy E. Li-ion battery failure: Linking external risks to internal events, Power Sources Conference Proceedings, Denver, 2018.

191. Robinson, J.B., Finegan, D.P., Heenan, T.M.M., Smith, K., Kendrick, E., Brett, D.J. and Shearing, P.R., 2018. Microstructural Analysis of the Effects of Thermal Runaway on Li-Ion and Na-Ion Battery Electrodes. Journal of Electrochemical Energy Conversion and Storage, 15(1), p.011010.

192. Tan, C., Daemi, S., Taiwo, O., Heenan, T.M.M., Brett, D. and Shearing, P., 2018. Evolution of Electrochemical Cell Designs for In-Situ and Operando 3D Characterization. Materials, 11(11), p.2157.

193. Lu, X., Li, T., Bertei, A., Cho, J., Heenan, T. M.M., Rabuni, M., Li, K., Brett, D. and Shearing, P., 2018. The Application of Hierarchical Structures in Energy Devices: New Insights into the Design of Solid Oxide Fuel Cells with Enhanced Mass Transport. Energy & Environmental Science.

194. Finegan, D.P., Darcy E., Keyser M., Tjaden B., Heenan T.M.M, Jervis R., Bailey J. Vo N.T., Magdysyuk O.V., Drakopoulos M., Michiel M. Di., Rack A., Hinds G., Brett D.J.L., Shearing P.R. Identifying the Cause of Rupture of Li-Ion Batteries during Thermal Runaway. Advanced Science 5, no. 1 (2018): 1700369.

195. 21. Finegan, D.P., Darcy E., Keyser M., Tjaden B., Heenan T.M.M, Jervis R., Bailey J. Vo N.T., Magdysyuk O.V., Drakopoulos M., Michiel M. Di., Rack A., Hinds G., Brett D.J.L., Shearing P.R. Identifying the Cause of Rupture of Li-Ion Batteries during Thermal Runaway. Advanced ScienceJournal Cover, (2017).

196. Taiwo, O. O., Paz-García, J.M., Hall S.A., Heenan T.M.M, Finegan D.P., Mokso R., Villanueva-Pérez P., Patera A., Brett D.J.L, and Shearing P.R. Microstructural degradation of silicon electrodes during lithiation observed via operando X-ray tomographic imaging. Journal of Power Sources 342 (2017): 904-912.

197. Finegan, D. P., Tjaden B., Heenan T.M.M, Jervis R., Michiel M. Di., Rack A., Hinds G., Brett DJL, and Shearing P.R. Tracking internal temperature and structural dynamics during nail penetration of lithium-ion cells. Journal of The Electrochemical Society 164, no. 13 (2017): A3285-A3291.

198. Lu, X., Li T., Taiwo O. O., Bailey J., Heenan T.M.M., Li K., Brett D. J. L., and Shearing P. R.. Study of the tortuosity factors at multi-scale for a novel-structured SOFC anode. In Journal of Physics: Conference Series, vol. 849, no. 1, p. 012020. IOP Publishing, 2017.

199. Finegan, D.P., Darcy, E., Keyser, M., Tjaden, B., Heenan, T.M.M., Jervis, R., Bailey, J.J., Malik, R., Vo, N.T., Magdysyuk, O.V. and Atwood, R., 2017. Characterising thermal runaway within lithium-ion cells by inducing and monitoring internal short circuits. Energy & Environmental Science, 10(6), pp.1377-1388.

200. Finegan, D.P., Darcy, E., Keyser, M., Tjaden, B., Heenan, T.M.M., Jervis, R., Bailey, J.J., Malik, R., Vo, N.T., Magdysyuk, O.V. and Atwood, R.,. Characterising thermal runaway within lithium-ion cells by inducing and monitoring internal short circuits. Energy & Environmental Science, Journal Cover, (2017).

201. Jervis, R., Brown L.D., Neville T.P., Millichamp J., Finegan D.P., Heenan T.M.M., Brett D.J.L., and Shearing P.R.. Design of a miniature flow cell for in situ X-ray imaging of redox flow batteries. Journal of Physics D: Applied Physics 49, no. 43 (2016): 434002.

202. Robinson, J. B., Brown L.D., Jervis R., Taiwo, O.O., Heenan T.M.M., Millichamp, J., Mason, T.J., Neville T.P., Clague R., Eastwood D.S., Reinhard C., Lee P. D. , Brett D. J.L., Shearing P.R. Investigating the effect of thermal gradients on stress in solid oxide fuel cell anodes using combined synchrotron radiation and thermal imaging. Journal of Power Sources 288 (2015): 473-481.